

ZEOLITE CHEMISTRY STUDIED AT THE LEVEL OF SINGLE PARTICLES, MOLECULES AND ATOMS

Zeolietchemie Bestudeerd op het Niveau
van Individuele Deeltjes, Moleculen en Atomen
(met een samenvatting in het Nederlands)

Proefschrift

ter verkrijging van de graad van doctor aan de Universiteit Utrecht
op gezag van de rector magnificus, prof. dr. G. J. van der Zwaan,
ingevolge het besluit van het college voor promoties in het openbaar
te verdedigen op woensdag 30 maart 2016 des ochtends te 10.30 uur

door

Zoran Ristanović
geboren op 26 november 1985 te Čačak, Servië

Promotor: Prof. dr. ir. B. M. Weckhuysen

This PhD thesis was accomplished with financial support from the European Research Council (ERC) in the form of an advanced ERC grant (321140).

“You can kiss your family and friends good-bye and put miles between you, but at the same time you carry them with you in your heart, your mind, your stomach, because you do not just live in a world but a world lives in you.”

Frederick Buechner

*“Pa u tome i jeste sve: vraćati se.
S jedne tačke na zemlji čeznuti, polaziti i ponovo stizati.”*

M. Selimović

Mojim roditeljima

To my parents

Author: Ristanović, Zoran

Title: Zeolite Chemistry Studied at the Level of Single Particles, Molecules and Atoms

ISBN: 978-90-393-6523-6

Printed by: Gildeprint – The Netherlands

Table of Contents

CHAPTER 1	General Introduction	7
CHAPTER 2	Zeolite H-ZSM-5 Crystals as Model Systems: Crystallographic Architecture and Aluminium Distribution	25
CHAPTER 3	Quantitative 3D Fluorescence Imaging of Spatiotemporal Gradients in Reactivity of Zeolite H-ZSM-5 Crystals	55
CHAPTER 4	High-Resolution Fluorescence Imaging of Zeolite H-ZSM-5 Aggregates within Real-Life Fluid Catalytic Cracking Particles	81
CHAPTER 5	Acid-Catalyzed Oligomerization of Styrenes as a Versatile Probe for Single Molecule Fluorescence Microscopy Studies of Zeolite H-ZSM-5 Crystals	97
CHAPTER 6	X-ray Excited Optical Fluorescence and Diffraction Imaging of Chemical Reactivity and Crystallinity in a Zeolite Crystal: Crystallography and Molecular Spectroscopy in One X-ray Shot	125
CHAPTER 7	Summary, Concluding Remarks and Future Perspectives Nederlandse Samenvatting	147 159
List of Abbreviations		164
List of Publications and Presentations		166
Acknowledgements		169
About the Author		175

Chapter I

General Introduction

Ever since their discovery the impact and use of zeolites has no precedence in the field of heterogeneous catalysis. In our society, where sustainable energy resources are on high demand, it has become increasingly important to understand the fundamental aspects of zeolite chemistry that can lead to the rational design of better performing zeolite-based catalysts. The advancement of this knowledge is in part dependent on the available characterization tools that can resolve the intricate physicochemical changes taking place during catalytic processes. This PhD thesis uses modern characterization methods to study the crystallographic structure, aluminium distribution and related acidity, and spatio-temporal reactivity changes of zeolite crystals. Within this content, the purpose of this introduction is to familiarize the reader with the most important concepts of zeolite chemistry and the current status of characterization tools that are used to unravel zeolite catalysis.

1.1 Zeolites

Zeolites are microporous aluminosilicates with a well-defined crystalline structure and pores of molecular dimensions.^[1-3] A framework of a zeolite material is built of SiO_4 and AlO_4 tetrahedra, where each Si and Al atom are connected via oxygen atoms (Figure 1.1). These primary entities define a limited number of secondary building units,^[4] but the connection of secondary building blocks may result in a large variety of zeolite structures with different interconnections of atoms defining the pores of various sizes and connectivity. In general, zeolite structures are classified by their topologies, which define the type and size of small (< 0.45 nm, 8 member rings), medium (< 0.60 nm, 10 member rings), large (< 0.8 nm, 12 member rings), and ultra-large micropores (> 0.80 nm, > 14 member rings). The pores of different sizes can selectively accommodate molecules based on their dimensions. The connectivity of

zeolite pores determines the diffusion of guest molecules in 1-D, 2-D, or 3-D channel systems. Currently, there are 229 different zeolite topologies verified by the International Zeolite Association (IZA)^[5] and this number is constantly growing. It has been predicted that there are over 2.6 million possible ways to arrange atoms into a stable zeolite structure.^[6] This number clearly reflects an unexhausted potential to synthesize new zeolite materials with potentially improved catalytic properties.

Since their first application as catalysts, zeolites have inspired chemists to constantly explore endless ways to connect atoms into well-defined porous structures. This quest has led to discoveries of novel materials with improved catalytic properties. Based on this knowledge, several other fields of porous materials have recently emerged, such as mesoporous materials, hierarchical systems, metal-organic frameworks and zeotype molecular sieves.^[2] Clearly, the immense impact of zeolite chemistry and its general applicability to other fields of heterogeneous catalysis and materials science presents incentives for further fundamental studies of this class of heterogeneous catalysts.

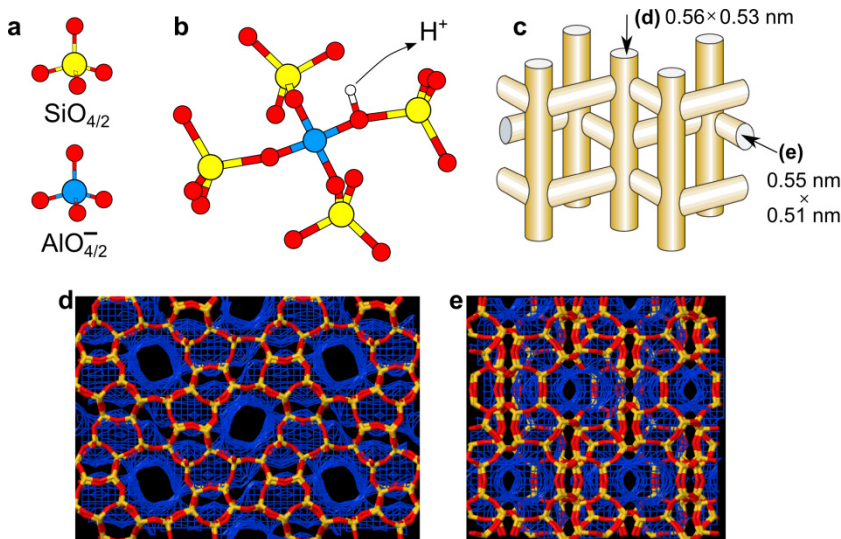


Figure 1.1 Building blocks of the zeolite framework and pore architecture of zeolite ZSM-5. a) Si and Al oxygen-shared tetrahedra as building units of zeolite materials. b) Si-O-Al-O-Si sequences as an example of their connectivity. The Brønsted acid site is presented in a close proximity of Al atom. c) Pore structure of zeolite ZSM-5 reproduced from ref. [7]. d,e) Views along the straight (d) and sinusoidal (e) pores of ZSM-5.^[5] The yellow-red framework represents Si-O atoms, whereas the blue network illustrates the propagation of the straight and sinusoidal pores.

1.2 Catalytic properties of zeolites and their industrial applications

The task of presenting the principles of zeolite chemistry and their applications is a daunting one considering the number of books and papers that have been published on this topic.^[1-3] The unique combination of acidic and shape-selective properties has made zeolites the work horse in oil-refining and petrochemical industry.^[2,8,9] Zeolites are also used in many other fields of application, such as detergents, water purification, nuclear industry, medicine, and agriculture.^[10]

In 1962 synthetic faujasites were introduced to the oil refining industry by Mobil Oil Corporation as new fluid catalytic cracking (FCC) catalysts of heavy petroleum distillates.^[7,11] The new zeolite-based catalysts were not only orders of magnitude more active than previously used amorphous silica-alumina catalysts, but they also produced significantly higher yields of gasoline – the most valuable product of the FCC process.^[11] Since then, zeolites have shown enormous synthetic potential for the production of high-value fine chemicals and organic intermediates. More than 90% of the industrial zeolite catalysts are applied in petrochemistry and refining industries that are technologically mature sectors.^[12,13] The success of zeolites in industry can be explained by their outstanding catalytic properties. Their highly crystalline structure with a precisely defined arrangement of building blocks enables good reproducibility in synthesis and controlled incorporation of acid sites.^[7] Zeolite micropores act as a shape-selective medium that prevents larger molecules of entering and reacting – a property that justifies the term “molecular sieves”. Numerous industrial processes are based on the concept of shape-selectivity, which, depending on the size of zeolite pores, enables selectivity towards reactants, products or transition states.^[7] Among many, the most important industrial applications of zeolites as catalysts are in fluid catalytic cracking,^[8,13] hydrocracking,^[14] dewaxing,^[7] isomerization and alkylation of hydrocarbons,^[15,16] and methanol-to-gasoline.^[17,18] Despite the large number of known topologies, only a few zeolites have found their way to wide-spread industrial applications, including mordenite (MOR), beta (BEA), Y (FAU), ferrierite (FER), and ZSM-5 (MFI), better known as the “big five”.

1.3 Zeolite ZSM-5

This PhD thesis entirely focuses on catalysis of zeolite ZSM-5 with the MFI topology. The framework structure of zeolite ZSM-5 consists of 10 membered-rings that form a 3-D network of channels, commonly known as straight and sinusoidal pores (Figure 1.1c-e). The size of the straight ($0.56\text{ nm} \times 0.53\text{ nm}$) and sinusoidal pores ($0.55\text{ nm} \times 0.51\text{ nm}$) is suitable for the accommodation of numerous small organic molecules. Furthermore, acid sites of ZSM-5 (Figure 1.1b) are considered stronger than of many other zeolites.^[19,20] This unique combination of acidic properties and pore architecture, enabled their use as solid acid catalysts in the alkylation and isomerization of aromatics,^[16] the oligomerization of light olefins,^[21] and the methanol-to-hydrocarbon reaction.^[17,22]

The ability to synthesize well-defined zeolite crystals and to tune their Si to Al ratio, as well as the architecture of microporous voids, according to the application is certainly without parallel in heterogeneous catalysis.^[23] The benefits of using well-defined single zeolite crystals are mostly related to the fundamental understanding of catalytic processes taking place in zeolites. In space- and time-averaged experiments, such as the ones in a catalytic bed, many details of sorption, diffusion, and catalysis are either lost or difficult to obtain. In many cases it is useful to know whether the catalysis takes place in the micropores of zeolite crystals or only close to the external surface. It is also very important to determine in which channels/cages the reaction takes place and if there is any role of crystalline defects in the observed catalysis.^[24]

Numerous synthetic procedures have reported the syntheses of highly crystalline zeolite ZSM-5 crystals.^[25–32] In order to better understand the chemistry of zeolite ZSM-5, large coffin-shaped zeolite ZSM-5 crystals have been extensively investigated as model systems (Figure 1.2). Their interesting morphology and complex intergrowth structure determine the accessibility of the crystalline interior and ability of reactants (products) to reach (leave) active sites. One of the intriguing discussions is related to the precise 3-D structure of the zeolite intergrowth,^[30,33–36] consisting of at least six individual subunits,^[30] and its impact on the diffusion and reactivity of a wide range of probe molecules and catalytic reactions. The examples include methanol-to-olefins (MTO),^[37–39] and staining oligomerization reactions with furfuryl alcohol,^[40] thiophene,^[41] and styrene derivates.^[42,43] Furthermore, due to their size ($100 \times 20 \times 20$

μm^3), combined with high crystallinity and well-defined intergrowth subunits, large zeolite ZSM-5 crystals have been an ideal subject for a wide variety of microscopy and spectroscopy methods, as well as structural analyses combined with sputtering and milling. This topic has been extensively investigated in our group for MFI- and CHA-type zeolite crystals within the scope of PhD theses by Kox,^[44] Karwacki,^[45] Mores,^[46] and Qian.^[47]

Both two- and three-component models for zeolite ZSM-5 intergrowths have been previously described in the literature.^[33,34,48] The two-component model describes a zeolite crystal as a 90° intergrowth of six subunits that meet at the centre of the crystal (Figure 1.2a). The three-component model contains three types of components in the zeolite crystal body (Figure 1.2b) with identical pore orientation in all subunits. As a consequence, these two intergrowth models differ in their overall pore geometry impacting also the molecular diffusion properties of the catalyst. Even though there is no general consensus on the crystal growth mechanism, it was noted that different types of crystals, originating from different synthesis procedures, or even from the same batch, may have different intergrowth structures.^[49]

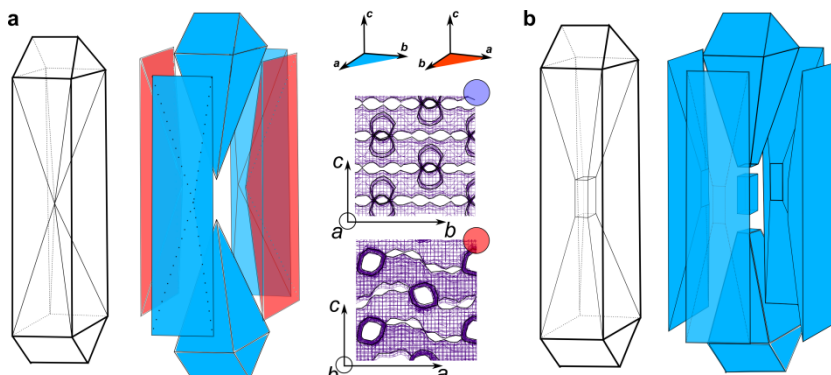


Figure 1.2 a) Two-component and b) three-component model of the intergrowth structure of a zeolite ZSM-5 crystal proposed in the literature. The red and blue subunits have different orientation of the crystallographic unit cell. In the middle, the orientation of the crystallographic unit cell vectors and directionality of the straight (along b lattice vector) and sinusoidal zeolite pores (along the a lattice vector).

Numerous techniques have been applied to visualize the structure and intergrowth-related chemistry of zeolite ZSM-5 crystals, comprising interference microscopy,^[50–53] UV-Vis and fluorescence microscopy,^[49,54–58] coherent anti-Stokes Raman scattering (CARS) microspectroscopy,^[59,60] synchrotron infra-red

microscopy,^[59,61,62] time-of-flight secondary ion mass spectrometry (TOF-SIMS),^[63] and electron backscatter diffraction (EBSD) combined with focused ion beam (FIB) milling.^[35,36] Unfortunately, none of the above-mentioned characterization studies provided non-invasive 3-D crystallographic information of a single zeolite ZSM-5 crystal. For example, optical microscopy techniques, such as UV-Vis, confocal fluorescence, and IR micro-spectroscopy, only gather *indirect* structural information via a detailed analysis of the location and orientation of specific probe molecules within the porous framework. Furthermore, as zeolites are poor electron scatterers the direct, invasive, and time-consuming FIB-EBSD approach may even lead to a complete amorphization of the probed crystalline material. In addition, the FIB-EBSD method suffers from the difficulties to interpret the inherently weak electron-backscattering diffraction patterns.^[64]

1.4 Zeolite acidity and aluminium distribution

Optimizing the number, nature, precise location, strength, and accessibility of acid sites in zeolite-based catalysts is of a paramount importance for their rational design.^[11,65] The acidic nature of zeolites is generally associated to bridging hydroxyl protons resulting from isomorphous substitution of Si (IV) by Al (III).^[66] Therefore, aluminum may be considered as the key element that introduces negative charge into the zeolite framework. This charge is often counterbalanced by protons leading to the formation of Brønsted acid sites (Figure 1.1b) that are responsible for catalytic activity. The concentration (often expressed as Si/Al ratio) and precise location of Al in the zeolite framework determine the number and strength of these acid sites^[66] and have detrimental effect on the success of various post-treatment methods that aim to improve molecular transport through the zeolite crystals, such as desilication and dealumination.^[67,68] Other examples of important Al-related species in zeolites include Lewis acid sites and extra-framework metal cations that are coordinated to Al atoms in zeolites.^[65]

The inhomogeneous distribution of Al within zeolites has been noted on numerous occasions and depends on the type of zeolite framework, Si/Al ratio, crystal size, and synthesis parameters.^[32] This leads to distinct Al distributions that are

characterized by either short-range (T-site distribution) or long-range (zoning or extra-framework) length scales, as illustrated in Figure 1.3.

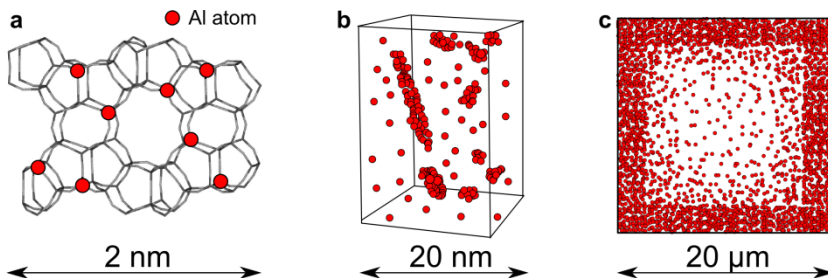


Figure 1.3 Inhomogeneous aluminium distribution on different length scales. a) Distribution over T crystallographic sites on the example of zeolite ZSM-5.^[69] b) Clustering of Al upon steaming of a zeolite framework. c) Long-range Al zoning on the example of large zeolite ZSM-5 crystals. The image represents a cross-section perpendicular to the long crystal axis (see Figure 1.2).

Determination of the Al distribution over T-sites is often complicated or not possible. For example, the unit cell of zeolite ZSM-5 has 12 distinct crystallographic T-sites, making their precise analysis very difficult.^[70–72] The distribution of Al atoms over specific T-sites is difficult to determine by X-ray diffraction (XRD) due to low scattering contrast between Si and Al. However, XRD studies that include ion-exchanged Cs-ZSM-5 and Tl-ZSM-5 zeolites have shown a non-random Al distribution over crystallographic T-sites.^[73,74] X-ray standing waves (XSW) have been successfully applied as a method to determine the T-position of Al in mm-sized crystals of zeolite scocelite.^[75] Al nuclear magnetic resonance (NMR) studies suggested that the Al distribution over the T-sites is kinetically controlled and not random, which can substantially depend on the conditions of zeolite synthesis.^[76,77] A recent study by Vjunov et al. confirms that identical zeolite types may have drastically different Al distribution over T-sites.^[78] Consequently, catalytic properties of zeolites (e.g., accessibility and strength of acid sites^[79,80]) may change dramatically depending on the distribution of Al over T-sites. While this problem has been widely recognized and extensively studied both experimentally and theoretically, to date the fundamental question as to the precise distribution of Al as a function of synthesis and how the distribution may change after processing remains elusive.

Another distinct type of Al distribution is commonly known as Al zoning and describes the long-range heterogeneous distribution of Al. Several studies have shown a heterogeneous surface and bulk distribution of Al within individual zeolite ZSM-5

crystals.^[26,30,31,81,82] Post-synthesis processing, such as exposure to steam, to either stabilize/activate or deactivate ZSM-5 also affects the long-range Al distribution through dealumination – a process in which aluminum is expelled from the framework structure leading to the generation of extra-framework Al.^[83] It is often speculated that the number and coordination of extra-framework Al species play a significant role in acid-catalyzed reactions.^[83–85]

Current analytical tools for studying Al distribution in zeolites and related acidity mostly rely on their bulk characterization. While providing very important chemical information, the major drawback of the bulk characterization methods is averaging the large ensemble of acid sites over many catalyst particles; therefore the spatial distribution of Al within individual particles goes undiscovered. Temperature programmed desorption (TPD) and infra-red (IR) spectroscopy of numerous probe molecules, such as pyridine^[86] and ammonia,^[87] represent valuable techniques to assess the Brønsted and Lewis acidity of zeolites and interactions of guest molecules with the zeolite framework.^[19,88–91] Solid-state ²⁷Al MAS NMR is frequently used to provide detailed information about the T-O-T angle and chemical nature of Al species and Brønsted acid sites,^[92–94] however the signal is averaged over the crystalline bulk and the analysis of T-site distribution still remains a difficult task.^[77,95] Conventional X-ray diffraction and electron-based techniques give no distinguishable contrast between Si and Al making high-resolution analysis very challenging. X-ray absorption fine structure (EXAFS) analysis in combination with NMR was recently used to quantitatively probe the bulk distribution of Al over T-sites in H- β zeolite.^[78] Other EXAFS studies have been used to determine in-situ structural changes of Al coordination in various zeolite topologies.^[96–99] X-ray standing waves (XSW) seem to offer a promising potential to locate Al at different crystallographic positions and study the strain changes in zeolite crystals during heating.^[75,100] X-ray tomography in the soft X-ray regime has allowed spatial mapping of Al and P coordination in zeolite ZSM-5, however still with a limited 3-D spatial resolution of ~ 70 nm.^[101–104] X-ray photoelectron spectroscopy (XPS)^[30,105,106] and energy-dispersive X-ray spectroscopy (EDX)^[31] are often used to provide surface and bulk characterization of Si/Al ratio and coordination of Al with penetrating depths of about 10 nm and 1 μ m, respectively. Each of the listed techniques provides very useful information about averaged chemical properties of acid sites. However, the exact spatial placement of Al in zeolite

materials before and after post-treatments is still difficult to assess and in most of the cases is still unknown.

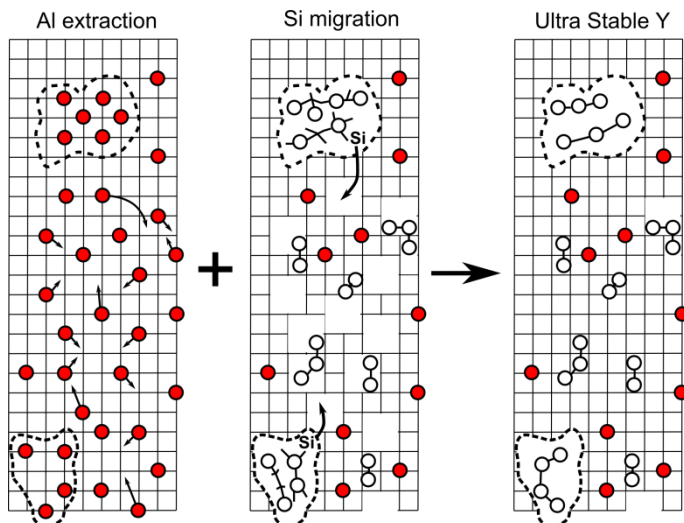


Figure 1.4 Dealumination of zeolite Y and formation of mesopores (reproduced from van Donk et al.^[107]). The grid denotes the zeolite framework, the red circles are framework aluminum atoms, the open circles are Al atoms extracted from the framework, and the dotted lines indicate the mesopores.

1.5 Steaming of zeolites

In Section 1.3 we have briefly discussed the benefits of large zeolite crystals as highly crystalline model systems to study fundamental aspects of zeolite catalysis. However, molecular transport – and therefore the reactivity – in purely microporous zeolite crystals is tremendously hindered by the slow diffusion of reactants and reaction products.^[108,109] For this reason, significant efforts in the zeolite synthesis were directed towards shortening the intracrystalline diffusion pathways and facilitating molecular transport. The most straightforward way to do this is to reduce the crystallite size or synthesize small sheets of zeolite.^[110,111] However, the use of small or delaminated zeolite crystals is not always feasible on a reactor scale.^[107,112] The alternative way to enhance the accessibility of crystalline bulk is to induce mesopores (2-50 nm in diameter) within individual, microporous zeolite crystals. The most common intracrystalline approaches for the creation of mesopores are steaming, acid, and base leaching.^[68,113,114] Recent research efforts in the field have recognized that the texture and quality of mesopores, more specifically their size, distribution, interconnection,

and surface accessibility, determine the catalytic properties of zeolites; i.e, the mass transport through zeolite particles, the degree of shape-selectivity for a particular catalytic process, and finally, the lifetime of hierarchically structured zeolite catalysts.^[115-117] The properties of mesopores determine the mass transport throughout the zeolite particle and the degree of shape-selectivity for a particular catalytic process.

Steaming of zeolites (also known as hydrothermal treatment) is the most preferred, simple, and cost-efficient industrial post-treatment method to shorten the effective diffusion pathways and enhance the accessibility of acid sites via the creation of mesopores.^[68,107,118] Steaming is typically performed in a controlled manner, in the presence of steam and at temperatures higher than 773 K. The process can be also induced by water formed in high-temperature reactions or present in the gas-feed. During steaming the selective hydrolysis of Al-O bonds takes place, which inevitably leads to dealumination of the zeolite framework, as depicted in Figure 1.4.^[107,119] This results in a partial or a complete loss of Brønsted acidity. The resulting mesoporosity of the zeolite framework will depend on the content of framework Al and the degree of dealumination.^[120,121] Dealumination is naturally accompanied by a change in aluminum coordination and acid site strength and distribution. The extra-framework Al species are mobile in nature and together with partial amorphization of the framework may lead to extra-framework debris that is further blocking zeolite pores (Figure 1.4). Zeolite dealumination may significantly alter inter- and intraparticle distribution of acidity, leading to large differences in catalytic activity,^[122] or synergistic interaction between Brønsted (framework) and Lewis (extra-framework) acid sites.^[85] Dealumination of zeolites and coordination of Al upon steaming have been studied with numerous characterization techniques,^[119] but the exact distribution and displacement of Al atoms after steaming is not possible to map with conventional methods. Clearly, understanding and controlling the steaming process is critical for the most efficient use of hierarchical zeolite catalysts.

1.6 Scope and outline of the PhD thesis

This PhD thesis describes state-of-the-art characterization approaches used to study the crystallographic architecture, acidity, and reactivity of zeolite H-ZSM-5 crystals. More specifically, parent and steamed zeolite H-ZSM-5 model crystals were

characterized using an arsenal of diffraction, sputtering, and atom-probe tomography techniques. This approach was capable of resolving the long and short-range Al distribution, assessing the crystallography of Al zoning within single crystals and nearest neighbors of Al with atomic resolution in 3-D. The crystals characterized in such a way were further used as model systems to establish single molecule fluorescence methodologies capable to trace individual catalytic turnovers and the formation of single molecule fluorescent products at Brønsted acid sites.

In **Chapter 2**, a general approach to characterize the studied parent and steamed zeolite H-ZSM-5 crystals is presented. A novel micro-X-ray diffraction approach was used to resolve the crystallographic structure of individual H-ZSM-5 crystals, as well as Al zoning within the crystals. The distribution of Al in parent and steamed zeolite crystals is further studied by using time-of-flight secondary ion mass spectrometry, revealing large changes in Al distribution upon steaming. Finally, atom probe tomography was used to obtain unprecedented quantitative insights into the spatial arrangement of individual Al atoms and their nearest neighbors before and after steaming.

In **Chapter 3**, we introduce single molecule fluorescence microscopy as a highly sensitive and quantitative tool to study catalytic processes in real time and with the ultimate sensitivity of single catalytic turnovers. The furfuryl alcohol oligomerization in combination with nanometer accuracy by stochastic chemical reactions (NASCA) microscopy were used as a powerful methodology to resolve the spatiotemporal changes in reactivity of parent and steamed zeolite crystals, with quantitative emphasis on surface diffusion barriers and nanoscopic differences in reactivity.

In **Chapter 4** the concepts of high-resolution single molecule fluorescence were extended to a highly complex, real-life industrial catalyst, namely, zeolite ZSM-5-based fluid catalytic cracking (FCC) particles. The concepts presented in Chapter 3 are combined with another powerful imaging approach known as super-resolution optical fluctuation imaging (SOFI). We will demonstrate that both SOFI and NASCA methods can be successfully used for highly complex catalyst materials to localize zeolite particulates and extract information about their size and local catalytic activity.

In **Chapter 5**, the single molecule fluorescence methodology has been extended to the oligomerization of styrene derivatives as a probe reaction to study

Brønsted chemistry of zeolite H-ZSM-5. The effects of substituents on the styrene moiety and polarity of solvents were quantified with single turnover sensitivity. The probe reaction can be used to generate highly fluorescent and photostable single molecule products that enable studying the accessibility, product shape-selectivity, and proton transfer rates of H-ZSM-5 crystals in different solvent environments.

Chapter 6 combines the μ -XRD approach described in Chapter 2 and the styrene oligomerization reaction studied in Chapter 5 to develop a method that can simultaneously study the crystallographic structure and reactivity of zeolite H-ZSM-5 crystals upon steaming. Hard X-rays were used to record the spatially resolved maps of X-ray excited optical fluorescence (XEOF) spectra of the oligomeric 4-methoxystyrene molecules and XRD maps of individual zeolite H-ZSM-5 crystals. The method is further employed to correlate the crystallographic changes as studied by XRD, with the reactivity and product selectivity of individual zeolite H-ZSM-5 crystals, as studied by XEOF.

Chapter 7 summarizes the results presented in this PhD thesis and ends with some concluding remarks and future perspectives.

References

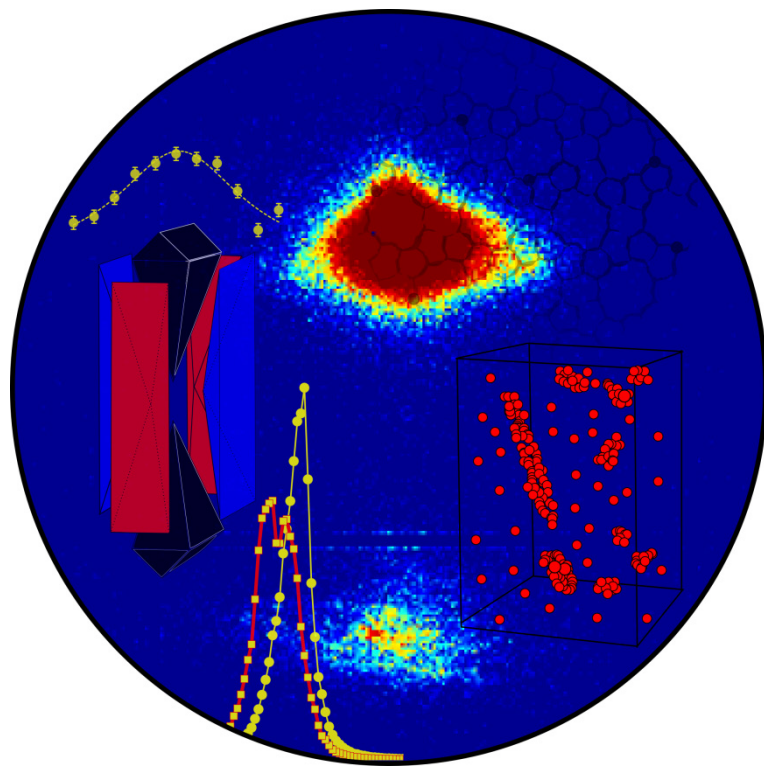
- [1] G. Ertl, H. Knözinger, F. Schüth, J. Weitkamp, Eds., *Handbook of Heterogeneous Catalysis*, Wiley-VCH, Weinheim, **2008**.
- [2] J. Čejka, A. Corma, S. Zones, Eds., *Zeolites and Catalysis: Synthesis, Reactions and Applications*, Wiley-VCH, Weinheim, **2010**.
- [3] F. Schüth, K. S. W. Sing, J. Weitkamp, Eds., *Handbook of Porous Solids*, Wiley-VCH, Weinheim, **2002**.
- [4] P. A. Wright, G. M. Pearce, in *Zeolites and Catalysis: Synthesis, Reactions and Applications* (Eds.: J. Čejka, A. Corma, S. Zones), Wiley-VCH, Weinheim, **2010**, pp. 171–207.
- [5] C. Baerlocher, L. B. McCusker, *Database of Zeolite Structures*. <http://www.iza-structure.org/databases/>, **2015**.
- [6] R. Pophale, P. A. Cheeseman, M. W. Deem, *Phys. Chem. Chem. Phys.* **2011**, *13*, 12407–12412.
- [7] J. Hagen, in *Industrial Catalysis*, Wiley-VCH, Weinheim, **2005**, pp. 239–259.
- [8] A. Corma, in *Studies in Surface Science and Catalysis* (Eds.: P.A. Jacobs and R.A. van Santen), Elsevier, Amsterdam, **1989**, pp. 49–67.
- [9] W. Vermeiren, J.-P. Gilson, *Top. Catal.* **2009**, *52*, 1131–1161.
- [10] V. Sebastián, C. Casado, J. Coronas, in *Zeolites and Catalysis* (Eds.: J. Čejka, A. Corma, S. Zones), Wiley-VCH, Weinheim, **2010**, pp. 389–410.
- [11] J. Weitkamp, *Solid State Ion.* **2000**, *131*, 175–188.
- [12] G. Bellussi, A. Carati, R. Millini, in *Zeolites and Catalysis: Synthesis, Reactions and Applications* (Eds.: J. Čejka, A. Corma, S. Zones), Wiley-VCH, Weinheim, **2010**, pp. 449–491.
- [13] E. T. C. Vogt, B. M. Weckhuysen, *Chem. Soc. Rev.* **2015**, 7342–7370.
- [14] M. Rigutto, in *Zeolites and Catalysis: Synthesis, Reactions and Applications* (Eds.: J. Čejka, A. Corma, S. Zones), Wiley-VCH, Weinheim, **2010**, pp. 547–584.
- [15] S. T. Sie, J. E. Maxwell, J. K. Minderhoud, W. J. H. Stork, J. a. R. van Veen, J. Weitkamp, Y. Traa, C. T. O'Connor, H. Heinemann, D. D. Whitehurst, M. L. Gorbaty, W. Vielstich, T. Iwasita, P. Pichat, in *Handbook of Heterogeneous Catalysis* (Eds.: G. Ertl, H. Knözinger, J. Weitkamp), Wiley-VCH, Weinheim, **1997**, pp. 2006–2122.
- [16] C. S. Lee, T. J. Park, W. Y. Lee, *Appl. Catal. Gen.* **1993**, *96*, 151–161.
- [17] M. Stöcker, *Microporous Mesoporous Mater.* **1999**, *29*, 3–48.
- [18] M. Stöcker, in *Zeolites and Catalysis: Synthesis, Reactions and Applications* (Eds.: J. Čejka, A. Corma, S. Zones), Wiley-VCH, Weinheim, **2010**, pp. 687–711.
- [19] L. Damjanović, A. Auroux, in *Zeolite Characterization and Catalysis* (Eds.: A.W. Chester, E.G. Derouane), Springer, Dordrecht, **2010**, pp. 107–167.
- [20] B. Xu, C. Sievers, S. B. Hong, R. Prins, J. A. van Bokhoven, *J. Catal.* **2006**, *244*, 163–168.
- [21] R. J. Quann, L. A. Green, S. A. Tabak, F. J. Krambeck, *Ind. Eng. Chem. Res.* **1988**, *27*, 565–570.
- [22] U. Olsbye, S. Svelle, M. Bjørgen, P. Beato, T. V. W. Janssens, F. Joensen, S. Bordiga, K. P. Lillerud, *Angew. Chem. Int. Ed.* **2012**, *51*, 5810–5831.
- [23] M. Boudart, *Chem. Rev.* **1995**, *95*, 661–666.
- [24] R. A. Schoonheydt, *Angew. Chem. Int. Ed.* **2008**, *47*, 9188–9191.
- [25] G. A. Jablonski, L. B. Sand, J. A. Gard, *Zeolites* **1986**, *6*, 396–402.
- [26] R. Althoff, B. Schulz-Dobrick, F. Schüth, K. Unger, *Microporous Mater.* **1993**, *1*, 207–218.
- [27] M. Ghamami, L. B. Sand, *Zeolites* **1983**, *3*, 155–162.
- [28] S. Z. Chen, K. Huddersman, D. Keir, L. V. C. Rees, *Zeolites* **1988**, *8*, 106–109.
- [29] J. Kornatowski, *Zeolites* **1988**, *8*, 77–78.

- [30] L. Karwacki, M. H. F. Kox, D. A. Matthijs de Winter, M. R. Drury, J. D. Meeldijk, E. Stavitski, W. Schmidt, M. Mertens, P. Cubillas, N. John, A. Chan, N. Kahn, S. R. Bare, M. Anderson, J. Kornatowski, B. M. Weckhuysen, *Nat. Mater.* **2009**, *8*, 959–965.
- [31] N. Danilina, F. Krumeich, S. A. Castelanelli, J. A. van Bokhoven, *J. Phys. Chem. C* **2010**, *114*, 6640–6645.
- [32] J. A. van Bokhoven, N. Danilina, in *Zeolites and Catalysis: Synthesis, Reactions and Applications* (Eds.: J. Čejka, A. Corma, S. Zones), Wiley-VCH, Weinheim, **2010**, pp. 283–300.
- [33] D. G. Hay, H. Jaeger, K. G. Wilshier, *Zeolites* **1990**, *10*, 571–576.
- [34] J. R. Agger, N. Hanif, C. S. Cundy, A. P. Wade, S. Dennison, P. A. Rawlinson, M. W. Anderson, *J. Am. Chem. Soc.* **2003**, *125*, 830–839.
- [35] E. Stavitski, M. R. Drury, D. A. M. de Winter, M. H. F. Kox, B. M. Weckhuysen, *Angew. Chem. Int. Ed.* **2008**, *47*, 5637–5640.
- [36] M. B. J. Roeffaers, R. Ameloot, A.-J. Bons, W. Mortier, G. De Cremer, R. de Kloe, J. Hofkens, D. E. De Vos, B. F. Sels, *J. Am. Chem. Soc.* **2008**, *130*, 13516–13517.
- [37] D. Mores, E. Stavitski, S. P. Verkleij, A. Lombard, A. Cabiac, L. Rouleau, J. Patarin, A. Simon-Masseron, B. M. Weckhuysen, *Phys. Chem. Chem. Phys.* **2011**, *13*, 15985–15994.
- [38] D. Mores, E. Stavitski, M. H. F. Kox, J. Kornatowski, U. Olsbye, B. M. Weckhuysen, *Chem. – Eur. J.* **2008**, *14*, 11320–11327.
- [39] J. P. Hofmann, D. Mores, L. R. Aramburo, S. Teketel, M. Rohnke, J. Janek, U. Olsbye, B. M. Weckhuysen, *Chem. – Eur. J.* **2013**, *19*, 8533–8542.
- [40] M. B. J. Roeffaers, B. F. Sels, H. Uji-i, B. Blanpain, P. L’hoëst, P. A. Jacobs, F. C. De Schryver, J. Hofkens, D. E. De Vos, *Angew. Chem. Int. Ed.* **2007**, *46*, 1706–1709.
- [41] M. H. F. Kox, A. Mijovilovich, J. J. H. B. Sättler, E. Stavitski, B. M. Weckhuysen, *ChemCatChem* **2010**, *2*, 564–571.
- [42] M. H. F. Kox, E. Stavitski, B. M. Weckhuysen, *Angew. Chem. Int. Ed.* **2007**, *46*, 3652–3655.
- [43] C. Sprung, B. M. Weckhuysen, *J. Am. Chem. Soc.* **2015**, *137*, 1916–1928.
- [44] M. H. F. Kox, *Spatial Heterogeneities within an Individual Catalyst Particle during Reaction as Revealed by in-Situ Micro-Spectroscopy*, Utrecht University, **2009**.
- [45] L. Karwacki, *Internal Architecture and Molecular Transport Barriers of Large Zeolite Crystals*, Utrecht University, **2010**.
- [46] D. Mores, *In-Situ Micro-Spectroscopy on Coke Formation Processes in Zeolites*, Utrecht University, **2011**.
- [47] Q. Qian, *Catalytic Conversion of Alcohols into Olefins: Spectroscopy, Kinetics and Catalyst Deactivation*, Utrecht University, **2014**.
- [48] G. D. Price, J. J. Pluth, J. V. Smith, J. M. Bennett, R. L. Patton, *J. Am. Chem. Soc.* **1982**, *104*, 5971–5977.
- [49] M. B. J. Roeffaers, R. Ameloot, M. Baruah, H. Uji-i, M. Bulut, G. De Cremer, U. Müller, P. A. Jacobs, J. Hofkens, B. F. Sels, D. E. De Vos, *J. Am. Chem. Soc.* **2008**, *130*, 5763–5772.
- [50] O. Geier, S. Vasenkov, E. Lehmann, J. Kärger, U. Schemmert, R. A. Rakoczy, J. Weitkamp, *J. Phys. Chem. B* **2001**, *105*, 10217–10222.
- [51] D. Tzoulaki, L. Heinke, W. Schmidt, U. Wilczok, J. Kärger, *Angew. Chem. Int. Ed.* **2008**, *47*, 3954–3957.
- [52] F. Hibbe, C. Chmelik, L. Heinke, S. Pramanik, J. Li, D. M. Ruthven, D. Tzoulaki, J. Kärger, *J. Am. Chem. Soc.* **2011**, *133*, 2804–2807.
- [53] C. Chmelik, J. Kärger, *Chem. Soc. Rev.* **2010**, *39*, 4864–4884.

- [54] C. Weidenthaler, R. X. Fischer, R. D. Shannon, O. Medenbach, *J. Phys. Chem.* **1994**, *98*, 12687–12694.
- [55] L. Karwacki, E. Stavitski, M. H. F. Kox, J. Kornatowski, B. M. Weckhuysen, *Angew. Chem. Int. Ed.* **2007**, *46*, 7228–7231.
- [56] M. H. F. Kox, E. Stavitski, J. C. Groen, J. Pérez-Ramírez, F. Kapteijn, B. M. Weckhuysen, *Chem.–Eur. J.* **2008**, *14*, 1718–1725.
- [57] G. D. Cremer, B. F. Sels, D. E. De Vos, J. Hofkens, M. B. J. Roeffaers, *Chem. Soc. Rev.* **2010**, *39*, 4703–4717.
- [58] R. A. Schoonheydt, *Chem. Soc. Rev.* **2010**, *39*, 5051–5066.
- [59] M. H. F. Kox, K. F. Domke, J. P. R. Day, G. Rago, E. Stavitski, M. Bonn, B. M. Weckhuysen, *Angew. Chem. Int. Ed.* **2009**, *48*, 8990–8994.
- [60] K. F. Domke, J. P. R. Day, G. Rago, T. A. Riemer, M. H. F. Kox, B. M. Weckhuysen, M. Bonn, *Angew. Chem. Int. Ed.* **2012**, *51*, 1343–1347.
- [61] E. Stavitski, M. H. F. Kox, I. Swart, F. M. F. de Groot, B. M. Weckhuysen, *Angew. Chem. Int. Ed.* **2008**, *47*, 3543–3547.
- [62] E. Stavitski, B. M. Weckhuysen, *Chem. Soc. Rev.* **2010**, *39*, 4615–4625.
- [63] J. P. Hofmann, M. Rohnke, B. M. Weckhuysen, *Phys. Chem. Chem. Phys.* **2014**, *16*, 5465–5474.
- [64] G. M. Pennock, A. Barnhoorn, A. J. Bons, M. R. Drury, *J. Mater. Sci. Lett.* **2001**, *20*, 1099–1101.
- [65] M. Hunger, in *Zeolites and Catalysis: Synthesis, Reactions and Applications* (Eds.: J. Čejka, A. Corma, S. Zones), Wiley-VCH, Weinheim, **2010**, pp. 493–546.
- [66] G. J. Kramer, R. A. Van Santen, *J. Am. Chem. Soc.* **1993**, *115*, 2887–2897.
- [67] J. A. van Bokhoven, D. C. Koningsberger, P. Kunkeler, H. van Bekkum, A. P. M. Kentgens, *J. Am. Chem. Soc.* **2000**, *122*, 12842–12847.
- [68] J. C. Groen, T. Bach, U. Ziese, A. M. Paulaime-van Donk, K. P. de Jong, J. A. Moulijn, J. Pérez-Ramírez, *J. Am. Chem. Soc.* **2005**, *127*, 10792–10793.
- [69] J. Dědeček, Z. Sobálik, B. Wichterlová, *Catal. Rev.* **2012**, *54*, 135–223.
- [70] G. T. Kokotailo, S. L. Lawton, D. H. Olson, W. M. Meier, *Nature* **1978**, *272*, 437–438.
- [71] D. H. Olson, G. T. Kokotailo, S. L. Lawton, W. M. Meier, *J. Phys. Chem.* **1981**, *85*, 2238–2243.
- [72] H. van Koningsveld, J. C. Jansen, H. van Bekkum, *Zeolites* **1990**, *10*, 235–242.
- [73] D. H. Olson, N. Khosrovani, A. W. Peters, B. H. Toby, *J. Phys. Chem. B* **2000**, *104*, 4844–4848.
- [74] N. H. Heo, C. W. Kim, H. J. Kwon, G. H. Kim, S. H. Kim, S. B. Hong, K. Seff, *J. Phys. Chem. C* **2009**, *113*, 19937–19956.
- [75] J. A. van Bokhoven, T.-L. Lee, M. Drakopoulos, C. Lamberti, S. Thieß, J. Zegenhagen, *Nat. Mater.* **2008**, *7*, 551–555.
- [76] O. H. Han, C.-S. Kim, S. B. Hong, *Angew. Chem. Int. Ed.* **2002**, *41*, 469–472.
- [77] S. Sklenak, J. Dědeček, C. Li, B. Wichterlová, V. Gábová, M. Sierka, J. Sauer, *Angew. Chem. Int. Ed.* **2007**, *46*, 7286–7289.
- [78] A. Vjunov, J. L. Fulton, T. Huthwelker, S. Pin, D. Mei, G. K. Schenter, N. Govind, D. M. Camaioni, J. Z. Hu, J. A. Lercher, *J. Am. Chem. Soc.* **2014**, *136*, 8296–8306.
- [79] U. Eichler, M. Brändle, J. Sauer, *J. Phys. Chem. B* **1997**, *101*, 10035–10050.
- [80] G. Barone, G. Casella, S. Giuffrida, D. Duca, *J. Phys. Chem. C* **2007**, *111*, 13033–13043.
- [81] R. von Ballmoos, W. M. Meier, *Nature* **1981**, *289*, 782–783.
- [82] K. Chao, J. Chern, *Zeolites* **1988**, *8*, 82–85.

- [83] R. M. Lago, W. O. Haag, R. J. Mikovsky, D. H. Olson, S. D. Hellring, K. D. Schmitt, G. T. Kerr, in *Studies in Surface Science and Catalysis* (Eds.: A.I. and J.W.W. Y. Murakami), Elsevier, Amsterdam, **1986**, pp. 677–684.
- [84] F. Lónyi, J. H. Lunsford, *J. Catal.* **1992**, *136*, 566–577.
- [85] R. A. Beyerlein, C. Choi-Feng, J. B. Hall, B. J. Huggins, G. J. Ray, *Top. Catal.* **1997**, *4*, 27–42.
- [86] F. Jin, Y. Li, *Catal. Today* **2009**, *145*, 101–107.
- [87] G. V. A. Martins, G. Berlier, C. Bisio, S. Coluccia, H. O. Pastore, L. Marchese, *J. Phys. Chem. C* **2008**, *112*, 7193–7200.
- [88] W. K. Hall, B. E. Spiewak, R. D. Cortright, J. A. Dumesic, H. Knözinger, H. Pfeifer, V. B. Kazansky, G. C. Bond, in *Handbook of Heterogeneous Catalysis* (Eds.: G. Ertl, H. Knözinger, J. Weitkamp), Wiley-VCH, Weinheim, **1997**, pp. 689–770.
- [89] F. Thibault-Starzyk, I. Stan, S. Abelló, A. Bonilla, K. Thomas, C. Fernandez, J.-P. Gilson, J. Pérez-Ramírez, *J. Catal.* **2009**, *264*, 11–14.
- [90] S. Bordiga, C. Lamberti, F. Bonino, A. Travert, F. Thibault-Starzyk, *Chem. Soc. Rev.* **2015**, *44*, 7262–7341.
- [91] A. W. Chester, E. G. Derouane, Eds., *Zeolite Characterization and Catalysis: A Tutorial*, Springer, Dordrecht, **2009**.
- [92] S. Ramdas, J. Klinowski, *Nature* **1984**, *308*, 521–523.
- [93] L. Mafra, J. Klinowski, *eMagRes* **2013**, *2*, 149–184.
- [94] E. Brunner, H. Pfeifer, in *Acidity and Basicity*, Springer, Heidelberg, **2008**, pp. 1–43.
- [95] J. Dedecek, M. J. Lucero, C. Li, F. Gao, P. Klein, M. Urbanova, Z. Tvaruzkova, P. Sazama, S. Sklenak, *J. Phys. Chem. C* **2011**, *115*, 11056–11064.
- [96] J. A. van Bokhoven, H. Sambe, D. E. Ramaker, D. C. Koningsberger, *J. Phys. Chem. B* **1999**, *103*, 7557–7564.
- [97] J. A. van Bokhoven, D. C. Koningsberger, P. Kunkeler, H. van Bekkum, *J. Catal.* **2002**, *211*, 540–547.
- [98] J. A. van Bokhoven, A. M. J. van der Eerden, D. C. Koningsberger, *J. Am. Chem. Soc.* **2003**, *125*, 7435–7442.
- [99] J. A. van Bokhoven, A. M. J. van der Eerden, R. Prins, *J. Am. Chem. Soc.* **2004**, *126*, 4506–4507.
- [100] W. Cha, N. C. Jeong, S. Song, H. Park, T. C. Thanh Pham, R. Harder, B. Lim, G. Xiong, D. Ahn, I. McNulty, J. Kim, K. B. Yoon, I. K. Robinson, H. Kim, *Nat. Mater.* **2013**, *12*, 729–734.
- [101] L. R. Aramburo, E. de Smit, B. Arstad, M. M. van Schooneveld, L. Sommer, A. Juhin, T. Yokosawa, H. W. Zandbergen, U. Olsbye, F. M. F. de Groot, B. M. Weckhuysen, *Angew. Chem. Int. Ed.* **2012**, *51*, 3616–3619.
- [102] L. R. Aramburo, Y. Liu, T. Tyliszczak, F. M. F. de Groot, J. C. Andrews, B. M. Weckhuysen, *ChemPhysChem* **2013**, *14*, 496–499.
- [103] H. E. van der Bij, D. Cicmil, J. Wang, F. Meirer, F. M. F. de Groot, B. M. Weckhuysen, *J. Am. Chem. Soc.* **2014**, *136*, 17774–17787.
- [104] H. E. van der Bij, B. M. Weckhuysen, *Phys. Chem. Chem. Phys.* **2014**, *16*, 9892.
- [105] F. Collignon, P. A. Jacobs, P. Grobet, G. Poncelet, *J. Phys. Chem. B* **2001**, *105*, 6812–6816.
- [106] L. R. Aramburo, L. Karwacki, P. Cubillas, S. Asahina, D. A. M. de Winter, M. R. Drury, I. L. C. Buurmans, E. Stavitski, D. Mores, M. Daturi, P. Bazin, P. Dumas, F. Thibault-Starzyk, J. A. Post, M. W. Anderson, O. Terasaki, B. M. Weckhuysen, *Chem. – Eur. J.* **2011**, *17*, 13773–13781.
- [107] S. van Donk, A. H. Janssen, J. H. Bitter, K. P. de Jong, *Catal. Rev.* **2003**, *45*, 297–319.
- [108] J. van den Bergh, J. Gascon, F. Kapteijn, in *Zeolites and Catalysis: Synthesis, Reactions and Applications* (Eds.: J. Čejka, A. Corma, S. Zones), Wiley-VCH, Weinheim, **2010**, pp. 361–387.

- [109] S. Brandani, H. G. Karge, J. Weitkamp, Eds., *Molecular Sieves: Science and Technology. Vol. 7: Adsorption and Diffusion*, Springer, Berlin, **2008**.
- [110] X. Zhang, D. Liu, D. Xu, S. Asahina, K. A. Cychosz, K. V. Agrawal, Y. A. Wahedi, A. Bhan, S. A. Hashimi, O. Terasaki, M. Thommes, M. Tsapatsis, *Science* **2012**, *336*, 1684–1687.
- [111] J. Zečević, K. P. de Jong, *ChemCatChem* **2013**, *5*, 417–418.
- [112] S. Mitchell, N.-L. Michels, J. Pérez-Ramírez, *Chem. Soc. Rev.* **2013**, *42*, 6094–6112.
- [113] D. Verboekend, G. Vilé, J. Pérez-Ramírez, *Adv. Funct. Mater.* **2012**, *22*, 916–928.
- [114] D. Fodor, F. Krumeich, R. Hauert, J. A. van Bokhoven, *Chem. – Eur. J.* **2015**, *21*, 6272–6277.
- [115] L. Zhang, A. N. C. van Laak, P. E. de Jongh, K. P. de Jong, in *Zeolites and Catalysis: Synthesis, Reactions and Applications* (Eds.: J. Čejka, A. Corma, S. Zones), Wiley-VCH, Weinheim, **2010**, pp. 237–282.
- [116] M. Milina, S. Mitchell, P. Crivelli, D. Cooke, J. Pérez-Ramírez, *Nat. Commun.* **2014**, *5*, 3922.
- [117] Y. Wei, T. E. Parmentier, K. P. de Jong, J. Zečević, *Chem. Soc. Rev.* **2015**, *44*, 7234–7261.
- [118] N.-L. Michels, S. Mitchell, M. Milina, K. Kunze, F. Krumeich, F. Marone, M. Erdmann, N. Marti, J. Pérez-Ramírez, *Adv. Funct. Mater.* **2012**, *22*, 2509–2518.
- [119] L. H. Ong, M. Dömök, R. Olindo, A. C. van Veen, J. A. Lercher, *Microporous Mesoporous Mater.* **2012**, *164*, 9–20.
- [120] T. Sano, H. Ikeya, T. Kasuno, Z. B. Wang, Y. Kawakami, K. Soga, *Zeolites* **1997**, *19*, 80–86.
- [121] T. Sano, N. Yamashita, Y. Iwami, K. Takeda, Y. Kawakami, *Zeolites* **1996**, *16*, 258–264.
- [122] K.-L. Liu, A. V. Kubarev, J. Van Loon, H. Uji-i, D. E. De Vos, J. Hofkens, M. B. J. Roeckaers, *ACS Nano* **2014**, *8*, 12650–12659.



Chapter 2 is based on the following manuscripts:

- [1] “Intergrowth Structure and Aluminium Zoning of a Zeolite ZSM-5 Crystal as Resolved by Synchrotron-Based Micro X-Ray Diffraction Imaging”, Z. Ristanović[§], J. P. Hofmann[§], U. Deka, T. U. Schülli, M. Rohnke, A. M. Beale, and B. M. Weckhuysen, *Angew. Chem. Int. Ed.* **2013**, *52*, 13382–13386.
- [2] “Determining the Location and Nearest Neighbours of Aluminium in Zeolites with Atom Probe Tomography”, D. E. Perea[§], I. Arslan[§], J. Liu, Z. Ristanović, L. Kovarik, B. W. Arey, J. A. Lercher, S. R. Bare, and B. M. Weckhuysen, *Nat. Commun.* **2015**, *6*, 7589.

[§] Both authors contributed equally to this work.

Chapter 2

Zeolite H-ZSM-5 Crystals as Model Systems: Crystallographic Architecture and Aluminium Distribution

Abstract

Three distinct types of large zeolite H-ZSM-5 crystals are introduced as model systems studied throughout the PhD thesis. A set of three powerful characterization tools is employed to resolve the crystallographic intergrowth structure of the studied crystals and to determine the exact 3-D location and long-range redistribution of Al atoms upon steaming. Synchrotron-based micro-X-ray diffraction imaging (μ -XRD) has been used to resolve the crystallographic structure of H-ZSM-5 intergrowths and to visualize aluminium zoning at the single catalyst particle level. The Al zoning of individual zeolite crystals and further insights into dealumination during steaming post-treatments have been confirmed by using time-of-flight secondary ion mass spectrometry (TOF-SIMS) combined with sputter-depth profiling analysis. Finally, atom probe tomography (APT) is employed to obtain unprecedented quantitative insights into the spatial distribution of individual Al atoms, including their 3-D distribution and extent of segregation. The method revealed the precise short-range distribution of Al and Al-Al neighboring distances within parent and steamed H-ZSM-5 crystals. Upon steaming, Al atoms were found to distribute in clusters and patches of high Al content.

2.1 Introduction

The catalytic performance of zeolite H-ZSM-5 crystals depends on the crystallographic orientation of their intergrowth subunits and distribution of Al before and after different post-treatments. In both cases, a direct, spatially resolved information is difficult to obtain experimentally. In this Chapter we present an arsenal of characterization techniques that can be used for this purpose – namely, synchrotron-based micro-X-ray diffraction imaging (μ -XRD), time-of-flight secondary ion mass spectrometry (TOF-SIMS) combined with sputter-depth profiling analysis, and atom probe tomography (APT). These techniques have been employed to study the influence of the zeolite H-ZSM-5 synthesis and subsequent steaming treatments on the crystalline structure and Al distribution in three distinct types of zeolite H-ZSM-5 crystals - namely, *parent crystals* (H-ZSM-5-P), with preserved Brønsted acidity and intact microporosity; *mildly steam-treated crystals* (H-ZSM-5-MT), with induced surface mesoporosity and preserved Brønsted acidity; and *severely steam-treated crystals* (H-ZSM-5-ST), with a high degree of mesoporosity (surface and bulk) and low Brønsted acidity.

It will be shown that μ -XRD imaging can be used to *crystallographically* resolve the intergrowth structure of a single zeolite H-ZSM-5-P crystal and provide further insights into Al zoning on the single particle level. TOF-SIMS sputter-depth profiling confirmed a macroscopically heterogeneous distribution of Al and indicated the deposition of Al in surface layers of steamed zeolite H-ZSM-5-MT and H-ZSM-5-ST crystals. Finally, the APT method has been used to determine 3-D compositional maps of the atomic constituents in H-ZSM-5-P and H-ZSM-5-ST crystals. The method can precisely quantify the most probable Al-Al neighbouring distance, the extent of aggregation of individual Al atoms, and assess the long-range Al redistribution upon steaming.

2.2 Experimental

The work in this PhD thesis is based on use of three types of large zeolite H-ZSM-5 systems as model catalysts. Parent zeolite crystals (H-ZSM-5-P) were used as well-defined model systems characterized with high crystallinity, preserved microporosity, and Brønsted acidity determined by the amount of framework Al. Two sets of

steaming conditions were chosen to mimic mild steaming (773 K, 5 h) and severe steaming (973 K, 5 h) – commonly used post-treatments to simultaneously alter structural and acidic properties of zeolites. We refer further to these crystals as mildly treated (*H-ZSM-5-MT*) and severely treated (*H-ZSM-5-ST*) samples. Table 2.1 summarizes the characterization techniques that have been used in this thesis and in the work of Aramburo and colleagues^[1] to gain more insights into the structure and Al distribution in the zeolite H-ZSM-5 crystals under study. Our attention in this Chapter will be directed towards structural properties of the crystals, while their reactivity will be discussed more in detail in the following chapters.

Table 2.1 Characterization techniques used to study the structural properties of the parent (H-ZSM-5-P), mildly steamed (H-ZSM-5-MT), and severely steamed (H-ZSM-5-ST) zeolite crystals. The gray part denotes the characterization techniques presented in this Chapter.

	H-ZSM-5-P	H-ZSM-5-MT	H-ZSM-5-ST
μ -XRD	+	-	+ ^(a)
TOF-SIMS	+	+	+
APT	+	-	+
FIB-SEM ^(b)	+	+	+
AFM ^(b)	+	+	+
Pyridine IR ^(b)	+	+	+
XPS ^(b)	+	+	+
N ₂ physisorption ^(b)	+	+	+

^(a) Results presented in Chapter 6.

^(b) Results are published in the work of Aramburo et al.^[1,2]

Abbreviations: μ -XRD – X-ray diffraction with micrometer resolution; TOF-SIMS – time-of-flight secondary ion mass spectrometry; APT – atom probe tomography; FIB-SEM – focused ion beam scanning electron microscopy; AFM – atomic force microscopy; pyridine IR – infra-red spectroscopy with pyridine adsorption; XPS – X-ray photoelectron spectroscopy;

2.2.1 Synthesis of large zeolite ZSM-5 crystals

The coffin-shaped large ZSM-5 crystals (with dimensions of $\sim 20 \times 20 \times 20 \mu\text{m}^3$) were synthesized from the following raw materials: Ludox AS40, tetrapropylammonium (TPA) bromide (TPABr, Fluka), $\text{Al}_2(\text{SO}_4)_3 \cdot 18\text{H}_2\text{O}$ (Baker), and NH_4OH (29%) with molar compositions of 6.65 $(\text{NH}_4)_2\text{O}/0.67 \text{TPA}_2\text{O}/0.025 \text{Al}_2\text{O}_3 / 10 \text{SiO}_2/121 \text{H}_2\text{O}$. For synthesis, Ludox AS40 and TPABr were mixed. Subsequently, $\text{Al}_2(\text{SO}_4)_3 \cdot 18\text{H}_2\text{O}$ was added and mixed for 5 min, followed by the addition of NH_4OH and further mixing for 7 min. Heating was carried out over 2 h to 453 K (7 days soak time under static conditions), followed by washing and drying at 393 K for 12 h.^[1] The synthesis resulted in an average Si/Al ratio of 17, as determined by energy-dispersive X-ray spectroscopy (EDX) and XPS analysis.^[3,4] The crystals were used as provided by ExxonMobil (Machelen, Belgium).

2.2.2 Preparation of parent H-ZSM-5-P crystals in their acidic form

The organic TPA template molecules were removed by a careful calcination (1 K/min) at 823 K for 8 h. After the template removal, the zeolite crystals were converted into their acidic form by a triple ion-exchange with 10 wt% ammonium nitrate (99%, Acros Organics) at 353 K, followed by 6 h calcination (2 K/min) at 773 K to release ammonia attached to the acid sites. The sample after this treatment is denoted as parent H-ZSM-5-P and this type of material will be further used in the thesis as a model crystal.

2.2.3 Preparation of steamed H-ZSM-5-MT and H-ZSM-5-ST crystals

The zeolite H-ZSM-5-P crystals in acidic form have been used for further preparation of steamed samples. The preparation procedure followed the work of Aramburo et al.^[1] Steaming was performed under two sets of conditions, with the intention to simulate mild steaming (H-ZSM-5-MT) and severe steaming (H-ZSM-5-ST) of parent H-ZSM-5-P crystals. Prior to steaming, the zeolite crystals were preheated to 393 K (5 K/min) for 60 min in a quartz tubular oven (Thermoline 79300) and heated further to 773 K (H-ZSM-5-MT) and 973 K (H-ZSM-5-ST) at a heating rate of 5 K/min. Further steaming treatment for both samples was performed using water saturated (373 K) N_2 flow (150 ml/min) for 5 h. Such prepared samples are further

denoted as H-ZSM-5-MT (mildly steamed at 773 K) and H-ZSM-5-ST (severely steamed at 973 K).

2.2.4 Synchrotron-based X-ray diffraction

Micro-diffraction experiments were performed at beam line ID01 at the ESRF synchrotron in Grenoble, France. To probe the crystallographic structure of the large zeolite H-ZSM-5-P crystals, the X-ray diffraction response of the crystals was collected with a 2-D (516×516) pixel array Maxipix X-ray detector with a pixel size of $50 \times 50 \mu\text{m}^2$. Lateral imaging of the diffraction response over a selected zeolite crystal was realized by scanning the sample by a 3-D piezo positioning device with a travel range of $100 \mu\text{m}$ in all three directions (x, y, z) and an encoded precision of 10 nm. In our case steps of $2\text{-}3 \mu\text{m}$ were chosen, which was the optimum compromise based on the size of the crystals and scanning time. In order to improve the spatial resolution and minimize the footprint of the 8.5 keV X-ray beam, large incident angles in the range of $\theta = 35^\circ\text{-}45^\circ$ were used. Accordingly, diffraction was collected in the range of $2\theta = 70^\circ\text{-}90^\circ$ under Bragg conditions. The beam was focused by a set of compound refractive Be lenses yielding a beam size of about $1 \times 2 \mu\text{m}^2$. The incident angle of the X-ray beam was tuned in steps of $0.05^\circ\text{-}0.1^\circ$ around angular values expected for Bragg conditions. The high precision diffractometer at ID01 beamline is working in a 3+2 circle geometry with three sample circles (no χ circle for improved stability) and two independent detector circles.

2.2.5 TOF-SIMS sputter depth profiling

The time-of-flight secondary ion mass spectrometry (TOF-SIMS) experiments were carried out on a TOF-SIMS 5.100 machine (ION-TOF GmbH, Münster, Germany). For data evaluation the software SurfaceLab 6.3 has been used. The UHV chamber had a base pressure $< 5 \times 10^{-10}$ mbar, which increased during the work on the zeolite H-ZSM-5-P crystals to 10^{-8} mbar. Charge compensation of the non-conducting samples was provided by an electron flood gun. Samples were transferred into the UHV chamber of the TOF-SIMS machine without further preparation. The crystals were sprinkled on conductive 0.2 mm thick polycarbonate stickers with graphite powder mixed in the adhesive as commonly used for scanning electron microscopy (Plano GmbH, Wetzlar, Germany). All measurements were conducted at room temperature.

TOF-SIMS surface analysis was done using Bi^+ primary ions ($E(\text{Bi}^+) = 25 \text{ keV}$, $I(\text{Bi}^+) = 0.40 \text{ pA}$). For sputter depth profiling, O_2^+ ions ($E(\text{O}_2^+) = 1 \text{ keV}$, $I(\text{O}_2^+) = 325 \text{ nA}$) were used. The sputter area was $120 \times 120 \mu\text{m}^2$. The analysis itself was carried out in an area of $120 \times 120 \mu\text{m}^2$ (128×128 pixels) with Bi^+ ions in low current bunch mode (lateral resolution $\sim 2 \mu\text{m}$) in the center of the sputter area. The data were obtained by periodic cycling of 2 s of Bi^+ analysis, 5 s of O_2^+ sputtering for the parent crystal and 10 s for the steamed crystals, and 1 s resting time. The TOF analyzer was operated in a positive ion mode. For evaluation of the Si^+/Al^+ secondary ion ratio, the mass spectra were reconstructed based on the signal originated from the defined region-of-interest. It is important to note that the obtained ratio is not an atomic Si/Al ratio, but merely the Si^+/Al^+ secondary ion ratio. Niemantsverdriet reported the secondary ion yields of Si^+ and Al^+ from their pure oxides being 0.58 and 0.7, respectively.^[5] Based on the ratio of the secondary ion yields ($Y_{\text{ox.}}(\text{Si}^+)/Y_{\text{ox.}}(\text{Al}^+) = 0.83$), a calibration of the Si/Al ratio could be achieved. We noted small variations in the absolute values of Si^+/Al^+ signals recorded for different crystals. However, the trends of the obtained curves Si/Al ratio vs. sputter time or sputter depth remained unchanged. The sputter depth was estimated by measuring the sputtered crystals by confocal microscopy height profiling. An average sputter depth of $10 \pm 2 \mu\text{m}$ was achieved, indicating that the middle of the crystal has been reached. A coarse calibration of the depth profiling data was assumed based on a linear relation between sputter time and sputter depth.

2.2.6 FIB-SEM specimen preparation for APT analysis

The two batches of H-ZSM-5-P and H-ZSM-5-ST crystals were imaged using a Zeiss Orion Helium Ion Microscope. An FEI Helios 600 dual beam FIB/SEM was used to image and prepare the specimens on Si micropost arrays for APT analysis. A 30 kV Ga ion beam was used to trench and cut the lamella and annular mill into the needle shape. A final low 2 kV shower over the tip was used to remove most of the remaining Pt/C cap and remove deep surface damage from the 30 kV beam. Microfabricated Si micropost arrays for APT analysis are commercially available from the Atom Probe Tomography (APT) division of Cameca Instruments. For a more detailed description of the FIB-based specimen preparation procedure, we refer the reader to the work of Thompson *et al.*^[6] Following FIB fabrication, a $\sim 20 \text{ nm}$ thick Cr metal film was deposited uniformly on the specimens using a South Bay Technologies IBS/e

deposition system, which included simultaneous specimen rotation and tilting to ensure the conformal coating of all the needle specimens. Qualitatively, it was found that APT analysis yield increased with ~ 10-30 nm Cr coating. A LEAP 4000X HR local electrode atom probe tomography system from CAMECA Instruments was used to map the atomic composition of individual zeolite specimens. The following parameters were used for both H-ZSM-5-P and H-ZSM-5-ST: laser energy = 200 pJ; detection rate = 0.2%, temperature = 44 K.

2.2.7 Tomographic reconstructions of atom probe data

The tomographic reconstructions and analysis, including nearest-neighbor and cluster analysis were performed with an $x = 1.0 \text{ nm}$ (3.0 nm), $y = 1.0 \text{ nm}$ (3.0 nm), $z = 1.0 \text{ nm}$ (1.5 nm) voxel grid size (delocalization) using Cameca's Integrated Visualization & Analysis Software (IVAS) version 3.6.6. IVAS was also used for the cluster analysis with parameters $D_{\max} = 1.7 \text{ nm}$ and $N_{\min} = 10$. For the nearest neighbor analysis, the expected nearest neighbor distribution (random) was determined from a simulated random distribution of the same solute composition and reconstructed dimensions. The error bars for the 1-D composition profiles reported

throughout represent the propagation point counting error as $E = \sqrt{\frac{C_i(1-C_i)}{N}}$ where $C_i = (x_i/N)$, x_i is the number of i solute ions and N is the total number of counts within the given bin. The error in the 1NN distances is reported as 1 standard deviation. The most probable distance (mode) of the Al-Al 1NN distribution was determined from distance corresponding to the value of greatest probability. When possible, a comparison of both *before* and *post* SEM images were used to estimate the volume of evaporated material and guide the choice of reconstruction parameters to obtain a reconstruction of reasonable volume. For a more detailed description of atom probe analysis and data reconstruction and analysis using a LEAP, the reader is referred to the published user's guide.^[7]

2.3 Results and Discussion

2.3.1 μ -XRD imaging of a single zeolite H-ZSM-5-P crystal

The diffraction responses of a single large zeolite H-ZSM-5 crystal have been mapped with 2 μm lateral resolution by applying a micro-focused 8.5 keV X-ray beam. After detection of the diffraction peaks of interest, spatially resolved maps were recorded by moving the crystal with a piezo stage with respect to the X-ray beam and detecting the responses with a 2-D X-ray detector in fixed geometry. Figure 2.1a schematically illustrates the experimental approach undertaken. In order to minimize the footprint of the X-ray beam, higher order Bragg reflections of $(h\ 0\ 0)$ and $(0\ k\ 0)$ lattice planes in the range $2\theta > 70^\circ$ were used. These reflections clearly show the splitting for higher diffraction orders due to small differences in a and b lattice parameters of H-ZSM-5 (Figure 2.1b). This observation indicates that two different orientations of the crystal lattice (rotated by 90°) are present along the beam trajectory, which was subsequently used for the determination of the crystalline phases and orientation of the intergrowth subunits.

Figure 2.1c shows the diffraction response on the 2-D X-ray pixel detector for one (x,y) position of the crystal. It is striking that two related reflections of the single zeolite H-ZSM-5 crystal appear very close in 2θ space, making them ideally suited for further crystallographic analysis. The two separate peaks are assigned to higher order $(16\ 0\ 0)$ and $(0\ 16\ 0)$ Bragg reflections of the MFI framework. Their integrated intensity (as defined by ROI1 and ROI2 in Figure 2.1c) plotted over the (x,y) piezo movement yields diffraction intensity maps. The lateral distribution of the integrated intensities represents the contribution of a particular crystallographic phase in the zeolite crystal. In this way, diffraction intensity maps with 2 μm lateral resolution can be reconstructed for any specific higher order Bragg reflection. Figure 2.1d reveals an hourglass pattern, as typically observed for the ZSM-5 intergrowth by optical micro-spectroscopy techniques,^[8] indicating the distribution of the $(0\ 16\ 0)$ Bragg reflection originating from the pyramidal *side* subunits. The diffraction response of the remaining four subunits, assigned to the closely related $(16\ 0\ 0)$ Bragg peak, supports the conclusion that two different crystallographic orientations coexist together in the intergrowth structure of large zeolite ZSM-5 crystals (Figure 2.1e).

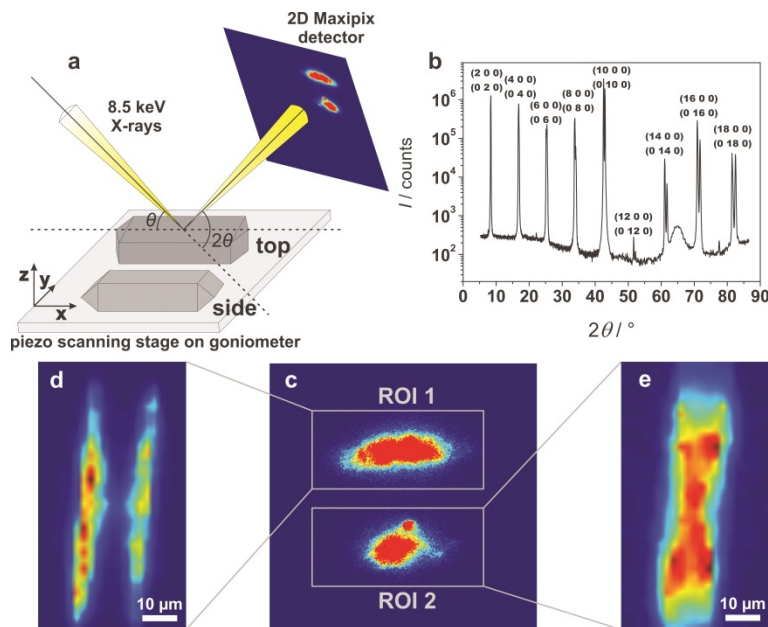


Figure 2.1 a) Schematic representation of the experimental setup; b) θ - 2θ XRD scan of a large zeolite H-ZSM-5 crystal corresponding to $(h\ 0\ 0)$ and $(0\ k\ 0)$ Bragg reflections; c) 2-D diffraction response of a zeolite H-ZSM-5 crystal at a fixed θ - 2θ diffraction geometry, zoomed in, resolution 154 pixels/ $^\circ$ 2θ ; d, e) diffraction intensity maps of regions of interest (ROI) 1 and 2.

2.3.2 1-D representation of μ -XRD data

To further represent 2-D diffraction information originating from different subunits we will describe a 2θ representation of the experimental results. The direction of the X-ray beam in our experiments was parallel to the long axis of the crystal. At each single (x,y) position of the sample the whole depth of the crystal is probed (around 20 μm). As a result, the diffraction response will depend on the crystallographic structure of the probed subunits (Figure 2.2a). At each point (x,y) of a corresponding piezo scan, the diffraction response is recorded using the X-ray detector, with the pixel coordinates $S(i,j)$ as schematically illustrated in Figure 2.2b. The vertical position j (in pixels) of the reflected X-ray beam on the detector is in linear relation to the 2θ angle of the corresponding Bragg reflection. Based on the position of the direct beam at $j = 192$ pixels and change of 154 pixels per 1° (2θ), the 2θ calibration of the diffraction images was carried out. Besides the direct false-colour images of the diffraction response on the detector, we chose so-called line integrals $I(j) = \sum_{i=1}^{516} S_{i,j}$ as an alternative 1-D 2θ representation of the 2-D diffraction images. Examples of the

recorded diffraction images are shown in Figures 2.2c and 2.2d. The line integrals $I(j)$ akin to standard XRD scans allow for the accurate determination of the peak position (Figures 2.2e and 2.2f). Deviation along the i -axis represents an angular deviation of the micro-crystalline domains from the specular path of the beam. Even though this method can resolve small differences in domain orientation (typically in order of 0.1°), integration along i -axis was not considered in our analysis. The described representation of the fine structure of the diffraction features helped us to resolve and discuss subtle differences in 2θ and with that in d-spacing.

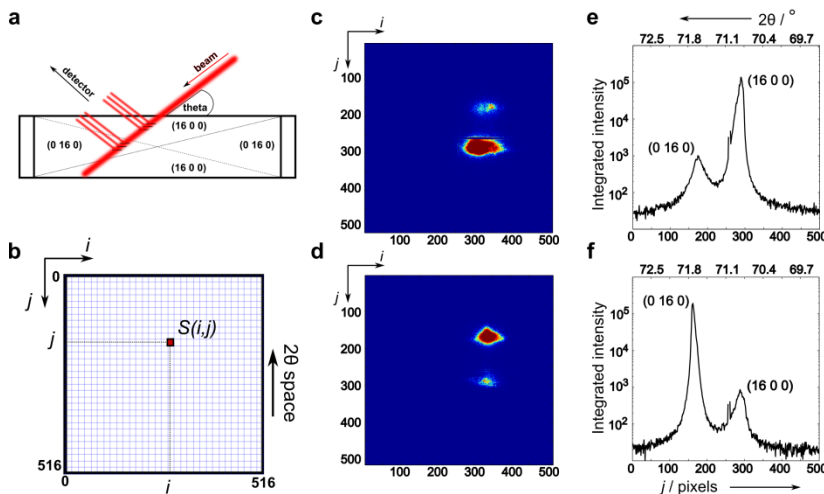


Figure 2.2 a) Direction of the X-ray beam and beam projection with respect to the zeolite crystal size and orientation, b) schematic representation of the 2-D detector and coordinate assignments used in the analysis, c,d) 2-D Maxipix detector response indicating intensive (16 0 0) reflection (c) and (0 16 0) reflection (d) in false-colour (blue = low, red = high intensity), e,f) corresponding line integrals of detector response from (c) and (d), in both detector coordinate j and calibrated to 2θ . The bimodal distribution of intensity, as described later in the text, relates to the splitting of the higher order Bragg reflections (16 0)/(0 16 0) of the MFI lattice.

2.3.3 Intergrowth structure of a zeolite H-ZSM-5 single crystal

In order to demonstrate the strength of our experimental approach and to provide more detailed insight into the crystallographic structure of the different subunits of large zeolite H-ZSM-5 crystals, two crystal orientations with respect to the incident X-ray beam have been studied: *i*) orientation denoted as *top* in Figure 2.3a, *ii*) orientation denoted as *side* in Figure 2.3b. To probe the diffraction response of different subunits in these orientations, the diffraction patterns for Bragg incident angles of the beam were recorded from several positions along the crystals, as shown

colour coded in Figures 2.3a,b. The corresponding detector responses are displayed in Figures 2.3c,d and can be translated to a 2 θ representation as explained in the Section 2.3.2. It is notable that for both orientations of the crystal, two distinct diffraction peaks appear as a result of the intergrowth structure and orientation of the crystal lattice within the subunits. The contribution of each specific Bragg reflection will depend on the fraction of the probed subunits in the corresponding crystallographic orientation. The crystal in the *top* orientation (Figures 2.3a,c,e) reveals a diffraction pattern at lower angles that is attributed to top and bottom pyramidal subunits (red), while reflections from the remaining four subunits (blue and black) appear shifted by 0.9° in 2 θ towards higher angles (lower interplanar d-spacings) (Figure 2.3e). Based on this, the lattice parameters are calculated to be $a_{\text{ZSM-5}} = 20.11 \text{ \AA}$ and $b_{\text{ZSM-5}} = 19.92 \text{ \AA}$, which is in excellent agreement with the values of the corresponding parameters reported for calcined powder ZSM-5 zeolite (monoclinic framework, $a_{\text{ZSM-5}} = 20.107 \text{ \AA}$ and $b_{\text{ZSM-5}} = 19.879 \text{ \AA}$).^[9] The diffraction intensity corresponding to the (16 0 0) reflection originates from the top and bottom pyramidal subunits, suggesting that sinusoidal channels (running along the $a_{\text{ZSM-5}}$ lattice vector) are normal to the surface of these subunits and the support (Figure 2.3a, red), whereas straight channels are parallel to the support. The diffraction response assigned to the (0 16 0) reflection is distributed over the side pyramidal subunits (blue) and the closing subunits (black). Therefore, in these subunits the $b_{\text{ZSM-5}}$ lattice vector and with that the straight channels are oriented normal to the support (and sinusoidal channels are parallel), referring to a 90° rotation of the side pyramidal subunits with respect to the top pyramidal subunits.

When the zeolite H-ZSM-5 crystal is rotated 90° along the long crystal axis, referring now to the the *side* orientation (Figures 2.3b,d,f), all six subunits are rotated by 90° with respect to the X-ray beam. However, despite the physical rotation of the crystal by 90°, the diffraction response and the relative positions of the diffraction peaks originating from the top/bottom and side pyramidal subunits remain essentially the same. The bulk crystallography thus can be considered as equal for the top/bottom and side pyramidal subunits being rotationally congruent. This implies that the porous network is rotated by 90° between the top/bottom and side pyramidal subunits. In *side* orientation, the diffraction signal from the closing subunits (black, Figures 2.3b,f) now occurs at lower angles, unambiguously proving our working hypothesis on the pore

orientation of these subunits; the pore orientation of the closing subunits is now parallel to the pore orientation of the top/bottom pyramidal subunits.

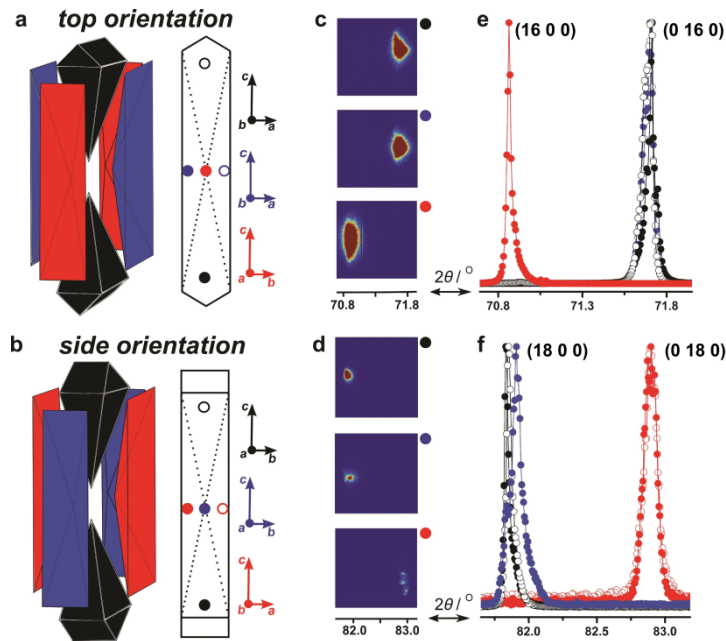


Figure 2.3 Crystallographic analysis of the intergrowth structure of a single zeolite H-ZSM-5 crystal: a, b) Schematic representation of the zeolite H-ZSM-5 crystal intergrowth (left) and the scheme of colour-coded regions from where the diffraction response was recorded (right) in the top (a) and side (b) orientation, respectively. The crystallographic orientation of each subunit is shown by colour-coded vectors. c, d) Corresponding diffraction patterns on the 2-D detector for the colour-coded spots; for clarity the patterns are intentionally rotated by 90°. e, f) Corresponding normalized X-ray diffractograms, presented for the fulfilled Bragg conditions of designated reflections.

One may argue that the single zeolite H-ZSM-5 crystal observations are obscured by the existence of an additional phase, more specifically the MEL (ZSM-11) phase, which is a framework topology closely related to MFI (ZSM-5). However, the 2-D XRD analysis of $(h\ 0\ 0)$ and $(0\ k\ 0)$ reflections and the consistence with the lattice parameters of the MFI structure excluded the macroscopic existence of the MEL phase.

2.3.4 Al zoning resolved by μ -XRD

Our experimental approach enables monitoring of crystallographic changes on very small (bond distances) length scales, which provides unprecedented details in the

differences of crystallographic parameters along the zeolite H-ZSM-5-P crystal. The high lateral resolution and the angular resolving power of $0.007^\circ/\text{pixel}$ provide the possibility to resolve subtle differences within lattice parameters along the crystal bulk.

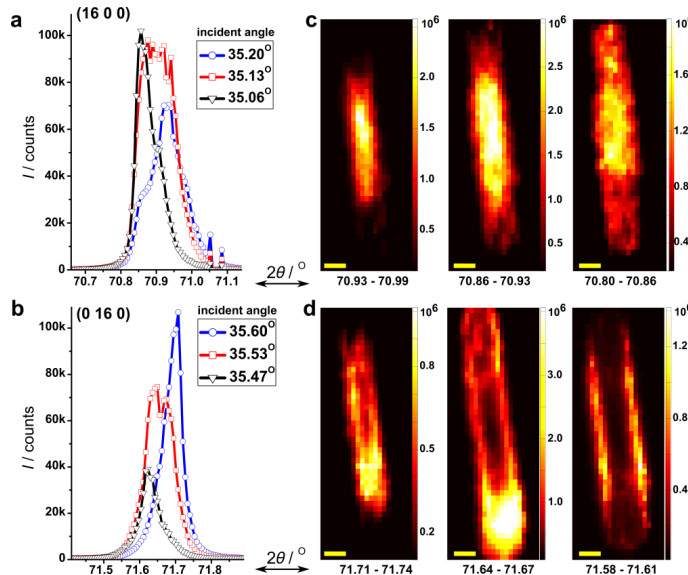


Figure 2.4 Fine structure of the diffraction peaks and corresponding lateral distribution of the diffraction intensities resulting from small changes in the incident diffraction angles. a) Reconstructed single pixel diffractograms of $(16\ 0\ 0)$ reflection for different incident angles of the beam; b) similar as (a) but for $(0\ 16\ 0)$ reflection; c) diffraction intensity maps for different 2θ regions of the $(16\ 0\ 0)$ reflection; d) similar as (c) but for $(0\ 16\ 0)$ reflection. Single (x,y) pixel diffractograms are intentionally chosen to show the complexity of scattering collected from one spot on the crystal. Diffraction maps are reconstructed for a given 2θ region over all probed incident angles. The scale bars are $10\ \mu\text{m}$.

Figures 2.4a,b present typical $(16\ 0\ 0)$ and $(0\ 16\ 0)$ diffractograms of a particular (x,y) spots on a zeolite H-ZSM-5 crystal in the *top* orientation, plotted for different incident angles of the X-ray beam. Close examination of these so-called single (x,y) pixel diffractograms shows differences in shape and position of the diffraction peaks. This is a result of the scattering geometry, optical path of the beam, and crystal structure. Even though only one of the two Bragg reflections is at the specular path for a certain incident angle, the existence of the two crystallographically different phases within a single diffraction peak is evident for both reflections (Figures 2.4a,b). This observation clearly indicates that the interplanar d -spacing of the observed crystallographic planes changes along the crystal. In order to further analyze these

features we have reconstructed diffraction intensity maps over relevant 2θ intervals within the (16 0 0) and (0 16 0) reflections (Figures 2.4c,d).

The resulting diffraction intensity maps reveal zones with different values of lattice parameters along the zeolite H-ZSM-5 crystal. The expansion of the crystal lattice is evident for both a and b lattice parameters when going from the middle towards the edges of the crystal. The trend is more visible in Figure 2.4d, where diffraction maps show a core-like region toward the lower values of the lattice parameter (here presented as higher 2θ angles), and a 2-3 μm thick rim that indicates a noticeable expansion of the b lattice parameter towards higher interplanar spacings. A similar reasoning holds for the (16 0 0) reflection (Figure 2.4c), if the intergrowth structure model (Figure 2.3a) is kept in mind. In this case the top and bottom intergrowth subunits are imaged and lattice parameters expand from the middle of the crystal towards the surface (Figure 2.4d), at the same time reflecting pyramidal geometry of the intergrowths. A similar behavior was noted for all of the studied crystals, including the ones in *side* orientation.

The explanation for the observed trends can be found in the phenomenon of aluminium zoning. If aluminium is incorporated into tetrahedral positions of a pure silica parent framework, the crystal lattice expands due to increased Al-O distance (1.75 Å) as compared to Si-O (1.61 Å).^[10] This is further demonstrated in Figure 2.5a where values of the b lattice parameter for the crystal in the *side* orientation are plotted over the short crystal coordinate (20 μm). The typical change of the diffraction response is about 0.1° in 2θ , which translates to approximately 0.02 Å change in the b lattice parameter. Complementary results also hold for the a lattice parameter. This is in line with early crystallographic studies of ZSM-5, where several powders with Si/Al ratio of 70 to 3000 were studied, reporting up to a maximum change of 0.04 Å in lattice parameter.^[11] It has already been reported that the synthesis of zeolite ZSM-5 starting from tetrapropylammonium (TPA) template can indeed lead to gradients in Al concentration.^[12-14] Our results crystallographically prove the observed zoning, providing at the same time information on the crystal lattice parameters. Furthermore, our findings are in line with the electron microprobe experiments on Al zoning by von Ballmoos and Meier, reporting a similar rim structure of Al enrichment for ZSM-5 crystals.^[15]

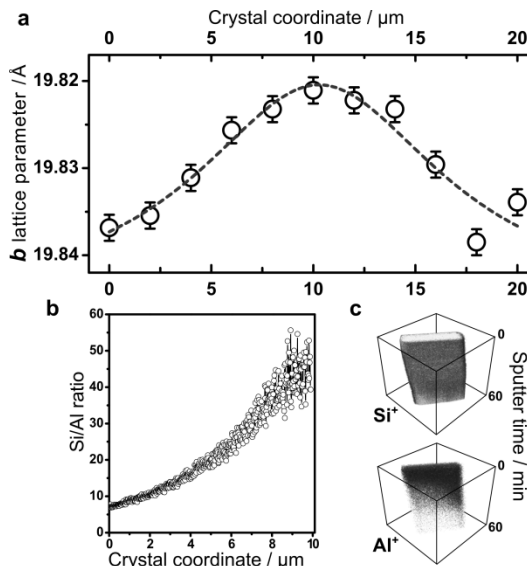


Figure 2.5 Evidence for the presence of an aluminium gradient along the short crystal axis, as recorded in side orientation. a) The b lattice parameter plotted along the short crystal axis; error bars determined in respect to the size of a single pixel on the 2-D detector. b) TOF-SIMS sputter depth profiling of the crystal indicating the estimated Si/Al ratio. c) 3-D representation of depth profiles of Si^+ and Al^+ secondary ions, as a function of sputter time.

2.3.5 TOF-SIMS analysis of Al zoning in parent and steamed zeolite crystals

The presence of Al zoning crystallographically observed in Figures 2.4 and 2.5a was further confirmed by using a surface sensitive time-of-flight secondary ion mass spectrometry (TOF-SIMS) technique, combined with sputter depth profiling analysis. Previously, only the surface layers of H-ZSM-5 crystals up to approximately 200 nm in thickness were studied by XPS analysis.^[1,4] For the TOF-SIMS analysis, the entire surface of the *top* subunit has been sputtered and Si^+ and Al^+ ion count rates were measured simultaneously as a function of sputter time (depth). The ratio of Si^+/Al^+ can be considered in rough approximation as being proportional to the actual Si/Al ratio of the zeolite material, as explained in Experimental Section 2.2.5. The results for H-ZSM-5-P are summarized in Figures 2.5b,c. Figure 2.5b presents the estimated Si/Al ratio within the zeolite H-ZSM-5-P crystal as a function of increasing sputter depth, indicating a strong gradient in concentration of aluminium with the sputtering time. The variation of the Si^+ count rate was less than 10%, whilst the count rate of Al^+ decreased by factor of 15 when going from surface of the crystal towards the middle of the crystal (10 μm). The depletion of Al^+ as compared to Si^+ is visualized in Figure

2.5c. Sputtering confirms our hypothesis about aluminium zoning, and explains diffraction maps in Figures 2.4c,d.

The TOF-SIMS method has proven to be a valuable tool to quantify the concentrations of Si and Al atoms in zeolite H-ZSM-5 crystals and to resolve interesting properties of Al zoning by using depth-profile analysis. For this reason we have further subjected all three types of zeolite H-ZSM-5 crystals to the TOF-SIMS analysis. The results are summarized in Figure 2.6. Parent H-ZSM-5-P crystals typically show a depletion of Al in a surface layer of approximately 50 nm (first sputter depth profiling point), while mildly and severely treated crystals H-ZSM-5-MT and H-ZSM-5-ST exhibit significant Al enrichment in this region. Previous XPS sputter depth profiling measurements^[1] have indicated that the most remarkable difference in Al distribution can be noticed in the near-surface regions of the crystals.

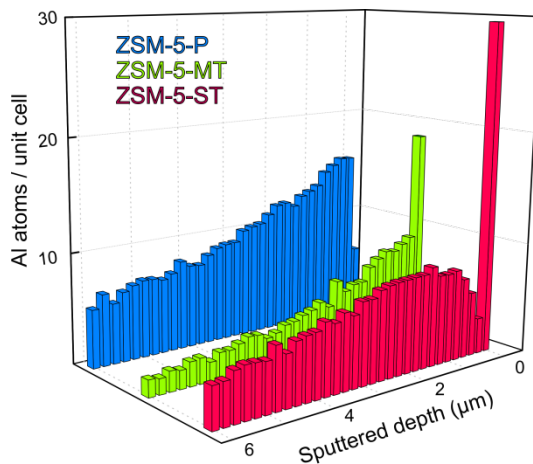


Figure 2.6 Aluminium TOF-SIMS sputter depth profiles for single zeolite crystals: H-ZSM-5-P (blue), H-ZSM-5-MT (green) and H-ZSM-5-ST (red). The approximate number of Al atoms is calculated based on the TOF-SIMS response of the Si^+/Al^+ signal in respect to 96 T atoms per unit cell of zeolite H-ZSM-5.

A depletion in Al concentration at the near-surface of the parent H-ZSM-5-P crystal is inherent to the synthesis procedure. In contrast, the mild and severe steaming treatments create extra-framework Al species that most probably migrate and deposit close to the surface, which explains the significant Al-enrichment in this region. However, mild steaming does not seem to affect the inner regions of the zeolite material. This is also an indirect indication of the formation of mesoporous defects in the surface layers of H-ZSM-5-MT crystals that are responsible for the enhanced

diffusion and higher reactivity, despite the loss in the number of Brønsted acid sites due to dealumination.^[1] It should be noted here that, apart from the differences in the near-surface layers, we observe very similar trends in the TOF-SIMS depth profiles of both H-ZSM-5-P and H-ZSM-5-MT. However, the absolute values for measured Si/Al ratio vary from crystal to crystal, as visible in Figure 2.6 where the concentration of Al atoms seems to be lower for H-ZSM-5-MT. Finally, the first experimental point in the TOF-SIMS profile of H-ZSM-5-ST indicates the deposition of Al in the surface layer of zeolite crystal, most probably due to the high degree of dealumination that is visible up to $\sim 1 \mu\text{m}$ of the depth profile. Evidently, severe steaming causes migration of Al species towards the surface of the zeolite crystal.

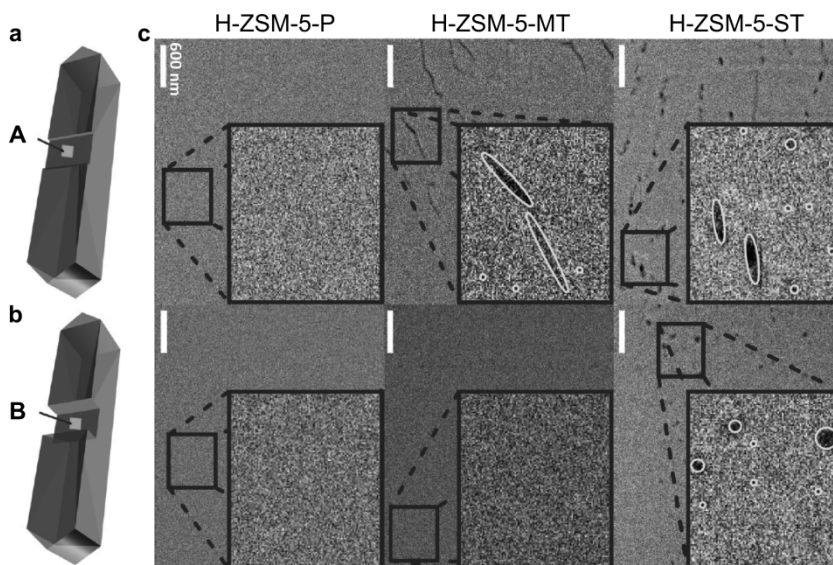


Figure 2.7 HR-SEM imaging of parent and steamed zeolite crystals, reproduced with permission from ref. [1]. a,b) Schematic representation of an H-ZSM-5 crystal with FIB cross-section area chosen for the SEM imaging near the surface of the crystal (a) and for the cross-section dissected from the middle of the crystal. c) SEM microphotographs of areas A (top) and B (bottom) for H-ZSM-5-P, H-ZSM-5-MT, and H-ZSM-5-ST, showing the studied cross-sections milled near the surface and middle regions of the crystal. Inserts are magnified 64 times and are indicated by the black rectangles. Recorded mesopores are highlighted in the SEM insertions with the contours.

It is interesting to compare the results of the TOF-SIMS analysis with the FIB-SEM method reported in the work of Aramburo, Karwacki, and co-workers.^[1,16] Their results are summarized in Figure 2.7. Both surface regions (Figure 2.7a) and inner domains (Figure 2.7b) have been subjected to FIB-SEM analysis. The authors

have noted only near-surface mesoporosity in the case of H-ZSM-5-MT crystals, whereas the inner crystalline regions remained intact (Figure 2.7c, middle). On the other hand, severe steaming in the case of H-ZSM-5-ST crystals has led to mesoporosity distributed throughout the whole crystal volume, including the inner crystalline regions (Figure 2.7c, bottom). This finding is in line with our TOF-SIMS analysis, showing that both techniques complement each other in describing dealumination of the steamed zeolite H-ZSM-5 crystals. In the following chapters we will further evaluate the reactivity of the three types of zeolite crystals by using probe reactions based on furfuryl alcohol and styrene derivates.

2.3.6 FIB-SEM characterization prior to atom probe tomography experiments

For atom probe tomography (APT) experiments we opted to study the H-ZSM-5-P and H-ZSM-5-ST zeolite crystals. The typical morphology of the parent and steamed H-ZSM-5 crystals is shown in Figure 2.8b, which exhibit a coffin-like geometry with $20 \times 20 \times 100 \mu\text{m}^3$ dimensions. No distinguishable difference in the bulk morphology between both H-ZSM-5-P and H-ZSM-5-ST was observed when imaged via helium ion microscopy (HIM) or scanning electron microscopy (SEM) at a nominal spatial resolution of $\sim 1 \text{ nm}$. To prepare specimens from a portion of individual H-ZSM-5 crystals into the needle-like geometry necessary for APT analysis, a dual-beam focused ion beam/scanning electron microscope (FIB/SEM) was used.

A scheme of the sample preparation procedure is shown in Figure 2.8a. An electron beam and ion beam deposited a Pt/C cap of dimensions $2 \times 30 \mu\text{m}^2$ with $\sim 500 \text{ nm}$ total thickness centered longitudinally, which protects the underlying region of interest from unintentional Ga ion damage during trenching to form a lamellar structure (Figure 2.8c). An OmniProbe nano-manipulator was then attached to the lamella and lifted out (Figure 2.8d), and $\sim 2-3 \mu\text{m}$ portion was positioned on a Si micropost structure (Figures 2.8e,f). Using an annular milling pattern, the specimen was milled into a needle-like shape with a final tip radius curvature of $\sim 50 \text{ nm}$ (Figure 2.8g). An estimate of the analyzed volume is made by comparison of the specimen before and after the APT analysis (Figures 2.8g,h). Note that from a single lamella $30 \mu\text{m}$ long, approximately 9-11 individual microposts can be populated and shaped into needles for analysis.

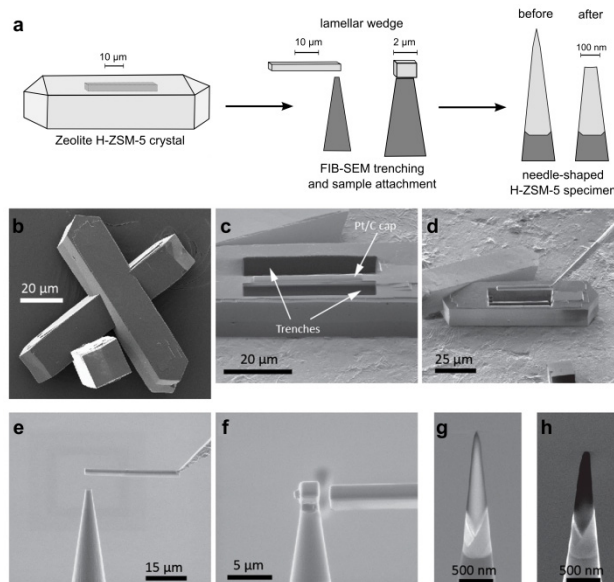


Figure 2.8 a) Schematic of the FIB-based preparation of specimens for APT analysis. b) Helium ion microscope image of typical coffin-shaped zeolite H-ZSM-5 crystals under study. c) First step in the APT specimen preparation using the FIB-SEM approach: Trenching of lamellar wedge with a protective Pt cap. d) Lift-out. e,f) Attachment to Si micropost. g) Final specimen morphology with tip diameter of ~ 100 nm. h) Same tip shown in (g) but after APT analysis. An estimate of the analyzed volume is made by comparison of (g) and (h).

2.3.7 Beam damage in APT experiments

Maintaining the crystallinity of the H-ZSM-5 samples was found to be relatively sensitive to the Ga-ion beam current. A high ion beam current of 1 nA at 30 kV during the trenching of specimen wedge (Figure 2.8c) resulted in a fully amorphized structure, as shown in Figure 2.9a-c. Using a relatively low ion beam current of 240 pA at 30 kV during the trenching resulted in a mostly crystalline structure as shown in Figure 2.9d,e. Interestingly, at the lower ion beam current, we consistently found an amorphous ‘shell’ surrounding a crystalline core (Figure 2.9d). The thickness of the amorphous region between the Pt/C cap and crystalline core ranged from ~ 40 -100 nm, while the amorphous layer thickness on the surface ranged between ~ 5 -20 nm. With both the high and low ion beam current cases, the same 2 kV exposure was used to remove the damaged surface layer,^[17] so we conclude that this low kV exposure did not result in amorphization, rather the tendency to fully amorphize was sensitive to the ion beam current during the trenching step.

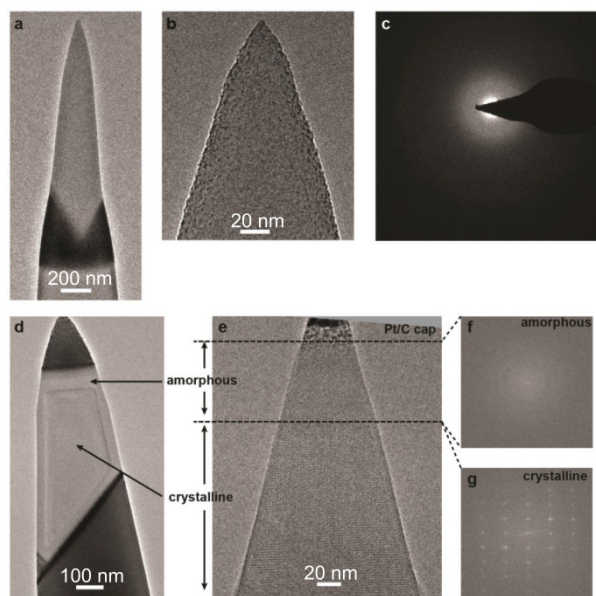


Figure 2.9 Characterization of Ga ion beam damage during FIB specimen preparation. a-c) Transmission electron micrographs (a,b) and related diffraction pattern (c) from a FIB-prepared APT needle specimen using a high Ga ion beam current. d-e) Transmission electron micrographs from FIB-prepared APT needle specimens using a low Ga ion beam current. f,g) Related diffraction patterns taken from the amorphous (f) and crystalline regions (g).

2.3.8 Atom probe tomography of H-ZSM-5-P and H-ZSM-5-ST crystals

Atom probe tomography is a destructive method that has recently reached the sensitivity and precision to reconstruct a 3-D atomic image of a sample and provide more chemical information about the types of atoms and their nearest neighbor distances.^[18,19] The method uses a combination of the laser pulses, high-magnification electric fields, and a position sensitive, time-of-flight mass detector in order to determine the exact position of the atoms removed from the surface and their mass-to-charge ratio, as depicted in Figure 2.10. In this way a 3-D image of all atomic constituents can be reconstructed with great precision. The method has been previously used for metallic-like catalysts,^[20,21] but its application was not possible to fragile, zeolite-like materials. In this Chapter we demonstrate that, by a careful preparation of the needle-like H-ZSM-5 specimen and the subsequent optimization of the APT analysis parameters, it is possible to achieve atomically resolved images of zeolite materials. The use of large zeolite H-ZSM-5 crystals turned out to be crucial in the optimization process.

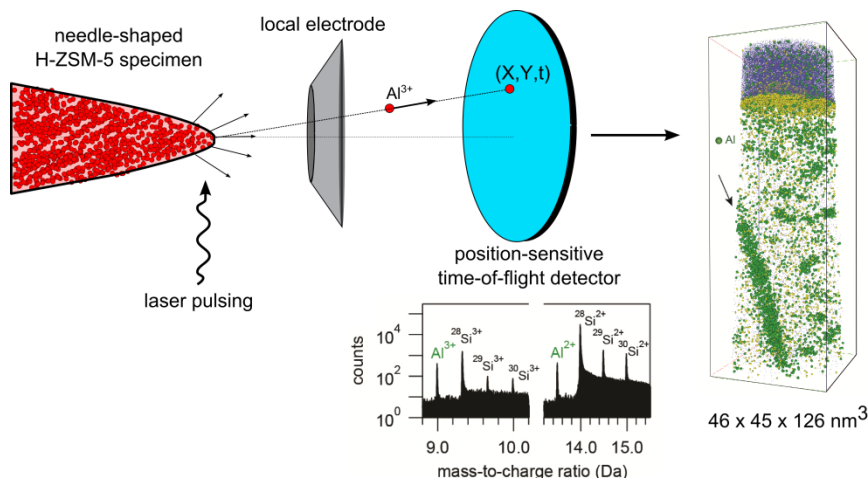


Figure 2.10 Schematic of the atom probe tomography measurement. Near-surface atoms are removed from the needle-shaped zeolite H-ZSM-5 specimen and directed by the strong electric field towards the position-sensitive mass spectrometer detector. The resulting 3-D image of Al atoms is reconstructed based on the detected atoms.

APT allows both a qualitative and quantitative analysis of the Al distribution in zeolites. Qualitatively, the distribution of Al within the H-ZSM-5-P crystal is found to be homogeneous as shown in Figure 2.11. A mass spectrum is shown in Figure 2.11a indicates Si and O as the major species, with Si detected as singly, doubly, and triply charged ions. Complex ions made up of Si and O are also observed; for example O_2^{+} , SiO^{2+} , and SiO_2^{+} . We also observe distinct carbon peaks in the mass spectrum. We can only speculate as to the origin of C as being either a remnant of the synthesis and subsequent calcination process or simply adsorbed hydrocarbons from air during sample handling. The presence of Al is shown in the zoomed in mass spectrum of Figure 2.11b. Note that the mass resolution is high enough to easily distinguish the three individual isotopes of Si from mono-isotopic Al. The tomographic reconstruction qualitatively shows a homogeneous distribution of Si and O (Figure 2.11c) as well of Al (Figure 2.11d), where each sphere represents the 3-D position of an individual color-coded atom.

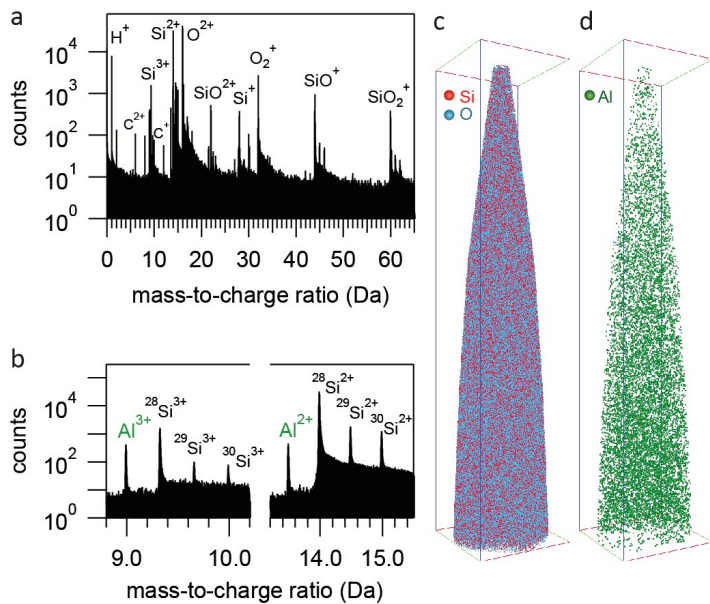


Figure 2.11. Detection and homogeneous distribution of individual Al atoms in parent H-ZSM-5-P. a) Typical APT mass spectrum showing Si and O and related complex ion mass peaks. b) Mass spectrum of selected region around the detected Al peaks. c,d) 3-D atom distribution map of Si and O and Al from within a parent zeolite H-ZSM-5-P crystal. Bounding box dimensions are $60 \times 59 \times 298 \text{ nm}^3$.

In stark contrast, the Al distribution in the severely steam-treated H-ZSM-5-ST crystal is found to be very heterogeneous, with regions of high Al concentration. The 3-D atom maps of H-ZSM-5-ST in Figures 2.12a,b display the distribution of Si, O, and Al, respectively. Visually, the Si and O distribution is homogeneous and similar to that found in Figure 2.11c for H-ZSM-5-P. However, the Al distribution shows a visually clear heterogeneous distribution with Al tending to form local regions of high Al concentration. In addition, we observe both the ion-sputtered Cr coating and a remnant of the FIB-deposited protective Pt capping layer that was not completely removed during the final FIB-milling. The presence of both the Cr and Pt does not negatively affect the analysis; rather, the Pt specifically provides a very important fiducial marker for quantitative compositional depth profiling relative to the initial exposed surface of the steam-treated zeolite.

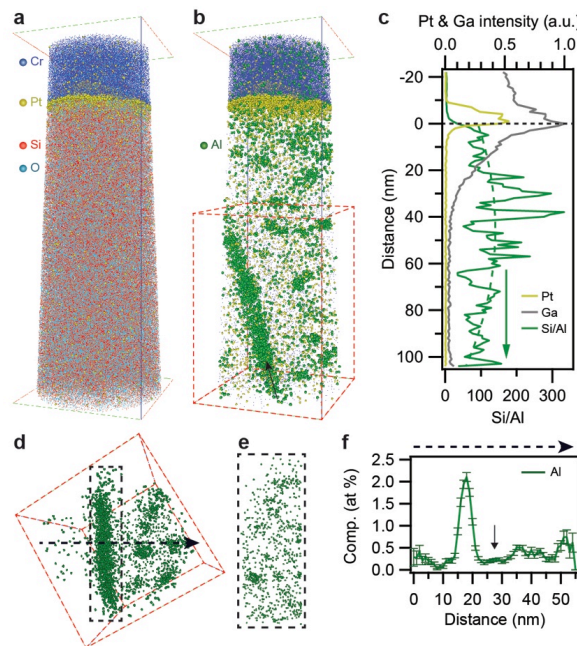


Figure 2.12 Detection and heterogeneous distribution of individual Al atoms in steam-treated H-ZSM-5-ST: a) Si and O and b) Al atom distributions from within an H-ZSM-5-ST crystal. The Cr and Pt layers serve as a fiducial to mark the position of the zeolite crystal surface. Bounding box dimensions are $46 \times 45 \times 126 \text{ nm}^3$. c) Si/Al ratio as a function of distance from the surface marked by black dashed line. A least squares polynomial fit is shown as a green dotted curve to guide the eye to the distribution. The Pt and Ga intensities as well as the Si/Al ratio values are averaged over each cross section when moving from the top to the bottom of the analyzed volume. d) Al distribution of isolated sub-volume (red dashed box) viewed normal to the arrow direction in b. Bounding box dimensions $53 \times 58 \text{ nm}^2$. e) Plane-view of the isolated sub-volume outlined by dashed box in d. Bounding box dimensions $26 \times 67 \text{ nm}^2$. f) 1-dimensional composition profile with associated error bars taken across the arrowed black dashed line in d.

In Figure 2.12c, the Si/Al ratio (green) is plotted as a function of distance from the surface; the surface is marked by the horizontal dashed line below the Pt layer. Large fluctuations in the Si/Al ratio are observed and arise from atomic deviations in the distribution within the 1 nm bins. Using a least squares polynomial fit (green dashed curve), the Si/Al ratio shows a maximum of 140 at a depth of about 50 nm. We note that the unintentional implantation of Ga (Figure 2.12c) during the Pt deposition has the potential to affect the Al distribution. However, it seems that any perturbation from Ga to the Si/Al ratio measured here is not significant considering our results are consistent with a previously published Si/Al ratio determined from X-ray photoemission spectroscopy depth profiling of the same steamed H-ZSM-5-ST sample.^[1] The individual particle-to-particle reproducibility of

Al distribution in both H-ZSM-5-P and H-ZSM-5-ST as measured by APT analysis is established in additional measurements for different crystals of H-ZSM-5-P and H-ZSM-5-ST. A homogeneous distribution of Al within H-ZSM-5-P has been observed, while Al clustering was apparent in H-ZSM-5-ST, consistent with the analyses described in Figure 2.11 and Figure 2.12, respectively.

As can be discerned visually in a 3-D reconstruction of the H-ZSM-5-ST sample, discrete regions of high Al concentration are found both distributed evenly in the bulk, as well as segregated along a planar feature highlighted by the black arrow in Figure 2.12b. Isolation of a sub-volume (Figure 2.12d) reveals that the Al distribution within the planar feature occurs as discrete clusters similar to the surrounding material (Figure 2.12e). In Figure 2.12f, the 1-D composition profile taken from left to right along the black dashed line of Figure 2.12d shows an approximately 4 times higher Al concentration within the volume of planar feature relative to the surrounding material. A slight depletion in the Al composition is observed adjacent to this planar feature (arrow in Figure 2.12f), which supports Al diffusion to the grain boundary region.

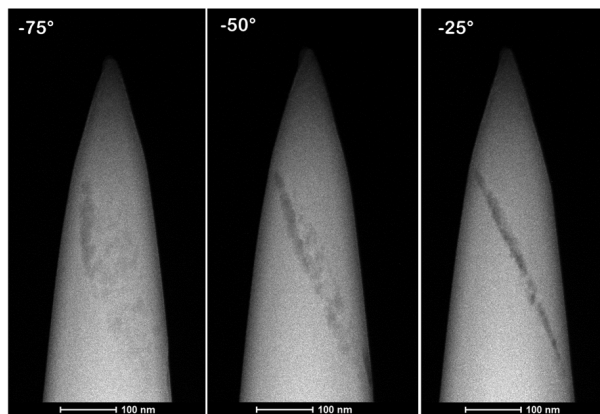


Figure 2.13 STEM Characterization of a H-ZSM-5-ST specimen prior to APT analysis. Scanning transmission electron microscopy images taken at three different angles using a tomography holder.

This feature is also observed through scanning transmission electron microscopy (STEM), as illustrated in Figure 2.13. Figure 2.13 shows that at -25° the feature appears to be a line. As the specimen is rotated to -50° and -75° , it can be seen that the line is actually made up of small, finite clusters. These clusters, and their alignment in one plane, are consistent with the APT results showing the higher concentration of Al atoms in clusters that align in a plane. The darker contrast in the

STEM image is indicative of voids. We postulate that these voids form along the grain boundaries during the steaming process, and the Al subsequently segregates to these locations.

2.3.9 Statistical analysis of the 3-D atomic-scale distribution of Al in H-ZSM-5 crystals

Using grid-based frequency distribution analyses, the unique 3-D nature of the APT data provides unprecedented means to quantify the atomic-scale distribution of the Al atoms and the extent of segregation in the as-prepared parent and steam-treated zeolite catalysts. An isolated sub-volume of the steam-treated H-ZSM-5 sample is shown in Figure 2.14a with 2.0% Al-iso-concentration mesh surfaces encompassing regions enriched in Al, where the volume inside (outside) is greater (less) than 2.0% Al. The heterogeneous distribution and morphology of the Al-rich regions are easily discerned. A proximity histogram (proxygram) analysis^[22] was performed for each iso-concentration surface in Figure 2.14a. The analysis is similar to a 1-D composition profile that follows the contours normal to iso-concentration surface. Figure 2.14c shows a proxygram composition profile averaged over all the surfaces shown in Figure 2.14a. Over a distance of approximately 1 nm, the Al composition increases to approximately 10% with a correlated decrease in the Si composition.

To quantify the extent of Al enrichment, an Al-Al nearest-neighbor analysis was performed on the experimental 3-D Al distribution of both parent and steamed H-ZSM-5 and compared to a randomized Al distribution.^[19] In Figures 2.14d,e the experimental and random Al-Al 1st nearest neighbor (1NN) distribution is shown for the H-ZSM-5-P and H-ZSM-5-ST material, respectively. Little deviation is visually observed between the experimental and random Al-Al 1NN distribution for the parent H-ZSM-5 (Figure 2.14d), as opposed to the steamed H-ZSM-5 (Figure 2.14e). A chi-squared (χ^2) statistical test was performed to quantitatively confirm or refute deviation from randomness, while a calculated Pearson coefficient (μ) was used to compare the relative strength of any deviation.^[19] For the χ^2 statistical test applied here, the null hypothesis is that the observed distribution is consistent with the expected random distribution. For the parent H-ZSM-5-P in Figure 2.14d, an experimental $\chi^2 = 107$ is determined which is greater than the expected $\chi^2 = 33.9$ with 22 degrees of freedom

and a 95% confidence level, thus we reject the null hypothesis and confirm that the experimental Al-Al 1NN distribution is non-random.

Similarly, we quantitatively confirm a non-random Al-Al 1NN distribution for the steamed H-ZSM-5-ST in Figure 2.14e from an experimental $\chi^2 = 2540$ with the same expected $\chi^2 = 33.9$ and 22 degrees of freedom, and a 95% confidence level. Although both the parent and steamed H-ZSM-5 Al-Al 1NN distributions show non-randomness, it is quite obvious that there is a greater departure from randomness for the steamed versus parent specimen. We can determine a relative strength of the randomness by comparing the Pearson coefficient, μ , whose value lies between 0 and 1, where $\mu = 1$ is completely non-random and $\mu = 0$ is completely random.^[23] With $\mu_{\text{parent}} = 0.7$ and $\mu_{\text{steamed}} = 1$, we confirm that there is a much stronger deviation from randomness of the steamed Al-Al 1NN experimental distribution compared to the parent distribution, which is also qualitatively apparent for the steamed specimen showing obvious regions enriched in Al.

In addition to a greater volume of regions enriched in Al, the steamed ZSM-5-ST also exhibits a shorter most probable Al-Al 1NN distance compared to the parent specimen. Fitting the experimental distributions in Figures 2.14d,e to a Poisson distribution of the form $P(r) = 4\pi r^2 qc \exp\left(-\frac{4}{3}\pi qc'r^3\right)$ adapted from Philippe et al.^[19], where q = detector efficiency (0.36 used in the reconstructions) is fixed and c' is a free parameter related to the atomic density. From the relation $E(r^k) = \int_0^\infty r^k P(r)$, the most probable 1NN Al-Al distance (mode) was calculated from the first moment ($k = 1$) of $E(r^k)$, and standard deviation (σ) estimated from first and second moments: $\sigma = \sqrt{E(r^2) - E(r)^2}$.^[24]

For the ZSM-5-P crystal, the mode of the Al-Al 1NN distance distribution is 18 ± 6 Å, while for the ZSM-5-ST crystal the mode is 9 ± 3 Å. We note that the co-field evaporation of different phases with different evaporation fields from a heterogeneous material could lead to perturbations in local magnification resulting in the measurement of artificially-diffuse distributions.^[25,26] However, with respect to the Al-Al nearest neighbor distance distributions reported here, we assert that local magnifications from regions of high Al content are negligible since Al does not seem to form distinct precipitates of pure Al metal or oxide.

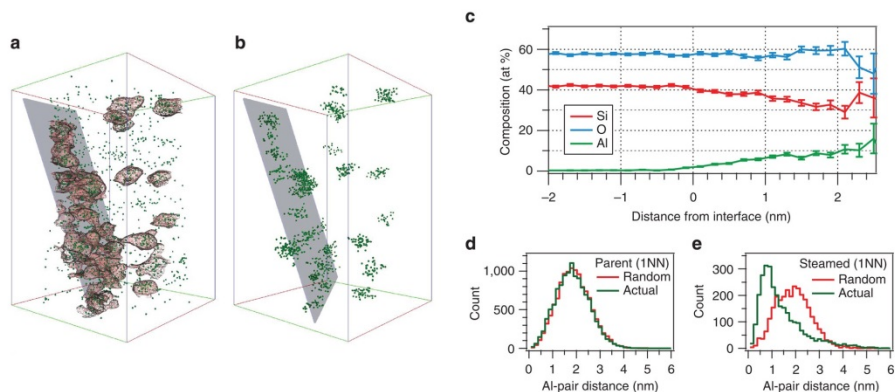


Figure 2.14 Quantification of Al distribution and clustering in H-ZSM-5-P and H-ZSM-5-ST. a) A selected sub-volume of the reconstruction shown in Figure 2.12 where only isolated and clustered Al atoms (green) are shown encompassed by 2.0% Al-iso-concentration surfaces (wire mesh). A semi-transparent plane is shown to highlight the orientation of clusters lying along the grain boundary highlighted in Figure 2.12b (arrow). Bounding box dimensions are $46 \times 45 \times 66 \text{ nm}^3$. b) Isolated Al solute atoms belonging to defined clusters; see text. c) Proximity histogram averaged over all iso-concentration surfaces in (a). d) 1st Al-Al nearest neighbor distance distributions in H-ZSM-5-P and e) 1st Al-Al nearest neighbor distance distributions in H-ZSM-5-ST.

To further quantify the Al distribution, a cluster analysis was performed following a method outlined in references^[7,27]. The cluster analysis is based on the assumption that the distance between solute (Al) atoms that are clustered together is smaller than the distance when randomly distributed in the matrix. Using a maximum spacing between two Al atoms of 1.7 nm and a minimum number of 10 Al atoms defining a cluster, 25 distinct Al clusters were found in the steamed HZSM-5-ST sample and are shown in Figure 2.14b. We find that the Al density within the cluster is 20 times greater in the steamed H-ZSM-5-ST sample at $0.5 \text{ atoms nm}^{-3}$, which corresponds to 2.7 Al atoms per unit cell (UC), compared with $0.025 \text{ atoms nm}^{-3}$ ($0.135 \text{ Al atoms/UC}$) for the parent H-ZSM-5-P material.

2.4 Conclusions

Three characterization tools have been used to resolve the crystallographic structure and Al distribution within three distinct types of zeolite H-ZSM-5 crystals. μ -XRD imaging crystallographically resolved the 90° intergrowth structure model of zeolite H-ZSM-5-P crystals and indicated an expansion of the crystal lattice towards the surface. This expansion was attributed to a macroscopic Al zoning and was further confirmed

by TOF-SIMS sputter-depth profiling analysis. TOF-SIMS also indicated further Al depletion in the surface regions of the H-ZSM-5-P crystals. In contrast, steamed H-ZSM-5-MT and H-ZSM-5-ST crystals have shown to exhibit a considerable enrichment of extra-framework Al at the surface of the crystals. Finally, by using APT it was possible to localize the 3-D arrangement of individual Al atoms within H-ZSM-5-P and H-ZSM-5-ST crystals. The highly crystalline parent zeolite crystals were characterized with a non-random Al distribution, whereas upon steaming this non-randomness of Al distribution further developed as a clear long-range redistribution of Al and migration into large Al clusters.

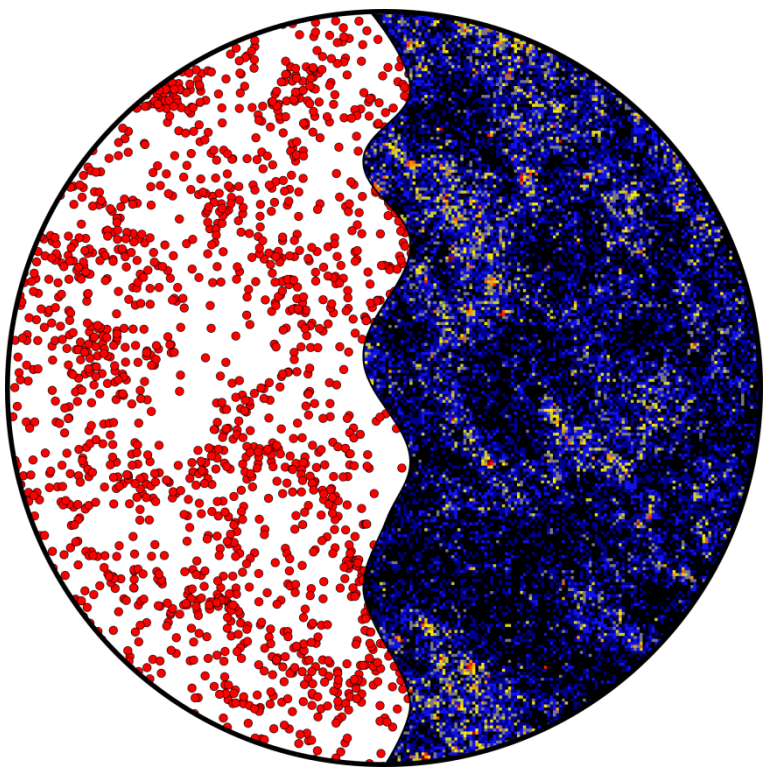
Acknowledgements

The APT experiments were performed under a science theme user proposal at the Environmental Molecular Science Laboratory (EMSL), a national scientific user facility located at Pacific Northwest National Laboratory (PNNL). The European Synchrotron Radiation Facility (ESRF) is acknowledged for providing beamtime for micro-XRD experiments. Staff members of ESRF beamline ID01 and Zafer Öztürk from Utrecht University are acknowledged for experimental support. Prof. Jürgen Janek (Justus-Liebig-University Giessen) is thanked for granting access to the TOF-SIMS facilities and Dr. Julia Kokesch-Himmelreich (Justus-Liebig-University Giessen) for confocal microscopy height profiling measurements. Dr. Machteld Mertens (ExxonMobil, Machelen, Belgium) is thanked for providing the H-ZSM-5 zeolite crystals. Dr. Luis Aramburo (Utrecht University) is kindly acknowledged for the discussions related to the synthesis and properties of the steamed zeolite crystals.

References

- [1] L. R. Aramburo, L. Karwacki, P. Cubillas, S. Asahina, D. A. M. de Winter, M. R. Drury, I. L. C. Buurmans, E. Stavitski, D. Mores, M. Daturi, P. Bazin, P. Dumas, F. Thibault-Starzyk, J. A. Post, M. W. Anderson, O. Terasaki, B. M. Weckhuysen, *Chem. – Eur. J.* **2011**, *17*, 13773–13781.
- [2] L. R. Aramburo, *Spatiotemporal Spectroscopy of Molecular Sieves: Interplay between Hydrothermal Treatments and the Methanol-To-Hydrocarbons Reaction*, Utrecht University, **2012**.
- [3] M. H. F. Kox, E. Stavitski, B. M. Weckhuysen, *Angew. Chem. Int. Ed.* **2007**, *46*, 3652–3655.
- [4] L. Karwacki, M. H. F. Kox, D. A. Matthijs de Winter, M. R. Drury, J. D. Meeldijk, E. Stavitski, W. Schmidt, M. Mertens, P. Cubillas, N. John, A. Chan, N. Kahn, S. R. Bare, M. Anderson, J. Kornatowski, B. M. Weckhuysen, *Nat. Mater.* **2009**, *8*, 959–965.
- [5] J. W. Niemantsverdriet, in *Spectroscopy in Catalysis*, Wiley-VCH, Weinheim, **2007**, pp. 85–119.

- [6] K. Thompson, D. Lawrence, D. J. Larson, J. D. Olson, T. F. Kelly, B. Gorman, *Ultramicroscopy* **2007**, *107*, 131–139.
- [7] D. J. Larson, T. J. Prosa, R. M. Ulfig, B. P. Geiser, T. F. Kelly, *Local Electrode Atom Probe Tomography*, Springer, New York, **2013**.
- [8] C. Weidenthaler, R. X. Fischer, R. D. Shannon, O. Medenbach, *J. Phys. Chem.* **1994**, *98*, 12687–12694.
- [9] H. van Koningsveld, J. C. Jansen, H. van Bekkum, *Zeolites* **1990**, *10*, 235–242.
- [10] J. B. Jones, *Acta Crystallogr. Sect. B* **1968**, *24*, 355–358.
- [11] E. L. Wu, S. L. Lawton, D. H. Olson, A. C. Rohrman, G. T. Kokotailo, *J. Phys. Chem. C* **1979**, *83*, 2777–2781.
- [12] K. Chao, J. Chern, *Zeolites* **1988**, *8*, 82–85.
- [13] R. Althoff, B. Schulz-Dobrick, F. Schüth, K. Unger, *Microporous Mater.* **1993**, *1*, 207–218.
- [14] N. Danilina, F. Krumeich, S. A. Castelanelli, J. A. van Bokhoven, *J. Phys. Chem. C* **2010**, *114*, 6640–6645.
- [15] R. von Ballmoos, W. M. Meier, *Nature* **1981**, *289*, 782–783.
- [16] L. Karwacki, D. A. M. de Winter, L. R. Aramburo, M. N. Lebbink, J. A. Post, M. R. Drury, B. M. Weckhuysen, *Angew. Chem. Int. Ed.* **2011**, *50*, 1294–1298.
- [17] K. Nishi, R. W. Thompson, in *Handbook of Porous Solids* (Eds.: F. Schüth, K.S.W. Sing, J. Weitkamp), Wiley-VCH, Weinheim, **2008**, pp. 736–814.
- [18] D. E. Perea, J. E. Allen, S. J. May, B. W. Wessels, D. N. Seidman, L. J. Lauhon, *Nano Lett.* **2006**, *6*, 181–185.
- [19] T. Philippe, F. De Geuser, S. Duguay, W. Lefebvre, O. Cojocaru-Mirédin, G. Da Costa, D. Blavette, *Ultramicroscopy* **2009**, *109*, 1304–1309.
- [20] K. Tedsree, T. Li, S. Jones, C. W. A. Chan, K. M. K. Yu, P. A. J. Bagot, E. A. Marquis, G. D. W. Smith, S. C. E. Tsang, *Nat. Nanotechnol.* **2011**, *6*, 302–307.
- [21] P. Felfer, P. Benndorf, A. Masters, T. Maschmeyer, J. M. Cairney, *Angew. Chem. Int. Ed.* **2014**, *53*, 11190–11193.
- [22] O. C. Hellman, J. A. Vandenbroucke, J. Rüsing, D. Isheim, D. N. Seidman, *Microsc. Microanal.* **2000**, *6*, 437–444.
- [23] M. P. Moody, L. T. Stephenson, A. V. Ceguerra, S. P. Ringer, *Microsc. Res. Tech.* **2008**, *71*, 542–550.
- [24] T. Philippe, S. Duguay, G. Grancher, D. Blavette, *Ultramicroscopy* **2013**, *132*, 114–120.
- [25] A. Devaraj, R. Colby, F. Vurpillot, S. Thevuthasan, *J. Phys. Chem. Lett.* **2014**, *5*, 1361–1367.
- [26] F. Vurpillot, A. Bostel, D. Blavette, *Appl. Phys. Lett.* **2000**, *76*, 3127–3129.
- [27] B. Gault, M. P. Moody, J. M. Cairney, S. P. Ringer, *Atom Probe Microscopy*, Springer, New York, **2012**.



Chapter 3 is based on the following manuscript:

“Quantitative 3D Fluorescence Imaging of Single Catalytic Turnovers Reveals Spatiotemporal Gradients in Reactivity of Zeolite H-ZSM-5 Crystals upon Steaming”, Z. Ristanović, J. P. Hofmann, G. De Cremer, A. V. Kubarev, M. Rohnke, F. Meirer, J. Hofkens, M. B. J. Roeijers, and B. M. Weckhuysen, J. Am. Chem. Soc. 2015, 137, 6559–6568.

Chapter 3

Quantitative 3-D Fluorescence Imaging of Spatiotemporal Gradients in Reactivity of Zeolite H-ZSM-5 Crystals

Abstract

A detailed 3-D single molecule – single turnover sensitive fluorescence microscopy study is presented to quantify the reactivity of Brønsted acid sites in parent and steamed zeolite H-ZSM-5 crystals. This approach, in combination with the oligomerization of furfuryl alcohol as a probe reaction, allowed investigating with great precision the stochastic behavior of single catalytic turnovers and temporally resolved turnover frequencies of zeolite domains smaller than the diffraction limited resolution. It was found that the single turnover kinetics of the parent zeolite crystal proceeds with significant spatial differences in turnover frequencies at the nanoscale, and non-correlated temporal fluctuations. Mild steaming of zeolite H-ZSM-5 crystals at 500 °C led to an enhanced surface reactivity with up to 4 times higher local turnover rates than of the parent H-ZSM-5 crystals and revealed remarkable heterogeneities in surface reactivity. In strong contrast, severe steaming at 700 °C significantly dealuminated the zeolite H-ZSM-5 material leading to a 460 times lower turnover rate. The differences in measured turnover activities are explained by changes in the 3-D aluminium distribution due to migration of extra-framework Al-species and their subsequent effect on pore accessibility.

3.1 Introduction

Fluorescence microscopy has revolutionized life sciences and the chemical understanding of numerous biological processes.^[1–5] The significance of the developments in the field of super-resolved fluorescence microscopy techniques was recognized with the Nobel Prize in Chemistry for 2014. Besides offering the ultimate sensitivity limit of an analytic method, single molecule fluorescence microscopy opens possibilities to overcome the diffraction limited resolution of the optical microscopy by localizing single fluorescent molecules with nanometer precision. In the fields of heterogeneous catalysis and material science several examples have demonstrated the remarkable potential of this technique for visualizing the diffusion of fluorescent molecules in mesoporous materials^[6,7] and the reactivity of catalyst particles.^[8–17] However, despite the fact that there are no obstacles in instrumentation, the application of this method in the field of catalysis is lagging behind its biological applications.^[18–20]

The concept of Nanometer Accuracy by Stochastic Chemical reActions (NASCA) microscopy represents an important single molecule fluorescence method that is based on the localization of stochastically formed chemical (and catalytic) events that are accompanied with changes in fluorescence.^[10] It was used previously to resolve the individual catalytic conversions of furfuryl alcohol (FA) on individual zeolite H-ZSM-5^[10] and H-MOR^[16] crystals. In this chapter, by using the 3-D NASCA approach we follow real-time changes in the stochastic dynamics of catalytic turnovers in parent and steamed zeolite H-ZSM-5 crystals. It will be shown that the unique sensitivity and spatial resolution of NASCA microscopy enables the accurate quantification of the local turnover frequencies in 3-D for nanoscopic zeolite domains within the individual, parent and steamed zeolite H-ZSM-5 crystals characterized in detail in Chapter 2. The approach can be used to visualize enhanced catalytic activity and large micron-scale heterogeneities in local turnover frequencies of mildly steamed H-ZSM-5-MT zeolite crystals, as well as to measure a significant loss of turnover activity of severely steamed H-ZSM-5-ST zeolite crystals. Furthermore, the approach allows studying the stochastic behavior of single catalytic turnovers and their temporal correlations within nanoscopic zeolite domains. Based on this method it was found that the single turnover kinetics of the seemingly homogeneous parent H-ZSM-5-P

zeolite crystal proceeds with significant spatial, nano-scale differences, and non-correlated temporal fluctuations.

3.2 Experimental

3.2.1 Sample preparation

Parent H-ZSM-5-P, mildly steamed H-ZSM-5-MT, and severely steamed H-ZSM-5-ST zeolite crystals were prepared as described in the experimental section of Chapter 2. Prior to single molecule fluorescence microscopy experiments, the crystals were activated at 773 K (1 K/min) for 24 h in static air to avoid residual fluorescence.

3.2.2 Wide-field fluorescence microscopy setup

A schematic of the experimental approach is presented in Figure 3.1a. Single molecule fluorescence experiments were performed using an inverted epi-fluorescence wide-field microscope (Olympus IX-71), equipped with a 100 \times oil immersion objective lens (1.4 NA) and a highly sensitive Electron Multiplying – CCD (EM-CCD) camera (ImagEM Enhanced C9100-23B, Hamamatsu). Wide-field illumination was achieved by circularly polarized 532 nm light from a diode laser (Excelsior 532, Spectra-Physics). Fluorescent emission was imaged by the EM-CCD after passing through a dichroic mirror and a 545 nm long-pass filter removing the excitation light. The image was expanded by a 3.3 \times camera lens resulting in a field of view of 24.6 \times 24.6 μm^2 and 48 \times 48 nm 2 per pixel. Wide-field images of catalytic turnovers were recorded approximately at the middle of the zeolite crystal (Figure 3.1b) with a frame rate of 10 images per second.

3.2.3 Experiment

The oligomerization of furfuryl alcohol (Figure 3.1c) was performed on activated zeolite H-ZSM-5 crystals loaded on the top of a cover glass in a reactor designed for liquid-phase experiments. The crystals were exposed to furfuryl alcohol (99%, Sigma Aldrich), previously diluted in Milli-Q water, to achieve the desired catalytic activity. The optimal concentration of FA for high-resolution imaging was determined in a series of concentration dependent measurements. The reaction was then monitored focusing at the surface of the bottom subunit (denoted here as Z = 0) or by moving

the focus to any provisional focal depth in axial Z-direction up to $Z = 20 \mu\text{m}$ (Figure 3.1a), with the estimated precision of $\pm 0.2 \mu\text{m}$. Prior to the experiments, the absence of residual fluorescence was verified on individual H-ZSM-5 crystals. All experiments were performed at room temperature.

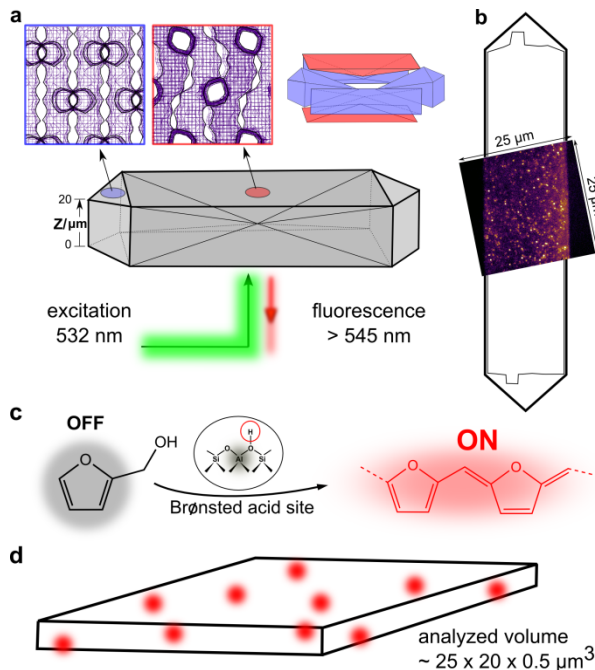


Figure 3.1 Schematic of the single molecule fluorescence approach used to map in 3-D the reactivity of a single H-ZSM-5 crystal. a) Intergrowth structure of a zeolite H-ZSM-5 crystal indicating the direction of the straight and sinusoidal pores in different subunits (color-coded). b) Accumulated image of individual fluorescent products depicted with respect to the size of the zeolite crystal. c) Formation of fluorescent products (red) upon the protonation of FA (black) on a Brønsted acid site. d) Estimate of the analyzed crystalline volume depicting the 3-D distribution of fluorescent molecules (red). Note that the localization precision in Z-direction is estimated to be $\sim 500 \text{ nm}$.

3.2.4 Data analysis

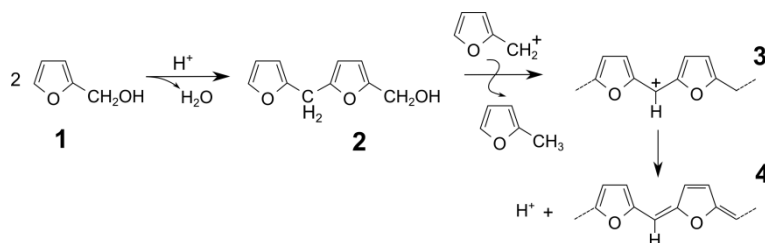
The recorded movies were analyzed with the Localizer analysis software^[21] developed for *Igor Pro* (Wavemetrics) and *Matlab* (MathWorks). The sub-diffraction localization of fluorescent events was done by independent segmentation of each frame into emissive spots and background using the approach of Sergé et al.^[22] The pixels identified by this segmentation were reduced to a list of initial emitter positions by considering adjacent active pixels as belonging to a single emitter. The locations of these emitters were subsequently determined with sub-diffraction limited resolution by

fitting a two-dimensional Gaussian using the Levenberg-Marquardt least-squares algorithm as implemented in the GNU Scientific Library. The correct functioning and absence of systematic errors in the algorithm were verified by visual inspection of the processed results.

3.3 Results and Discussion

3.3.1 Oligomerization of furfuryl alcohol

The acidic properties of H-ZSM-5 crystals were tested using the oligomerization of furfuryl alcohol (FA) – a fluorogenic reaction used to probe the Brønsted acid sites of zeolites H-ZSM-5 and H-MOR.^[10,16,23] The oligomerization of non-fluorescent FA at the Brønsted acid sites of zeolite H-ZSM-5 leads to the formation of fluorescent oligomeric species (Figure 3.1c). As depicted in Scheme 3.1, the initial protonation and dimerization of furfuryl alcohol (**1**) leads to the formation of non-colored bisfurfurylmethyl (**2**). This molecule further undergoes hydride transfer to result in the formation of resonance-stabilized carbenium ion (**3**) and its conjugated structure formed after a proton loss (**4**). The carbenium ion (**3**) has a reported extinction coefficient of $55000 \text{ cm}^{-1}\text{M}^{-1}$ at 490 nm, whereas the structure (**4**) has an estimated extinction coefficient of $110000 \text{ cm}^{-1}\text{M}^{-1}$ at 610 nm.^[24] In the single molecule experiments a 532 nm laser has been used to efficiently excite compound (**4**) and its derivates.



Scheme 3.1 The proposed formation of chromophores during the acid-catalyzed condensation of furfuryl alcohol. Reproduced from ref. [25].

3.3.2 Single molecule fluorescence microscopy of zeolite H-ZSM-5 crystals

The fluorescence emission of the product molecules formed upon the protonation of FA can be subsequently detected using a highly sensitive EMCCD detector (Figure 3.1b). Their steric confinement in the zeolite pores contributes to their excellent

fluorescence properties and enhanced contrast in respect to the molecules that have diffused into the bulk solution. An inspection of fluorescent movies illustrates that fluorescent events are taking place at different focal depths with respect to the surface of the zeolite crystal – a consequence of the intracrystalline diffusion and the stochastic nature of the catalytic process. Their location in axial direction can be determined with an estimated precision in the order of ~ 500 nm – a value that is used in the later quantification analysis.^[14] Based on this, it can be approximated that the single molecule events are simultaneously recorded within a crystalline volume of approximately $25 \times 20 \times 0.5 \mu\text{m}^3$, where $25 \times 20 \mu\text{m}^2$ represents a projected area of the crystal (Figure 3.1d). Within this volume, we estimate 2.7×10^{11} Brønsted acid sites if all Al atoms are considered to be catalytically active. Clearly, the concentration of FA is a critical variable to achieve turnover activity optimal for imaging.

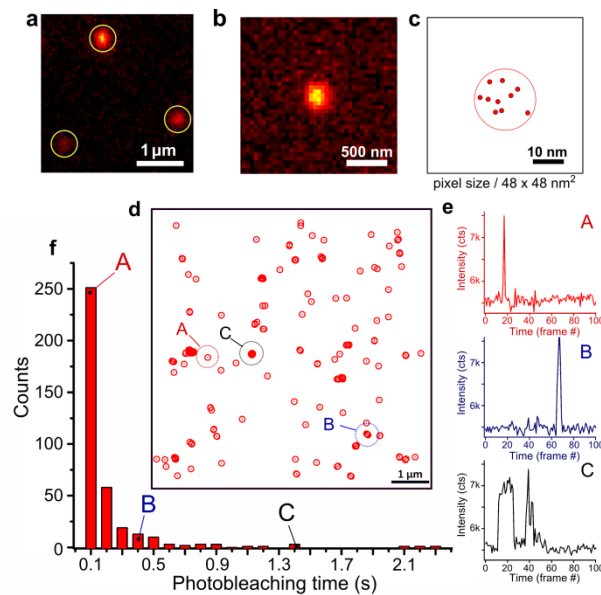


Figure 3.2 The NASCA localization approach. a) Three isolated catalytic events (bursts) as identified by the 2-D Gaussian localization algorithm. b) Single burst as detected by the EMCCD camera, and c) subsequent localization of a fluorescent event appearing in 10 consecutive frames. The red circle denotes a diameter of 20 nm, indicating the lateral spatial precision of the method. d) High-resolution map of fluorescence activity based on 100 consecutive frames. e) Typical fluorescence trajectories of the events shown in (d). f) Histogram of the photobleaching times for 370 single molecules.

Low reaction rates – typically in a range of 1-1000 detected product molecules per second and per crystal section – enable successful quantification of

individual fluorescent events and prevent simultaneous spatial overlapping of the fluorescent product molecules (Figure 3.2a). Each fluorescent reaction product manifests on the detector through a fluorescent burst with an intrinsic point spread function (PSF) of ~ 230 nm at FWHM (Figure 3.2b). However, the lateral localization precision of the method is substantially improved by fitting the PSF of a fluorescent molecule by a 2-D Gaussian localization algorithm, resulting in a typical localization precision in order of 20 nm (Figure 3.2c). Following this localization approach for many repetitive frames, single turnovers can be localized in 3-D for any specific focal depth within the crystal Z-axis (20 μm , as illustrated in Figure 3.1a, with the axial (Z) localization precision estimated to be ~ 500 nm). This results in reactivity maps that indicate the precise 2-D location of the detected fluorescent events (Figure 3.2d).

Fluorescent events may reappear in several consecutive frames before they permanently photobleach (Figure 3.2e). The histogram of photobleaching lifetimes shows that the majority of fluorescent products are photobleached within a short time interval of 0.5 s (Figure 3.2f). Fast photobleaching of fluorescent products is essential for the quantification of the catalytic turnovers. Furthermore, the photobleaching prevents fast accumulation of the background fluorescence and enables stable monitoring over an extended period of time. The analysis of the products brightness did not indicate substantial attenuation of fluorescence in the deeper regions of the single zeolite crystals. Hence, the single molecule products were efficiently localized despite a slight increase in the scattered background signal, mostly originating from the side subunits (for details of the analysis see Section 3.3.4).

3.3.3 Emitter tracking analysis and optimization of the localization parameters

A necessary step in order to quantify individual turnovers is to correct for the reappearance of fluorescent events in repetitive frames. For this purpose we have used the emitter tracking algorithm as implemented in the *Localizer* analysis software. The algorithm is using two parameters that take into account the reappearance of a molecule at a certain distance (*pixel jump*) and after a certain period of time (*blinking gap*). An iterative procedure was further used to optimize the parameters of the algorithm that take into account the experimental results of a single molecule

reappearance in the subsequent localizations (*pixel jump*) and blinking of the fluorescent molecule (*blinking time*).

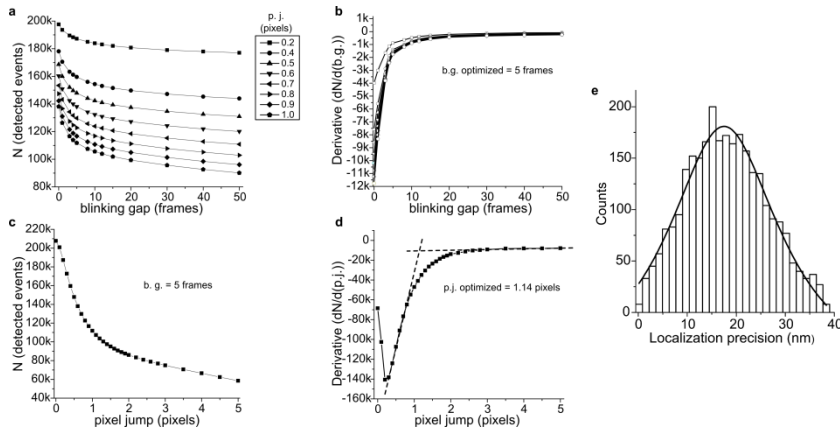


Figure 3.3 Optimization of the *pixel jump* (*p.j.*) and *blinking gap* (*b.g.*) parameters, as determined based on the experimental data. a) Number of detected events as function of *blinking gap* values, for constant values of *pixel jump*. b) Corresponding derivatives of (a) with the optimized *blink gap* = 5 frames. c) Number of detected events as function of *pixel jump* for the constant *blinking gap* = 5 frames. d) Corresponding derivative of (c) illustrating determination of the optimal value of *pixel jump* = 1.14 pixels. 1 pixel = 48 nm, 1 frame = 100 ms. e) Estimated localization precision histogram calculated based on the emitter tracking algorithm for more than 2800 single molecules re-appearing in the consecutive frames. The Lorentzian fit has a maximum at 17 nm, σ = 9 nm (FWHM = 21 nm). Note that the estimated localization precision of an individual molecule depends on the molecule's brightness, background signal, Z-position, and fitting parameters.

The optimal values of localization parameters are determined by using an experimentally recorded fluorescence movie with a high number of detected turnovers (> 200 000) as follows:

- the total number of detected events was calculated by systematically changing the *blinking gap* for the constant *pixel jump* values (Figure 3.3a);
- the change in the number of detected turnovers (Figure 3.3b) indicates the optimal value for *blinking gap* = 0.5 s (5 frames);
- determined value for *blinking gap* is subsequently used to calculate the total number of turnovers for different values of *pixel jump* (Figure 3.3c); the derivative of this graph (Figure 3.3d) gives the optimal value of *pixel jump* = 55 nm (1.14 pixels).

Summarizing, optimal values of 55 nm for the *pixel jump* and 0.5 s for the *blinking time* were found to be a good experimental correction for the summed effects of photobleaching, blinking, localization precision and molecular diffusion. In other words, if a fluorescent event reappears within a distance of 55 nm and within time

interval of 0.5 s it will be counted as one catalytic event. Once the fluorescent product is photobleached we account for the formation of new fluorescent molecules that may appear in this area. It should be noted that the criteria for localization only changes to a minor extent the total number of detected events, but does not change the relative trends in the quantification precision. The optimization of the localization parameters has shown that the localization precision is the most limiting factor in the analysis. The large majority of fluorescent events can be localized with an estimated lateral precision of 17 ± 9 nm (Figure 3.3e). However, the optimized algorithm accounts also for the extremes in the localization efficiency (e.g. when one molecule appears in many consecutive frames) in order to eliminate artificially generated hotspots of reactivity. This approach is sensible considering that the probability of consecutively finding two fluorescent molecules within the diameter of 55 nm is very low.

3.3.4 Localization efficiency with different focal depths

Single molecule fluorescence microscopy can be routinely used to record fluorescence movies from any provisional focal depth of the zeolite crystal. One of the concerns related to the imaging at higher focal depths is the attenuation of the fluorescence light and the background scattering. Therefore, we have analyzed integrated fluorescence intensities of individual fluorescent events and corresponding background signals as a function of focal depth (Figure 3.4a). We did not observe substantial weakening of the single molecule fluorescence signal with the change in focal depth (Figure 3.4b). A small shift towards lower intensities is notable at $Z = 4$ μm and $Z = 6$ μm . It is important to note that the high number of detected turnovers at the surface ($Z = 0$) will also contain a certain fraction of low-intensity events, but this number seems to be proportional for any focal depth as the plotted intensity distributions are very similar.

The effect of the background signal is more complex and is related to the intergrowth structure of the crystal, the polarization effect, photobleaching, and reaction time. Scattering of the fluorescence light mostly originates from the side subunits and therefore a bimodal-like distribution is visible for the background intensity at $Z = 4$ μm and $Z = 6$ μm (Figures 3.4c,d). For this reason, and to avoid the inefficient, polarization-dependent excitation present at the side subunits, we have only calculated the catalytic activity of the top subunit. In this region, the signal to noise ratio is sufficiently high to efficiently resolve single fluorescent turnovers, even

after 4 h of reaction time. Note also that the number of the observed catalytic turnovers is so low at $Z = 6 \mu\text{m}$ for all studied examples (due to slow diffusion of the reactant molecules) that it cannot account for any substantial experimental error.

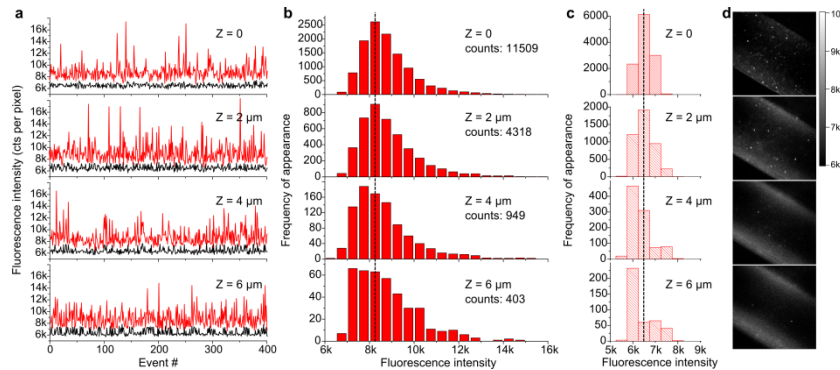


Figure 3.4 a) Average fluorescence intensity per pixel (red) of the exemplified 400 individual fluorescent events and the corresponding plots of the fitted baseline background signal (black), calculated for the fluorescent events detected at four different focal depths after 3 h of reaction in 5.75 mM solution of FA. The average fluorescence intensity per pixel is estimated based on the total fitted integrated intensity of the single fluorescent event and assuming the average of approximately 25 pixels per event. b) Histograms of the averaged fluorescence intensities (per pixel), from the focal depths presented in (a). Note a significant decrease in the total number of detected events (counts) when moving deeper into the particle. c) Corresponding histograms of the background fluorescence intensity. The dotted lines in (b) and (c) indicate the position of the maximum at $Z = 0$. d) Examples of the single-frame photomicrographs illustrating the distribution of the scattered background signal. Note that the turnover rates in the later quantification analysis are calculated in the regions of the lower background intensity (i.e. for the top subunit).

3.3.5 Time-dependent quantification of the stochastic single turnover dynamics

To follow the dynamics of catalytic turnovers taking place in the micropores of zeolite H-ZSM-5-P crystals we have optimized the reaction conditions that favor efficient detection of the reaction products – i.e. the photobleaching of the catalytically formed fluorescent products is compensated by the formation of novel reaction products catalyzed by abundantly present Brønsted acid sites. Using the developed method, it is possible to temporally resolve and quantify single catalytic turnovers that simultaneously take place within the analyzed volume. This is illustrated in Figure 3.5a, where the turnover rate is monitored over 4 h of catalytic reaction taking place close to the surface of the single H-ZSM-5-P crystal. The number of catalytic turnovers counted over 100 ms time intervals follows a Poisson distribution with an increased broadening and shift towards higher mean values as a function of time (Figure 3.5b).

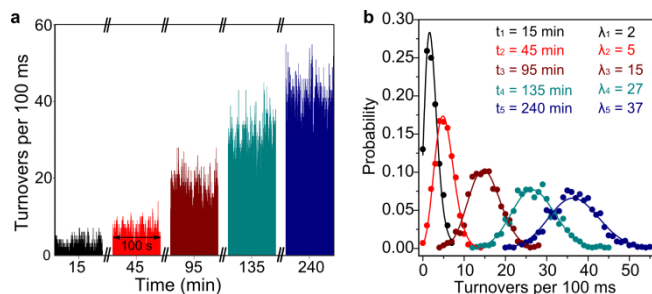


Figure 3.5 Single turnover stochastics of the oligomerization reaction monitored at the surface of the H-ZSM-5-P single crystal for 4 h in a 5.75 mM solution of FA. a) Total number of detected turnovers per frame as function of time. Each time interval is 100 s. Note the large time gaps between the measurements. b) Poisson distributions of the corresponding color-coded trajectories presented in (a), including the Poisson parameter λ .

The parameters of the Poisson distribution describe the stochastic nature of the catalytic process for an arbitrary region of interest which is ultimately limited by the resolution of our method. Figure 3.5 suggests that the turnover rates fluctuate stochastically around mean values that are a function of time and the concentration of the reaction intermediates. The latter is limited by the slow intracrystalline diffusion of FA molecules into microporous voids of H-ZSM-5. Therefore, in order to study the reactivity in deeper crystalline regions, reaction conditions should be optimized to yield moderate turnover rates. We found that 5.75 mM solution of FA is an optimal concentration to quantify single turnover dynamics in 3-D for the studied zeolite crystals.

3.3.6 3-D imaging of steaming effects on reactivity

Using the NASCA approach we have compared the 3-D reactivity of the parent zeolite H-ZSM-5-P crystals with the mildly steamed H-ZSM-5-MT and severely steamed H-ZSM-5 ST zeolite crystals. The material characterization of these zeolite crystals was presented in Chapter 2. Figure 3.6 summarizes the accumulated high-resolution reactivity maps, taken after 3 h of reaction at the middle of the three zeolite crystals, for the three different focal depths – $Z = 0 \mu\text{m}$ (surface), $Z = 2 \mu\text{m}$, and $Z = 4 \mu\text{m}$ below the surface. The reactivity maps qualitatively suggest the following order of reactivity: H-ZSM-5-MT > H-ZSM-5-P >> H-ZSM-5-ST.

Three important conclusions follow from Figure 3.6. First, mild steaming increases the single turnover activity in the near-surface regions of a single zeolite

crystal and induces clearly visible spatial inhomogeneities in reactivity. Second, severe steaming greatly reduces the turnover activity at all focal depths. Finally, the reactivity maps at $Z = 2 \mu\text{m}$ and $Z = 4 \mu\text{m}$ reveal regions of lower fluorescence activity that are a consequence of a different pore orientation in the crystal subunits, as indicated by the yellow arrows in Figure 3.6. From this point on, we will further elaborate on these observations in a quantitative manner by measuring spatio-temporal changes in the turnover frequencies of zeolite domains.

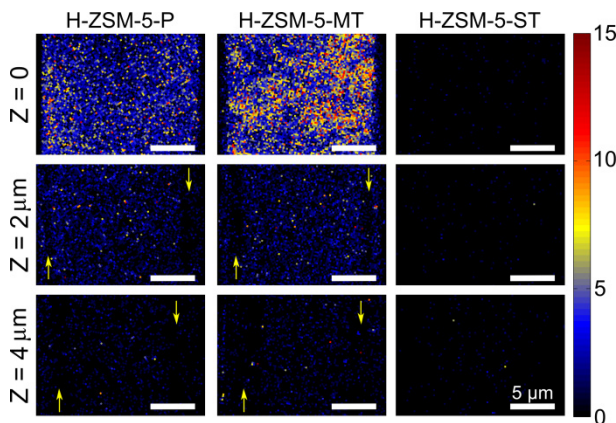


Figure 3.6 Single molecule reactivity maps for H-ZSM-5-P, H-ZSM-5-MT and H-ZSM-5-ST crystals described and characterized in Chapter 2, recorded at three different focal depths ($Z = 0$ (surface), $Z = 2 \mu\text{m}$ and $Z = 4 \mu\text{m}$). Reactivity is accumulated for 1000 frames, after 3 h of reaction in 5.75 mM solution of FA. Yellow arrows indicate the regions with lower reactivity due to a different crystallographic orientation of the subunits. Color bar: turnovers per $200 \times 200 \text{ nm}^2$.

3.3.7 Influence of the structural anisotropy on the catalytic performance of H-ZSM-5 crystals

The crystallographic analysis of zeolite H-ZSM-5-P crystals in Chapter 2 has resolved their 90° intergrowth structure, proving the strong anisotropy of individual zeolite crystals. The impact of the intergrowth structure on reactivity can be clearly visualized when sufficient quantity of single molecule products is accumulated in inner regions of the H-ZSM-5-P crystal, as illustrated for $Z = 2 \mu\text{m}$ and $Z = 4 \mu\text{m}$ (Figure 3.7). It is striking that the formation of linear fluorescent oligomers proceeds mainly along the straight pores of the zeolite H-ZSM-5-P crystal, even though the access to the crystalline bulk of the top/bottom subunits is mainly provided via the sinusoidal pores (Figure 3.1a).^[10] This implies that the circularly polarized laser light interacts predominantly with the transition dipole moments of fluorescent products oriented

along the straight pores of zeolite H-ZSM-5. Likewise, the molecules that are aligned within the straight pores of the side subunits (see Figure 3.7) are not efficiently excited with the perpendicular vector component of the laser light; hence, these subunits are not taken into account in our quantitative analysis. A strong dependence of the recorded signal from the crystalline anisotropy and the preferential orientation of the guest molecules has been observed on several occasions for H-ZSM-5 and H-MOR crystals using different microscopic techniques.^[16,25–27]

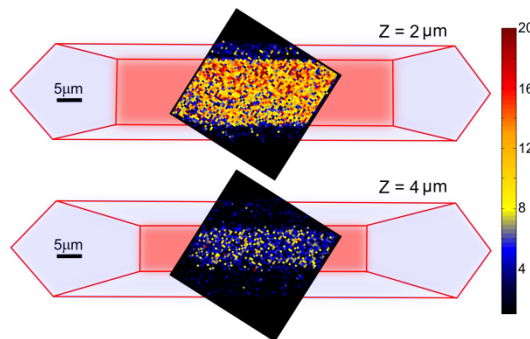


Figure 3.7 Models of the H-ZSM-5 intergrowth structure according to the results of μ -XRD analysis presented in Chapter 2; red (top/bottom subunits): straight pores run parallel to the image plain, blue (side subunits): straight pores run perpendicular to the image plain). The overlaid single molecule maps indicate differences in reactivity for planes that are 2 μm and 4 μm below the surface, after 2.5 h in a 5.75 mM solution of FA. Color bar: turnovers per $800 \times 800 \text{ nm}^2$.

3.3.8 3-D quantification of the single catalytic turnovers

We have further examined the 3-D reactivity profiles of FA in order to provide a more complete quantitative picture of the effect of steaming on Brønsted reactivity. Figure 3.8 illustrates the temporal evolution of the normalized turnover activities, recorded for the parent (H-ZSM-5-P), the mildly steamed (H-ZSM-5-MT), and the severely steamed (H-ZSM-5-ST) zeolite crystals at four different focal depths. The most notable difference in reactivity of the parent H-ZSM-5-P and mildly steamed H-ZSM-5-MT zeolite crystals is in the surface regions (depth $Z = 0$). The reactivity profiles evidence slow intracrystalline diffusion of FA, with most of the fluorescent events detected within the 500 nm near-surface layers of the single crystals. The initial uptake of FA molecules and the subsequent oligomerization in the H-ZSM-5-MT proceeds faster and reaches a 4 times higher reaction rate after 1 h of reaction than for H-ZSM-5-P. The reactivity profile of H-ZSM-5-P shows a longer induction period

and reaches a maximal turnover activity of 0.63 turnovers per μm^3 per second. This value is about 1.8 times lower than for H-ZSM-5-MT after 4 h (Figure 3.8).

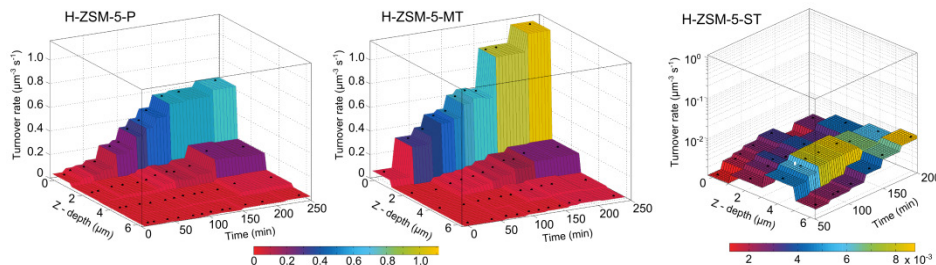


Figure 3.8 Normalized turnover activities of zeolites H-ZSM-5-P, H-ZSM-5-MT and H-ZSM-5-ST in a 5.75 mM solution of FA plotted as a function of time and focal depth Z. The turnover rates are calculated and normalized for the top subunit (see Figure 3.7) in order to eliminate the polarization effect and higher background scattering from the side subunits. The first two experimental points for the H-ZSM-5-MT crystal (after 5 min and 42 min) were recorded from two different crystals. The color bars indicate turnover rates as plotted in the 3-D graphs. Note the logarithmic z-axis for H-ZSM-5-ST. The black dot markers in the 3-D graphs indicate the experimental values.

The surface turnover rates of the measured regions indicate improved accessibility of the H-ZSM-5-MT crystals achieved by mild steaming. It is worth noting that the H-ZSM-5-MT crystals show consistently higher near-surface turnover rates than H-ZSM-5-P crystals. However, the reaction rates recorded at $Z = 2 \mu\text{m}$ do not differ significantly, indicating that mild steaming does not affect substantially the inner crystalline regions of the zeolite material. In contrast to both parent and mildly steamed zeolite crystals, severely steamed H-ZSM-5-ST crystals showed a 460 times lower surface turnover rate than H-ZSM-5-MT, without notable time-dependent changes. Furthermore, the turnover rates of H-ZSM-5-ST at $Z = 4 \mu\text{m}$ are 3 times higher than at $Z = 0$ (turnover rate of 2×10^{-3} turnovers per μm^3 per second), suggesting a drastic change in the amount and distribution of active Brønsted acid sites upon severe steaming.

The measured turnover rates are the summed result of mass transfer limitations and the concentration of accessible acid sites. We have learned in Chapter 2 that the acid sites of H-ZSM-5-P are not homogeneously distributed throughout the crystal and their distribution changes further upon steaming post-treatments. The study presented in Chapter 2 indicated that there is a strong gradient in Al concentration (often referred to as Al zoning) present in parent H-ZSM-5-P crystals. TOF-SIMS analysis (Section 2.3.5) has shown the most remarkable differences in Al

distribution in the near-surface regions of the crystals (Figure 2.6). Parent H-ZSM-5-P crystals typically show a depletion of Al in a surface layer of approximately 50 nm, while mildly and severely treated crystals H-ZSM-5-MT and H-ZSM-5-ST exhibit significant Al enrichment in this region (Figure 2.6). These differences in the surface distribution of Al help understanding the observed trends in the reactivity measured by the single molecule fluorescence method. The lower reaction rates in the surface regions of the parent crystals are not only related to slow molecular diffusion in H-ZSM-5-P, but also to the presence of a silicalite layer at the surface (a Si/Al ratio of 160 has been measured by XPS)^[28] that may significantly hinder reactivity.^[29] This explains the initially low turnover rates recorded at the surface of H-ZSM-5-P crystals. In contrast, a mild steaming treatment creates extra-framework Al species in the surface region but does not affect the inner regions of the zeolite material, as observed by HR-SEM.^[28] The presence of mesoporous defects in the surface layers of H-ZSM-5-MT crystals is responsible for the enhanced diffusion and higher single turnover rates, despite a loss in the number of Brønsted acid sites due to dealumination. The observed trends are in line with findings of Aramburo and Karwacki.^[28,30] Both H-ZSM-5-P and H-ZSM-5-MT have shown strong coloration upon exposure to 4-fluorostyrene. However, the average coloration of H-ZSM-5-MT was approximately twice as intense as that of H-ZSM-5-P. This is an indication that surface mesoporosity contributes to higher accessibility of acid sites in the former case. In contrast, H-ZSM-5-ST crystals have shown very weak UV-Vis bands with limited reactivity, confirming severe dealumination of zeolite H-ZSM-5-ST crystals.^[28]

The measured TOF-SIMS profiles discussed in Chapter 2 only indicate the total concentration of Al atoms, but not all of them are necessarily tetrahedrally coordinated and incorporated in the framework of zeolite – hence, not all of them are necessarily catalytically active. The example of severely steamed crystals strongly illustrates this point. The recorded turnover frequencies of H-ZSM-5-ST are significantly lower than for H-ZSM-5-P and H-ZSM-5-MT. This can be rationalized by an abundance of extra-framework Al species formed upon severe steaming. The TOF-SIMS Al depth profile indicates that Al is still present within the crystal, but does not provide the Brønsted acidity necessary for the oligomerization reaction. The first experimental point in the TOF-SIMS profile of H-ZSM-5-ST (Figure 2.6) indicates the deposition of Al in the surface layer of zeolite crystal, most probably due

to the high degree of dealumination that is visible up to $\sim 1 \mu\text{m}$ of the depth profile. Quite in contrast, the reactivity observed in the surface layer of H-ZSM-5-ST is very low and cannot be correlated with the concentration of Al determined by TOF-SIMS. Remarkably, the observed Al zoning of the H-ZSM-5-P single crystals has a profound effect on the degree of dealumination upon mild and severe steaming, as H-ZSM-5 zeolite with lower Al content is more resistant to dealumination.^[31–33] Therefore, mild steaming will lead to the selective dealumination mostly in the surface regions of the H-ZSM-5-MT crystals where Al has the highest initial concentration, as also noted by FIB-SEM analysis (Figure 2.7).^[28] Similarly, severe steaming affects more surface regions of H-ZSM-5-ST crystals than deeper parts, where we consistently observe several times higher turnover rates.

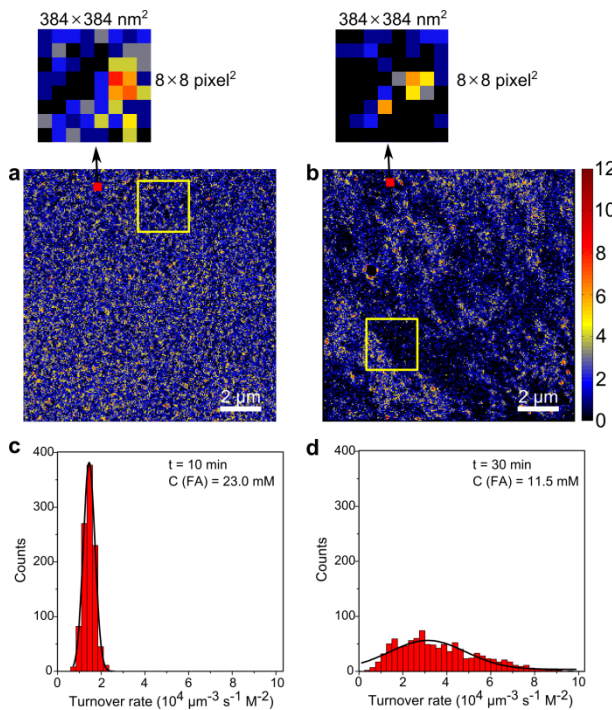


Figure 3.9 High-resolution imaging of accessible acid sites. a,b) High-resolution images of surface reactivity based on movies (2000 frames) for a) a H-ZSM-5-P crystal in a 23 mM solution of FA, and b) a H-ZSM-5 MT crystal in a 11.5 mM solution of FA. The color bar denotes the number of detected turnovers per $48 \times 48 \text{ nm}^2$. Insets marked with arrows indicate high-resolution images of $384 \times 384 \text{ nm}^2$ domains, used for calculating the histograms displayed in (c) and (d). The yellow squares in (a,b) indicate the regions of interest used to construct the scatter plots in Figure 3.10. c,d) Corresponding histograms of turnover activity, calculated from $384 \times 384 \text{ nm}^2$ binned regions in (a) and (b), and normalized to the molar concentration of FA, for c) H-ZSM-5-P and d) H-ZSM-5-MT.

3.3.9 High-resolution imaging of the surface activity

The NASCA method further provides in-depth insights into the spatio-temporal changes taking place in nanoscopic domains of the H-ZSM-5-P and H-ZSM-5-MT. The question arises whether the surface of a zeolite crystal is homogeneously affected by the mild steaming method. A closer look into the surface high-resolution reactivity maps of the H-ZSM-5-P and H-ZSM-5-MT zeolite crystals, presented in Figure 3.6, indicates substantial differences in the spatial distribution of catalytic turnovers. These differences become highly visible when the crystals are exposed to a higher concentration of FA (10-30 mM), enabling the fast accumulation of catalytic turnovers.

Qualitatively, the reactivity of the H-ZSM-5-P was macroscopically homogeneous on a micrometer length scale (Figure 3.9a), while the surface of the H-ZSM-5-MT shows significant heterogeneities in reactivity (Figure 3.9b). To quantify the extent of those differences the high-resolution maps from Figures 3.9a,b were divided into $384 \times 384 \text{ nm}^2$ (8×8 binned pixels) regions, as illustrated in Figure 3.9. Such regions are used to construct the histograms of the turnover activity, as presented for H-ZSM-5 P (Figure 3.9c) and H-ZSM-5-MT (Figure 3.9d). While H-ZSM-5-P has a fairly narrow distribution of turnover rates determined for $384 \times 384 \text{ nm}^2$ regions of interest, the H-ZSM-5-MT shows a broad reactivity histogram with regions of high and low reactivity, spanning nearly one order of magnitude. A TOF-SIMS sputter depth profile of the mildly steamed crystal (Figure 2.6) indicated the deposition of extra-framework Al species in the near-surface regions of H-ZSM-5-MT crystals. Therefore, a non-uniform turnover activity of the nanoscopic domains of H-ZSM-5-MT could be related to large differences in the accessibility of Brønsted acid sites caused by the migration of Al and blockage of micropores. Such near-surface layers of extreme heterogeneity seem to be responsible for the large transport barriers that may significantly affect the uptake of molecules and unevenly reduce the local permeabilities.^[34,35]

The high-resolution map of turnover activity of H-ZSM-5-P (Figure 3.9a) indicates observable nanoscopic differences in reactivity even for the parent zeolite crystal. A scatter plot in Figure 3.10a shows the locations of individual catalytic turnovers for a $2.4 \times 2.4 \mu\text{m}^2$ region of interest indicated in Figure 3.9a. The

inhomogeneous distribution of catalytic turnovers in Figure 3.10a could be a consequence of the stochastic nature of the process, which is described by Poisson statistics in Figure 3.5. To verify this hypothesis, we have simulated a scatter plot that describes a completely random, stochastic process (Figure 3.10b). As the scatter plots are constructed based on the identical number of catalytic turnovers (3709) we would expect a similar distribution of nearest neighbors (NN) for both H-ZSM-5-P and the simulated pattern. A histogram in Figure 3.10c does not support the hypothesis of randomness. The number of NNs in a radius of 100 nm calculated for zeolite H-ZSM-5-P suggests a substantial deviation from the simulated random distribution of catalytic turnovers. The observed heterogeneities in reactivity recorded for parent zeolite crystals could be a direct consequence of intrinsic differences in the surface accessibility and acidity introduced to the zeolite framework during the synthesis, ion exchange, or activation.

Figure 3.9b shows clear micron-scale heterogeneities in reactivity of a mildly treated H-ZSM-5-MT single crystal. This is further illustrated in Figure 3.10d where the two regions of distinctly different reactivity coexist within the sample. Clearly, as compared to the scatter plot from the simulated pattern (Figure 3.10e), the histogram of NN distribution for H-ZSM-5-MT shows significant deviation with a very broad distribution of the number of nearest neighbors. (Figure 3.10f).

It is noteworthy to add that the difference in the measured and simulated distribution of the nearest neighbors is clearly visible only within the radius distances of ~ 100 nm. For example, the histogram for a 48 nm radius (Figure 3.11a) indicated a small difference between the measured distributions. Increasing further the radius of NN analysis to 480 nm and 720 nm leads to very similar NN histograms (Figures 3.11b,c).

The observed changes in reactivity for the H-ZSM-5-P crystals can be resolved with temporal resolution of 100 ms per frame. We studied the reactivity of the zeolite domain presented in Figure 3.9a and divided it into 784 smaller domains with the lateral size of 384×384 nm² (see Figure 3.9a). This size was chosen based on the observed density of catalytic events. Smaller domains can be analyzed in a similar manner, but yield low numbers of detected events per domain. By applying the described quantification procedure we reconstructed turnover trajectories of all analyzed domains. A digital single turnover trajectory of an exemplified region of

interest is shown in Figure 3.12a. Each turnover trajectory can be described by the time between subsequent catalytic events, denoted here as *waiting time*. This parameter was used in single enzyme kinetics to derive memory effects in enzyme conformation dynamics.^[2,36,37]

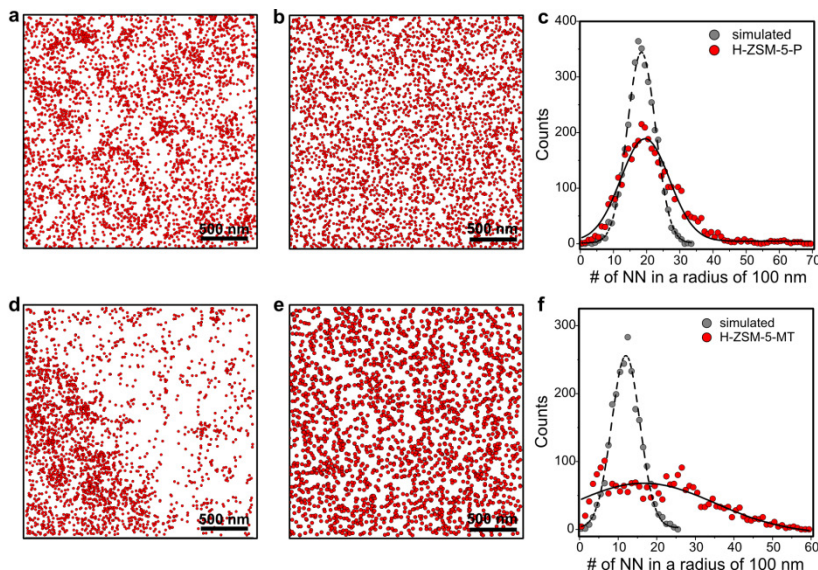


Figure 3.10 Scatter plots of reactivity and nearest neighbors analysis for H-ZSM-5-P (top row) and H-ZSM-5-MT (bottom row). a,d) Scatter plots of reactivity for H-ZSM-5-P (a) and H-ZSM-5-MT (d) regions of interest indicated by yellow squares in Figure 3.9; b,e) corresponding simulated, random scatter plots for H-ZSM-5-P (b) and H-ZSM-5-MT(e). Each dot in the scatter plots represents one catalytic turnover. c,f) Histograms of the number of nearest neighbors (NN) detected within a radius of 100 nm. c) Comparison of H-ZSM-5-P and the simulated pattern, calculated from the scatter plots in (a) and (b). f) Comparison of H-ZSM-5-MT and the corresponding simulated pattern, calculated from the scatter plots in (d) and (e)

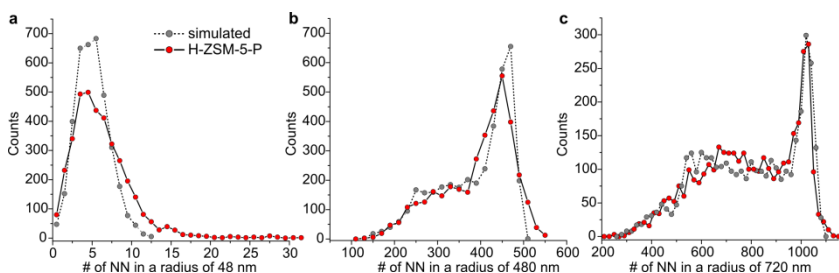


Figure 3.11 Distribution of the number of detected nearest neighbors for H-ZSM-5-P (red circles) and for simulated scatter plots (gray circles) in a radius of a) 48 nm (1 pixel), b) 480 nm (10 pixels), and c) 720 nm (15 pixels). Note that the distortion of the distributions is due to the “finite-size” effects of the simulation box.

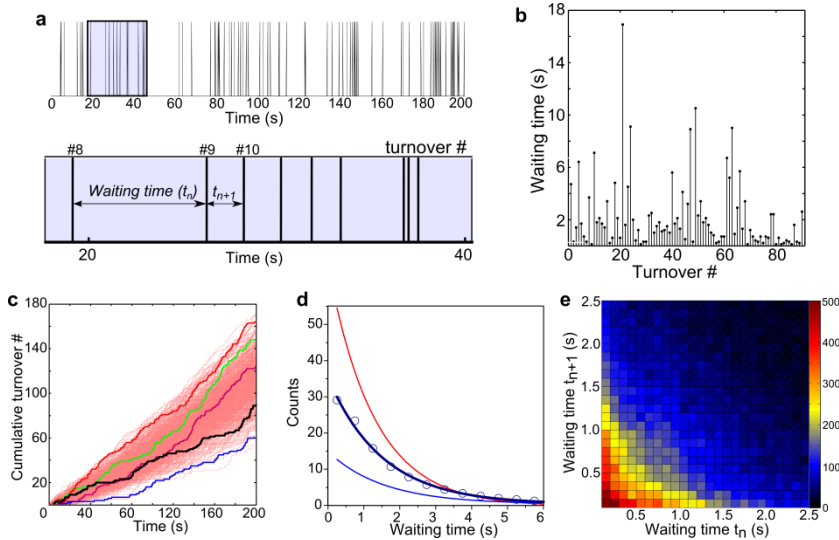


Figure 3.12 a) Single turnover trajectory recorded for a $384 \times 384 \text{ nm}^2$ zeolite domain. Inset: the definition of the waiting time as the time between two subsequent catalytic turnovers. b) A waiting time trajectory reconstructed from (a). c) Evolution of turnover numbers for five exemplified zeolite domains: the black line is derived from (b), the red lines in the background represent all 784 trajectories. d) Mean distribution of waiting times calculated for all 784 surface domains (dark blue). The blue and red lines denote the fitted exponential decays of the waiting time histograms for the red and blue trajectories in (c). e) 2-D conditional histogram of consecutive waiting times recorded at t_n and t_{n+1} . The color-bar indicates the occurrence of pairs of waiting times.

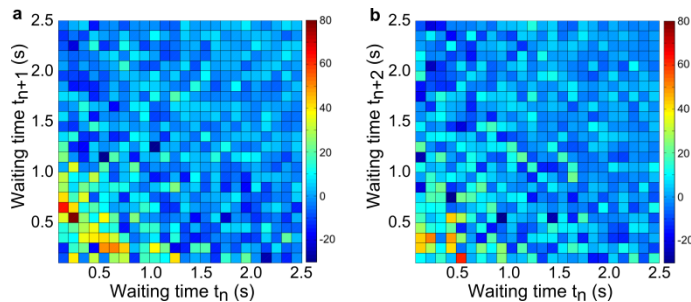


Figure 3.13 The 2-D difference histograms of waiting times, calculated for a) waiting times t_n and t_{n+1} , b) t_n and t_{n+2} .

A typical turnover trajectory of a zeolite domain illustrates the stochastic appearance of waiting times (Figure 3.12b). We compared the turnover trajectories and the resulting cumulative sums of turnovers of all 784 analyzed domains. A selection of five trajectories that differ significantly in their reactivity is shown in Figure 3.12c. It is evident that individual zeolite domains within a single zeolite particle may differ significantly in their average turnover frequencies.

The distribution of individual waiting times follows the exponential decay function for all analyzed turnover trajectories (Figure 3.12d), while the parameters of the distribution change with turnover frequencies recorded at individual zeolite domains. The question arises whether these fluctuations of waiting times have a temporal correlation component, i.e. whether the appearance of two consecutive waiting times can be statistically correlated to temporal changes in the oligomerization reaction mechanism. A summed 2-D histogram of adjacent waiting times (t_n and t_{n+1}) calculated for all analyzed trajectories shows a symmetrical distribution of pairs of waiting times (Figure 3.12e). This distribution describes the stochastic behavior of the single turnover trajectories, where higher turnover rates may be followed with the longer time intervals of low activity. As a test of time-correlated features we have examined the 2-D difference histograms and the autocorrelation functions of the recorded waiting time trajectories, as described in the following sections.

3.3.10 Construction of the 2-D difference histograms of waiting times

The 2-D conditional histogram of waiting times (Figure 3.12e) describes joint probability of finding (t_n and t_{n+1}) pairs of waiting times $p(t_n, t_{n+1})$. However, the statistical analysis of the temporal correlation between pairs of waiting times requires construction of difference histograms of waiting times, defined as $\delta(t_n, t_{n+i}) = p(t_n, t_{n+i}) - p(t_n) \times p(t_{n+i})$, where i represents the number of turnovers that separate waiting times t_n and t_{n+i} . Described statistical test is used in the analysis of the dynamic disorder in enzymatic catalysis.^[36,38] Such difference histograms calculated for $i = 1$ (Figure 3.13a) and $i = 2$ (Figure 3.13b) reveal no significant time-correlated features. Thus, the conditional probabilities of finding pairs of waiting times $p(t_n, t_{n+i})$ do not differ from the product of the individual probabilities $p(t_n) \times p(t_{n+i})$. Note that the feature from 0.6 s to 1.0 s in Figure 3.13a originates from the blinking of single molecules that cannot be completely removed in our parametrization analysis (Figure 3.3), i.e. the molecules with the blinking gap larger than 0.5 s.

3.3.11 Autocorrelation analysis of the waiting time trajectories

We have also performed the additional auto-correlation analysis of the individual waiting time trajectories, as the ultimate evidence of non-correlated turnover dynamics. The autocorrelation function (ACF) measures the correlation between

waiting times t_n and t_{n+i} , where $i = 0, \dots, N$ and t_n is a stochastic process. Autocorrelation for time lag i is calculated as $r_i = c_i / c_0$, where c_0 is the sample variance of the time series, and

$$c_i = \frac{1}{N-1} \sum_{n=1}^{N-i} (t_n - \bar{t})(t_{n+i} - \bar{t}),$$

where N is the total number of observations.^[39] Figure 3.14 illustrates the examples of the waiting time trajectories and their corresponding autocorrelation functions that support the conclusions derived from the 2-D difference histograms of waiting times.

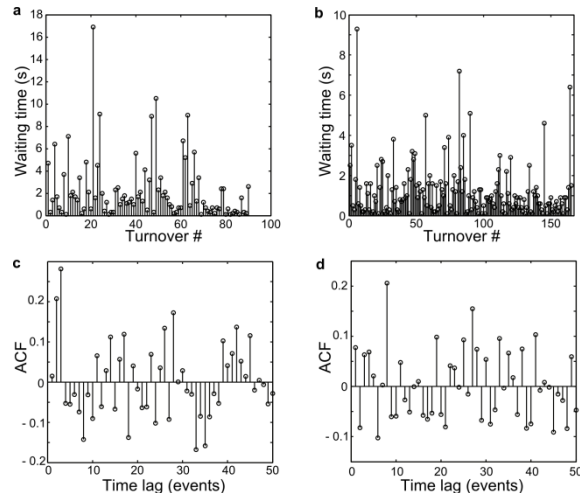


Figure 3.14 a,b) Examples of the waiting time trajectories represented in Figure 3.12c, and c,d) corresponding autocorrelation functions. Autocorrelation function (ACF) is calculated as described in the text.

Similar kinetic studies performed earlier for enzymes^[2,36,38] and nanoparticles^[9] found a correlation of catalytic turnover frequencies in time due to conformational and surface reconstruction changes. Our analysis did not show the presence of similar correlation effects in H-ZSM-5 most probably due to the significantly different nature of the catalytic processes taking place at enzymes and nanoparticles. Very low turnover rates over large zeolite domains, as compared to the size of enzymes and nanoparticles, may not be sufficient to study dynamic disorder at present time/space scales. However, the reasons for the observed behavior could well be explained by the interplay of diffusion and Langmuir-Hinshelwood adsorption-

reaction mechanism, taking into account the complexity of the overall process that may lead to the non-periodic, chaotic oscillations in reactivity.^[40–42]

We note here a remarkable observation related to measuring the turnover frequency of a single catalyst particle. By definition, the turnover frequency is calculated with respect to the total number of catalytically active sites.^[43] While the rate of the product formation can be precisely calculated with the NASCA method, the local number of catalytically active sites (and not the local Al concentration) cannot be directly measured in 3-D at the same length scales. However, stimulated Raman microscopy with probe molecules recently demonstrated this information at diffraction limited resolutions.^[16] The reactivity of zeolite H-ZSM-5 is measured in conditions of extremely low turnover frequencies. Taking into account the maximum in recorded reactivity of 10 events per $\mu\text{m}^3 \text{ s}^{-1}$ (which corresponds to a reaction rate of $1.7 \times 10^{-8} \text{ mol dm}^{-3} \text{ s}^{-1}$ for detected fluorescent products) and a bulk Si/Al ratio of 17, the average recorded turnover frequency of the reaction is in the order of 10^{-8} s^{-1} . In comparison, typical turnover frequencies recorded at a bulk level in zeolites are in order of 10^{-3} s^{-1} – marking a difference of at least five orders of magnitude. The practical upper limit of the NASCA technique applied to studied zeolite crystals is close to the measured values, since a higher reactivity of the probe molecules would lead to the fast accumulation of bursts that could not be optically resolved anymore. In practice, the window of turnover values that can be recorded for the studied zeolite H-ZSM-5 crystals ranges from 10^{-12} to 10^{-8} s^{-1} , representing more than four orders of magnitude difference in reactivity. In principle, even lower turnover numbers can be determined at the expense of longer acquisition times.

3.4 Conclusions

The effect of steaming post-treatments on the catalytic performance of individual H-ZSM-5 crystals has been quantified in 3-D by using the high sensitivity and spatiotemporal resolution of single molecule super-resolution fluorescence microscopy. Mild steaming of H-ZSM-5 crystals at 500 °C altered the surface porosity via dealumination and notably enhanced the accessibility and reactivity. However, this also causes a highly heterogeneous distribution of accessible acid sites at macroscopic level. Further steaming at 700 °C has led to a significant loss of Brønsted acidity and a

two orders of magnitude lower average turnover frequency. Surface diffusion barriers of the parent zeolite crystals were attributed to the depletion of Al in the surface region of the material, while changes in the 3-D distribution of Al upon steaming significantly affected the surface accessibility and reactivity of mildly steamed crystals. Finally, the correlation analysis of waiting times between subsequent turnovers pointed towards significant temporal fluctuations and differences in the turnover frequencies of nanoscopic zeolite domains of the parent material.

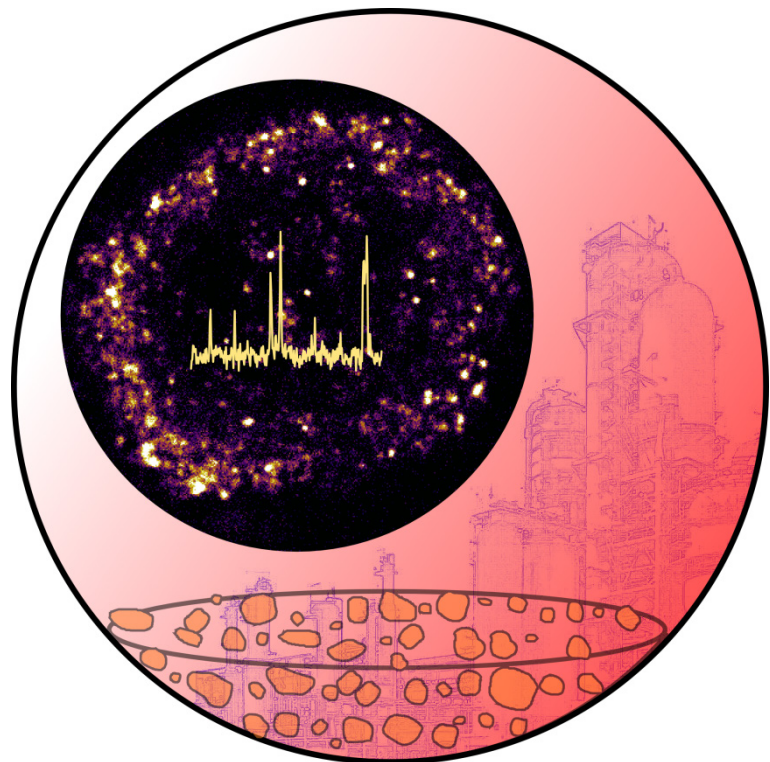
Acknowledgements

Dr. Peter Dedecker (KU Leuven) is acknowledged for the help with *Localizer* software and related discussions. Carla Izzara (KU Leuven) is acknowledged for the assistance in the preparation of experiments. Dr. Machteld Mertens (ExxonMobil) is thanked for providing the parent ZSM-5 crystals.

References

- [1] R. M. Dickson, A. B. Cubitt, R. Y. Tsien, W. E. Moerner, *Nature* **1997**, *388*, 355–358.
- [2] H. P. Lu, L. Xun, X. S. Xie, *Science* **1998**, *282*, 1877–1882.
- [3] E. Betzig, G. H. Patterson, R. Sougrat, O. W. Lindwasser, S. Olenych, J. S. Bonifacino, M. W. Davidson, J. Lippincott-Schwartz, H. F. Hess, *Science* **2006**, *313*, 1642–1645.
- [4] S. W. Hell, M. Kroug, *Appl. Phys. B* **1995**, *60*, 495–497.
- [5] T. A. Klar, S. Jakobs, M. Dyba, A. Egner, S. W. Hell, *Proc. Natl. Acad. Sci.* **2000**, *97*, 8206–8210.
- [6] A. Zürner, J. Kirstein, M. Döblinger, C. Bräuchle, T. Bein, *Nature* **2007**, *450*, 705–708.
- [7] C. Jung, J. Kirstein, B. Platschek, T. Bein, M. Budde, I. Frank, K. Müllen, J. Michaelis, C. Bräuchle, *J. Am. Chem. Soc.* **2008**, *130*, 1638–1648.
- [8] M. B. J. Roeffaers, B. F. Sels, H. Uji-i, F. C. De Schryver, P. A. Jacobs, D. E. De Vos, J. Hofkens, *Nature* **2006**, *439*, 572–575.
- [9] W. Xu, J. S. Kong, Y.-T. E. Yeh, P. Chen, *Nat. Mater.* **2008**, *7*, 992–996.
- [10] M. B. J. Roeffaers, G. De Cremer, J. Libeert, R. Ameloot, P. Dedecker, A.-J. Bons, M. Bückins, J. A. Martens, B. F. Sels, D. E. De Vos, J. Hofkens, *Angew. Chem. Int. Ed.* **2009**, *48*, 9285–9289.
- [11] T. Tachikawa, T. Majima, *J. Am. Chem. Soc.* **2009**, *131*, 8485–8495.
- [12] N. M. Andoy, X. Zhou, E. Choudhary, H. Shen, G. Liu, P. Chen, *J. Am. Chem. Soc.* **2013**, *135*, 1845–1852.
- [13] P. Chen, X. Zhou, H. Shen, N. M. Andoy, E. Choudhary, K.-S. Han, G. Liu, W. Meng, *Chem. Soc. Rev.* **2010**, *39*, 4560–4570.
- [14] G. De Cremer, M. B. J. Roeffaers, E. Bartholomeeusen, K. Lin, P. Dedecker, P. P. Pescarmona, P. A. Jacobs, D. E. De Vos, J. Hofkens, B. F. Sels, *Angew. Chem. Int. Ed.* **2010**, *49*, 908–911.
- [15] T. Tachikawa, T. Majima, *Chem. Soc. Rev.* **2010**, *39*, 4802–4819.

- [16] K.-L. Liu, A. V. Kubarev, J. Van Loon, H. Uji-i, D. E. De Vos, J. Hofkens, M. B. J. Roeffaers, *ACS Nano* **2014**, *8*, 12650–12659.
- [17] A. V. Kubarev, K. P. F. Janssen, M. B. J. Roeffaers, *ChemCatChem* **2015**, *7*, 3646–3650.
- [18] M. B. J. Roeffaers, G. D. Cremer, H. Uji-i, B. Muls, B. F. Sels, P. A. Jacobs, F. C. D. Schryver, D. E. De Vos, J. Hofkens, *Proc. Natl. Acad. Sci.* **2007**, *104*, 12603–12609.
- [19] T. Cordes, S. A. Blum, *Nat. Chem.* **2013**, *5*, 993–999.
- [20] K. P. F. Janssen, G. D. Cremer, R. K. Neely, A. V. Kubarev, J. V. Loon, J. A. Martens, D. E. De Vos, M. B. J. Roeffaers, J. Hofkens, *Chem. Soc. Rev.* **2014**, *43*, 990–1006.
- [21] P. Dedecker, S. Duwé, R. K. Neely, J. Zhang, *J. Biomed. Opt.* **2012**, *17*, 126008–126008.
- [22] A. Sergé, N. Bertaux, H. Rigneault, D. Marguet, *Nat. Methods* **2008**, *5*, 687–694.
- [23] A. V. Kubarev, K. P. F. Janssen, M. B. J. Roeffaers, *ChemCatChem* **2015**, *7*, 3646 – 3650.
- [24] M. Choura, N. M. Belgacem, A. Gandini, *Macromolecules* **1996**, *29*, 3839–3850.
- [25] M. B. J. Roeffaers, B. F. Sels, H. Uji-i, B. Blanpain, P. L'hoëst, P. A. Jacobs, F. C. De Schryver, J. Hofkens, D. E. De Vos, *Angew. Chem. Int. Ed.* **2007**, *46*, 1706–1709.
- [26] K. F. Domke, J. P. R. Day, G. Rago, T. A. Riemer, M. H. F. Kox, B. M. Weckhuysen, M. Bonn, *Angew. Chem. Int. Ed.* **2012**, *51*, 1343–1347.
- [27] C. Sprung, B. M. Weckhuysen, *J. Am. Chem. Soc.* **2015**, *137*, 1916–1928.
- [28] L. R. Aramburo, L. Karwacki, P. Cubillas, S. Asahina, D. A. M. de Winter, M. R. Drury, I. L. C. Buurmans, E. Stavitski, D. Mores, M. Daturi, P. Bazin, P. Dumas, F. Thibault-Starzyk, J. A. Post, M. W. Anderson, O. Terasaki, B. M. Weckhuysen, *Chem. – Eur. J.* **2011**, *17*, 13773–13781.
- [29] L. Karwacki, M. H. F. Kox, D. A. Matthijs de Winter, M. R. Drury, J. D. Meeldijk, E. Stavitski, W. Schmidt, M. Mertens, P. Cubillas, N. John, A. Chan, N. Kahn, S. R. Bare, M. Anderson, J. Kornatowski, B. M. Weckhuysen, *Nat. Mater.* **2009**, *8*, 959–965.
- [30] L. Karwacki, D. A. M. de Winter, L. R. Aramburo, M. N. Lebbink, J. A. Post, M. R. Drury, B. M. Weckhuysen, *Angew. Chem. Int. Ed.* **2011**, *50*, 1294–1298.
- [31] S. M. Campbell, D. M. Bibby, J. M. Coddington, R. F. Howe, R. H. Meinhold, *J. Catal.* **1996**, *161*, 338–349.
- [32] T. Sano, N. Yamashita, Y. Iwami, K. Takeda, Y. Kawakami, *Zeolites* **1996**, *16*, 258–264.
- [33] T. Sano, H. Ikeya, T. Kasuno, Z. B. Wang, Y. Kawakami, K. Soga, *Zeolites* **1997**, *19*, 80–86.
- [34] F. Hibbe, C. Chmelik, L. Heinke, S. Pramanik, J. Li, D. M. Ruthven, D. Tzoulaki, J. Kärger, *J. Am. Chem. Soc.* **2011**, *133*, 2804–2807.
- [35] F. Hibbe, J. Caro, C. Chmelik, A. Huang, T. Kirchner, D. Ruthven, R. Valiullin, J. Kärger, *J. Am. Chem. Soc.* **2012**, *134*, 7725–7732.
- [36] B. P. English, W. Min, A. M. van Oijen, K. T. Lee, G. Luo, H. Sun, B. J. Cherayil, S. C. Kou, X. S. Xie, *Nat. Chem. Biol.* **2006**, *2*, 87–94.
- [37] X. S. Xie, H. P. Lu, *J. Biol. Chem.* **1999**, *274*, 15967–15970.
- [38] G. De Cremer, M. B. J. Roeffaers, M. Baruah, M. Sliwa, B. F. Sels, J. Hofkens, D. E. De Vos, *J. Am. Chem. Soc.* **2007**, *129*, 15458–15459.
- [39] G. E. P. Box, G. M. Jenkins, G. C. Reinsel, *Time Series Analysis: Forecasting and Control*, Wiley-VCH, Weinheim, **2008**.
- [40] R. Imbihl, G. Ertl, *Chem. Rev.* **1995**, *95*, 697–733.
- [41] K. F. Jensen, W. H. Ray, *Chem. Eng. Sci.* **1980**, *35*, 241–248.
- [42] R. de Levie, *J. Chem. Educ.* **2000**, *77*, 771–774.
- [43] M. Boudart, *Chem. Rev.* **1995**, *95*, 661–666.



Chapter 4 is based on the following manuscript:

"High-Resolution Fluorescence Imaging of Zeolite Aggregates within Real-Life Fluid Catalytic Cracking Particles", Z. Ristanović, M. M. Kerssens, A. V. Kubarev, F. C. Hendriks, P. Dedecker, J. Hofkens, M. B. J. Roeffaers, and B. M. Weckhuysen, *Angew. Chem. Int. Ed.* 2015, 54, 1836-1840.

Chapter 4

High-Resolution Fluorescence Imaging of Zeolite H-ZSM-5 Aggregates within Real-Life Fluid Catalytic Cracking Particles

Abstract

The concepts of high-resolution fluorescence imaging presented in Chapter 3 are further extended to study the catalytic activity of sub- μm zeolite H-ZSM-5 domains within real-life fluid catalytic cracking (FCC) catalyst particles. Super-resolution optical fluctuation imaging (SOFI) and NASCA imaging were used in combination with a fluorogenic probe reaction based on furfuryl alcohol. The formation of fluorescent product molecules taking place at Brønsted acid sites was monitored with single turnover sensitivity and high spatiotemporal resolution, providing detailed insight in dispersion and catalytic activity of zeolite H-ZSM-5 aggregates. Most of the zeolite domains are well dispersed within FCC particles with a diameter below 500 nm. The quantitative analysis of catalytic activity points towards substantial differences in turnover frequencies between the individual zeolite aggregates. The average turnover frequency of highly active zeolite H-ZSM-5 domains was found to be 5 turnovers per second per μm^2 , which is approximately an order of magnitude difference in activity when compared to the least reactive zeolite H-ZSM-5 domains.

4.1 Introduction

Fluid Catalytic Cracking (FCC) is a major industrial process to convert crude oil into gasoline and valuable hydrocarbons, such as propylene.^[1-4] In this catalytic process 50–150 µm-sized spherical particles are used, which contain an acidic zeolite embedded in a matrix of clay, silica and alumina. The zeolite components with acidic properties, being either zeolite Y or ZSM-5, play a crucial role in the overall catalytic cracking properties.^[5-7] The acidity of zeolite domains changes during catalyst activation and aging, but a detailed characterization of the acidity distribution within a single FCC catalyst particle has proven to be extremely difficult due to their intrinsic chemical and structural complexity.

More recently, FCC catalyst particles have been the subject of detailed studies at the single particle level. Buurmans et al. have shown, by applying confocal fluorescence microscopy (CFM) in combination with acid-catalyzed staining reactions, that it is possible to visualize in 3-D the domains of zeolites Y and H-ZSM-5 within FCC particles.^[8,9] The anisotropy of zeolite H-ZSM-5 crystals can be used to estimate by CFM the dispersion and overall weight content of the zeolite fraction within a single FCC particle.^[10] Finally, by integrating a fluorescence microscope within a transmission electron microscope Karreman et al. have been able to correlate the changes in acidity as probed with fluorescence microscopy, with structural changes and damage.^[11] Using the CFM approach, complemented by the results of X-ray microscopy techniques,^[12] it is now possible to evaluate the aging process of the catalyst due to the metal deposition (poisoning) and steaming (dealumination). Unfortunately, the spatial resolution of CFM is limited by the diffraction of light. The technique cannot resolve sub-µm zeolite domains and does not provide the quantitative information about catalytic activity of individual zeolite aggregates. This limitation of CFM can be addressed by developing a method that is sensitive to record and spatially resolve single catalytic turnovers taking place within the zeolite domains of a single, real-life FCC particle.

In this Chapter we report the first application of single molecule fluorescence microscopy and the required analysis methods to quantitatively study Brønsted-catalyzed reactivity of hierarchically structured, real-life industrial FCC catalyst particles, containing zeolite H-ZSM-5 as the active cracking phase. The presented

approach, based on the use of furfuryl alcohol as a probe molecule, can be widely applied to other complex catalyst materials like granulated particles that suffer from an elevated background luminescence. We also anticipate that this approach will broaden the scope of fluorogenic reactions that can be used for quantitative reactivity mapping since it possesses less stringent demands on the fluorophore properties. Since individual catalytic events no longer need to be isolated, measurements with higher catalytic turnover densities can be used for quantitative analysis leading to more information in the same experiment time.

4.2 Experimental

4.2.1 Sample preparation

Freshly prepared FCC catalyst particles based on zeolite H-ZSM-5 were provided by Albemarle Catalyst Company BV. The catalyst particles were thoroughly calcined in a static air oven at 823 K (heating ramp 0.5 K/min, 1 h dwell time at 353 K and 393 K) for 48 h prior to use in order to eliminate the residual fluorescence of impurities. Prior to the experiments the FCC catalyst particles were spin-coated over a cover slip and kept overnight in a static oven at 723 K (1 K/min, with 1 h dwell time at 393 K).

4.2.2 Single molecule fluorescence experiment

Single molecule fluorescence experiments were performed using an inverted epifluorescence wide-field microscope (Olympus IX-71), with 100 \times oil immersion objective lens (1.4 NA). Wide-field illumination was achieved by circularly polarized 532 nm light from a diode-pumped solid-state laser (Excelsior 532 single mode 200 mW, Spectra-Physics), providing 25 mW power on the sample. Fluorescence emission is imaged by the EM-CCD (ImagEM Enhanced C9100-13) after passing through a dichroic mirror and a 545 nm long-pass filter removing the excitation light. The image was expanded by a 3.3 \times camera lens resulting in a field of view of 24.6 \times 24.6 μm^2 and 48 \times 48 nm 2 per pixel. Wide-field images were recorded with frame acquisition time of 75 ms. The catalytic reaction is performed at room temperature in a reactor designed for a liquid-phase experiment using 0.44 M solution of furfuryl alcohol (Sigma Aldrich, 98%) in water. The optimal concentration for imaging was determined in a series of concentration-dependent experiments. Prior to adding

furfuryl alcohol the catalyst particles exhibited low residual fluorescence, which was additionally removed by 5 min of photobleaching with the intense laser light.

4.2.3 Thresholding and segmentation analysis of SOFI images

SOFI images were analyzed with *Localizer* software^[13] using a second-order cross-correlation based on previously published algorithms.^[14,15] Images depicting the intensity of all pixels after SOFI analysis were loaded into *Matlab* (*MathWorks*) where they were cropped to solely display the area of interest. A circular crop was then applied to remove the inner regions of the particle with lower SOFI intensities. This simultaneously minimizes differences in depth (due to the spherical nature of the catalysts particle) and related intensity differences due to absorption effects. The image was then converted into a binary, black-white (BW) image, using a threshold and a gray scale image. Thresholds were chosen based upon the amount of detected (white) pixels. This was done by analyzing thresholds between 0 and 1 and selecting the optimal threshold, which was also verified by visual inspection of bright domains. The isolated pixelated areas of 1 pixel in size were then removed and holes filled in the BW image. The gray scale image and the resulting BW image were then loaded into the ‘imageprops’ *Matlab* (*MathWorks*) routine, which analyzed the area of all white domains on a black background. Finally, histograms of size distribution were reconstructed based on the chosen thresholds. The domains smaller than $0.01 \mu\text{m}^2$ (2×2 pixel areas) were not included in the histograms.

4.3 Results and Discussion

4.3.1 UV-Vis and confocal fluorescence microscopy of FCC particles

To selectively study the reactivity of acidic zeolite domains within the FCC catalyst particles we have used the oligomerization of furfuryl alcohol as a probe reaction, previously described in Chapter 3 (Scheme 3.1). Prior to single molecule experiments, the reactivity of zeolite H-ZSM-5-based FCC particles with furfuryl alcohol has been characterized by UV-Vis and confocal fluorescence microscopy. The oligomerization leads to immediate formation of colored species with two distinct absorption bands at around 525 nm and 590 nm, as detected by UV-Vis microscopy (Figure 4.1a).

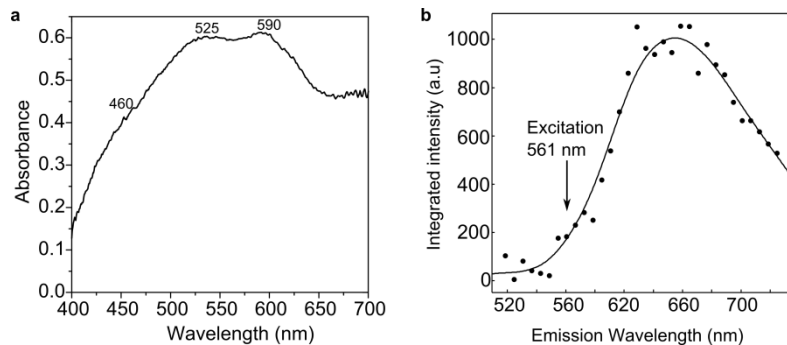


Figure 4.1 a) UV-Vis and b) fluorescence spectra of oligomeric species recorded at FCC catalyst particles exposed to furfuryl alcohol. The fluorescence spectrum is recorded using a confocal fluorescence microscope equipped with a spectral detection unit and a 561 nm laser excitation. Note that in the single molecule experiment we have used a 532 nm laser excitation.

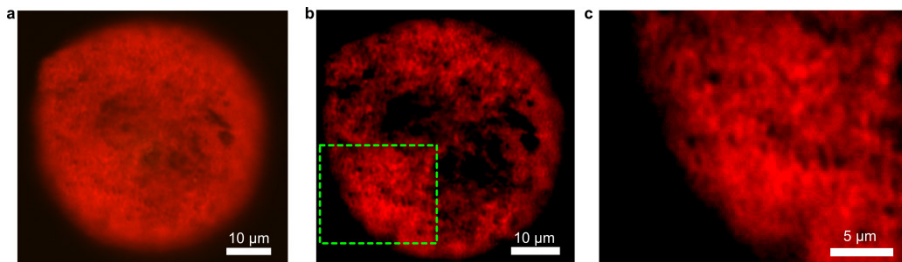


Figure 4.2 Confocal fluorescence images of an FCC particle recorded after exposure to non-diluted furfuryl alcohol, focal depth $\sim 3 \mu\text{m}$. a) Raw image of fluorescence intensities, b) Rescaled image of fluorescence intensities, c) Magnified region from b) showing zeolite particulates smaller than $1 \mu\text{m}^2$.

Confocal fluorescence microscopy confirmed that the 561 nm excitation of the oligomeric species leads to fluorescence emission at 650 nm (Figure 4.1b). Individual FCC particles stained with furfuryl alcohol were then subjected to confocal fluorescence imaging, similarly to previously reported methods.^[8,10] Figure 4.2a indicates a fairly homogeneous dispersion and size-distribution of fluorescent zeolites domains. Further artificial thresholding was attempted in order to isolate individual zeolite domains (Figure 4.2b). The inner region of the particle is characterized by high attenuation of the excitation/emission light. A closer look at the sub-particle domain in Figure 4.2c reveals significant local differences in fluorescence intensity between zeolite domains, as well as notably the high background signal. These parameters are critical for the thresholding procedures that determine the size of zeolite domains and may artificially introduce systematic errors in the analysis.

4.3.2 Single molecule fluorescence methodology

A schematic of the single molecule fluorescence method used to study the reactivity of FCC particles is shown in Figure 4.3a. We have used an inverted epi-fluorescence microscope identical to the one described in Chapter 3. The 532 nm laser light can efficiently excite fluorescent oligomers that are catalytically formed from non-fluorescent furfuryl alcohol molecules (Figure 4.3b). As the fluorescent products are formed exclusively on Brønsted acid sites, their fluorescence can be used for the 3-D localization of zeolite H-ZSM-5 domains embedded within the matrix material of a single FCC particle (Figure 4.3c). The individual fluorescent reaction products are detected with an EM-CCD camera (Figure 4.3d).

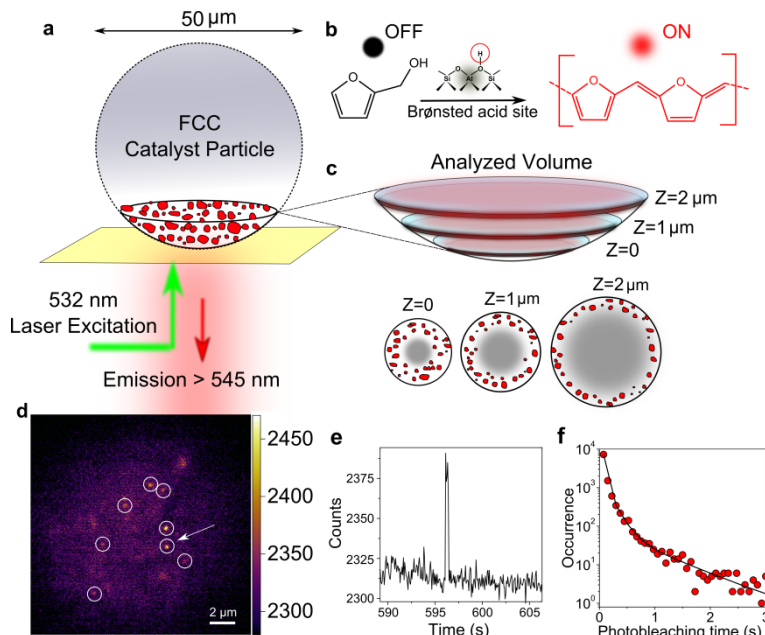


Figure 4.3 Schematic of the single molecule fluorescence approach. a) Single FCC catalyst particle, containing zeolite H-ZSM-5 domains depicted in red, studied with a wide-field fluorescence microscope setup. b) Formation of the fluorescent products (red) upon oligomerization of non-fluorescent furfuryl alcohol (black) on a Brønsted acid site. c) Geometry of the analyzed focal slices and denoted focal depths. The inner regions of the FCC particles (depicted in gray) were not included in the later analysis due to the attenuation of fluorescent light and mass transfer limitations. d) Wide field fluorescence micrograph of an FCC particle recorded during the oligomerization of furfuryl alcohol (exposure time of 75 ms). White circles indicate localized fluorescence bursts originating from fluorescent products. e) Photo-trajectory of a representative single catalytic turnover, indicated with a white arrow in (d). f) Distribution of measured survival times of ~ 10000 fluorescent product molecules before photobleaching, fitted with the multi-exponential function with the exponential time constants of 0.035 s, 0.15 s and 0.74 s.

A typical fluorescence intensity trajectory of an individual hotspot is shown in Figure 4.3e. It was found that the characteristic survival time of fluorescent products before photobleaching is typically < 0.3 s (Figure 4.3f). Therefore, we may conclude that fluctuations in the fluorescence intensity happening at specific locations at the second time scale are mostly caused by the formation of new fluorescent product molecules on Brønsted acid sites of individual zeolite domains. This observation is essential for further localization of zeolite domains and quantification analysis with SOFI method.

4.3.3 NASCA and SOFI high-resolution imaging

To study the reactivity of the FCC catalyst particles we have used two high-resolution single molecule fluorescence methods, summarized in Figure 4.4. Figure 4.4a illustrates four isolated fluorescent product molecules localized by fitting their point spread functions (PSF) with a 2-D Gaussian. This method of localizing stochastic catalytic turnovers in heterogeneous catalysis, commonly known as NASCA microscopy,^[16] is described in Chapter 3. Recording a fluorescence movie allows reconstructing of a high-resolution NASCA image based on the precise localization of individual reaction events, as illustrated in Figure 4.4b. However, NASCA measurements typically require highly controlled reaction conditions with a high signal to noise ratio and therefore are challenging for the industrial catalysts with high structural complexity and intrinsic background fluorescence. Ideally, a complementary method that can operate under less stringent conditions and in a wider range of concentrations is necessary to support the results of the NASCA analysis.

The question now arises if we can complement the limitations of the NASCA method by looking at the fluctuations of fluorescent signal to localize catalytically active zeolite domains and quantify single turnover kinetics originating from them. For this purpose we opted to use the Super-resolution Optical Fluctuation Imaging (SOFI) analysis – a method that is developed recently for imaging of cellular structures in experiments with low signal to noise ratio.^[13,14,17,18] This method relies on statistical analysis of temporal fluctuations in consecutive fluorescence images to provide essentially background-free, contrast-enhanced images with improved resolution in all three dimensions.^[14] In our experiments, independent stochastic fluctuations of fluorescent emitters appear as a result of the constant formation, diffusion, and photobleaching of fluorophores taking place at zeolite domains.

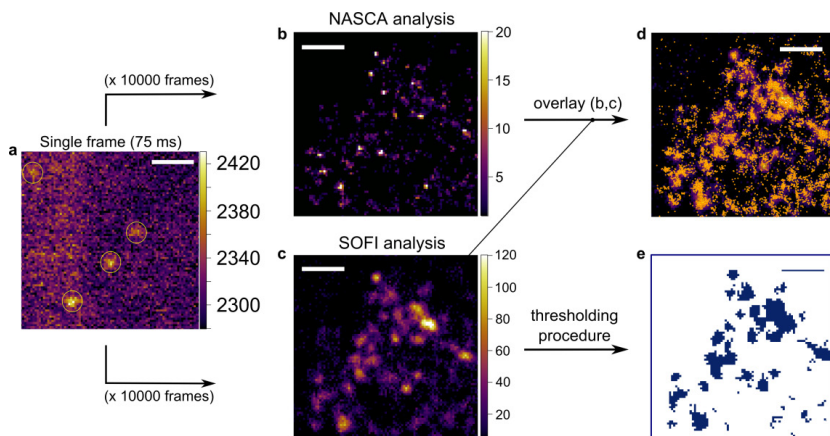


Figure 4.4 a) Zoom-in 75 ms frame; white circles indicate localized single molecule fluorescence bursts. b) Accumulated NASCA high-resolution map of individual catalytic turnovers. Color scale represents the number of detected turnovers per pixel ($48 \times 48 \text{ nm}^2$). c) Corresponding SOFI image. Color scale denotes calculated SOFI intensities. d) Overlay of the SOFI image from c) and localized emitters positions obtained from NASCA analysis presented in b), yellow circles represent detected catalytic events. e) Reconstructed binary image of the fluorescent regions from (c). Scale bars are 1 μm .

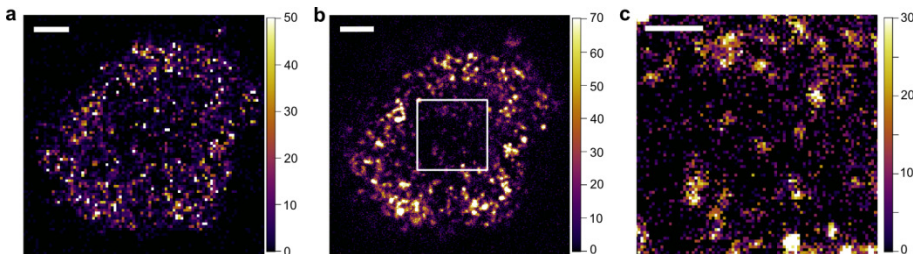


Figure 4.5 a) Binned NASCA image ($144 \times 144 \text{ nm}^2$ per pixel), and b) corresponding SOFI image, illustrating higher fluorescence activity in the outer region of an FCC particle; c) Magnified region of interest from b), illustrating lower SOFI intensities for inner zeolite domains. Scale bars are 2 μm .

The fluorescence signal in a SOFI image is not trivially related to the recorded fluorescence intensity.^[14,18] However, it is proportional to the local concentration of fluorophores, provided that they exhibit similar emission properties and fast fluctuations of fluorescence signal - conditions that are met in our experiment. As an example, Figure 4.4c shows an accumulated SOFI image reconstructed based on an identical movie as the NASCA image in Figure 4.4b. An overlay of the images based on the two methods in Figure 4.4d indicates that the brightest regions in the SOFI image are indeed the ones where most of the fluorescent events and thus catalytic turnovers are recorded.

We further demonstrate the strength of the SOFI approach to quantify the size and reactivity of the matrix-embedded zeolite H-ZSM-5 domains. Using SOFI images as a reference for the stochastic fluctuations of fluorescence signal, we applied a binary thresholding procedure in order to statistically analyze the size of the catalytically most active zeolite domains (Figure 4.4e). A detailed analysis of the size distribution and reactivity of individual zeolite domains requires also a consideration of the light attenuation in deeper regions of FCC particles, which is the topic of the next section.

4.3.4 Attenuation of fluorescence signal with focal depth

As already observed in confocal fluorescence experiments (Figure 4.2), imaging of the inner parts of an FCC particle is only possible to a limited extent, as the excitation and emission light is attenuated by the matrix additives of the FCC particle. Similar effect was noted in wide-field single molecule experiments (Figure 4.5). For instance, the SOFI image in Figure 4.5b was imaged at approximately $Z = 1 \mu\text{m}$ from the near-surface reference focal plane. The outer regions of the FCC particle typically show bright zeolite domains with the high SOFI signal, which is not the case for the inner regions that show considerably lower fluorescence intensity (Figure 4.5c). A closer inspection of fluorescence intensity distribution in these regions reveals significant attenuation of the emitted fluorescence, even though the real fluorescence activity in these regions may be comparable to the ones at the surface. Therefore, in our further analysis only the outer regions of similar brightness are investigated for reliable comparison and the subsequent thresholding analysis; attenuation effects and a complex mass transfer of the substrate in deeper regions of the particle were not a subject of this study.

4.3.5 Thresholding analysis of fluorescent domains

The reactivity of an individual FCC catalyst particle is monitored for three different focal depths, close to the surface ($Z = 0 \pm 0.3 \mu\text{m}$), for $Z = 1 \mu\text{m}$, and $Z = 2 \mu\text{m}$ below the surface. After the reconstruction of SOFI images, the inner regions of the particles were rejected, and the thresholding procedure was applied. The procedure separates the fluorescent domains with high intensity in SOFI images from the ones with low signal by setting a threshold value based on a systematic analysis of the domain brightness and size. This is illustrated in Figure 4.6. Threshold values from 0 to 1 were

applied to gray-scale SOFI images in order to find the optimum in the binary (black and white) images. Low threshold values (< 0.2) typically lead to the clustering and oversizing of zeolite domains while high values (> 0.3) underestimate the total fluorescent area, as also evidenced from the change in the total number of white pixels (Figure 4.6). The optimal threshold values were arbitrarily selected upon the inspection of individual bright domains. Different values for all three SOFI images are the consequence of i) different SOFI intensity distribution in the analyzed images, ii) local differences in brightness, and iii) overlapping of the neighboring fluorescent domains. Finally, the selected images were segmented for pixel artifacts, as explained in the Experimental Section 4.2.3.

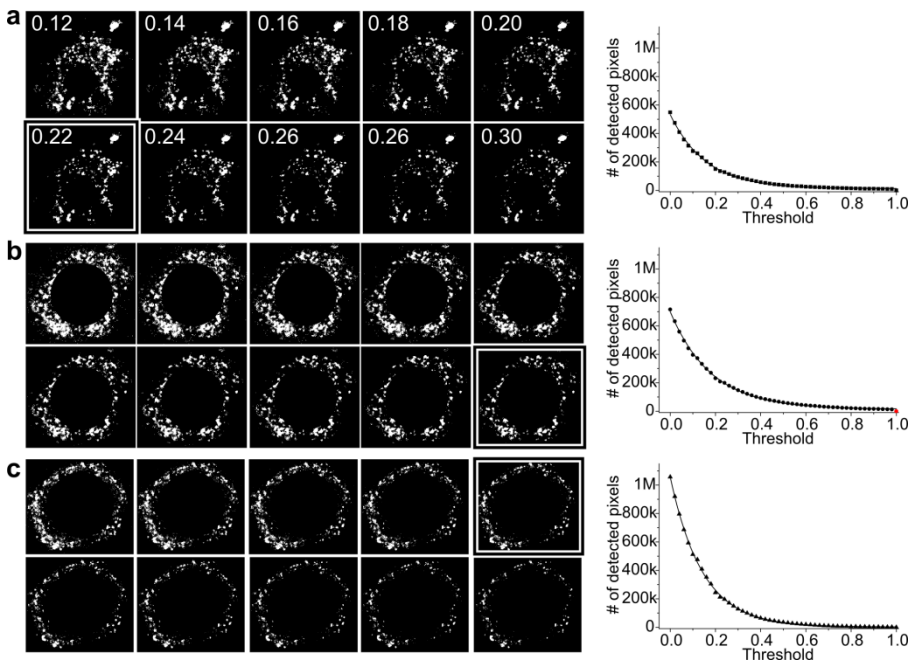


Figure 4.6 Thresholding procedure applied to SOFI images for three different focal depths: a) $Z = 0$, surface, b) $Z = 1 \mu\text{m}$, c) $Z = 2 \mu\text{m}$. (a) and (c) are reconstructed based on 10000 frames movie, while (b) was reconstructed based on 5000 frames movie. Thresholding values in the top left corners from the SOFI images in (a) are identical for (b) and (c). The graphs on the right represent the number of detected pixels above a certain threshold. The black-white frames indicate the optimal thresholding values of (a) 0.22, (b) 0.30, and (c) 0.20.

4.3.6 Size-distribution of zeolite domains

The described analysis procedure from Section 4.3.5 is summarized in Figure 4.7. After the thresholding of SOFI images (Figure 4.7, thresholding), the binary images of

highly active fluorescent domains are segmented further to account for pixel artefacts and attenuation of the fluorescence in the inner parts (Figure 4.7, segmentation). Based on this approach it was possible to estimate the size distribution of zeolite H-ZSM-5 aggregates within an FCC catalyst particle. Figure 4.7 shows the obtained histograms of the size distribution of zeolite domains.

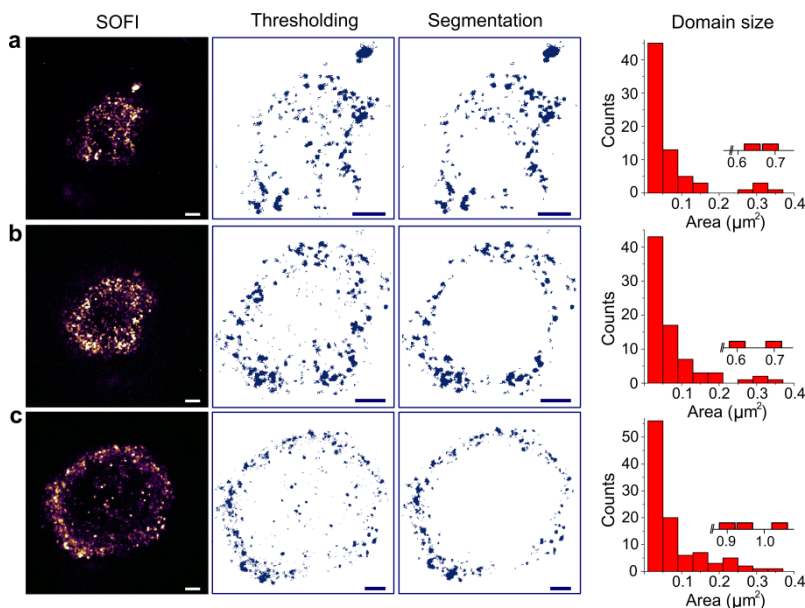


Figure 4.7 Cluster analysis of zeolite H-ZSM-5 domains size within a single FCC catalyst particle: a) $Z = 0$ (± 0.3) μm , b) $Z = 1 \mu\text{m}$, c) $Z = 2 \mu\text{m}$. Left: SOFI images of the FCC catalyst particle at three different focal depths; a) and c) reconstructed based on 10000 frames movie, and b) reconstructed based on 5000 frames movie. Middle: Corresponding binary images reconstructed based on the threshold analysis and further segmentation. Scale bars are 2 μm . Right: Corresponding histograms of the zeolite domains size distribution. Insets denote single clusters larger than 0.4 μm^2 .

Most of the zeolite domains are well dispersed in the analyzed 3-D volume and within the 2-D projection size of 0.2 μm^2 , which corresponds to spherical particles of about 500 nm in diameter. A similar distribution of zeolite particle sizes was recently reported in a CFM study, supporting the correctness of our approach.^[10] However, the in-depth analysis of smaller zeolite domains is hardly possible with confocal fluorescence microscopy due to its intrinsic limitations in resolution and sensitivity, as illustrated in Figure 4.2. This observation highlights the real strength of the fluorescence-based single molecule approach reported in this work. The NASCA method can localize single catalytic turnovers with 20 nm resolution, while the more

broadly applicable SOFI method routinely achieves a spatial resolution of 120 nm and significant background rejection with markedly improved contrast of fluorescent zeolite domains.

4.3.7 Fluorescence intensity trajectories of individual zeolite domains

Real-time single molecule fluorescence measurements enable following the temporal fluctuations in fluorescence intensity of individual zeolite domains. A temporal change of fluorescence intensity within a region of interest represents a fluorescence intensity trajectory. An example of such intensity trajectory integrated for an individual zeolite domain defined within $144 \times 144 \text{ nm}^2$ region of interest is shown in Figure 4.8a. From the statistical analysis of single turnover survival times (Figure 4.3f), it follows that each spike in a fluorescence intensity trajectory represents one catalytic turnover. By quantifying the number of peaks in the fluorescence intensity trajectory (Figure 4.8b) it is possible to determine the number of catalytic turnovers for a studied zeolite domain.

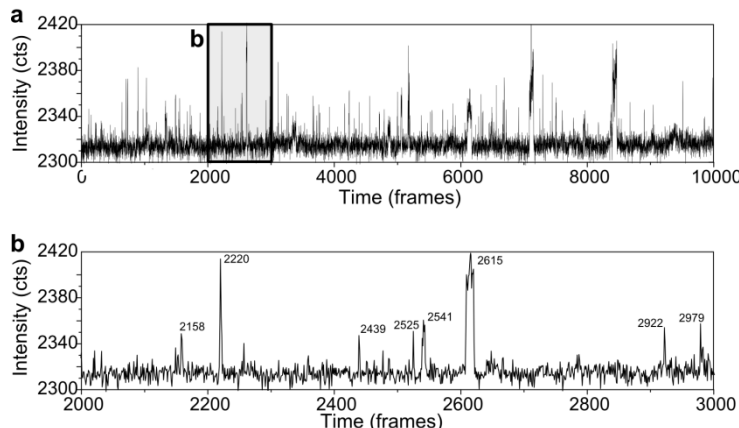


Figure 4.8 a) A fluorescence intensity trajectory of a single zeolite domain reconstructed by integrating fluorescence signal over 3×3 pixelated region of interest. b) A zoom-in from the trajectory in (a), indicating assigned single catalytic turnovers. Single turnovers were detected using a Peak Analyser routine, implemented into Origin 8.1. Local peaks are also checked manually, to verify correctness of the algorithm. 1 frame = 75 ms.

4.3.8 Quantitative analysis of reactivity differences between H-ZSM-5 domains

The analysis of NASCA and SOFI maps of reactivity indicates that zeolite H-ZSM-5 domains embedded within a single FCC particle differ in their overall fluorescence activity, which suggests potential differences in their catalytic reactivity. The

illustration of this observation is presented in Figure 4.9a. The fluorescence intensity trajectories in these regions confirm dependence of SOFI intensity from the catalytic activity of individual domains, such as the regions of high (Figure 4.9b), medium (Figure 4.9c), and low catalytic activity (Figure 4.9d). To support the quantitative aspect of the SOFI method 65 zeolite domains were localized within a $6 \times 6 \mu\text{m}^2$ region of interest from the SOFI image in Figure 4.7a. Their averaged SOFI intensities were correlated with the corresponding catalytic turnover frequencies measured at the very same region of interest.

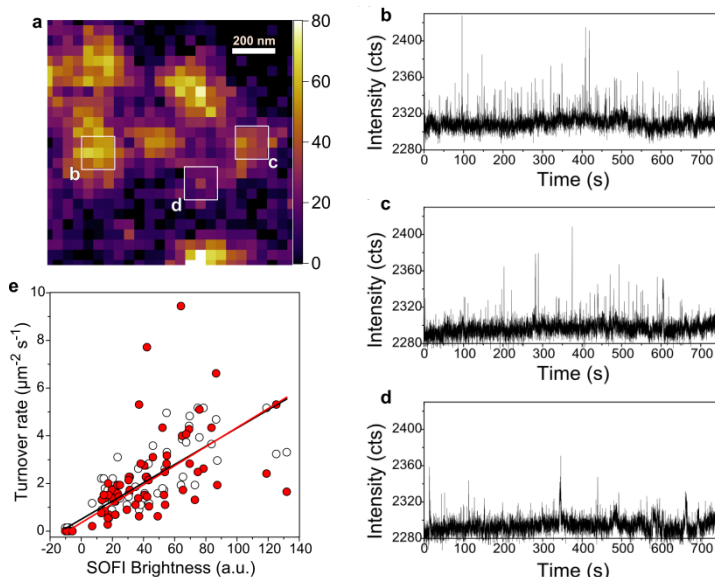


Figure 4.9 a) SOFI image of a selected $\sim 1 \mu\text{m}^2$ region of interest indicating fluorescent zeolite domains. b-d) Fluorescence intensity trajectories for the domains labelled in (a). e) Catalytic turnover rate as a function of average brightness in the SOFI image, calculated for 65 individual zeolite domains. White circles: values calculated based on fluorescence intensity trajectories; the black line is the best linear fit ($R^2 = 0.88, k = 0.038 \pm 0.002$). Red circles: values calculated based on Gaussian fitting procedure; the red line is the best linear fit ($R^2 = 0.69, k = 0.040 \pm 0.004$)

Turnover frequencies of zeolite H-ZSM-5 domains were calculated based on two separate quantification methods. The first method is based on the NASCA approach described in detail in Chapter 3. Gaussian localization of fluorescent events was performed within $144 \times 144 \text{ nm}^2$ regions of interest defined in the centers of zeolite domains. In the second method, we quantified the number of catalytic turnovers based on fluorescence intensity trajectories of individual zeolite H-ZSM-5 domains, as described in Section 4.3.7. Turnover rates of individual zeolite domains

are then determined by normalizing the number of detected turnovers by the integration time (750 s) and the size of the regions of interest ($144 \times 144 \text{ nm}^2$).

The comparison of both methods is presented in Figure 4.9e. The average brightness of the domains in a SOFI image seems to be in a good approximation proportional to the corresponding numbers of detected catalytic turnovers. The deviation from the linear trend is a consequence of inherent properties of the applied methods. For instance, brighter emitters will have a higher contribution to the intensity of a SOFI image.^[14] However, if the fluorescent signal of an emitter or background does not fluctuate over a longer period of time, it will not be visible in the SOFI image. Figure 4.9e suggests that the zeolite H-ZSM-5 domains may differ significantly in their SOFI brightness, thus catalytic reactivity. The average turnover frequency of highly active zeolite H-ZSM-5 domains is calculated to be around 5 events/s per μm^2 at the studied experimental conditions. This is approximately an order of magnitude difference in activity when compared to the least reactive zeolite H-ZSM-5 domains. Most probably, the origin of this difference in reactivity is related to differences in framework aluminium content of zeolite domains or local accessibility differences.

4.4 Conclusions

Single molecule fluorescence microscopy proved as a very sensitive tool to localize with high spatial resolution and a single turnover sensitivity the activity of acidic zeolite domains within a hierarchically structured, industrially used FCC catalyst particles containing H-ZSM-5 zeolite as the active phase. A combination of SOFI and NASCA method has enabled high-resolution localization of individual zeolite domains and quantification of their turnover frequencies. The SOFI localization analysis determined the size-distribution of zeolite H-ZSM-5 domains with diameters below 500 nm. The quantitative correlation between SOFI intensities and calculated catalytic activity pointed out nearly one order of magnitude difference in turnover frequencies between individual zeolite domains. The introduced SOFI analysis emerged as a practical method that can bridge the inherent deficiencies of confocal and single molecule fluorescence microscopy methods, especially in experiments with

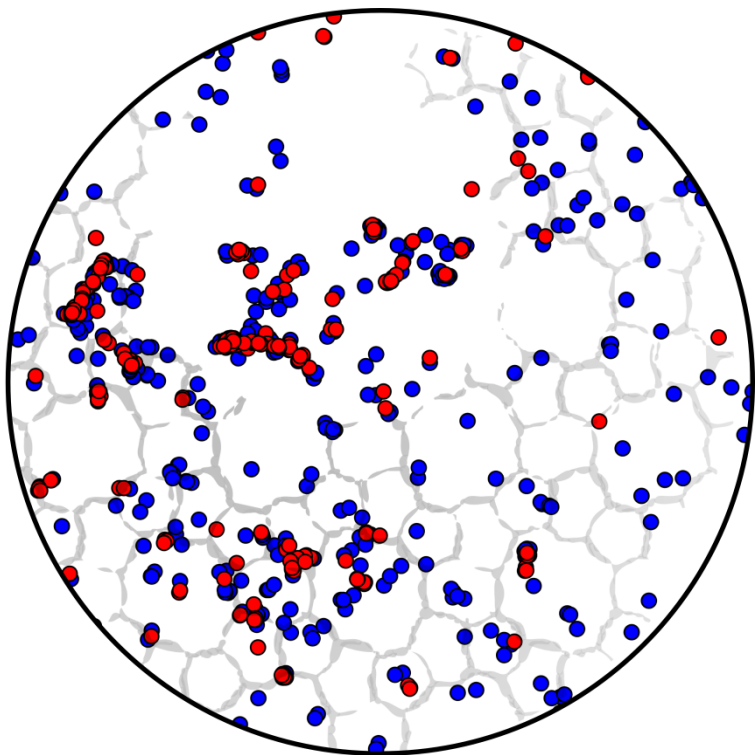
pronounced intra-particle differences in reactivity and low signal-to-noise ratio, which are most probably more a rule than an exception for many industrial catalyst systems.

Acknowledgements

Albemarle is acknowledged for providing the FCC catalyst particles.

References

- [1] G. Bellussi, A. Carati, R. Millini, in *Zeolites and Catalysis: Synthesis, Reactions and Applications* (Eds.: J. Čejka, A. Corma, S. Zones), Wiley-VCH, Weinheim, **2010**, pp. 449–491.
- [2] C. D. Chang, R. Prins, J. H. Sinfelt, R. von Ballmoos, D. H. Harris, J. S. Magee, A. Stüwe, C.-P. Hälsig, H. Tschorr, S. T. Sie, in *Handbook of Heterogeneous Catalysis* (Eds.: G. Ertl, H. Knözinger, J. Weitkamp), Wiley-VCH, Weinheim, **1997**, pp. 1900–2006.
- [3] W. Vermeiren, J.-P. Gilson, *Top. Catal.* **2009**, *52*, 1131–1161.
- [4] E. T. C. Vogt, B. M. Weckhuysen, *Chem. Soc. Rev.* **2015**, 7342–7370.
- [5] A. Corma, in *Studies in Surface Science and Catalysis* (Eds.: P.A. Jacobs and R.A. van Santen), Elsevier, Amsterdam, 1989, pp. 49–67.
- [6] A. Corma, *Chem. Rev.* **1995**, *95*, 559–614.
- [7] M. Rigo, in *Zeolites and Catalysis: Synthesis, Reactions and Applications* (Eds.: J. Čejka, A. Corma, S. Zones), Wiley-VCH, Weinheim, **2010**, pp. 547–584.
- [8] I. L. C. Buurmans, J. Ruiz-Martínez, W. V. Knowles, D. van der Beek, J. A. Bergwerff, E. T. C. Vogt, B. M. Weckhuysen, *Nat. Chem.* **2011**, *3*, 862–867.
- [9] I. L. C. Buurmans, J. Ruiz-Martínez, S. L. van Leeuwen, D. van der Beek, J. A. Bergwerff, W. V. Knowles, E. T. C. Vogt, B. M. Weckhuysen, *Chem. – Eur. J.* **2012**, *18*, 1094–1101.
- [10] C. Sprung, B. M. Weckhuysen, *Chem. – Eur. J.* **2014**, *20*, 3667–3677.
- [11] M. A. Karreman, I. L. C. Buurmans, J. W. Geus, A. V. Agronskaia, J. Ruiz-Martínez, H. C. Gerritsen, B. M. Weckhuysen, *Angew. Chem. Int. Ed.* **2012**, *51*, 1428–1431.
- [12] J. Ruiz-Martínez, A. M. Beale, U. Deka, M. G. O'Brien, P. D. Quinn, J. F. W. Mosselmans, B. M. Weckhuysen, *Angew. Chem. Int. Ed.* **2013**, *52*, 5983–5987.
- [13] P. Dedecker, S. Duwé, R. K. Neely, J. Zhang, *J. Biomed. Opt.* **2012**, *17*, 126008–126008.
- [14] T. Dertinger, R. Colyer, G. Iyer, S. Weiss, J. Enderlein, *Proc. Natl. Acad. Sci.* **2009**, *106*, 22287–22292.
- [15] T. Dertinger, R. Colyer, R. Vogel, J. Enderlein, S. Weiss, *Opt. Express* **2010**, *18*, 18875–18885.
- [16] M. B. J. Roeffaers, G. De Cremer, J. Libeert, R. Ameloot, P. Dedecker, A.-J. Bons, M. Bückins, J. A. Martens, B. F. Sels, D. E. De Vos, J. Hofkens, *Angew. Chem. Int. Ed.* **2009**, *48*, 9285–9289.
- [17] S. Geissbuehler, C. Dellagiacoma, T. Lasser, *Biomed. Opt. Express* **2011**, *2*, 408–420.
- [18] P. Dedecker, G. C. H. Mo, T. Dertinger, J. Zhang, *Proc. Natl. Acad. Sci.* **2012**, *109*, 10909–10914.



Chapter 5 is based on the following manuscript:

“Acid-catalyzed Oligomerization of Styrenes as a Versatile Probe for Single Molecule Fluorescence Microscopy Studies of Zeolite H-ZSM-5 Crystals”, Z. Ristanović, A. V. Kubarev, J. Hofkens, M. B. J. Roeffaers, and B. M. Weckhuysen, *in preparation*.

Chapter 5

Acid-Catalyzed Oligomerization of Styrenes as a Versatile Probe for Single Molecule Fluorescence Microscopy Studies of Zeolite H-ZSM-5 Crystals

Abstract

The oligomerization of 4-methoxystyrene and 4-fluorostyrene was used to study Brønsted acidity and accessibility of zeolite H-ZSM-5 crystals via the formation of fluorescent carbocations detected by single molecule fluorescence microscopy. The large difference in reactivity of 4-methoxystyrene and 4-fluorostyrene enables studying acid-catalyzed processes within zeolite H-ZSM-5 under a broad range of reaction conditions. UV-Vis and confocal fluorescence microscopy indicated the formation of the dimeric and trimeric fluorescent species of 4-methoxystyrene, distinguished by a different photostability. The remarkably photostable trimeric carbocations of 4-methoxystyrene were found to be formed predominantly near defect-rich and more spacious regions of the zeolite crystals, which was confirmed by deliberately introducing crystalline defects via mild steaming of H-ZSM-5. Replacing n-heptane with 1-butanol as a solvent led to a several orders of magnitude decrease in the catalytic activity due to strong chemisorption of 1-butanol onto Brønsted acid sites. Based on the measured turnover frequencies under different zeolite framework/solvent environments we establish a quantitative, single turnover approach for comparing the catalytic activity of individual H-ZSM-5 zeolite crystals under various reaction conditions.

5.1 Introduction

As demonstrated in Chapters 3 and 4, single molecule fluorescence microscopy can be used a powerful method to study the formation of fluorescent species within catalytic solids at the single molecule and single particle level.^[1–12] The technique can be used to study catalytic reactions with a remarkable spatial and temporal resolution in the orders of 10 nm and 10 ms. At the same time it offers single molecule sensitivity, provided that the fluorescent species possess sufficient brightness and photostability. Expanding the scope of chemical reactions and probe molecules that can be used for fluorogenic labeling would help understanding zeolite catalysis from the perspective of the single molecule chemistry. Selective staining of zeolite acidity^[13] is a popular strategy to study Brønsted acidity of zeolite particles where colored and fluorescent species are generated upon the protonation of specific probe molecules, such as furfuryl alcohol,^[14] as well as substituted thiophenes,^[15–17] and styrenes.^[18–20]

Among the mentioned fluorogenic reactions, the Brønsted-acid catalyzed oligomerization of styrene-based compounds has received high interest due to the existence of the highly stable, carbocationic species that are considered as very important reaction intermediates in zeolite chemistry.^[21] Importantly, styrene and its derivatives can fit inside the pores of medium and large pore zeolites and oligomerize further to generate carbocationic species that absorb and emit light in the visible region. Furthermore, by changing the substituents on the styrene moiety it is possible to probe the acidic and shape selective properties of the zeolite framework.^[19] Previous studies of styrene oligomerization have shown that, depending on the substituent, a number of highly fluorescent, carbocationic species can be formed in the porous environment of zeolite H-ZSM-5 crystals^[18–20,22] and powders.^[23,24] The formed species can provide further information about the acidity and shape-selectivity of zeolite particles. The oligomerization reactions using 14 different styrene substituents were initially performed on large H-ZSM-5 crystals as well-defined model systems^[18,19,25] and further extended to industrially relevant zeolite-based catalysts, such as fluid catalytic cracking particles based on H-ZSM-5 and H-Y,^[26–28] and H-ZSM-5-based catalyst bodies.^[16,29]

In this Chapter, we extend the applicability of the styrene oligomerization reaction to single molecule fluorescence microscopy studies with the idea to gain new

insights into the acid-catalyzed chemistry of zeolite H-ZSM-5 at the single particle – single molecule level. The staining approach based on 4-methoxystyrene and 4-fluorostyrene derivatives is used to study the acidic and accessibility properties of the parent H-ZSM-5-P and steamed zeolite H-ZSM-5-MT crystals. Using these probe molecules as a showcase we demonstrate the importance of accessibility for the selective formation of different reaction intermediates. Finally, the versatility of the approach was demonstrated in both non-polar (i.e., n-heptane) and polar (i.e., 1-butanol) solvent environments. Based on these data, it was possible to quantify the catalytic turnover rates of sub-particle zeolite domains and visualize the intra- and inter-particle heterogeneities in reactivity of the large zeolite H-ZSM-5 crystals under study.

5.2 Experimental

5.2.1 Zeolite materials

Parent H-ZSM-5-P and mildly steamed H-ZSM-5-MT zeolite crystals were prepared as described in the Experimental Section of Chapter 2. Prior to single molecule fluorescence microscopy experiments, the crystals were activated at 773 K (1 K/min) for 24 h in static air to avoid residual fluorescence.

5.2.2 UV-Vis microspectroscopy

UV-Vis spectra were measured with an Olympus BX41 upright microscope working in reflectance mode, equipped with a 50 \times 0.5 NA high working-distance microscope objective lens. A 75 W tungsten lamp was used for illumination. Reflected light was directed to a CCD video camera (ColorView IIIu, Soft Imaging System GmbH) via a 50/50 double viewport tube, and to a UV-Vis spectrometer (AvaSpec-2048TEC, Avantes BV) via a 200 μ m core fiber.

5.2.3 Confocal fluorescence microscopy

The fluorescence microscopy measurements were carried out using an upright Nikon Eclipse 90i confocal laser scanning microscope, equipped with a 100 \times 0.73 NA dry objective lens. Confocal fluorescence microscopy images were recorded using excitation from two laser light sources (488 nm and 561 nm) connected to a Nikon-

Eclipse A1R scanning head equipped with corresponding dichroic mirrors to reject the excitation light. The long axes of the zeolite crystals were aligned perpendicular to the polarization vector of the laser light in order to efficiently excite the fluorescent molecules, as explained in reference.^[20] The emission light was detected in the range of (495-700 nm) by using a spectral detection unit equipped with a diffraction grating and a 32 photomultiplier tube array. The fluorescence spectra obtained by 488 nm (from 490-600 nm) and 561 nm lasers (from 570-700 nm) were overlapped to yield the total fluorescence spectra.

5.2.4 Single molecule fluorescence detection and emitter tracking analysis

Single molecule fluorescence microscopy experiments were carried out as described in the Experimental Section 3.2.3. A 532 nm excitation (with a 545 nm long-pass filter) was used for the reaction in n-heptane, while the reaction in 1-butanol was performed with 561 nm excitation light (a 575 nm long-pass filter). The fluorescence microscopy movies were recorded with frame rates of 30 and 100 ms per frame. The emitter tracking algorithm, described in Section 3.3.3, has been used for the analysis of the single emitter survival time before photobleaching. An iterative procedure was used to optimize the parameters of the algorithm that take into account single molecule reappearance in subsequent localizations and blinking of the fluorescent molecule. The optimal values of 57.6 nm for *pixel jump* and 2 s for *blinking time* were found to approximate well the contribution of the highly photostable/blinking molecules.

5.2.5 Experiments

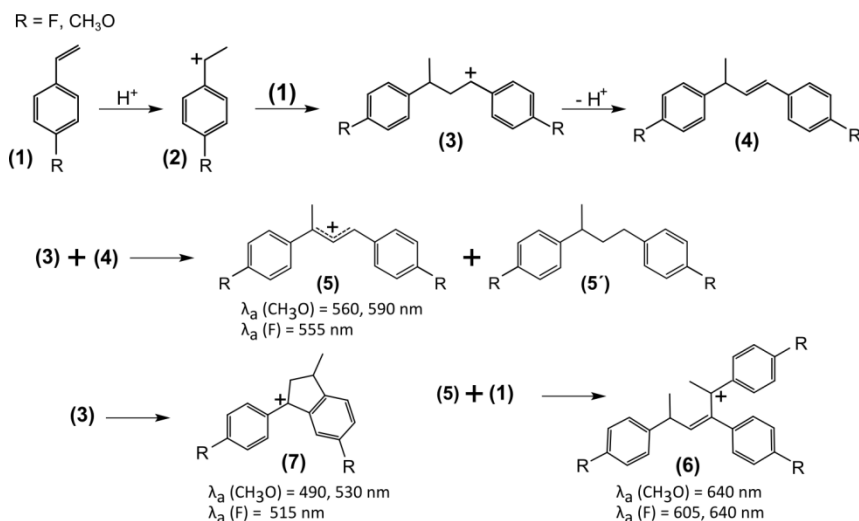
For the above described UV-Vis and confocal fluorescence microscopy experiments, 10 µL of solution containing 4-methoxystyrene (Sigma-Aldrich, > 98%) or 4-fluorostyrene (Sigma-Aldrich, > 99%) was added to color the zeolite crystals. For 4-fluorostyrene, a Linkam heating stage was used to reach the reaction temperature of 393 K (heating rate 5 K/min). The experiments for 4-methoxystyrene were conducted in the liquid phase at room temperature. For single molecule fluorescence microscopy experiments, zeolite H-ZSM-5 crystals were loaded on a cover glass that was previously attached in a reactor designed for liquid-phase experiments. Typically, 1 ml of the solution containing 4-methoxystyrene or 4-fluorostyrene dissolved in either heptane (spectroscopic grade) or butanol (spectroscopic grade, vacuum distilled) was

subsequently added. The reaction was then monitored by focusing at the surface of the bottom facet or by moving the focus to any provisional focal depth in axial Z-direction up to $Z = 20 \pm 0.2 \mu\text{m}$. Prior to the experiments, the absence of residual fluorescence was verified in individual crystals. All single molecule fluorescence microscopy experiments were performed at room temperature.

5.3 Results and Discussion

5.3.1 Acid-catalyzed oligomerization of substituted styrenes

Previous studies of the styrene oligomerization reaction suggested a reaction mechanism for the formation of colored (and fluorescent) carbocationic species, as outlined in Scheme 5.1. Here we concentrate on the styrene moiety with the remark that the mechanism is applied for any of the substituted styrenes (in this case 4-methoxystyrene and 4-fluorostyrene). Upon the protonation of the neutral styrene molecule (**1**), the initial, benzylic carbocation (**2**) is formed. Further dimerization leads to the formation of the linear dimeric 1,3-bis(phenyl)-1-butylium cation (**3**), that can transform into neutral diphenyl alkene upon proton transfer to the zeolite framework (**4**), or undergo cyclization to the cyclic dimeric 3-methyl-1,4-phenylindanyl (indanyl) carbocation (**7**).



Scheme 5.1 Potential reaction pathways and molecular species proposed for the oligomerization reaction of styrene derivatives in acidic zeolites.^[19,20,23,30] The absorption maxima for the species (5 - 7) represent the experimentally observed absorption bands shown in Figure 5.1.

The formation of the linear allylic carbocation (**5**) has been the subject of particular interest. According to Cozens et al.^[30] and Buurmans et al.^[23], molecules (**3**) and (**4**) can undergo bimolecular hydride transfer to form allylic carbocation (**5**). The charged carbocations (**5**) and (**7**) are reported in the literature as the stable carbocations that can absorb light in the visible region. The absorption originating from trimeric species (**6**) was reported previously,^[18,20] but to this moment their precise molecular structure is not known in detail.

5.3.2 UV-Vis microspectroscopy of styrene-derived carbocations

Understanding the chemistry of styrenes in zeolite H-ZSM-5 requires a comprehensive knowledge of the absorption and emission properties of the carbocationic species that can form during the reaction at Brønsted acid sites. A significant difference in reactivity between 4-methoxy and 4-fluoro analogs is noticed with an UV-Vis microscope. The oligomerization of 4-methoxystyrene readily proceeds at room temperature, coloring the H-ZSM-5 crystals due to the formation of the stable carbocationic species.^[18] In contrast to 4-methoxystyrene, 4-fluorostyrene does not show visible reactivity at room temperature due to the high electronegativity of the fluoro-substituent that hinders the proton transfer from the Brønsted acid sites to the double bond of the styrene moiety.^[19]

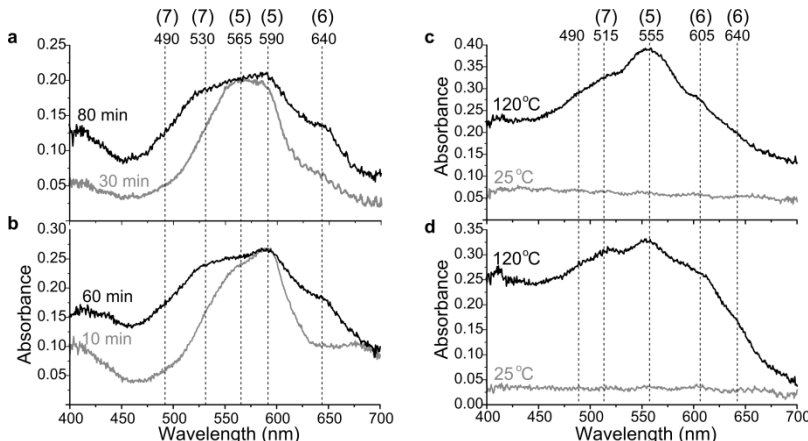


Figure 5.1 UV-Vis spectra of the studied oligomerization reactions recorded for the parent H-ZSM-5-P (a,c) and steamed H-ZSM-5-MT zeolite crystals (b,d). a,b) UV-Vis spectra of 4-methoxystyrene oligomers recorded at 298 K from a) H-ZSM-5-P crystals (measured at two different crystals) and b) H-ZSM-5-MT crystal. c,d) UV-Vis spectra of 4-fluorostyrene oligomers recorded at 298 K and 393 K from c) H-ZSM-5-P crystals and d) H-ZSM-5-MT crystals. The numbers above the absorption maxima indicate the tentative assignment to the carbocationic species shown in Scheme 5.1.

The difference in reactivity of the probed molecules is visible in the comparison of their UV-Vis spectra, summarized in Figure 5.1. The UV-Vis spectra of the colored parent H-ZSM-5-P and steamed H-ZSM-5-MT crystals subjected to 4-methoxystyrene are presented in Figures 5.1a,b, respectively. Two distinct absorption bands initially appear for both types of H-ZSM-5 crystals at around 565 nm and 590 nm. Similar absorption profile was recorded earlier by Kox et al. and the absorption at around 585 nm was attributed to the linear dimeric carbocation.^[18,30,31] We attribute these bands to the existence of two isomers of the allylic dimeric carbocation (**5**). The absorption bands at 490, 530, and 640 nm appear later in the spectrum, but notably faster on steamed H-ZSM-5-MT crystals (Figure 5.1b). An appearance and evolution of these bands lags behind the formation of linear dimeric species, resulting in a dark purple coloration of the crystals. The highest energy band at 490 nm has been assigned before to cyclic dimeric carbocations (**7**),^[30,31] while the absorption band at around 640 nm has been previously attributed to the trimeric carbocationic species (**6**).^[18,22] Despite the lack of evidence for their precise molecular structure(s), the extent of conjugation and late appearance of these species suggests their trimeric nature. The assignment of the band at 530 nm has never been attempted before for 4-methoxystyrene as it appears as a satellite band to the observed linear dimeric species. Sprung and Weckhuysen^[20] have recently reported 20-40 nm shifts in the absorption bands of cyclic carbocations in sinusoidal pores. Additionally, as the formation of the absorption band follows similar trends as for the trimeric (**6**) and cyclic species (**7**), suggesting their bulkier nature, we attribute this band to the cyclic dimeric species.

The low reactivity of 4-fluorostyrene at room temperature is evidenced in Figures 5.1c,d. A thermal activation at 393 K leads to an intense coloration and the formation of the absorption bands at around 490, 515, 555, 605, and 640 nm, which is in agreement with the data reported recently by Sprung and Weckhuysen.^[20] A similar response with somewhat faster and stronger coloration is noted for H-ZSM-5-MT crystals (Figure 5.1d). Alike to the assigned absorption bands in the case of 4-methoxystyrene, the trends in absorption energies for fluorostyrene were similar. The band at 515 nm has been attributed to the cyclic species, followed by the linear dimeric (555 nm), and trimeric species (605 nm), as reported in the literature.^[20,23,24] In what follows, we will use the previously reported assignments to support the

experimental observations from the (single molecule) fluorescence microscopy measurements.

It is noteworthy to mention that the extent of crystal coloration, time-dependent changes, as well as the number of absorption bands may significantly differ when going from one zeolite crystal to another. Some H-ZSM-5-P crystals did not show visible absorption, even after 1 h of reaction in 4-methoxystyrene, whereas others reached dark-purple coloration, as illustrated in Figure 5.2a. Except readily notable differences in the coloration, the measured zeolite H-ZSM-5 crystals have shown differences in their spectral response, i.e., the concentration of the linear dimeric and bulkier, cyclic, and trimeric species. While some H-ZSM-5-MT crystals showed the presence of all absorption bands after 1 h (Figure 5.2b), for other crystals that exhibited a light blue coloration, the absorption bands at 565 nm and 640 nm were not pronounced (Figure 5.2c). However, the positions of the absorption bands were independent of the zeolite crystal, confirming the existence of several different carbocationic intermediates that form under different reaction conditions.

5.3.3 Confocal fluorescence microspectroscopy of styrene-derived carbocations

Understanding the fluorescence properties of different carbocationic species is essential for their subsequent single molecule fluorescence characterization. Therefore we have directly compared the UV-Vis micro-spectroscopy data with confocal fluorescence microscopy results recorded for both probe molecules as well as for the H-ZSM-5-P and H-ZSM-5-MT zeolite crystals, as shown in Figure 5.3. The fluorescence spectra of H-ZSM-5-P crystals exposed to 4-methoxystyrene exhibit in all cases two distinct emission bands at around 600 nm and 650 nm (Figure 5.3a). The linear dimeric and trimeric species are likely to contribute to the fluorescence transitions at 600 nm and 650 nm, respectively. Both emission bands are found for the parent H-ZSM-5-P and steamed zeolite H-ZSM-5-MT crystals. The additional fluorescence emission at 540 nm is recorded only at the most fluorescent zeolite crystals for both H-ZSM-5-P and H-ZSM-5-MT zeolite crystals, but noticed more frequently on the steamed crystals (Figure 5.3b).

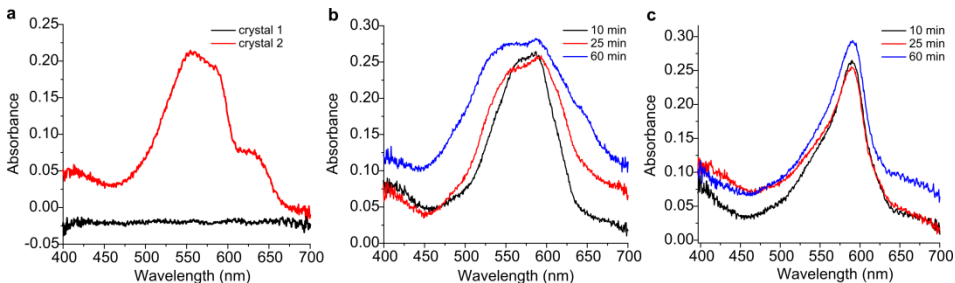


Figure 5.2 a) UV-Vis spectra of the reactive and non-reactive zeolite H-ZSM-5-P crystals recorder after 1 h of a reaction with 4-methoxystyrene. b,c) Time evolution of UV-Vis spectra for two H-ZSM-5-MT zeolite crystals indicating a difference in the distribution of the colored products.

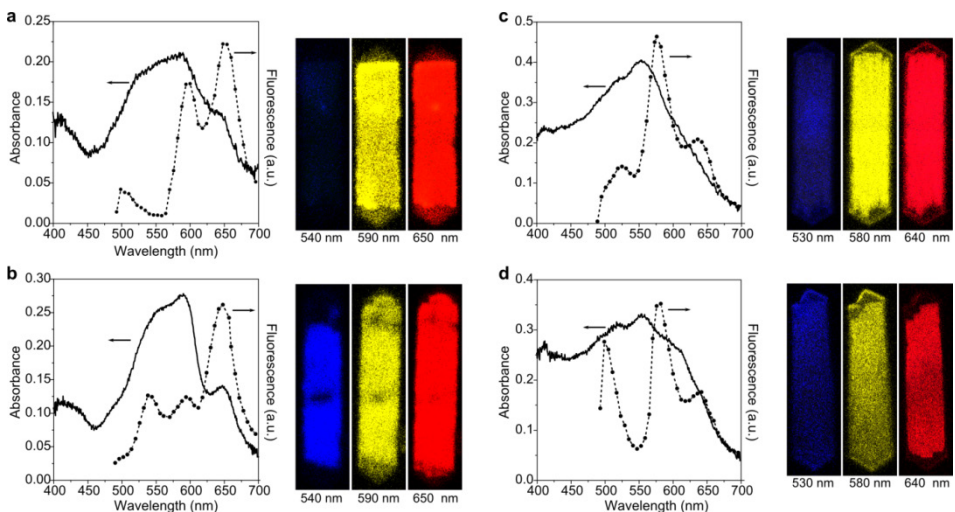


Figure 5.3 Comparison of the UV-Vis (solid line) and fluorescence spectra (dashed line) of the oligomerization reaction products recorded for parent H-ZSM-5-P (top) and steamed zeolite H-ZSM-5-MT crystals (bottom). a,b) 4-methoxystyrene oligomerization recorded at room temperature; c,d) 4-fluorostyrene oligomerization recorded at 393 K. Confocal fluorescence microscopy images are indicating the spatial distribution of different fluorescent species around their maximum in fluorescence (± 25 nm).

The advantage of the confocal fluorescence microscopy method is that it can provide a 3-D distribution of the fluorescent molecules in H-ZSM-5 crystals.^[20,32] The spatial distribution of the most abundant fluorescent species present for both studied probe molecules is included in Figure 5.3. The fluorescence bands for 4-methoxystyrene at 600 and 650 nm overlap spatially for the top subunits of H-ZSM-5 zeolite crystals (Figures 5.3a,b), while at the edge the 600 nm band seems to be higher in intensity, as reported in the literature.^[18] However, both emission bands predominantly originate from the molecules aligned in the direction of the straight

pores, which was verified in a polarization-sensitive experiment by rotating the zeolite crystal for 90°, as recently explained in the work of Sprung and Weckhuysen.^[20] The emission band at 540 nm does not overlap spatially with the bands at 600 nm and 650 nm and is likely to belong to the cyclic species, considering their higher energy transitions at 490 and 530 nm. However, it should be noted that for the majority of zeolite crystals the emission band at around 540 nm was not detected despite an absorption band in this region. In these cases we observed high fluorescence intensity only in the 650 nm region. Thus, based solely on confocal fluorescence microscopy measurements, we concluded that the concentration of the bulkier trimeric and cyclic species depends on the interparticle differences in reactivity, with the formation of trimeric species being more visible in fluorescence.

Our experiments suggest that a more intense coloration of zeolite H-ZSM-5-P crystals exposed to 4-methoxystyrene does not simply relate to higher fluorescence intensity, which is an indication of different non-radiative relaxation pathways that may take place. This behavior was pronounced for 4-methoxystyrene and most probably relates to its high reactivity that leads to a complex photo-chemistry and quenching of fluorescence at high concentrations of reactant and products. Similar conclusions can be made with respect to the origin of the fluorescence bands related to 4-fluorostyrene oligomerization at 393 K (Figure 5.3c,d). In this case we observe emission bands at around 525, 580, and 640 nm. More details about the confocal fluorescence microscopy measurements of the 4-fluorostyrene oligomerization reaction at higher reaction temperatures can be found in the work of Sprung and Weckhuysen.^[20]

5.3.4 Single molecule fluorescence microscopy of 4-methoxystyrene-derived carbocations

The oligomerization of 4-methoxystyrene was further tested under the conditions of the single molecule fluorescence detection. To achieve this, the reaction rate was optimized so that the individual products can be spatially resolved. For the large majority of individual zeolite H-ZSM-5 crystals, a room temperature reaction in liquid 4-methoxystyrene resulted in a quick coloration and therefore fast accumulation of the fluorescence signal. However, by using zeolite H-ZSM-5 crystals with very low activity, such as the non-reactive “crystal 1” in Figure 5.2a, it was possible to follow

the oligomerization of 4-methoxystyrene without dilution in a solvent. The localization of the single molecule fluorescence events in each frame of a fluorescence movie results in a high-resolution map of photoactivity where each fluorescent burst is detected as an individual photo-event by using a 2-D Gaussian localization procedure described in Chapter 3. This procedure is repeated for each time frame, thus allowing the precise localization of fluorescent events over the course of the reaction. Figure 5.4 presents such high-resolution maps of photoactivity during the oligomerization of 4-methoxystyrene at a zeolite H-ZSM-5-P crystal. Here we show the results recorded at two different focal depths, i.e., at the surface ($Z = 0 \pm 0.2 \mu\text{m}$) and towards the middle of the crystal ($Z = 8 \mu\text{m}$). The reaction was followed with 100 ms temporal resolution and individual product molecules were localized with lateral resolution of $17 \pm 7 \text{ nm}$. This is more than a ten-fold improvement of the diffraction limited resolution and a remarkable improvement in sensitivity as compared to UV-Vis and confocal fluorescence microscopy studies reported previously.^[20,22]

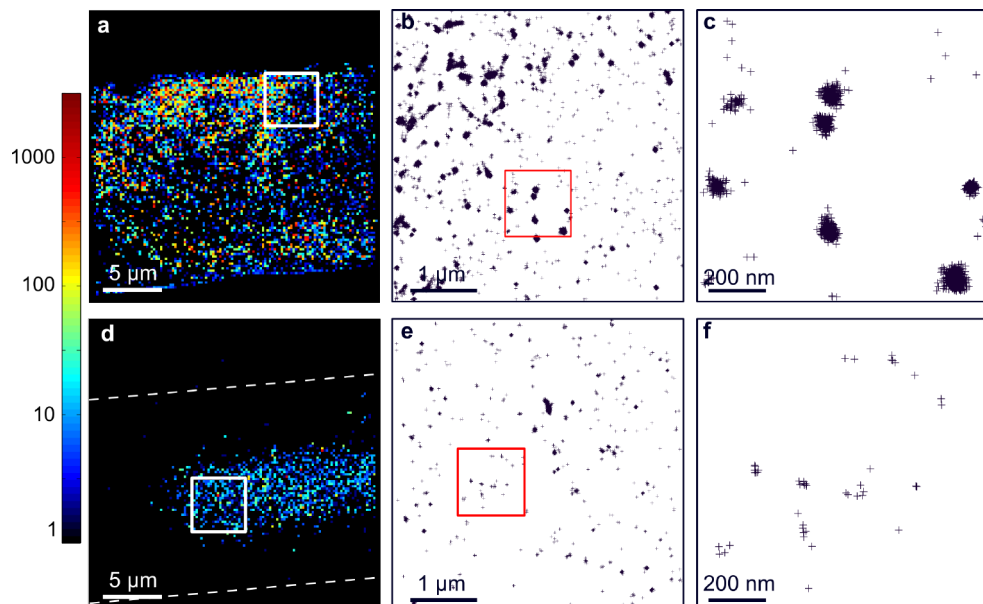


Figure 5.4 High-resolution single molecule fluorescence microscopy imaging of fluorescent products recorded after 1 h during 500 s of the oligomerization of 4-methoxystyrene on a parent zeolite H-ZSM-5-P crystal. a) Accumulated map of photoactivity recorded at the zeolite surface (colour bar: number of events per $200 \times 200 \text{ nm}^2$ presented in the logarithmic scale), b) Scatter plot derived from the white square region in (a), c) magnified region from the red square in (b). d-f) The same as (a-c), but for $Z = 8 \mu\text{m}$. Each cross-point in the scatter maps represents one photo-event detected in one exposure frame (100 ms).

The accumulated high-resolution single molecule fluorescence microscopy maps in Figure 5.4 indicate a highly heterogeneous spatiotemporal distribution of catalytic turnovers in a zeolite H-ZSM-5-P crystal. At the surface, photo-events seem to agglomerate in the regions of the high and low photoactivity (Figure 5.4a), whereas at $Z = 8 \mu\text{m}$ a core of reactivity with more evenly distributed single catalytic events is present (Figure 5.4d). The unusually low reactivity at the surface of the studied parent H-ZSM-5-P zeolite crystal (as compared to the more reactive crystals) indicates that Brønsted acid sites are not much present or inaccessible due to the extremely high surface diffusion resistance and blockage of the pores.

An important observation from Figures 5.4a,d is that the survival time of fluorescent products (i.e., the time before fluorescent molecules are photobleached) significantly differs at the surface and at $Z = 8 \mu\text{m}$ below the surface. More quantitatively, the accumulated map of photoactivity at the surface (Figure 5.4a) contains a significant number of pixelated hotspots with photoactivity of 100-4000 detected photo-events per $200 \times 200 \text{ nm}^2$, whereas this quantity in Figure 5.4d rarely exceeds 10-50 detected photo-events per $200 \times 200 \text{ nm}^2$. This is an indication that the extremely photostable molecules predominantly form at the near surface – which is confirmed by a close inspection of fluorescence intensity trajectories for individual molecules. In contrast, the reaction products formed inside of the zeolite crystal photobleach within significantly shorter period of time. This is further illustrated by the scatter plots of photoactivity, which depict all detected photo-events in the magnified regions of interest (Figures 5.4b,c,e,f). Figure 5.4c shows a region of interest with the highly localized photo-events that belong to the photostable molecules, rather than originating from numerous short photo-events. This is, however, not the case for the region presented in Figure 5.4f. The high-resolution accumulated maps and scatter plots of photoactivity presented in Figure 5.4 should not be confused with the reactivity maps. The applied localization algorithm detects photo-events in every individual frame of a fluorescence movie. Thus, if a highly photostable molecule appears in the fluorescence movie, it will be detected in multiple frames (e.g., see Figure 5.4c). Therefore, in this Chapter we will use the described representation for the purpose of visualizing the differences in the photostability of the formed carbocations. As detected products are highly localized, this representation can be used to distinguish between the fluorescent products with higher and lower photostability.

The observed differences in photostability suggest the formation of different types of molecules – the products formed in the micropores of the zeolite H-ZSM-5 framework seem to possess a lower photostability, while the highly photostable products are formed close to the surface, near crystalline defects or more accessible acid sites.

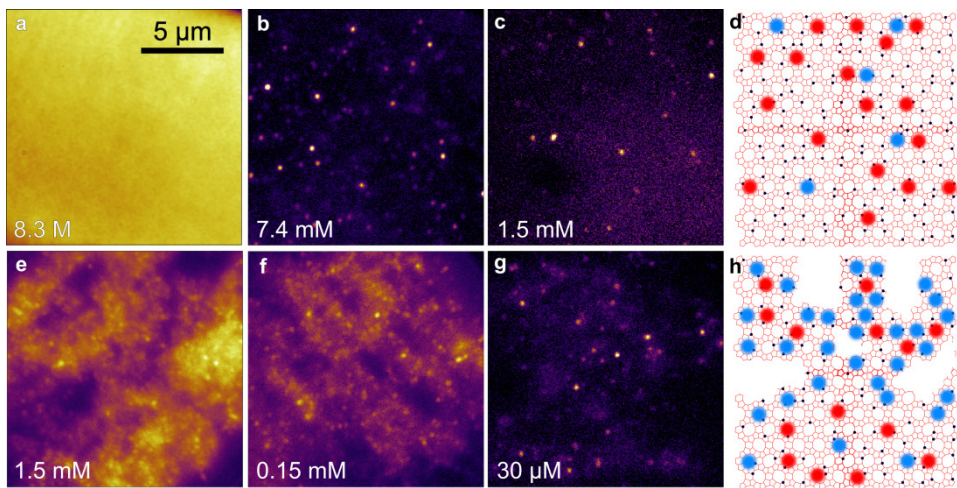


Figure 5.5 Probing the accessibility of the parent H-ZSM-5-P (top) and steamed H-ZSM-5-MT zeolite crystals (bottom). The oligomerization of 4-methoxystyrene at different molar concentrations in heptane, recorded close to the surface of the parent (a-c) and steamed (e-g) crystals; the numbers in the bottom left indicate the concentration of 4-methoxystyrene in heptane, with (a) recorded in liquid 4-methoxystyrene (8.3 M). d,h) Schematic representation of the photo-product formation in parent (d) and steamed (h) crystals. Red dots indicate the formation of linear dimeric carbocations; blue represent the bulkier molecules, such as trimeric carbocations, formed close to defects/mesopores.

5.3.5 Visualizing the accessibility of the H-ZSM-5-P and H-ZSM-5-MT crystals in heptane

To further test our hypothesis of detecting different types of fluorescent species we have investigated the sensitivity of 4-methoxystyrene towards the presence of crystalline defects that were deliberately induced by dealumination of H-ZSM-5-P crystals via mild steaming at 773 K. As discussed in Chapters 2 and 3 mild steaming only partially dealuminates the zeolite framework and improves the accessibility of the Brønsted acid sites via the formation of mesopores.^[33] For comparison, we have tested the reactivity of H-ZSM-5-P and H-ZSM-5-MT zeolite crystals in a series of experiments with a heptane solution of 4-methoxystyrene. As mentioned earlier, the exposure of the parent H-ZSM-5 crystals to liquid (non-diluted) 4-methoxystyrene

generally leads to the fast accumulation of fluorescence where single molecule products cannot be resolved anymore, as illustrated in Figure 5.5a. Significant dilution of 4-methoxystyrene in heptane (7.4 mM) was necessary to observe well-separated single molecule products (Figure 5.5b). We observed very slow intracrystalline diffusion of 4-methoxystyrene with the fluorescent events predominantly detected in the near surface region (~ 0.5 µm) of zeolite H-ZSM-5-P crystals. As expected, the reactivity decreased approximately 10 times when the crystals were exposed to a 1.5 mM solution of 4-methoxystyrene. However, when the steamed H-ZSM-5-MT crystals were exposed to a 1.5 mM concentration of the reactant, we observed an abundant fluorescence response where individual single molecules could not be resolved due to a high background fluorescence (Figure 5.5e). The response qualitatively did not change at a 0.15 mM concentration of the probe molecule (Figure 5.5f). Only at a significantly lower 30 µM concentration of 4-methoxystyrene we have observed isolated single molecule events (Figure 5.5g).

As discussed in Chapters 2 and 3, mild steaming generates surface mesoporosity via dealumination, leading to higher accessibility of acid sites.^[33] However, such a striking difference in a fluorescence response cannot be explained solely by an increase in reactivity due to the formation of mesopores. In Chapter 3 it was shown that the turnover frequencies of the zeolite H-ZSM-5-P and H-ZSM-5-MT crystals differ by factors of 2 to 5. The very pronounced change in the fluorescence response at crystalline defects of H-ZSM-5-P and H-ZSM-5-MT indicates a shape-selective formation of different reaction products. This is due to the significantly different accessibility properties of H-ZSM-5-P and H-ZSM-MT crystals. As resolved by TOF-SIMS sputter-depth profiling analysis in Chapter 2, parent H-ZSM-5-P crystals showed a silicalite layer close to the surface (up to 100 nm in thickness), that is characterized by a Si/Al ratio of ~ 160.^[33,34] This layer also acts as a microcrystalline, non-reactive, surface diffusion barrier – therefore hindering diffusion and formation of bulkier fluorescent products at the very surface (Figure 5.5d). Furthermore, the concentration of the crystalline defects in the highly crystalline H-ZSM-5-P zeolite crystal is expected to be minimized. The situation is drastically changed in the case of steamed zeolite H-ZSM-5-MT crystals where the formation of mesopores significantly facilitates the molecular diffusion^[35] and the formation of the highly photostable fluorescent products (Figure 5.5h).

5.3.6 Distinct photo-stability of the dimeric and trimeric carbocations of 4-methoxystyrene

In order to further quantify the observed differences in fluorescence response we examined the lifetime of the fluorescent molecules from the two showcases presented in Figures 5.4 and 5.5. The difference in photo-stability between single molecule products of H-ZSM-5-P and H-ZSM-5-MT can be further quantified using a particle-tracking localization algorithm that accounts for a reappearance of individual fluorescent molecules. Figure 5.6 summarizes the occurrence of calculated survival times of fluorescent molecules before they permanently photobleach (within the tracking time defined in our trace analysis). The results are presented for the case of 4-methoxystyrene reaction at different focal depths (Figure 5.6a) and for different concentrations of the reactant in n-heptane (Figure 5.6b).

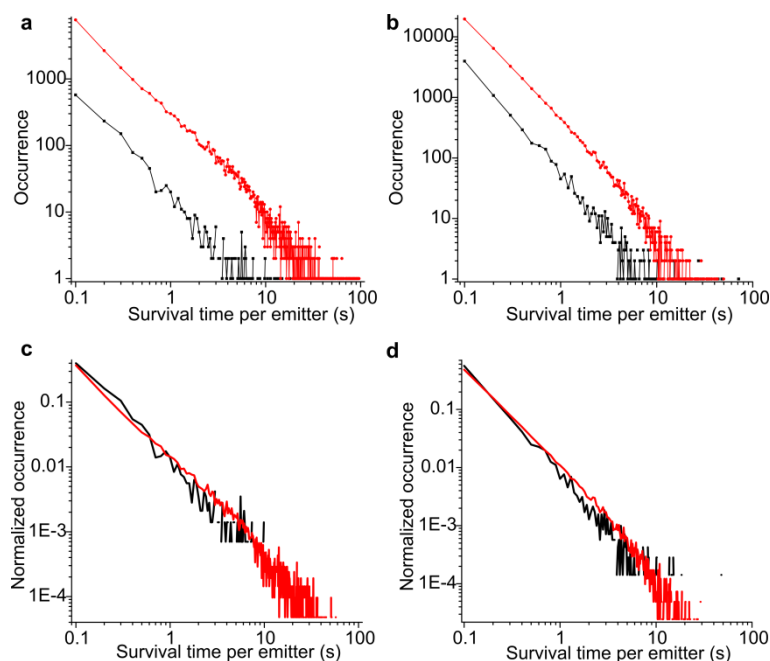


Figure 5.6 Occurrence of survival times of fluorescent emitters of 4-methoxystyrene, a) measured at the surface of H-ZSM-5-P (red) and Z = 8 μm below the zeolite surface (black), as determined from Figures 5.4a,d; b) measured at the surface of H-ZSM-5-P for 7.5 mM (red) and 1.4 mM (black) solutions of 4-methoxystyrene in heptane. c,d) Normalized occurrence of emitters from the graphs in (a) and (b). Note the logarithmic axes in all cases.

The results presented in Figure 5.6 indicate a broad range of survival times for fluorescent emitters, covering 3 orders of magnitude from 100 ms to 100 s. However,

there is a significant difference in the fraction of molecules with longer lifetimes (> 1 s) between the surface and $Z = 8 \mu\text{m}$ (Figure 5.6a). The difference is more visible when normalized occurrences are compared for both cases (Figure 5.6c). The fraction of molecules with the lower survival times ($< 700 \text{ ms}$) is higher for the movie recorded at $Z = 8 \mu\text{m}$, whereas the movie recorded at the surface of the H-ZSM-5-P crystal has a significantly higher contribution of the photostable emitters (survival times $> 1 \text{ s}$). Similar trends are observed in Figures 5.6b,d. A more concentrated 7.5 mM solution of the reactant has a higher contribution of the emitters with longer survival times. The quantified differences indicate that the more stable fluorescent species form near the surface of zeolite H-ZSM-5-crystals and at higher concentrations of the reactant.

An explanation of the described behavior can be found in the types of fluorescent products that are formed within zeolite H-ZSM-5. As previously discussed, the linear dimeric carbocations (**5**) form easily in the zeolite H-ZSM-5 micropores and under highly diluted conditions they should be the predominant species. The trimeric (**6**) and cyclic (**7**) carbocations are likely to be formed at more accessible acid sites, as suggested in the previous work from our group.^[20,23,24] The formation of the trimeric species (**6**) seems to be kinetically controlled and follows the formation of the dimeric species (**5**), as evidenced from the UV-Vis experiments (Figure 5.1). The low concentrations of 4-methoxystyrene that are used in the single molecule fluorescence microscopy experiments highly favor the formation of the dimeric carbocations. Considering the high density of Brønsted acid sites, the formation of trimeric species is certainly expected to be more promoted close to the surface, at more accessible acid sites. The statistical analysis of the survival time of the fluorescent molecules indicates that the initial concentration of 4-methoxystyrene kinetically controls the formation of the trimeric species. In the single molecule fluorescence microscopy experiments we use a 532 nm laser excitation, meaning that we simultaneously and efficiently excite both linear dimeric (**5**) (emission at 600 nm) and trimeric species (**6**) (emission at 650 nm). The emission band at 540 nm is occasionally observed at H-ZSM-5-MT crystals, suggesting that we cannot exclude the formation of the cyclic species (**7**) at the crystalline defects. The photostability of the trimeric and cyclic species is most probably related to their low reactivity, as their further oligomerization is not likely to happen.

5.3.7 High-resolution localization of crystalline defects in H-ZSM-5-MT

After rationalizing the origin of the highly photostable reaction products at defect-rich H-ZSM-5-MT crystals, we attempted to localize the fluorescent products by controlling the rate of their formation in 30 μM solution of 4-methoxystyrene. The formation of fluorescent products at four different focal depths of a steamed H-ZSM-5-MT crystal is illustrated in Figure 5.7a.

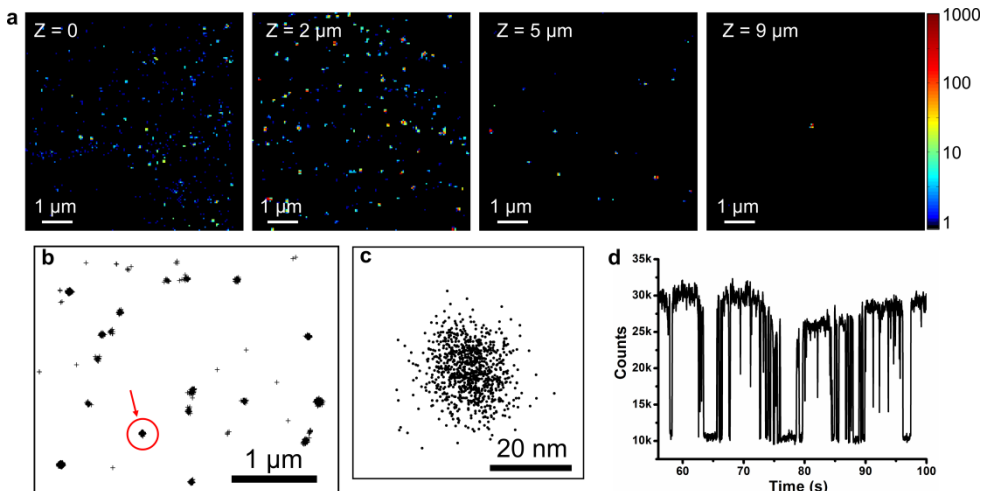


Figure 5.7 High-resolution fluorescence microscopy imaging of defect-induced reactivity of 4-methoxystyrene, recorded in 30 μM solution in heptane. a) Accumulated images of photoactivity for different focal depths denoted in the top left corner, recorded after ~ 1 h from the start of the reaction. The color bar represents number of detected photo-events per $48 \times 48 \text{ nm}^2$. b) High resolution scatter plot indicating the location of fluorescent products formed in a zeolite H-ZSM-5-MT crystal at $Z = (2 \pm 0.3) \mu\text{m}$. c,d) Corresponding c) scatter plot and d) fluorescence intensity trajectory of the single molecule indicated with the red arrow in (b).

The majority of the photostable products is formed in a 2-3 μm thick surface layer of the zeolite crystal. The high-resolution SEM study of large H-ZSM-5-MT crystals detected near-surface mesopores with diameters of 5-50 nm. However, almost no damage of the crystalline structure (i.e., mesoporosity) was noted in the deeper regions of the zeolite crystal (see also Figure 2.7).^[33,36] The turnover rates measured with furfuryl alcohol in Chapter 3 also point towards similar conclusions. This leads us to suggest that the formation of the highly photo-stable emitters was promoted by mesoporosity of H-ZSM-5-MT. The concentration of 4-methoxystyrene in this experiment (30 μM) corresponds to only 17 molecules per 100 nm^3 , indicating that the probe reaction is extremely sensitive to the accessible Brønsted acid sites. At $Z = 2$

μm below the surface we observe a high number of photostable fluorescent molecules (Figure 5.7b). The detected emitters did not show observable diffusion, as the fluorescent events were highly localized, within the localization precision of our method ($\sim 20 \text{ nm}$), as shown in Figure 5.7c. The observed emitter shows high photostability with occasional blinking, as evidenced from its fluorescence intensity trajectory (Figure 5.7d).

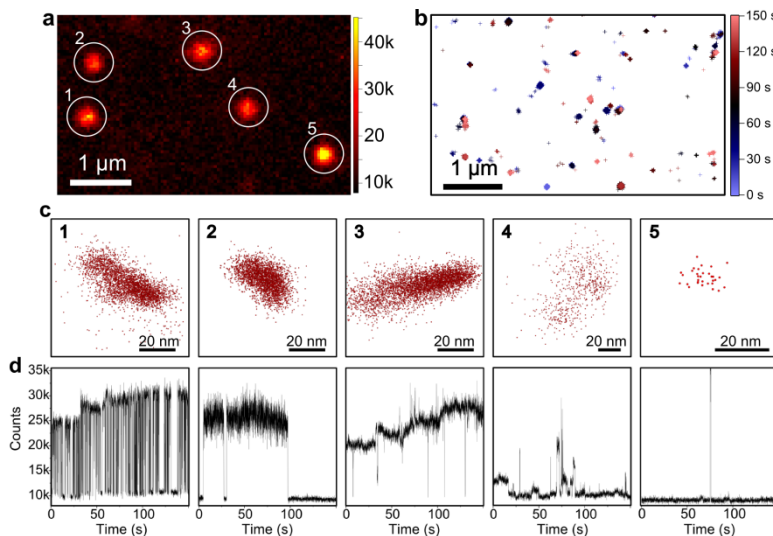


Figure 5.8 Examples of single molecule fluorescence intensity trajectories recorded during exposure of H-ZSM-5-MT crystal to $30 \mu\text{M}$ solution of 4-methoxystyrene in heptane. a) Single 30 ms frame indicating 5 fluorescent events presented in (c) and (d). b) Scatter plot of all photo-events accumulated during a time frame of 150 s. Color-coded bar represents the time of detection. c) Scatter plots of the photo-events labelled in (a), and d) corresponding photo-trajectories of the emitters shown in (c).

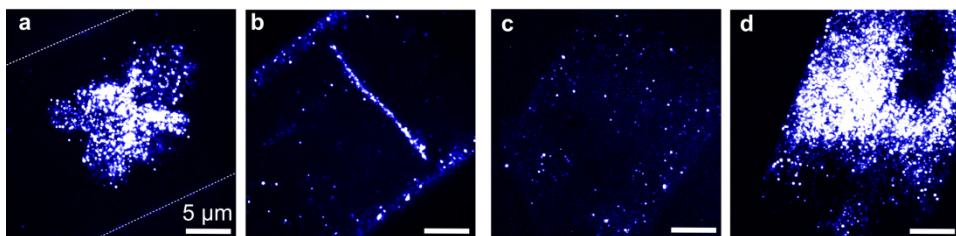


Figure 5.9 Intraparticle (a,b) and interparticle heterogeneities (c,d) imaged with single molecule fluorescence microscopy. a,b) the reactivity of H-ZSM-5-P crystals with significant intracrystalline defects, recorded at $Z = 4 \mu\text{m}$. c,d) The fluorescence response at the surface of two H-ZSM-5-MT crystals. All images represent accumulated fluorescence signal reconstructed with SOFI analysis. Brighter the color, the more photoactive the region of interest.

By using single molecule fluorescence microscopy with 30 ms time resolution it is possible to track the temporal changes in fluorescence for every observed fluorescent molecule. Several examples of different fluorescence intensity trajectories are presented in Figure 5.8. As it can be seen, some of the emitters exhibit permanent fluorescence over long time intervals, while others have more pronounced blinking behavior. The presented approach enables ensemble-free studies of the population of fluorescent molecules and observation of their real-time interactions with the zeolite framework and molecular environment.

5.3.8 Imaging of intra- and interparticle differences in surface accessibility

The sensitivity of 4-methoxystyrene to crystalline defects can be used to quickly assess and visualize crystalline imperfections in parent H-ZSM-5-P zeolite crystals. A significant fraction of the H-ZSM-5-P crystals appeared to have intra-crystalline defects, such as cracks and mesoporous imperfections, generated during the preparation and calcination. In these regions the oligomerization reaction seems to proceed significantly faster, producing an overwhelming fluorescence intensity as compared to the purely microcrystalline domains (Figures 5.9a,b). Notably, the important role of crystalline defects in base-leaching of H-ZSM-5 was reported recently on nano-sized ZSM-5 crystals, making the visualization of crystalline defects a relevant topic for zeolite chemistry.^[37,38] The presented methodology can be used to qualitatively visualize interparticle differences in uptake of the probe molecule. These become obvious for H-ZSM-5-MT crystals where different crystals can have strikingly different reactivity, most probably due to large differences in surface porosity and diffusion resistance (Figures 5.9c,d).

5.3.9 Solvent effects in 1-butanol

In order to control the high reactivity of 4-methoxystyrene we have also attempted to use 1-butanol as a polar solvent. While 4-methoxystyrene reacted readily with the Brønsted acid sites of H-ZSM-5-P in a 1.5 mM (0.02 vol%) solution in n-heptane, hardly any catalytic turnovers were observed in a highly concentrated 2.5 M (33.3 vol%) solution in 1-butanol. The fluorescence response was clearly different with respect to n-heptane, with extremely low reactivity mostly observed at the edges of a zeolite H-ZSM-5 crystal (Figures 5.10a,b). An examination of numerous crystals

confirmed very low to no observable single molecule formation under the studied reaction conditions. However, after one day we observed significant accumulation of the single molecule products along the sinusoidal pores of the crystal tips (Figure 5.10c). This subunit region of the zeolite crystal is more accessible, as molecules diffuse via the straight pores that are open to the surface.^[18]

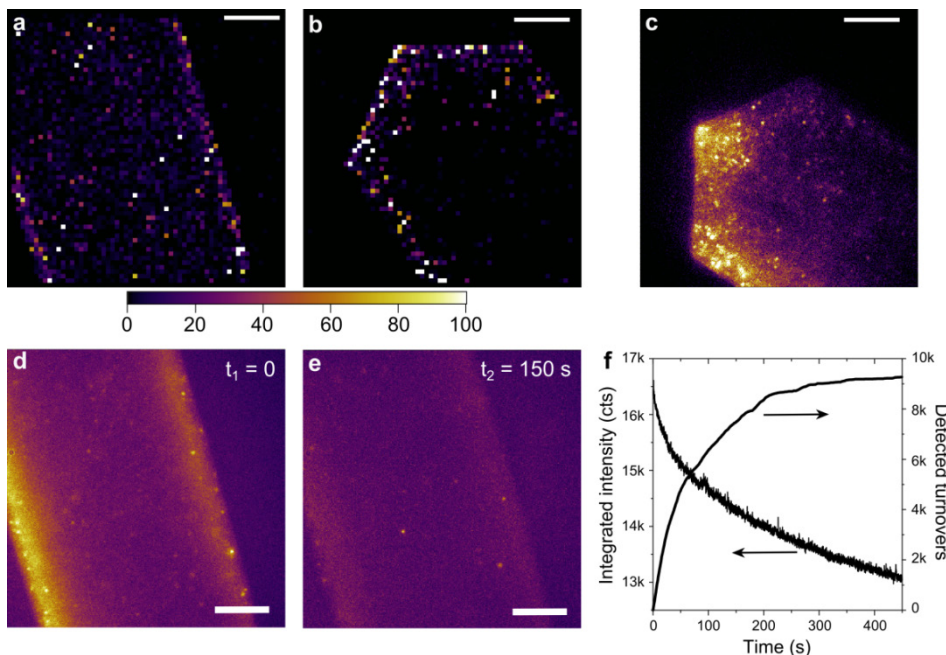


Figure 5.10 The oligomerization of 4-methoxystyrene in 1-butanol (2.5 M). Accumulated high-resolution maps of reactivity for parent H-ZSM-5-P zeolite crystals recorded at a) the middle of the zeolite crystal, b) the edge of the zeolite crystal. c) Fluorescence response recorded after one day for $Z = 4\text{ }\mu\text{m}$. d,e) Fluorescence response recorded at the middle of a zeolite H-ZSM-5-P crystal at d) $t = 0$, and e) $t = 150\text{ s}$ from the start of the recording; I frame = 100 ms. f) Integrated total fluorescence background intensity and the number of detected turnovers with time, as measured for the crystal in (b). Scale bars are 5 μm .

The majority of fluorescence emitters in n-butanol were easily photobleached within 300 ms. At the beginning of the experiment, high background fluorescence is typically recorded in the near-edge regions as compared to the middle (Figure 5.10d). The initial fluorescence signal vanishes after 150 s due to fast photobleaching of individual fluorescent molecules (Figures 5.10e) – a process that is not compensated by the newly formed products. The analyses of the number of detected turnovers and the average fluorescence background signal confirm this observation (Figure 5.10f).

Only the initially present fluorescent reaction products were observed, but after the molecules were photobleached, the rate of reaction seemed to be very low.

The tremendous change in reactivity is due to the strong chemisorption of 1-butanol at Brønsted acid sites. This solvent is known to occupy 96% of the zeolite volume with about 2 molecules per acid site (measured for a Si/Al ratio of 72).^[39] The close packing of 1-butanol molecules is due to their strong interaction with Brønsted acid sites but also due to favorable interactions of the hydrocarbon chain with the zeolite wall.^[40] Heptane on the other hand has a similar pore filling as butanol^[41] for the same reasons of C-H/zeolite wall interactions, but does not interact strongly with the Brønsted acid sites. The strong stoichiometric interaction of 1-butanol with acid sites is the main reason for the observed low reactivity of 4-methoxystyrene. This effect of solvent, measurable at the single molecule level, indicates several orders of magnitude lower reactivity when polar solvents are used. Similar tests in dioxane did not yield any visible photo-products. In line with our results, Yoon et al. have reported in their bulk experiments a full conversion of styrene in dichloromethane over zeolite H-Y powder, and no evidence of reaction in tetra-hydrofuran or acetonitrile.^[42]

5.3.10 Single molecule fluorescence spectroscopy of 4-fluorostyrene carbocations

The universality of the styrene oligomerization probe reaction presented in this Chapter can be extended successfully to any other para-styrene-substituted probe molecule. In this way a broad range of reaction conditions can be achieved considering the large difference in reactivity between differently substituted derivatives. For example, the oligomerization of 4-fluorostyrene requires significantly higher activation energy for the protonation of the double bond due to the low stability of the carbocationic intermediate.^[19] The UV-Vis and fluorescence microscopy were not sensitive to record any catalytic activity for 4-fluorostyrene oligomerization at room temperature. Therefore, only higher reaction temperatures were used in previous studies.^[18,20] Instead, the fluorescent products of 4-fluorostyrene oligomerization can be readily detected at room temperature by using single molecule fluorescence microscopy. This is shown for the edge (Figure 5.11a) and the middle of an H-ZSM-5-P crystal (Figure 5.11b). The response changed significantly in 1-butanol, as the reaction rate was very low. Interestingly, the fluorescent products were only detected at

the edges of the zeolite crystal in the direction of the sinusoidal pores (Figures 5.11c,d).

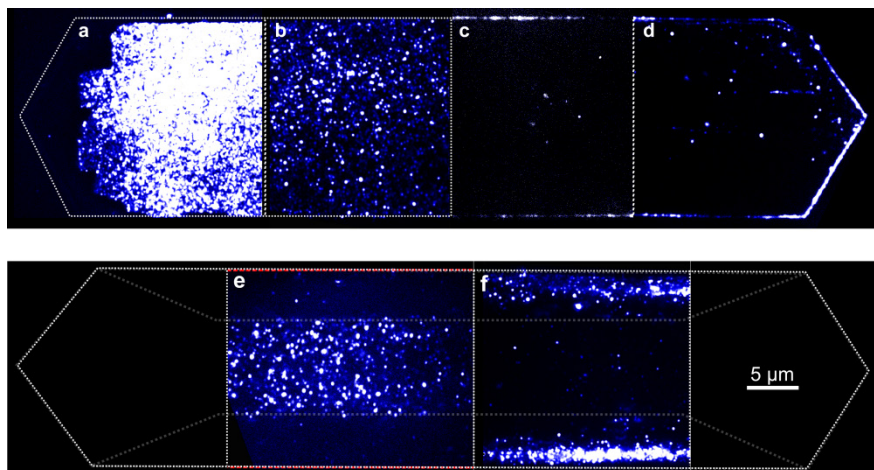


Figure 5.11 a-d) Comparison of fluorescence activities of 4-fluorostyrene recorded at the surface of H-ZSM-5-P zeolite crystals ($Z = 0$). Fluorescence activity is recorded at a) the edge in n-heptane, b) the middle in n-heptane, c) the middle in 1-butanol, and d) the edge in 1-butanol. e,f) Fluorescence activity recorded at $Z = 4 \mu\text{m}$ for e) H-ZSM-5-P zeolite crystal, and f) H-ZSM-5-MT zeolite crystal. The SOFI images are reconstructed based on fluorescent movies of photoactivity. Brighter the color, the more photoactive the region of interest. The dotted lines indicate the edges and subunit boundaries ($Z = 4 \mu\text{m}$) of the imaginary zeolite crystal.

Imaging of the crystalline interior is readily possible due to the absence of solvent molecules, as illustrated in Figures 5.11e for zeolite H-ZSM-5-P crystal. Visible fluorescence of the formed carbocations clearly follows the intergrowth structure of the zeolite crystal, indicating that the transition dipole moments of detected fluorescent products are aligned along the straight pores the crystal. However, the response changes significantly for the steamed H-ZSM-5-MT crystals, indicating that steaming had clearly affected the crystallinity and accessibility of the side subunits (Figure 5.11f). The results presented in Figure 5.11 are in line with the observations made with 4-methoxystyrene. The only substantial difference is that 4-fluorostyrene does not form the highly photostable fluorescent products at the crystalline imperfections, which we attribute to its lower tendency to form trimeric species at room temperature.

5.3.11 Quantification of the fluorescent emitters in different solvent environments

Single molecule fluorescence microscopy can be considered as a quantitative technique provided that conditions for efficient localization of fluorescent molecules are met. As explained in Chapter 3, by using the localization algorithm that takes into account the existence of the photostable events, it was possible to estimate the averaged turnover frequencies recorded in the studied oligomerization reactions. For simplicity we have considered any single molecule event to be one catalytic turnover. The results are summarized in Figure 5.12.

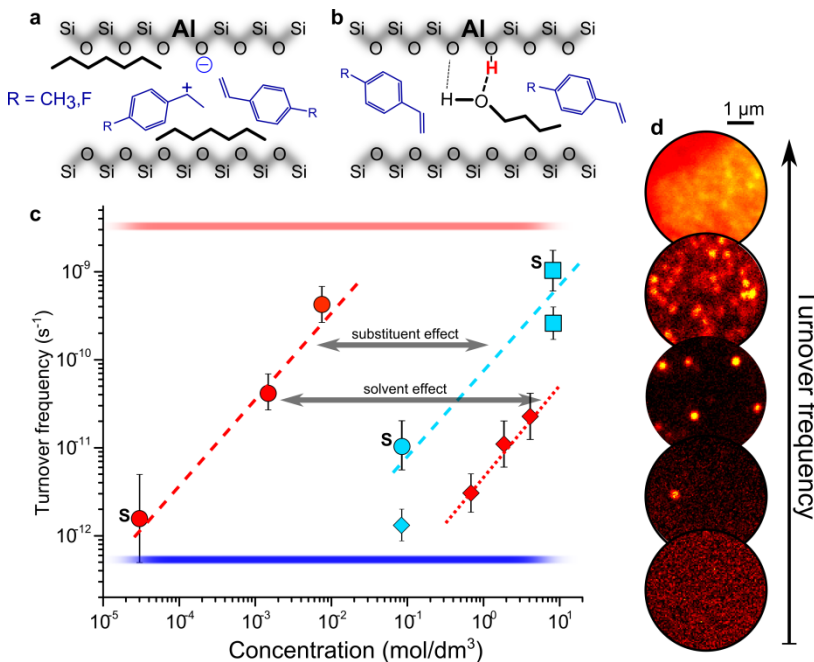


Figure 5.12 a,b) Schematic of the styrene oligomerization reaction in presence of a) n-heptane, and b) 1-butanol. c) Reactivity of 4-methoxystyrene (in red) and 4-fluorostyrene (in blue) as probe molecules for single molecule imaging in n-heptane (circles) and 1-butanol (rhombi). The squares represent 99% pure 4-fluorostyrene. Averaged turnover frequencies of the parent H-ZSM-5-P and steamed zeolite H-ZSM-5-MT crystals (denoted as "S") were recorded close to the outer surface of the single crystals. The concentration axis denotes the concentration of the probe molecules in the solvents. d) Frames indicating the density of the individual emitters and an approximate level of reactivity for corresponding turnover frequencies.

The calculated TOF numbers are presented as a function of the concentration of probe molecules and indicate the range of concentrations that enable quantification under single molecule fluorescence microscopy conditions. The maximum recorded

rate of photoproduct formation is in the order 10 events $\mu\text{m}^{-3} \text{s}^{-1}$, which translates to TOF values in the order of 10^{-8} s^{-1} (the red line in Figure 5.12). The low TOF numbers of 10^{-12} s^{-1} (the blue line Figure 5.12a) indicate the detection rate of < 0.01 events per $\mu\text{m}^3 \text{s}^{-1}$.

Obviously, a concentration range for successful single molecule fluorescence imaging of zeolites will depend on the reactivity of a probe molecule (the substituent effect) and the polarity of a solvent (the solvent effect). In both cases the oligomerization rate is determined by the tendency of the reactant to form the initial benzylic and dimeric carbocations. The role of solvent here is crucial, as polar solvents can strongly interact with Brønsted acid sites, as illustrated for the reactions in n-heptane (Figure 5.12a) and 1-butanol (Figure 5.12b). The oligomerization of 4-methoxystyrene at room temperature in zeolite H-ZSM-5 proceeds much faster than in the case of 4-fluorostyrene, as visible from the comparison of their reactivity in heptane (Figure 5.12c). Therefore, a successful single molecule fluorescence microscopy imaging of reactive zeolite H-ZSM-5 crystals with 4-methoxystyrene should include a high dilution of the reactant (10^{-5} - 10^{-2} M in n-heptane). In contrast, the experiments with 4-fluorostyrene can routinely be performed with the pure reagent (8.3 M) for at least 30 min, even for the highly acidic zeolite H-ZSM-5. The change of solvent from n-heptane to 1-butanol significantly inhibits the oligomerization of both compounds.

The estimated TOF values do not represent equilibrated values for reactivity of single particles, due to the time-dependent and diffusion-limited measurements. Based on the presented results, it is clear that the practical limit of the technique does not allow quantification of the majority of acid sites. Instead, the quantitative single molecule fluorescence approach relies on the accurate comparison of reaction rates recorded in a certain time frame, which ultimately determine the rate constants in the low-concentration regimes. It should also be noted that if the products are efficiently localized, lateral localization precision of single molecule fluorescence is at best 10-15 nm, which implies that the unambiguous quantification below this spatial limit is not yet possible.

5.4 Conclusions

The oligomerization of 4-methoxystyrene and 4-fluorostyrene at Brønsted acid sites of the parent H-ZSM-5-P and steamed H-ZSM-5-MT zeolite crystals was studied with single molecule fluorescence microscopy. The formation of the linear dimeric and trimeric carbocations has been experimentally confirmed by UV-Vis and confocal fluorescence microscopy. The fluorescent species could be distinguished by their photostability. It was found that the formation of bulkier, highly photostable, trimeric fluorescent species of 4-methoxystyrene predominantly proceeds at defect-rich zones and easily accessible Brønsted acid sites at the outer surface of zeolite H-ZSM-5. The method is further used to assess the highly accessible crystalline defects of H-ZSM-5-P and H-ZSM-5-MT. The formation of fluorescent species can be controlled by the polarity of a solvent medium. The reaction was severely hindered in 1-butanol, leading to several orders of magnitude lower single turnover rates as compared to results obtained in n-heptane. The conclusion made based on 4-methoxystyrene probe reaction were further validated by using less reactive 4-fluorostyrene. With this, we establish a quantitative single molecule fluorescence microscopy methodology that can operate in the conditions of extremely low and high concentrations of probe molecules and in various solvent environments.

Acknowledgements

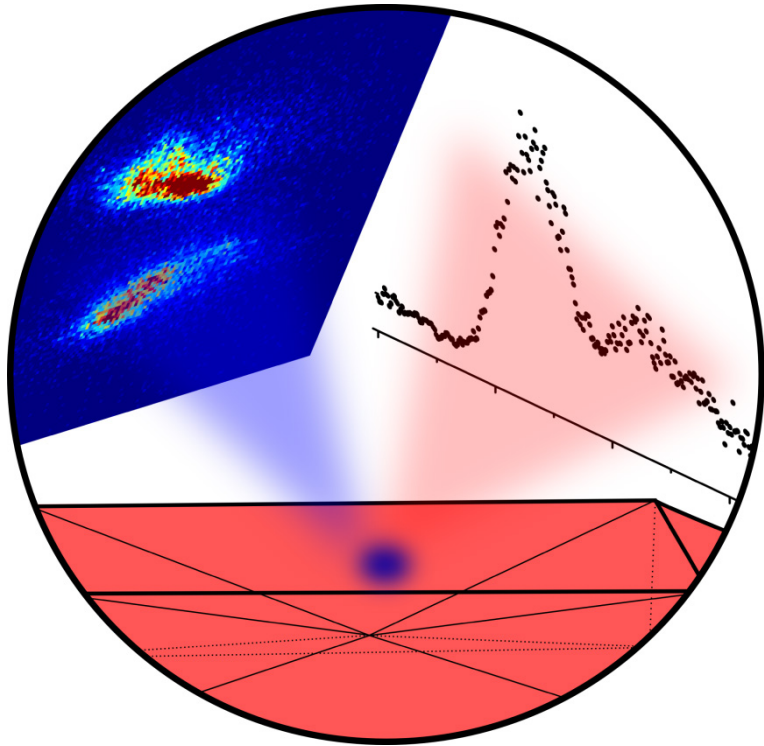
Dr. Gert de Cremer (KU Leuven) is acknowledged for his help with the single molecule fluorescence experiments and related discussions. Dr. Rasmus Brogaard (University of Oslo), Dr. Diego Valencia, Dr. Hendrik van der Bij, and Jarich Heitjema (all from Utrecht University), and are kindly acknowledged for numerous discussions related to the styrene chemistry taking place within zeolite H-ZSM-5.

References

- [1] M. B. J. Roeffaers, B. F. Sels, H. Uji-i, F. C. De Schryver, P. A. Jacobs, D. E. De Vos, J. Hofkens, *Nature* **2006**, *439*, 572–575.
- [2] M. B. J. Roeffaers, G. De Cremer, J. Libeert, R. Ameloot, P. Dedecker, A.-J. Bons, M. Bückins, J. A. Martens, B. F. Sels, D. E. De Vos, J. Hofkens, *Angew. Chem. Int. Ed.* **2009**, *48*, 9285–9289.
- [3] K.-L. Liu, A. V. Kubarev, J. Van Loon, H. Uji-i, D. E. De Vos, J. Hofkens, M. B. J. Roeffaers, *ACS Nano* **2014**, *8*, 12650–12659.

- [4] K. P. F. Janssen, G. D. Cremer, R. K. Neely, A. V. Kubarev, J. V. Loon, J. A. Martens, D. E. De Vos, M. B. J. Roeffaers, J. Hofkens, *Chem. Soc. Rev.* **2014**, *43*, 990–1006.
- [5] T. Cordes, S. A. Blum, *Nat. Chem.* **2013**, *5*, 993–999.
- [6] P. Chen, X. Zhou, H. Shen, N. M. Andoy, E. Choudhary, K.-S. Han, G. Liu, W. Meng, *Chem. Soc. Rev.* **2010**, *39*, 4560–4570.
- [7] W. Xu, J. S. Kong, Y.-T. E. Yeh, P. Chen, *Nat. Mater.* **2008**, *7*, 992–996.
- [8] N. M. Andoy, X. Zhou, E. Choudhary, H. Shen, G. Liu, P. Chen, *J. Am. Chem. Soc.* **2013**, *135*, 1845–1852.
- [9] T. Tachikawa, T. Majima, *Chem. Soc. Rev.* **2010**, *39*, 4802–4819.
- [10] G. D. Cremer, B. F. Sels, D. E. De Vos, J. Hofkens, M. B. J. Roeffaers, *Chem. Soc. Rev.* **2010**, *39*, 4703–4717.
- [11] I. L. C. Buurmans, B. M. Weckhuysen, *Nat. Chem.* **2012**, *4*, 873–886.
- [12] B. M. Weckhuysen, *Angew. Chem. Int. Ed.* **2009**, *48*, 4910–4943.
- [13] M. M. Kerssens, C. Sprung, G. T. Whiting, B. M. Weckhuysen, *Microporous Mesoporous Mater.* **2014**, *189*, 136–143.
- [14] M. B. J. Roeffaers, B. F. Sels, H. Uji-i, B. Blanpain, P. L’hoëst, P. A. Jacobs, F. C. De Schryver, J. Hofkens, D. E. De Vos, *Angew. Chem. Int. Ed.* **2007**, *46*, 1706–1709.
- [15] M. H. F. Kox, A. Mijovilovich, J. J. H. B. Sättler, E. Stavitski, B. M. Weckhuysen, *ChemCatChem* **2010**, *2*, 564–571.
- [16] G. T. Whiting, F. Meirer, D. Valencia, M. M. Mertens, A.-J. Bons, B. M. Weiss, P. A. Stevens, E. de Smit, B. M. Weckhuysen, *Phys. Chem. Chem. Phys.* **2014**, 21531–21542.
- [17] G. T. Whiting, F. Meirer, M. M. Mertens, A.-J. Bons, B. M. Weiss, P. A. Stevens, E. de Smit, B. M. Weckhuysen, *ChemCatChem* **2015**, *7*, 1312–1321.
- [18] M. H. F. Kox, E. Stavitski, B. M. Weckhuysen, *Angew. Chem. Int. Ed.* **2007**, *46*, 3652–3655.
- [19] E. Stavitski, M. H. F. Kox, B. M. Weckhuysen, *Chem. – Eur. J.* **2007**, *13*, 7057–7065.
- [20] C. Sprung, B. M. Weckhuysen, *J. Am. Chem. Soc.* **2015**, *137*, 1916–1928.
- [21] A. Corma, H. García, *J. Chem. Soc. Dalton Trans.* **2000**, 1381–1394.
- [22] M. H. F. Kox, E. Stavitski, J. C. Groen, J. Pérez-Ramírez, F. Kapteijn, B. M. Weckhuysen, *Chem. – Eur. J.* **2008**, *14*, 1718–1725.
- [23] I. L. C. Buurmans, E. A. Pidko, J. M. de Groot, E. Stavitski, R. A. van Santen, B. M. Weckhuysen, *Phys. Chem. Chem. Phys.* **2010**, *12*, 7032–7040.
- [24] L. R. Aramburo, S. Wirick, P. S. Miedema, I. L. C. Buurmans, F. M. F. de Groot, B. M. Weckhuysen, *Phys. Chem. Chem. Phys.* **2012**, *14*, 6967–6973.
- [25] D. Mores, E. Stavitski, S. P. Verkleij, A. Lombard, A. Cabiac, L. Rouleau, J. Patarin, A. Simon-Masseron, B. M. Weckhuysen, *Phys. Chem. Chem. Phys.* **2011**, *13*, 15985–15994.
- [26] I. L. C. Buurmans, J. Ruiz-Martínez, S. L. van Leeuwen, D. van der Beek, J. A. Bergwerff, W. V. Knowles, E. T. C. Vogt, B. M. Weckhuysen, *Chem. – Eur. J.* **2012**, *18*, 1094–1101.
- [27] M. A. Karreman, I. L. C. Buurmans, J. W. Geus, A. V. Agronskaia, J. Ruiz-Martínez, H. C. Gerritsen, B. M. Weckhuysen, *Angew. Chem. Int. Ed.* **2012**, *51*, 1428–1431.
- [28] M. A. Karreman, I. L. C. Buurmans, A. V. Agronskaia, J. W. Geus, H. C. Gerritsen, B. M. Weckhuysen, *Chem. – Eur. J.* **2013**, *19*, 3846–3859.
- [29] P. Castaño, J. Ruiz-Martínez, E. Epelde, A. G. Gayubo, B. M. Weckhuysen, *ChemCatChem* **2013**, *5*, 2827–2831.
- [30] F. L. Cozens, R. Bogdanova, M. Régimbald, H. García, V. Martí, J. C. Scaiano, *J. Phys. Chem. B* **1997**, *101*, 6921–6928.

- [31] V. Fornés, H. García, V. Martí, L. Fernández, *Tetrahedron* **1998**, *54*, 3827–3832.
- [32] M. B. J. Roeffaers, R. Ameloot, M. Baruah, H. Uji-i, M. Bulut, G. De Cremer, U. Müller, P. A. Jacobs, J. Hofkens, B. F. Sels, D. E. De Vos, *J. Am. Chem. Soc.* **2008**, *130*, 5763–5772.
- [33] L. R. Aramburo, L. Karwacki, P. Cubillas, S. Asahina, D. A. M. de Winter, M. R. Drury, I. L. C. Buurmans, E. Stavitski, D. Mores, M. Daturi, P. Bazin, P. Dumas, F. Thibault-Starzyk, J. A. Post, M. W. Anderson, O. Terasaki, B. M. Weckhuysen, *Chem. – Eur. J.* **2011**, *17*, 13773–13781.
- [34] L. Karwacki, M. H. F. Kox, D. A. Matthijs de Winter, M. R. Drury, J. D. Meeldijk, E. Stavitski, W. Schmidt, M. Mertens, P. Cubillas, N. John, A. Chan, N. Kahn, S. R. Bare, M. Anderson, J. Kornatowski, B. M. Weckhuysen, *Nat. Mater.* **2009**, *8*, 959–965.
- [35] S. van Donk, A. H. Janssen, J. H. Bitter, K. P. de Jong, *Catal. Rev.* **2003**, *45*, 297–319.
- [36] L. Karwacki, D. A. M. de Winter, L. R. Aramburo, M. N. Lebbink, J. A. Post, M. R. Drury, B. M. Weckhuysen, *Angew. Chem. Int. Ed.* **2011**, *50*, 1294–1298.
- [37] D. Fodor, F. Krumeich, R. Hauert, J. A. van Bokhoven, *Chem. – Eur. J.* **2015**, *21*, 6272–6277.
- [38] D. Fodor, A. Beloqui Redondo, F. Krumeich, J. A. van Bokhoven, *J. Phys. Chem. C* **2015**, *119*, 5447–5453.
- [39] M. T. Aronson, R. J. Gorte, W. E. Farneth, D. White, *Langmuir* **1988**, *4*, 702–706.
- [40] C. M. Nguyen, M.-F. Reyniers, G. B. Marin, *Phys. Chem. Chem. Phys.* **2010**, *12*, 9481–9493.
- [41] D. H. Olson, G. T. Kokotailo, S. L. Lawton, W. M. Meier, *J. Phys. Chem.* **1981**, *85*, 2238–2243.
- [42] K. B. Yoon, J. L. Lim, J. K. Kochi, *J. Mol. Catal.* **1989**, *52*, 375–386.



Chapter 6 is based on the following manuscript:

"X-ray Excited Optical Fluorescence and Diffraction Imaging of Chemical Reactivity and Crystallinity in a Zeolite Crystal: Crystallography and Molecular Spectroscopy in One X-ray Shot", Z. Ristanović, J. P. Hofmann, M.-I. Richard, T. Jiang, G. A. Chahine, T. U. Schülli, F. Meirer, and B. M. Weckhuysen, submitted.

Chapter 6

X-ray Excited Optical Fluorescence and Diffraction Imaging of Chemical Reactivity and Crystallinity in a Zeolite Crystal: Crystallography and Molecular Spectroscopy in One X-ray Shot

Abstract

Hard X-rays were used to generate sub-micrometer resolved, X-ray diffraction (μ -XRD) and X-ray excited optical fluorescence (μ -XEOF) intensity maps of individual zeolite crystals stained with 4-methoxystyrene. We demonstrate the feasibility of recording X-ray excited visible spectra of the fluorescent organic molecules formed at the Brønsted acid sites of a steamed zeolite H-ZSM-5-ST crystal. The chemical reactivity derived from the μ -XEOF intensity maps was spatially correlated with local crystallinity as determined by μ -XRD. The highest XEOF signal was recorded from the inner crystalline regions with preserved and accessible Brønsted acid sites. The concentration of the cyclic and linear dimeric species was subsequently used as a fluorescent marker of crystallinity and the extent of crystalline defects induced by steaming. The crystalline lattice of the steamed zeolite crystals was found to contract significantly along the sinusoidal pores, suggesting more severe dealumination in this crystallographic direction. The results illustrate the promising potential of this novel approach to simultaneously resolve the crystallographic structure of a porous host material and its reactivity via X-ray induced fluorescence of organic probe molecules.

6.1 Introduction

With the advance of modern synchrotron techniques it has become increasingly important to fully exploit the micro-spectroscopic potential of X-rays for catalytic studies at different length scales.^[1-11] Ideally, the potential benefits of X-rays should be combined with optical microscopy and spectroscopy to provide more complete information about the structure and performance of a catalyst. Only in this way the important information from e.g. X-ray absorption, emission, and diffraction could be complemented with the information from the UV-Vis spectral region often used in material characterization. Because the energies of both soft and hard X-rays are well above the energies of valence electron transitions in molecules, it is not always of high value to introduce optical spectroscopy techniques to a synchrotron toolbox. Here we demonstrate that such a possibility is still within reach by utilizing only one X-ray beam as the excitation source.

In previous chapters we have discussed the effects of mild and severe steaming of zeolite H-ZSM-5 crystals on their structure (Chapter 2), reactivity (Chapter 3), and surface accessibility (Chapter 5). These measurements were performed independently from each other, so no direct structure-reactivity relationship could be derived from the individual zeolite crystals. However, the structural and compositional properties of zeolite H-ZSM-5- crystals may have a vast impact on the success of different steaming post-treatments. Therefore, the connection between the structure and reactivity of different crystalline domains is essential for understanding overall performance of single catalyst particles. In this Chapter we take our work one step further and present a novel micro-spectroscopic approach based on μ -XRD imaging combined with μ -X-ray excited optical fluorescence (XEOF) used to simultaneously obtain a spatially resolved, structure-performance relationship of a model zeolite H-ZSM-5 crystal. The local zeolite crystallinity, as measured by XRD, is correlated with the local presence of Brønsted acidity, as measured by XEOF. As discussed in Chapter 5, upon the protonation of 4-methoxystyrene on H-ZSM-5, colored oligomeric carbocations are formed revealing the location of Brønsted acid sites and their accessibility.^[12,13] For this study we have utilized steamed H-ZSM-5-ST crystals to evaluate the scope of our μ -XRD/XEOF approach and its potential advantages and limitations to study zeolite catalyst particles. We simultaneously monitor the changes in the crystalline structure

of H-ZSM-5-ST crystals and their fluorescence due to the presence of colored oligomeric molecules in the vicinity of Brønsted acid sites. With this novel approach we are able to establish structure-reactivity relationship from localized crystalline regions in a catalyst material using solely X-rays as the excitation source.

X-ray excited optical fluorescence (XEOF) is a process of photo-emission in the optical region (UV-Vis, NIR) when a sample is excited by X-rays.^[14,15] Absorption of X-rays and inelastic scattering (energy loss) are the two possible mechanisms that provide energy for XEOF. The latter mechanism is dominant in the case of organic molecules (containing light elements) excited by hard X-rays. During inelastic scattering of X-rays, a large number of photo- and Auger electrons thermalize in the solid via cascade energy loss.^[14] These processes eventually lead to a radiative recombination of electrons (in LUMO orbitals) and holes (in HOMO orbitals) in organic molecules.^[14–16] Recently, numerous approaches were developed at synchrotrons to utilize the XEOF emission of visible light for micro-spectroscopic studies, mostly on quantum dots and wires.^[17–23] XEOF is frequently used as one of the methods to record X-ray absorption spectra by detection of visible photons.^[21,23–25] In certain cases, soft X-rays, commonly used for the excitation of the light elements, can be attenuated by the sample, but the optical signal can still be collected and gives (sub-)surface sensitive information.^[23,24] X-ray absorption spectra of organic molecules have also been measured using XEOF detection at the absorption edges of light elements.^[16,26]

Our method makes use of a less common approach to excite electronic transitions in organic molecules by hard X-rays and simultaneously resolve crystallographic parameters of zeolite H-ZSM-5. We believe that this method has a potential to combine spectroscopic information from X-rays (e.g., X-ray diffraction and absorption) and visible light for *in-situ* experiments under relevant reaction conditions. The high penetration power of hard X-rays and the benefits of detecting visible light could improve simplicity, speed and the sensitivity of detection. Obviously, this approach offers a lot of potential for studying catalytic solids, and in particular zeolite crystals stained with fluorescent molecules, which will be the topic of this Chapter.

6.2 Experimental

6.2.1 Materials

The parent H-ZSM-5-P and steamed H-ZSM-5-ST zeolite crystals were prepared as described in the Experimental Section of Chapter 2. Prior to use the crystals were activated at 723 K (0.7 K/min) for 6 h.

6.2.2 Experimental details

The experiments were performed at ID01 beamline of European Synchrotron Radiation Facility (ESRF) in Grenoble, France. Hard X-rays (8.5 keV) focused to a spot size of 500 nm were used for the simultaneous diffraction and XEOF imaging of a labeled zeolite H-ZSM-5 single crystal. The footprint of the beam was projected throughout the whole crystalline volume, with approximately 20 μm optical path in the axial direction. The emitted fluorescence light was collected via a 0.2 mm optical fiber and directed to a 300 mm focal length Czerny-Turner spectrograph (Andor Shamrock 300i) equipped with 150 lines/mm grating and a Peltier cooled highly sensitive EM-CCD camera (Andor Newton 970). The optical fiber was attached to the sample stage of the goniometer via a separate piezo X,Y,Z positioning stage with the travel range of 100 μm . Once the collection of light was optimized, the fiber was kept in the fixed geometry with respect to a zeolite crystal. An additional CCD camera was used to detect the weak fluorescence light and to align the X-ray beam with respect to the selected zeolite crystal and optical fiber. Diffracted X-rays were collected under Bragg conditions using a 2-D Maxipix X-ray detector in Bragg-Brentano diffraction geometry. The characteristic (16 0 0) and (0 16 0) reflections of single zeolite crystals were detected prior to a 2-D scan, as described in Chapter 2. Neutral density filters were used to minimize the damage of X-rays before XEOF mapping.

Combined 2-D μ -XEOF and μ -XRD maps were generated using a piezo driven scanning stage in x-y direction. The X-ray beam and the exposure time of the detector were synchronized with the external trigger, resulting in 2 s of excitation with X-ray beam and 1.95 s of acquisition time of XEOF signal per collection point. The collected XEOF signal was further enhanced by full vertical binning and additional horizontal binning of 4 adjacent pixels at high electron-multiplier gain of the EMCCD camera. During 2-D XEOF scans both the crystal and optical fiber were

kept in the fixed relative position on the sample stage, thus the collection efficiency of the fiber was constant during experiments. A raster scan with piezo steps of typically 4 μm in X and Y was performed for the collection of XEOF intensity maps. The μ -XRD intensity maps were collected by using fast diffraction scanning (K-map) developed at ID01, as described by Chahine *et al.*^[27] The 2-D mapping was typically performed in steps of 2 μm and 20-50 ms per collection point. The diffraction rocking maps were further collected by changing the incident angle of the beam and repeating X-Y scans for 10-15 rocking angles in a fast scanning mode. The μ -XRD/XEOF maps have thus been taken during the separate scans.

6.2.3 Data treatment

The 2-D μ -XEOF intensity maps were made by using home-build routines in *Matlab 2013a* (*MathWorks*). For each X,Y collection point a full XEOF spectrum was acquired and its integration (or deconvolution) within defined wavelengths, resulted in μ -XEOF intensity maps. Diffraction intensity maps were reconstructed by using XSOCS software written in the Python script language and developed at ESRF for the analysis of fast diffraction scanning data. A graphical interface for XSOCS has been developed using the PyGTK library.^[27] The diffraction response within a defined 20° region of interest was integrated over all incident angles as a function of X,Y coordinates of the piezo stage, yielding μ -XRD intensity maps.

Single-pixel XEOF spectra were deconvoluted by using simple Gaussian functions, fitted to the XEOF spectra in curve fitting toolbox (*Matlab R2013a*). Three Gaussian functions were centered at (530 ± 10) nm, (600 ± 20) nm, and (675 ± 5) nm with corresponding full widths at half maximum of (60 ± 8) nm, (50 ± 8) nm, and (67 ± 16) nm, respectively. An optimization procedure was applied to the data set by varying the positions and widths of Gaussian functions within the defined boundaries until the best fits were reached.

Principal component analysis (PCA) was performed on both the XEOF and the XRD data sets. PCA reduces dimensionality of the data space by describing the data set in a way which best explains the total data's variance. This is done whilst preserving the relevant information and without using any *a priori* knowledge about the characteristics of the variations.^[28,29] By choosing the amount of variance covered by the first N principal components (cumulative variance explained, CVE) it is

possible to reduce the dimensionality of the data set to fewer dimensions without losing significant information but effectively reducing noise. The reduced data set is then represented in N-dimensional PC space where k-means clustering^[30] was performed to pool pixels according to their (Euclidean) distances from cluster centers (centroid linkage method), effectively grouping pixels with similar spectra. This resulted in an effective image segmentation based on the spectral similarity of the measurement points.

The XEOF data set was constructed based on separate 2-D images each recorded at a specific wavelength channel. The 2-D diffractograms at each X,Y point were reconstructed by integration of the detector response with steps of 0.015°-0.05° in 20. Therefore both data sets consisted of a spectrum (XEOF spectrum or XRD diffractogram) in each point of the raster scan. Each data set formed a matrix ($I \times p$) where I denotes the intensity in the spectrum and p the pixel in the image. With each of those data matrices PCA and subsequent k-means clustering was performed separately to identify common spectral features and their distribution within the sample.

6.2.4 Staining of zeolite H-ZSM-5 single crystals

4-methoxystyrene (97%, Sigma-Aldrich) was used as a probe molecule for the oligomerization reaction. The zeolite crystals were exposed to 4-methoxystyrene vapor for 45 min (H-ZSM-5-P) and 4 h (H-ZSM-5-ST) in a closed glass container at room temperature.

6.3 Results and Discussion

6.3.1 Combined μ -XRD/XEOF imaging of a single zeolite H-ZSM-5 crystal

A scheme of the experimental setup that combines μ -XRD and μ -XEOF imaging of a single zeolite H-ZSM-5 crystal is illustrated in Figure 6.1a. We used a diffraction setup in the Bragg-Brentano diffraction geometry capable of spatially resolved diffraction experiments with high angular resolution (Figure 6.1b). An optical fiber for the collection of the XEOF signal was placed in the close proximity to the sample stage at approximately 200-300 μm distance (Figure 6.1c). Similarly to the experiment

described in Chapter 2, the diffracted X-rays were collected only for the specific (16 0 0) and (0 16 0) Bragg reflections (Figure 6.1d).

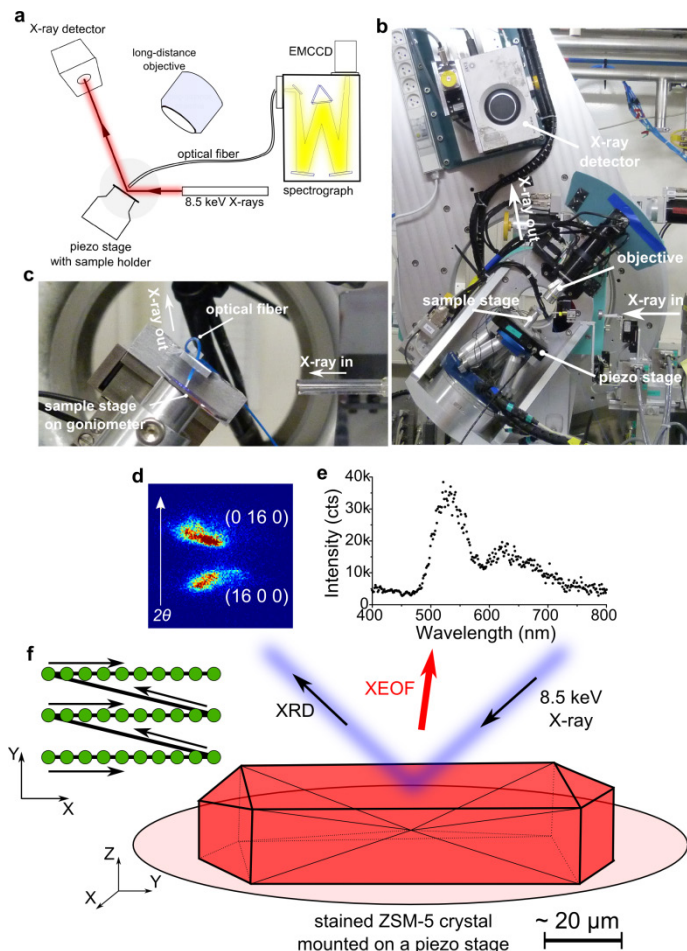


Figure 6.1 a) Schematic of the experimental setup used for the combined μ -XRD/XEOF study. X-rays were focused down to a 500 nm spot to excite styrene oligomers and generate visible fluorescence collected with the optical fiber; diffracted X-rays were detected by the X-ray detector. b) Photograph of the setup showing the real geometry of the diffraction experiment. c) Zoom-in into the sample stage with the optical fiber attached. d) Typical response of the X-ray detector upon detection of the characteristic (16 0 0) and (0 16 0) Bragg reflections. e) XEOF optical spectrum detected with the UV-Vis spectrograph. f) An X-Y scanning pattern used to acquire spatially resolved μ -XRD/XEOF intensity maps.

Upon the interaction of X-rays with the stained H-ZSM-5-ST crystal, the excitation of the formed 4-methoxystyrene oligomers takes place along the beam trajectory, which results in a XEOF spectrum (Figure 6.1e). A highly sensitive spectral detection was essential to collect the emitted light, considering the intrinsically low

concentration of fluorescent species and a 500 nm diameter of the X-ray excitation beam. The resulting fluorescence is related to the accessible and reactive Brønsted acid sites, where the formation of different fluorescent oligomers takes place, according to the mechanism already described in Chapter 5. As a compromise between the sampling frequency and scanning time, the spatially-correlated maps were acquired in steps of 2 μ m for diffraction (20-50 ms exposure time) and 4 μ m for XEOF (1.95 s exposure time) with the typical X-Y scanning pattern presented in Figure 6.1f.

6.3.2 Properties of X-ray excited optical fluorescence

The origin of the XEOF signal was verified in a series of control experiments related to the gas-phase oligomerization of 4-methoxystyrene. This compound readily colors zeolite H-ZSM-5 crystals at room temperature and the reaction appeared to be a convenient staining method for Brønsted acid sites. Unlabeled zeolite crystals, both in the templated and acidic form, did not show any emission of the XEOF signal in the absence of probe molecules. Figure 6.2a presents a spatially resolved XEOF intensity map for a stained zeolite H-ZSM-5-P crystal. The intensity map reflects a large heterogeneity in reactivity that is a consequence of structural defects visible in the optical image of the crystal (Figure 6.2b). The XEOF response matches well with the recorded wide-field fluorescence and confocal fluorescence microscopy map of the same zeolite H-ZSM-5-P crystal (Figures 6.2b,c). We note a small spatial broadening of the fluorescence intensities from the XEOF intensity map which originates from the geometry of the μ -XEOF experiment and relatively large scanning steps (4 μ m per acquisition point). Based on the remarkable spatial and spectral similarities between the μ -XEOF and confocal fluorescence microscopy results, we concluded that the oligomeric carbocationic species, formed upon reaction at Brønsted acid sites, are responsible for the observed XEOF signal.

Alike the laser-induced photobleaching of fluorescent molecules studied in Chapter 3, high energy X-rays turned out to cause an irreversible damage to the organic probe molecules, as it was confirmed later by the additional confocal fluorescence microscopy measurement. The parallel stripes in Figure 6.2c indicate the direction and damage caused by the X-ray beam. The damage may be considered localized as the mean-free path of photo-electrons defined by their thermalization path (estimated to be in order of 10 nm) may be considered too small as compared to the

size of the X-ray beam.^[14] Under the studied experimental conditions, the XEOF emission was characterized by the exponential decay of the fluorescence signal, with the decay time constant of 4.5 s (Figure 6.2d). Although the decay of the XEOF signal was irreversible, the photobleaching of the XEOF emission did not affect our results, as the beam was sampling a new point in space every 2 s. The decay of the XEOF signal exhibited a clear dose-dependent behavior, as it was affected by the exposure time (Figure 6.2e) and the intensity of the X-ray beam (Figure 6.2f). The measured XEOF yield turned out to be intrinsically low, as only the highest achievable intensity of X-rays (order of 10^9 photons per s) was sufficient to generate a reasonable quality of XEOF spectra.

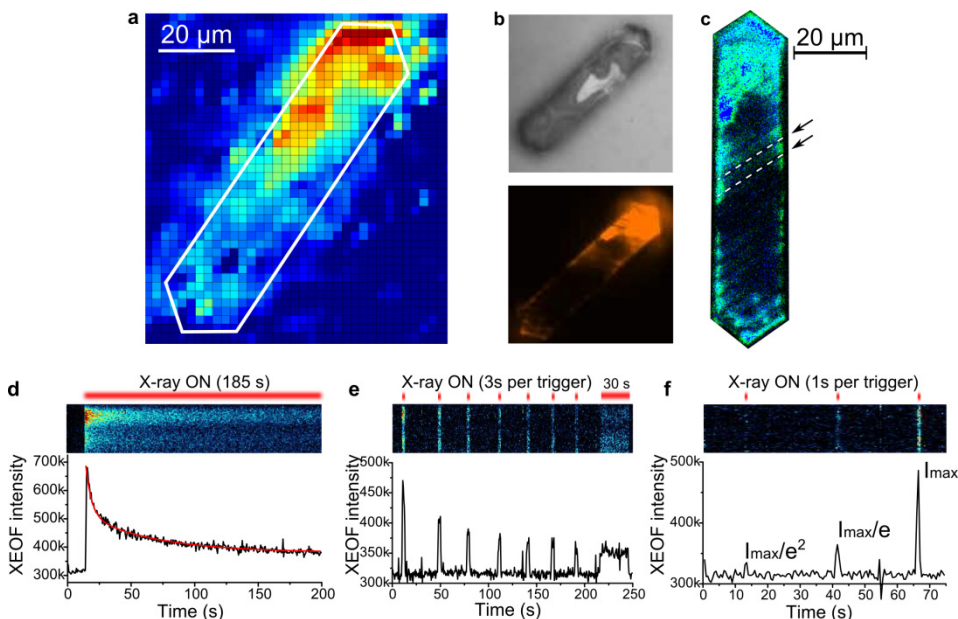


Figure 6.2 Properties of the XEOF emission and the photobleaching effect. a) μ -XEOF image of an H-ZSM-5 crystal stained with 4-methoxystyrene. b) Wide-field optical (top) and fluorescence image (bottom) of the crystal. c) Confocal fluorescence microscopy image of the crystal recorded 7 days after the XEOF measurement. The parallel dark stripes indicate irreversible beam damage; the arrows indicate the direction of an X-ray beam. d) Integrated intensity decay of the XEOF signal with constant exposure to X-rays, as measured on an agglomerate of H-ZSM-5-ST crystals. The exponential fit (red line) has a time constant of $t = 4.5 \pm 0.3$ s. e) Integrated intensity decay of the XEOF signal with the 3 s long pulsed exposure to the X-ray beam. f) XEOF signal response to X-rays of different intensity, with 1 s of the beam exposure. Spectral maps at the top of (d-f) represent the response of the detector for denoted exposure times. The red lines indicate that the beam was switched on.

6.3.3 X-ray diffraction analysis of a zeolite H-ZSM-5-ST single crystal

The crystallographic architecture and Al zoning of zeolite H-ZSM-5-P crystals was studied in detail in Chapter 2. In this Chapter we opted to investigate a deliberately chosen steamed zeolite H-ZSM-5-ST crystal with a more complex intergrowth structure, as visible from the optical micrograph of the crystal (Figure 6.3a).

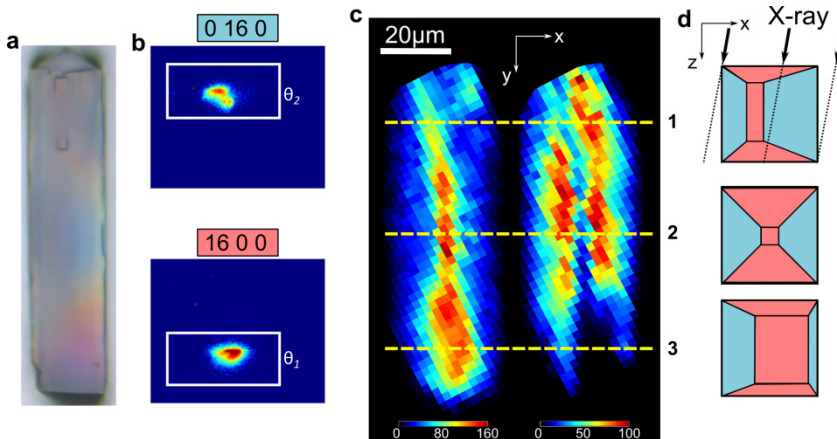


Figure 6.3 μ -XRD imaging of a zeolite H-ZSM-5-ST crystal. a) Optical micrograph of the crystal indicating an irregular intergrowth structure of the crystal. b) Typical X-ray detector responses for the studied $(16\ 0\ 0)$ and $(0\ 16\ 0)$ reflections. c) Spatial distribution of the diffraction signals for $(16\ 0\ 0)$ reflection (left) and $(0\ 16\ 0)$ reflection (right). The 2-D intensity maps are intentionally rotated for clarity. The yellow lines denote the cross-sections shown in (d). d) Top: exposure of the different crystallographic subunits along the optical path of an X-ray beam; the side dotted lines illustrate the effect of the image broadening. Each scheme depicts a vertical (X-Z) cross-section from the yellow lines in (c).

The 90° intergrowth of the crystal seems to be interconnected in an anomalous manner, as compared to the model explained in Chapter 2. The spatial distribution of the crystallographic phases was resolved by detecting the higher order $(16\ 0\ 0)$ and $(0\ 16\ 0)$ Bragg reflections (Figure 6.3b). Integrating the contributions of each reflection for a given range of X,Y positions resulted in the spatially resolved μ -XRD intensity maps. The obtained spatially resolved diffraction information reveals the highly heterogeneous distribution of the crystalline phases, indicating the asymmetrical crystal growth (Figure 6.3 c). The intensity of the diffraction signal is proportional to the total crystalline volume that is probed by the X-ray beam, which can give an indication of the phase abundance and crystallinity. The mapped diffraction responses are essentially related to the growth of the crystalline phases along the a and b crystallographic directions. The contribution of each phase in the

diffraction signal will depend on the orientation of the phase with respect to the optical path of the X-ray beam, as illustrated in Figure 6.3d. As the symmetry of the crystal is known, the complementary information about both 90° intergrown phases can be extracted from the recorded diffractograms. For example, one side of the zeolite H-ZSM-5-ST crystal was predominantly occupied by the phase that gives rise to the (0 16 0) reflection (cross section 1, the blue phase in Figure 6.3d), whereas the other side of the crystal was dominated by the 90° rotated crystalline phase (cross section 3, the red phase in Figure 6.3d). The resolved crystallography reveals an irregular intergrowth structure, where one crystallographic phase may grow at the expense of the other, which is not in accordance with the two-component model. In what follows, we will discuss how the observed anomaly in the crystalline growth may affect the reactivity and accessibility of the studied zeolite H-ZSM-5-ST crystal.

6.3.4 X-ray excited optical fluorescence analysis of a H-ZSM-5-ST single crystal

The zeolite H-ZSM-5-ST crystal presented in Figure 6.3 was tested to the XEOF response in the visible region by collecting X-ray excited fluorescence light during a raster scan of the crystal. An averaged XEOF spectrum summed over all collected data points is shown in Figure 6.4a (top). An intense emission band with the highest intensity in all XEOF spectra appeared at around 530 nm, followed by the two less intense bands at around 615 nm and 670 nm. The latter appeared to be slightly red shifted (up to 20 nm) as compared to the confocal fluorescence microscopy spectra (600 and 650 nm) of the same species (Figure 5.3). These two emission bands have been previously attributed to the linear dimeric and trimeric species that are confined along the straight pores of H-ZSM-5-P.^[12,13,31] The higher energy XEOF band at 530 nm is assigned to the cyclic dimeric species, which are formed in the defect-like, mesoporous voids of the steamed H-ZSM-5-ST crystals. Several indications point towards this conclusion. Unlike the lower energy bands, the band at 530 nm was not detected in the XEOF experiments with H-ZSM-5-P crystals. Furthermore, Fornes et al.^[32] and Stavitski et al.^[31] have reported the UV-Vis absorption band at 490 nm originating from the cyclic carbocations, which is about 40 nm shift as compared to the detected XEOF emission band. The same species are reported to be formed at the near-surface acid sites and crystalline defects induced by steaming, as shown in the studies with 4-fluorostyrene as a probe molecule.^[13,33,34] Therefore, the XEOF spectra

can be used to provide more information about the accessible Brønsted acid sites and related micro- and mesoporosity in the steamed H-ZSM-5-ST sample.

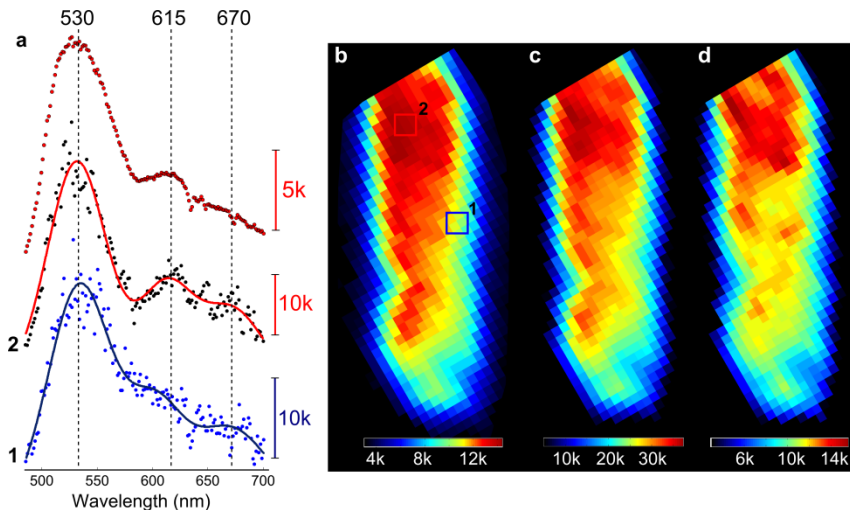


Figure 6.4 μ -XEOF imaging of the zeolite H-ZSM-5-ST crystal (from Figure 6.3) stained with 4-methoxystyrene. a) Examples of the XEOF spectra: bottom – spectrum 1 taken from the blue square region indicated in (b), middle – spectrum 2 taken from the red square region indicated in (b), top – total XEOF spectrum averaged over all measured emission spectra. b) Averaged μ -XEOF total intensity map; the color bar represents the average number of counts per pixel. c) μ -XEOF intensity map at 530 nm (cyclic species). d) μ -XEOF intensity map at around 610 nm (linear dimeric species). (c) and (d) are plotted based on the amplitudes of the fitted Gaussians.

The partial dealumination of the zeolite H-ZSM-5-ST crystals resulted in the formation of mesopores and more accessible crystalline bulk, which is confirmed by the amount of the abundantly present cyclic species. However, the intensities of the corresponding emission bands of the linear dimeric and cyclic species were dependent on the position along the crystal. This is illustrated in Figure 6.4a for the two XEOF spectra taken from the positions with different XEOF intensities (as indicated in Figure 6.4b). The two spectra differ in the intensity and position of the band at around 610 nm that is attributed to the linear dimeric species. We note that the position of the emission maximum around 610 nm changes depending on the total intensity of the XEOF signal. The emission maximum was typically around 615 nm for the highly reactive domains (e.g., spectrum 2 in Figure 6.4a), and shifted towards higher energies (600 nm) for the domains with lower XEOF intensity (e.g., spectrum 1 in Figure 6.4a). This characteristic spectral signature was noted earlier in the experiments with 4-fluorostyrene for the same types of carbocationic species.^[13] We

attribute the observed shift to the confinement of the closely packed linear dimeric carbocations within the pores of H-ZSM-5. The formation of excimer-like complexes between the adjacent linear dimeric carbocations could explain the measured trend.^[14]

The spectral information recorded at each point of the X-Y scan can be presented as a 2-D μ -XEOF intensity map of the fluorescence activity (Figure 6.4b). The map shows a notable gradient in XEOF intensity towards the bottom side of the crystal. We conclude that steaming has unevenly affected different parts of the crystal, as the total XEOF intensity will depend on the crystallinity/dealumination degree of the analyzed H-ZSM-5-ST domains. To resolve the differences in the positions and amplitudes of the emission bands we have applied the Gaussian deconvolution of the XEOF spectra, by fitting the XEOF spectra with three Gaussians centered around emission maxima at 530, 610, and 670 nm, as presented for the spectra in Figure 6.4a. The spatially resolved maps of the band intensities are shown in Figure 6.4c (for the cyclic species) and Figure 6.4d (for the linear dimeric species). The derived intensity maps look similar to the averaged μ -XEOF intensity map (Figure 6.4b). This is expected considering the similarities in the XEOF spectra shown in Figure 6.4a. The gradient in the intensity of the XEOF signal and changes in the emission spectra along the crystal require a more detailed look into the spatially correlated information between the recorded μ -XRD/XEOF data sets.

6.3.5 Correlation between μ -XRD and μ -XEOF spatially resolved maps

The strength of the combined μ -XRD/XEOF approach developed in this Chapter is the possibility to correlate the spatially resolved information about the crystallinity and chemical reactivity of the zeolite domains. This information is collected by using one X-ray beam as the excitation source. As both μ -XRD and μ -XEOF intensity maps were recorded in the nearly identical incident geometry, their corresponding intensities will originate from the identical crystalline regions along the optical path of the X-ray beam. However, the information extracted from the μ -XRD/XEOF intensity maps may not necessarily be complementary. Firstly, the XRD signal originates from only one of the two 90° intergrown subunits, whereas the XEOF intensity originates from the both types of subunits. Secondly, the complementarity will largely depend on the crystallinity of the sample and accessibility/reactivity of Brønsted acid sites. For example, the XEOF intensity in the parent zeolite H-ZSM-5-

P crystals depends largely on the accessibility of the individual subunits; thus, high crystallinity may result in the low XEOF intensity. This effect will be significantly less pronounced in steamed H-ZSM-5-ST crystals due the higher accessibility of the crystalline domains.

The spatially correlated information from the μ -XRD/XEOF measurement of the steamed zeolite H-ZSM-5-ST crystal is shown in Figure 6.5. Seven different points were chosen along the crystal (Figure 6.5a) to show the recorded XRD diffractograms (Figure 6.5b) and corresponding XEOF spectra (Figure 6.5c). The diffractograms in Figure 6.5b differ in the intensities and positions of the diffraction maxima for both measured reflections. The positions of diffraction peaks translate directly into the strain in the crystal lattice that is imposed by Al enrichment/depletion. The contribution of each individual reflection for a given (X,Y) position indicates the existence of at least two crystalline phases with significantly different framework Al content, making the analysis complicated.

Principal component analysis (PCA) turned out to be a convenient analytical method to further classify the recorded data sets according to their spectral features. The method provides (1) a clustering of pixels having similar spectra without using *a priori* knowledge about the spectra themselves, and (2) average spectra of the different phases present in the sample. PCA of the XRD data set divided the 2-D diffraction intensity map into five clusters that have distinct diffraction features, which are represented by different colors in Figure 6.5d. The color-coded diffractograms in Figure 6.5b represent the spectral information characteristic for each cluster. A close inspection of the diffractograms suggests that PCA divided the crystal based on the intensities of the (16 0 0) and (0 16 0) reflections. Naturally, this division has a physical meaning. The outer regions of the H-ZSM-5-ST crystal (the blue clusters #4 and #5 in Figure 6.5d) show significantly lower intensities of both reflections and notable broadening of the (0 16 0) peak. These observations point towards dealumination of the outer, Al-rich region, and a visible loss of crystallinity. The (0 16 0) peak is notably shifted towards higher d-spacings (lower 2θ values), as visible from the single pixel diffractograms #4 and #5 in Figure 6.5b. Interestingly, a maximum of the (16 0 0) peak seems to be shifted in the opposite direction towards higher 2θ values, meaning lower d-spacings.

The inner clusters, depicted in orange (#2, #3a, #3b) and red (#1) in Figures 6.5b,d, show more preserved crystallinity as compared to the outer regions. A very distinct feature is the green cluster (#6 in Figures 6.5b,d) that is a highly crystalline domain with the lowest d-spacing for (16 0 0) reflection, which is an indication of the Al-poor phase that is more resistant to steaming. PCA used in this study was performed on non-normalized diffraction and fluorescence data sets; therefore, the resulting analysis provided intensity-based clustering, because the dominant feature in the spectra is the overall intensity. In order to improve sensitivity towards spectral features it might be beneficial to use normalized spectra for future analyses.

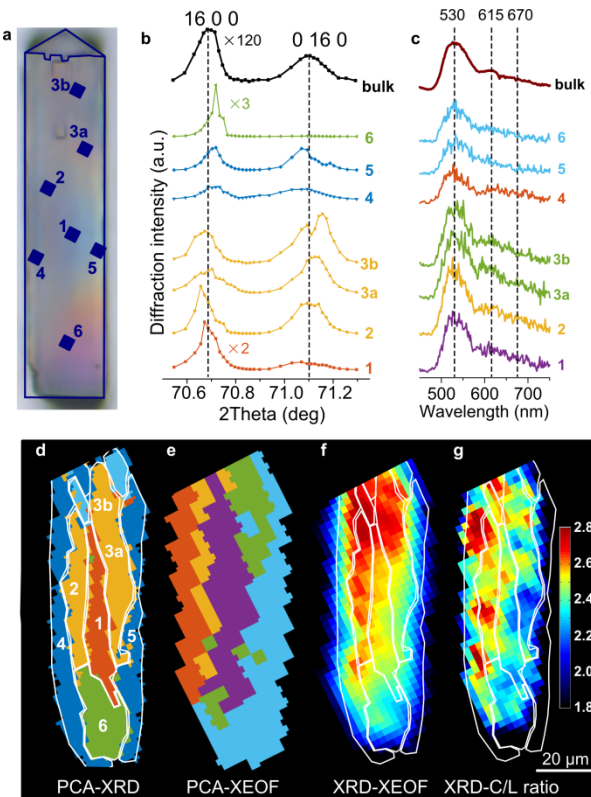


Figure 6.5 Spatial correlation between the 2-D μ -XRD/XEOF intensity maps measured for the zeolite H-ZSM-5-ST crystal. a) Optical micrograph with the approximate positions of the seven sampling points used to present the single-pixel diffractograms (b) and the XEOF spectra (c). b) Diffractograms of the regions of interest labeled in (a). The color-coding corresponds to the PCA-XRD clusters presented in (d). c) XEOF spectra of the regions of interest labeled in (a). The color-coding corresponds to the PCA-XEOF clusters presented in (e). d) PCA cluster map of the μ -XRD data set. The numbers denote the points used in (b) and (c). e) PCA cluster map of the μ -XEOF data set. f,g) Overlay of the PCA-XRD clustered regions shown in (d) and the μ -XEOF intensity maps for the cyclic species (f) and a cyclic-to-linear intensity ratio (g).

The crystallographic complexity of the studied zeolite H-ZSM-5-ST crystal is further reflected by its reactivity, and consequently, by the recorded XEOF response. A PCA-XEOF cluster map in Figure 6.5e divides the crystal into five spectrally distinct regions. The spectral signatures from clustered regions are presented as the color-coded XEOF spectra in Figure 6.5c. The applied intensity based clustering essentially divides the crystalline domains based on the intensities of the dominant emission bands in the XEOF spectra. A closer look into the spectral features (presented also in Figure 6.4a) indicates that the major changes in XEOF spectra are in the intensities of the emission bands originating from the cyclic and linear dimeric species. For the highly reactive zeolite domains the concentration of the cyclic species is higher, with the observed red shift in the emission maximum of the linear dimeric carbocations. The regions of lower reactivity contain a higher concentration of the linear dimeric species in respect to the cyclic species, which is expected for the domains that are less affected by steaming.

The effect of the crystalline structure on the reactivity of zeolite H-ZSM-5-ST domains can be explained by the overlay of the XRD cluster map from Figure 6.5d and the corresponding, integrated μ -XEOF intensity map of the cyclic species, as shown in Figure 6.5f. The most intense XEOF signal is recorded from the inner regions of the H-ZSM-5-ST crystal (clusters #1-3 in Figure 6.5d). These regions represent the most catalytically active domains, due to preserved acidity and induced mesoporosity. The lower XEOF intensity can be spatially correlated with the dealuminated outer shell (clusters #4 and #5 in Figure 6.5d) and the highly crystalline, but Al-poor, domain represented by the green cluster #6 in Figure 6.5d. Our analysis shows that even the domains belonging to the same clusters may have different diffractograms and XEOF spectra. Note that the average spectra of clusters depend on the resolution of the clustering (i.e. the number of clusters used) and will not necessarily provide pure chemical/crystallographic phases. As described earlier, the XEOF intensity ratio of the cyclic and linear dimeric species can be used as an indication of the extent of reactivity that is determined by the crystallinity and accessibility of the zeolite domains, as shown in the intensity map of this ratio (Figure 6.5g). The higher concentration of the cyclic species in respect to linear dimers correlates well with the total XEOF intensity and the loss of crystallinity in the crystal.

6.3.6 Influence of steaming and Al zoning on the lattice parameters of H-ZSM-5

So far we have shown that the results of μ -XRD cannot be interpreted in terms of a simple relation between the shifts in lattice parameters and the extent of dealumination. The first reason is related to the presence of the intergrowth structure and distinctly different crystallographic phases that may be unevenly affected by steaming. The second reason is the inherently inhomogeneous distribution of Al within the parent zeolite H-ZSM-5-P crystals. During steaming, the outer Al-rich phase is more prone to dealumination than the inner Al-poor crystalline domains.^[35–37] The correct interpretation of the results critically depends on understanding the effects of the crystal architecture and Al concentration on the extent of dealumination. The strength of the described synchrotron-based μ -XRD approach is visible when comparing the individual diffractograms in Figure 6.5b with the total diffraction intensity typically observed in the bulk experiments. The appearance of many distinct phases may pass unnoticed in an ensemble averaged measurement. Therefore, the results from Figure 6.5 should be ideally placed in the general context of the spatially resolved, structural, and reactivity changes of the studied zeolite H-ZSM-5-ST crystal.

In Chapter 2 we have discussed Al zoning of H-ZSM-5-P crystals where both a and b lattice parameters showed the expansion of the crystal lattice due to increased Al content in the outer layers of the parent H-ZSM-5-P crystals. The question arises whether this strain in the crystal lattice is maintained after steaming. The 2-D maps of the a and b lattice parameters are presented in Figure 6.6. The positions of the (16 0 0) and (0 16 0) reflections were determined by fitting their peak profiles, such as the ones in Figure 6.5b, with single Gaussians. We obtain averaged information about the relative shifts of the diffraction peaks. The results indicate a notable dilation of the b lattice parameter at the edges of the crystal as compared to the inner regions (Figure 6.6b), while this characteristic pattern is not observed for the a lattice parameter (Figure 6.6a). This is an indication that steaming has caused uneven crystallographic changes along the straight and sinusoidal pores of the zeolite H-ZSM-5-ST crystal. The broadening of the (0 16 0) peak was significant only at the edges of the crystal (0.14° in 2θ measured at the FWHM). The broadening of the (16 0 0) diffraction peak was less pronounced, reaching a maximum of approximately 0.08° in 2θ at FWHM.

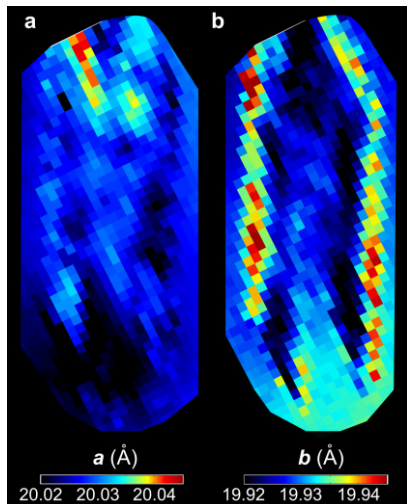


Figure 6.6 2-D strain maps of the lattice parameters a and b as measured from the peak positions of a) $(16\ 0\ 0)$ and b) $(0\ 16\ 0)$ reflections. The positions represent averaged values over the domains with different crystallinity.

It is interesting to compare the lattice parameters of the H-ZSM-5-P and H-ZSM-5-ST crystals as measured by μ -XRD. The crystal lattice of H-ZSM-5-P expands at the outer rim in both a and b directions due to Al zoning, with the lattice parameters of $a = 20.10 \pm 0.02 \text{ \AA}$ and $b = 19.92 \pm 0.02 \text{ \AA}$ (measured for two parent crystals). Upon steaming these parameters change to $a = 20.03 \pm 0.02 \text{ \AA}$ and $b = 19.93 \pm 0.02 \text{ \AA}$ (measured for two steamed crystals). The comparison of these values suggests a significant change in the a lattice parameter, meaning the crystal lattice contraction along the sinusoidal pores. The values of the b lattice parameter did not change significantly, within the accuracy of the method. Therefore, it seems tempting to suggest that dealumination mostly leads to large crystallographic changes along the sinusoidal pores. HR-SEM studies of Karwacki and Aramburo indicated the unidirectional nature of mesopores which mostly run along the sinusoidal pores in the main subunits of H-ZSM-5-ST.^[38,39] In addition, the authors found that the sinusoidal zeolite channels are much more susceptible towards dealumination, which explains our μ -XRD findings. Nevertheless, it remains unclear whether this effect is due to the higher resistance to steaming of Brønsted acid sites in the straight pores, or due to the intrinsically lower concentration of Al along the straight pores. Further studies should concentrate more on the role of Al zoning in the dealumination and the

impact of the different crystallographic architectures of the model zeolite H-ZSM-5 crystals.

6.4 Conclusions

The presented μ -XRD/XEOF approach combines two spectroscopic worlds in a single X-ray shot. We have demonstrated that hard X-rays can be used to acquire information from both X-ray and visible spectral regions when studying the impact of the crystalline structure and mesoporous defects of zeolite H-ZSM-5-ST on its Brønsted reactivity. The study demonstrates that the local reactivity of a single zeolite crystal can be studied simultaneously with the changes in its local crystalline structure and that the intraparticle differences in reactivity are the consequence of the underlying crystalline structure. This principle was illustrated for a steamed H-ZSM-5-ST crystal, leading to a significantly different spatial distribution of fluorescent species that are further differentiated by their chemical nature and the occupancy of micro- and mesopores. This important structure-reactivity relationship is difficult to study by other characterization techniques. The developed method has the potential to substantiate the structural and spectral properties of other functional materials under relevant reaction conditions.

Acknowledgements

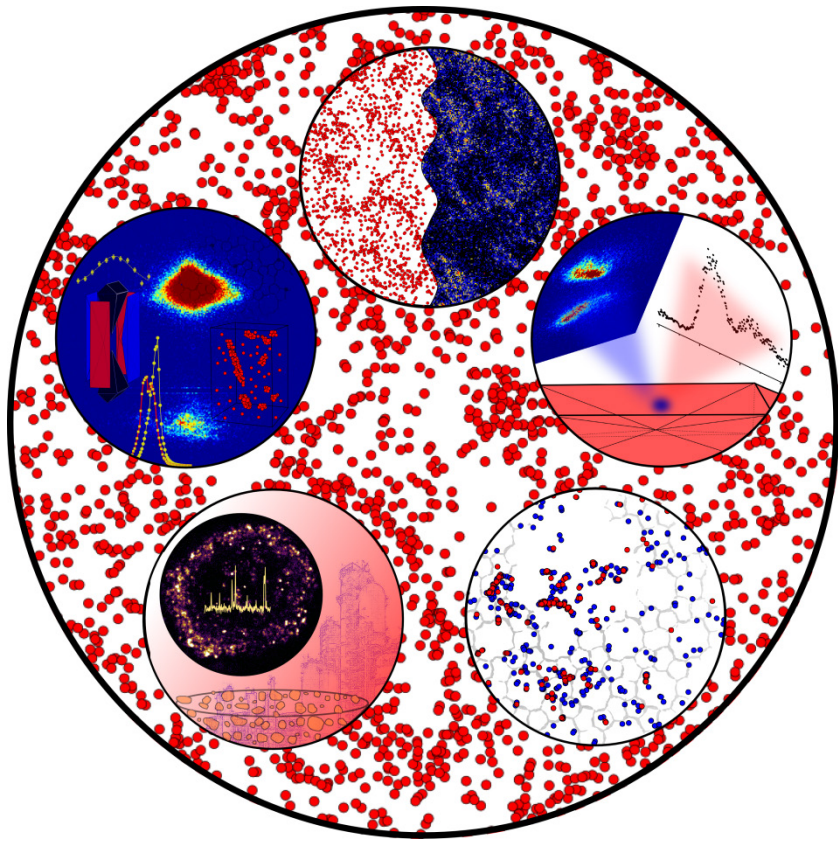
Dr. Dina Carbone, Dr. Marta Elzo-Aizarna, Genziana Bussone, and Raphael Grifone (ID01, ESRF) are acknowledged for their assistance and help with the beamtime. Dr. Gareth Whiting and Dr. Christoph Sprung (both from Utrecht University) are thanked for help with the experiments. Dr. Machteld Mertens (ExxonMobil) is thanked for providing the ZSM-5 crystals.

References

- [1] J. Gustafson, M. Shipilin, C. Zhang, A. Stierle, U. Hejral, U. Ruett, O. Gutowski, P.-A. Carlsson, M. Skoglundh, E. Lundgren, *Science* **2014**, *343*, 758–761.
- [2] D. Franz, S. Runte, C. Busse, S. Schumacher, T. Gerber, T. Michely, M. Mantilla, V. Kilic, J. Zegenhagen, A. Stierle, *Phys. Rev. Lett.* **2013**, *110*, 065503.
- [3] S. D. M. Jacques, M. Di Michiel, S. A. J. Kimber, X. Yang, R. J. Cernik, A. M. Beale, S. J. L. Billinge, *Nat. Commun.* **2013**, *4*, 2536.
- [4] J.-D. Grunwaldt, C. G. Schroer, *Chem. Soc. Rev.* **2010**, *39*, 4741–4753.

- [5] D. S. Wragg, M. G. O'Brien, F. L. Bleken, M. Di Michiel, U. Olsbye, H. Fjellvåg, *Angew. Chem. Int. Ed.* **2012**, *51*, 7956–7959.
- [6] Z. Ristanović, B. M. Weckhuysen, *Angew. Chem. Int. Ed.* **2014**, *53*, 8556–8558.
- [7] A. M. Beale, S. D. M. Jacques, B. M. Weckhuysen, *Chem. Soc. Rev.* **2010**, *39*, 4656–4672.
- [8] J. Ruiz-Martínez, A. M. Beale, U. Deka, M. G. O'Brien, P. D. Quinn, J. F. W. Mosselmans, B. M. Weckhuysen, *Angew. Chem. Int. Ed.* **2013**, *52*, 5983–5987.
- [9] F. Meirer, S. Kalirai, D. Morris, S. Soparawalla, Y. Liu, G. Mesu, J. C. Andrews, B. M. Weckhuysen, *Sci. Adv.* **2015**, *1*, e1400199.
- [10] F. Meirer, D. T. Morris, S. Kalirai, Y. Liu, J. C. Andrews, B. M. Weckhuysen, *J. Am. Chem. Soc.* **2015**, *137*, 102–105.
- [11] W. Cha, N. C. Jeong, S. Song, H. Park, T. C. Thanh Pham, R. Harder, B. Lim, G. Xiong, D. Ahn, I. McNulty, et al., *Nat. Mater.* **2013**, *12*, 729–734.
- [12] M. H. F. Kox, E. Stavitski, B. M. Weckhuysen, *Angew. Chem. Int. Ed.* **2007**, *46*, 3652–3655.
- [13] C. Sprung, B. M. Weckhuysen, *J. Am. Chem. Soc.* **2015**, *137*, 1916–1928.
- [14] T. K. Sham, *J. Electron Spectrosc. Relat. Phenom.* **2015**, *204*, 196–207.
- [15] T. K. Sham, R. Sammynaiken, Y. J. Zhu, P. Zhang, I. Coulthard, S. J. Naftel, *Thin Solid Films* **2000**, *363*, 318–321.
- [16] P.-S. G. Kim, N. O. Petersen, T. K. Sham, Y. F. Hu, *Chem. Phys. Lett.* **2004**, *392*, 44–49.
- [17] R. A. Rosenberg, S. Zohar, D. Keavney, R. Divan, D. Rosenmann, A. Mascarenhas, M. A. Steiner, *Rev. Sci. Instrum.* **2012**, *83*, 073701.
- [18] G. Martínez-Criado, B. Alén, J. A. Sans, A. Hom, I. Kieffer, R. Tucoulou, P. Cloetens, J. Segura-Ruiz, J. Susini, J. Yoo, et al., *Nucl. Instrum. Methods Phys. Res. B* **2012**, *284*, 36–39.
- [19] S. Larcheri, F. Rocca, F. Jandard, D. Pailharey, R. Graziola, A. Kuzmin, J. Purans, *Rev. Sci. Instrum.* **2008**, *79*, 013702.
- [20] N. R. J. Poolton, B. M. Towlson, B. Hamilton, D. A. Evans, *Nucl. Instrum. Methods Phys. Res. Sect. B Beam Interact. Mater. At.* **2006**, *246*, 445–451.
- [21] D. Pailharey, Y. Mathey, F. Jandard, S. Larcheri, F. Rocca, A. Kuzmin, R. Kalendarev, J. Purans, G. Dalba, R. Graziola, et al., *J. Phys. Conf. Ser.* **2007**, *93*, 012038.
- [22] G. Martínez-Criado, A. Hom, B. Alén, J. A. Sans, J. Segura-Ruiz, A. Molina-Sánchez, J. Susini, J. Yoo, G.-C. Yi, *Nano Lett.* **2012**, *12*, 5829–5834.
- [23] P.-J. Sabbe, M. Dowsett, M. Hand, R. Grayburn, P. Thompson, W. Bras, A. Adriaens, *Anal. Chem.* **2014**, *86*, 11789–11796.
- [24] M. G. Dowsett, A. Adriaens, G. K. C. Jones, N. Poolton, S. Fiddy, S. Nikitenko, *Anal. Chem.* **2008**, *80*, 8717–8724.
- [25] Z. Wang, X. Guo, T.-K. Sham, *Nanoscale* **2014**, *6*, 6531–6536.
- [26] V. Maiorano, F. Matino, R. Cingolani, J. Thompson, R. I. R. Blyth, *J. Synchrotron Radiat.* **2005**, *12*, 690–695.
- [27] G. A. Chahine, M.-I. Richard, R. A. Hom-Regojo, T. N. Tran-Caliste, D. Carbone, V. L. R. Jacques, R. Grifone, P. Boesecke, J. Katzer, I. Costina, et al., *J. Appl. Crystallogr.* **2014**, *47*, 762–769.
- [28] I. T. Jolliffe, *Principal Component Analysis*, Springer, New York, **2004**.
- [29] J. E. Jackson, *A User's Guide to Principal Components*, Wiley-Interscience, Hoboken, **2003**.
- [30] J. MacQueen, in *Proc. 5-Th Berkeley Symp. Math. Stat. Probab.*, University Of California, **1967**, pp. 281–297.
- [31] E. Stavitski, M. H. F. Kox, B. M. Weckhuysen, *Chem. – Eur. J.* **2007**, *13*, 7057–7065.

- [32] V. Fornés, H. García, V. Martí, L. Fernández, *Tetrahedron* **1998**, *54*, 3827–3832.
- [33] I. L. C. Buurmans, E. A. Pidko, J. M. de Groot, E. Stavitski, R. A. van Santen, B. M. Weckhuysen, *Phys. Chem. Chem. Phys.* **2010**, *12*, 7032–7040.
- [34] L. R. Aramburo, S. Wirick, P. S. Miedema, I. L. C. Buurmans, F. M. F. de Groot, B. M. Weckhuysen, *Phys. Chem. Chem. Phys.* **2012**, *14*, 6967–6973.
- [35] S. M. Campbell, D. M. Bibby, J. M. Coddington, R. F. Howe, R. H. Meinholt, *J. Catal.* **1996**, *161*, 338–349.
- [36] T. Sano, N. Yamashita, Y. Iwami, K. Takeda, Y. Kawakami, *Zeolites* **1996**, *16*, 258–264.
- [37] T. Sano, H. Ikeya, T. Kasuno, Z. B. Wang, Y. Kawakami, K. Soga, *Zeolites* **1997**, *19*, 80–86.
- [38] L. Karwacki, D. A. M. de Winter, L. R. Aramburo, M. N. Lebbink, J. A. Post, M. R. Drury, B. M. Weckhuysen, *Angew. Chem. Int. Ed.* **2011**, *50*, 1294–1298.
- [39] L. R. Aramburo, L. Karwacki, P. Cubillas, S. Asahina, D. A. M. de Winter, M. R. Drury, I. L. C. Buurmans, E. Stavitski, D. Mores, M. Daturi, et al., *Chem. – Eur. J.* **2011**, *17*, 13773–13781.



Chapter 7

Summary, Concluding Remarks and Future Perspectives

7.1 Summary

The central theme of this PhD thesis is the chemistry of zeolite H-ZSM-5 studied at the level of single particles, molecules, and atoms. The crystallographic and atomic structure of zeolite H-ZSM-5 crystals were studied by micro-diffraction imaging (μ -XRD), time-of-flight secondary ion mass spectrometry (TOF-SIMS), and atom probe tomography (APT). Single molecule fluorescence microscopy and X-ray excited optical fluorescence (XEOF) were further employed to follow the spatio-temporal changes in reactivity of distinct H-ZSM-5 zeolite crystals – namely, parent H-ZSM-5-P, mildly steamed H-ZSM-5-MT, severely steamed H-ZSM-5-ST crystals, and H-ZSM-5-based fluid catalytic cracking (FCC) particles.

In **Chapter 2** we have introduced three distinct types of large H-ZSM-5 crystals that were used as model systems with different degrees of acidity and mesoporosity. Their intergrowth structure and distribution of Al were determined by three characterization methods. μ -XRD imaging of single zeolite H-ZSM-5-P crystals resolved the crystallographic orientation of the intergrowth subunits consisting of 90° rotated crystalline domains. Subtle changes in the lattice parameters indicated predominant zoning of aluminium in the outer layers of zeolite H-ZSM-5. Al zoning was confirmed by the TOF-SIMS analysis combined with sputter depth profiling. This method further resolved significant differences in Al concentration in the near-surface regions of the parent and steamed zeolite H-ZSM-5 crystals. Interestingly, parent zeolite H-ZSM-5-P crystals exhibited depletion of Al in a 100 nm tick near-surface region, while H-ZSM-5-MT and H-ZSM-5-ST showed significant deposition of extra-framework Al in that region. A remarkable breakthrough in mapping of the

atomic distribution of Al in H-ZSM-5 was achieved by using atom probe tomography. The technique resolved the exact 3-D spatial distribution of individual Al atoms and provided unprecedented insights into their nearest neighbor statistics. By applying statistical methods it was possible to confirm the non-random distribution of Al atoms in parent H-ZSM-5-P crystals. The atomic maps of Al in severely steamed H-ZSM-5-ST crystals revealed significant clustering of Al atoms and their migration towards the regions of high concentration of extra-framework Al.

The impact of structural properties on the reactivity of zeolite H-ZSM-5 crystals was further studied in **Chapter 3**. Single molecule fluorescence methodology based on the detection of stochastic catalytic turnovers was used to localize individual fluorescent products formed upon the reaction on Brønsted acid sites. This method, based on the oligomerization of furfuryl alcohol as a fluorogenic molecule, was used to quantify the Brønsted reactivity of the three types of large zeolite crystals. The fast photobleaching of fluorescent products enabled real-time monitoring of reactivity at any provisional focal depth. As expected, H-ZSM-5-P and H-ZSM-5-MT crystals exhibited significantly higher turnover frequencies than the H-ZSM-5-ST sample. The highest values of turnover rates were recorded in the near-surface regions of H-ZSM-5-P and H-ZSM-5-MT crystals, which is the combined result of Al zoning and the slow intracrystalline diffusion of furfuryl alcohol. Interestingly, H-ZSM-5-MT crystals have shown heterogeneous distribution of surface reactivity as compared to H-ZSM-5-P crystals. The mild steaming process clearly facilitated the migration of Al species towards the surface, which resulted in an uneven uptake of reactants and two times higher average turnover rates of H-ZSM-5-MT. By simultaneous monitoring of the large crystalline volume of an H-ZSM-5-P crystal, it was possible to gain in-depth insights into the differences in reactivity of sub-micrometer zeolite domains. The analysis of their local turnover frequencies revealed substantial differences in reactivity and a non-random spatial distribution of catalytic events within the domains.

Chapter 4 introduced a novel single molecule fluorescence approach based on furfuryl alcohol as a probe molecule, in order to study the reactivity and dispersion of zeolite H-ZSM-5 domains within the highly complex and industrially relevant FCC catalyst particles. The uneven fluorescence activity of zeolite H-ZSM-5 domains and inherently low signal to noise ratio were bridged by using a combination of two single molecule fluorescence microscopy techniques, namely, nanometer accuracy by

stochastic chemical reactions (NASCA) and super-resolution optical fluctuation imaging (SOFI). The latter one appeared to be particularly useful to localize the fluctuations in fluorescence intensity originating from the catalytically active zeolite domains. Based on this method it was possible to estimate the size and turnover activity of zeolite H-ZSM-5 domains by producing the high-resolution images with significantly improved contrast. A domain size distribution showed that the majority of zeolite domains are well dispersed with diameters below 500 nm. By using the quantitative possibilities of NASCA microscopy, combined with the analysis of individual turnovers derived from the fluorescence intensity trajectories, it was possible to establish a linear relationship between the intensity of SOFI signal and the frequency of catalytic turnovers. The results disclosed significant differences in the turnover rates of zeolite domains, spanning nearly one order of magnitude in frequency.

The single molecule fluorescence methodology has been extended to the oligomerization of styrene-derived probe molecules in **Chapter 5**. The reaction was tested with 4-methoxystyrene and 4-fluorostyrene – compounds with significantly different reactivity. A combination of UV-Vis and confocal fluorescence microscopy detected several absorption and emission bands that were attributed to dimeric and trimeric carbocations. The formation of the fluorescent products of 4-methoxystyrene showed a shape-selective behavior depending on the framework environment and the accessibility of acid sites. This was confirmed in a series of control experiments in n-heptane. The less photostable dimeric species were easily formed in the micropores, whereas the highly photostable trimeric and cyclic species predominantly formed at the crystalline defects, induced by steaming or synthesis. The introduction of mesoporosity via steaming tremendously changed the fluorescence response and facilitated the formation of the photostable trimeric and cyclic species. Their outstanding photo-properties were subsequently used to visualize the accessible mesopores in H-ZSM-5-MT crystals. The reaction kinetics dramatically changed with the introduction of 1-butanol as a polar solvent. The polarity of the solvent tremendously affected the accessibility of acid sites, as 1-butanol was strongly chemisorbed. Based on a series of experiments in n-heptane and 1-butanol we have established a quantitative turnover map of surface reactivity for the studied probe molecules under the broad range of reaction conditions.

An interesting combination of X-ray microscopy and styrene photochemistry is presented in **Chapter 6**. μ -XRD imaging was used in a combination with μ -X-ray excited optical fluorescence (μ -XEOF) to visualize the crystallographic and reactivity maps of the steamed zeolite H-ZSM-5-ST crystals. The XEOF emission spectra showed remarkable similarities with the conventional fluorescence spectra of the carbocationic species. Steaming of the crystals has led to significant dealumination of the zeolite framework and predominant formation of the cyclic species. Principal component analysis (PCA) showed that the inner regions of the steamed H-ZSM-5-ST crystals exhibited stronger resistance to steaming, while the outer regions were more prone to dealumination due to the initially higher Al concentration. The reactivity of the crystal as measured by XEOF was clearly reflected by the crystallographic changes in the intergrowth and the extent of dealumination of the individual subunits. The detailed analysis of the strain in the crystals indicated an uneven effect of steaming on a and b lattice parameters of H-ZSM-5-ST, causing more damage along the sinusoidal pores.

7.2 Concluding Remarks

Zeolite catalysis is determined by its structural properties and a complex interplay of numerous physicochemical phenomena that take place during a catalytic process. Research interests in this field span from the atomic scales (picometers) to the scales of catalytic reactors (meters), from fast bond making/breaking processes (femtoseconds) to slow catalyst deactivation timescales (hours, days, and years). The complexity of catalyst particles can range from a nanometer-sized zeolite crystals with high crystallinity to millimeter-sized, complex catalyst bodies composed of numerous components with different functionality. Finally, reaction conditions in catalytic reactors vary from a gas to liquid phase, from ambiental to highly elevated pressures and temperatures. As a result, a catalytic process happens under very dynamic conditions, with constant changes in space and time. Ideally, these processes should be followed with high spatiotemporal resolution and sensitivity to their structural and reactivity changes. It is clear that this tremendous task requires a plethora of characterization approaches that are capable of studying various aspects of heterogeneous catalysis mentioned above.

From the fundamental perspective, the structure of a catalyst particle has a pronounced effect on the catalytic activity, selectivity, and lifetime. Therefore, it is of importance to understand the architecture of individual catalyst particles and their structural changes in space and time. Nevertheless, an *a priori* knowledge of the catalyst structure is insufficient if it does not include real-time changes in catalytic activity studied under the reaction conditions of interest. Therefore, an *in-situ* monitoring of catalytic processes is equally important, preferably at the level of individual molecules and catalytic turnovers. In this respect, this PhD thesis presents progress towards understanding the structure and catalytic reactivity of individual zeolite H-ZSM-5 crystals, by using tools that can i) resolve the crystallographic structure of a single zeolite crystal with insights into Al distribution, ii) determine the 3-D distribution of individual Al atoms and their nearest neighbors, and iii) monitor the real-time changes in catalytic activity in different solvent environments, with the sensitivity to individual, fluorescent, single molecule products.

Several techniques presented in this thesis were applied for the first time to zeolite catalyst particles. To verify their capacity to study zeolite catalysis and develop necessary procedures for their successful implementation, we opted to use well-defined, large zeolite crystals as model systems. The advantage of this model-crystal approach is that it enables fundamental studies on a well-defined, highly crystalline catalyst with structural and catalytic properties that can be easily tested at the single particle level. This approach is even more important knowing that the majority of the advanced microscopic characterization tools could hardly be applied to irregular, sub-micrometer crystallites commonly used in industrial catalysts. For these reasons, model zeolite H-ZSM-5 crystals can be used for gaining unprecedented fundamental insights into zeolite chemistry and the further development of modern characterization techniques and methodologies.

The crystallographic and compositional complexity of individual zeolite H-ZSM-5 crystals is somewhat surprising. Structure-wise, single zeolite H-ZSM-5 crystals (Figure 7.1a) consist of at least six intergrown subunits with 90° intergrowths (Figure 7.1b). This crystallographic geometry has a profound influence on the highly anisotropic diffusion and reactivity properties of individual crystals. This has been confirmed by μ -XRD in Chapter 2, single molecule fluorescence microscopy in Chapter 3, and a combination of μ -XRD/XEOF in Chapter 6. The presented

structure is actually the simplified model, as the results presented in Chapter 6 indicate the presence of more irregular intergrowths. This complexity inevitably leads to heterogeneities in reactivity, or structural changes during post-treatments, as different crystalline phases will not be equally affected. Several studies have been undertaken on different types of zeolite H-ZSM-5 crystals, but the general conclusion about their crystal growth is not yet reached. Certainly, the reasons are hidden in the conditions of zeolite synthesis and early crystallization that are not fully understood at the moment.

Another important structural aspect of the studied zeolite H-ZSM-5 crystals is their compositional complexity and heterogeneous distribution of Al atoms in the parent material. Aluminium zoning has been recognized in the past in several publications and is most probably related to the TPA structural directing agent commonly used in the synthesis of zeolite ZSM-5. Consequently, most of Al atoms are concentrated in the outer crystalline layers of H-ZSM-5 (Figure 7.1c). Interestingly, according to TOF-SIMS analysis, and previous XPS studies, the very surface (50-100 nm) of parent zeolite H-ZSM-5-P crystals is silicon-rich. This microcrystalline layer imposes an additional surface diffusion barrier on the uptake and reactivity of guest molecules. The studies in this thesis have indicated large inter-particle differences in reactivity of individual zeolite H-ZSM-5-P crystals. It remains unanswered whether these differences are imposed by surface diffusion barriers or by other compositional heterogeneities.

The particular distribution of Al has a profound effect on the success of steaming, which was visible on the examples of the mildly steamed H-ZSM-5-MT and severely steamed H-ZSM-5-ST zeolite crystals. Single molecule fluorescence microscopy of the studied zeolite crystals has provided a wealth of quantitative insights into the reactivity patterns of the parent and steamed zeolite H-ZSM-5 crystals. The results of the reactivity measurements corroborate nicely with TOF-SIMS sputter-depth profile analysis and previous HR-SEM studies. For instance, mild steaming only partially dealuminates the surface regions of H-ZSM-5 crystals, but seemingly not the deeper layers. This led to enhanced diffusion of furfuryl alcohol and higher near-surface turnover rates, but also created large differences in the permeability of the surface layers due to deposition of extraframework Al (Figure 7.1d). In contrast, severe steaming resulted in almost complete dealumination of the zoned Al as evidenced by TOF-SIMS analysis and very low turnover frequencies in the near-surface regions.

Notably, some Brønsted acidity was preserved in the inner regions of the crystals (Figure 7.1e) where we consistently observed higher turnover rates. Although counterintuitive at first sight, the observed trends are related to the gradient in Si/Al ratio, as dealumination in Al-rich regions proceeds easier than in the regions with low Al concentration. The predominant dealumination and clustering of Al atoms is mapped in great detail with atom probe tomography. The clusters and elongated patches of extra-framework Al were found to form during the steaming process. Clearly, these observations have vast implications for industry-sized zeolite crystals as the porous network acts as highways for Al transport.

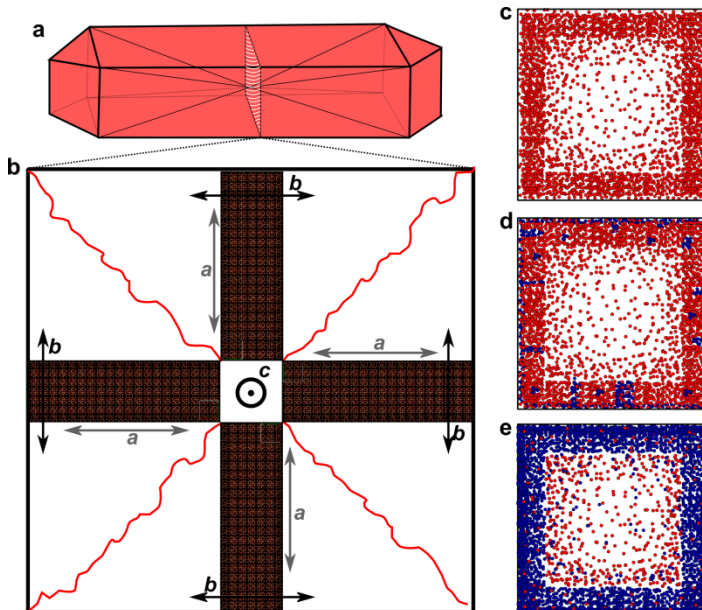


Figure 7.1. Structural and compositional complexity of large zeolite H-ZSM-5 crystals. a) The geometry of a large zeolite H-ZSM-5 crystal showing the cross-section presented in (b). b) The crystallographic architecture of the crystal as seen from the cross-section perspective (a). c-e) The distribution of Al in an c) H-ZSM-5-P, d) H-ZSM-5-MT, and e) H-ZSM-5-ST zeolite crystal. The red dots represent framework Al, the blue dots represent extra-framework Al.

Quantitative single molecule fluorescence imaging with furfuryl alcohol has proven to be a valuable method to study the Brønsted reactivity of zeolite H-ZSM-5 crystals. The possibility to follow an *in-situ* catalytic process in the liquid phase and to localize individual catalytic turnovers at any provisional focal depth in the crystal is certainly exceptional in zeolite catalysis. A very convenient feature of the furfuryl

alcohol oligomerization probe reaction is that the newly formed fluorescent molecules can be easily photobleached. In this way, an equilibrium between the reaction and photobleaching rate can be achieved and enables stable and fast monitoring of a catalytic process with 20 nm spatial resolution. For the first time, the stochastic nature of the catalytic processes in zeolites was followed by NASCA microscopy. The technique revealed details about the time-dependent changes of the turnover rates at the sub-diffraction limited zeolite domains. The concepts of NASCA microscopy could be further extended to a more complex catalytic system, namely, FCC catalyst particles based on sub- μm sized H-ZSM-5 domains. NASCA measurements typically require well-controlled reaction conditions with a good signal-to-noise ratio and therefore become challenging for highly complex industrial catalysts that typically have intrinsic residual fluorescence. This limitation was overcome by the introduction of the SOFI method. This approach appeared to be a good alternative for imaging of nanoscopic zeolite domains of FCC catalyst particles, as it can measure the intensity of fluorescence fluctuations in a region of interest, which correlates nicely with the frequency of catalytic turnovers (fluorescent bursts) at individual zeolite domains. In addition to this, the method produces markedly improved, high-contrast images of the catalytically active zeolite domains.

A development of fluorogenic reactions capable to study different aspects of zeolite chemistry is of equal importance. In this respect, the oligomerization of styrene-derived molecules has proven to be a very interesting and versatile probe reaction to study Brønsted reactivity of zeolite H-ZSM-5. The formation of different reaction products depending on the density of framework defects and the possibility to study the fluorescence of individual molecules over extended periods of time opens new possibilities to explore host-guest interactions and proton-transfer processes in different solvent environments. Furthermore, tuning the reactivity by introduction of different substituents offers a broad range of reaction conditions where this probe reaction can be used. The implications of the studied chemistry are generalized in Chapter 6. The similar photo-chemistry observed at the single molecule level was extended to X-ray excited optical fluorescence method. The combination of X-ray microscopy and styrene photochemistry represents an interesting approach to study the relationship between the local structure and catalytic performance of zeolite-based catalysts.

The techniques presented in this PhD thesis represent a significant improvement in efforts to localize Al atoms and Brønsted acidity in zeolite H-ZSM-5. It is however important to note that they provide only complementary, but not identical information. For instance, μ -XRD can only visualize *crystalline* domains and expansion of the crystalline lattice due to the presence of framework Al. Single molecule fluorescence methods are capable of localizing catalytic events only at *Brønsted acid sites*, i.e. at framework Al sites. On the other hand, the TOF-SIMS analysis and APT method can detect the *total* amount of Al, but not its chemical state (i.e. framework vs. extra-framework Al). Therefore, the information from these techniques should be ideally combined in order to derive quantitative structure-performance relationship.

7.3 Future Perspectives

A challenge for the rational design of better-performing zeolites is to tune the number, distribution, and nature of acid sites, as well as to facilitate the molecular diffusion of reactants and products via the formation of mesopores. This challenge is strongly dependent on insights into the molecular processes and spatiotemporal changes taking place within individual catalyst particles. It is clear that real-time changes in reactivity of zeolite catalyst particles remain challenging to be measured by conventional ensemble-averaging characterization methods, such as NMR, IR, UV-Vis, or X-ray spectroscopy. Many microscopic techniques were introduced in the last decade, but the majority of the methods are still limited by their low sensitivity and spatial resolution. As a consequence, inherent intra- and inter-particle heterogeneities may pass unnoticed despite significantly altering the catalytic activity in space and time. Therefore, in order to understand how the synthesis of zeolite influences its catalytic performance, it is of fundamental importance to further comprehend the nanoscopic differences in the acidity and reactivity of single zeolite particles. In this respect, the methods described in this thesis present a step forward towards zooming into the structure and molecular processes taking place in zeolite particles.

The presented arsenal of the techniques should help understanding the effects of zeolite synthesis on the catalytic performance of individual zeolite particles. Future efforts should be directed towards improved *synthesis procedures* that can control the

structure and composition of zeolite crystals, as discussed in the Concluding Remarks. A successful zeolite synthesis should ideally include: i) selectivity towards specific intergrowth structures; ii) better control over aluminium zoning and T-site distribution; iii) quantitative conversion of the synthesis mixture into highly crystalline particles without any residual oxidic material that may hamper surface accessibility; and iv) better control of the post-synthesis modifications, such as steaming and acid/base leaching.

Furthermore, understanding zeolite synthesis should be accompanied with mechanistic insights into their reactivity. In this respect, *theoretical studies* are equally important as they are needed to interpret the spectroscopic information, as discussed example for the styrene-derived carbocations. The nature of reactive sites and their reactivity should be studied with periodic DFT calculations. It is most likely that the advancements in this field will be crucial for the interpretation of experimental results, considering the nature, complexity, and diversity of catalytic pathways in zeolites. Finally, to bridge the material gap, the information from the single crystal model systems should be translated into more realistic, industrial catalyst particles. This challenge does not seem feasible at the moment for the majority of the available characterization techniques. However, the experimental approaches presented in this PhD thesis can be readily performed on significantly smaller, sub- μm -sized single zeolite crystals. The information from these studies could then be implemented into the more efficient engineering of catalytic processes.

It is almost certain that the experimental approaches demonstrated in this PhD thesis will continue to increase our understanding of zeolite catalysis at the level of single particles, molecules, and atoms. This being said, it is important to understand their potential to disclose numerous aspects of acid-catalyzed chemistry in zeolites. The synchrotron-based μ -XRD technique allows for creating diffraction intensity maps of single zeolite crystals with high angular resolution and sensitivity to chemical composition gradients. Furthermore, the penetration depth of hard X-rays could be utilized to study catalytic processes under relevant *in-situ* conditions. This would facilitate our understanding of the single-particle crystallography and changes in lattice parameters due to gradients in the composition and chemical reactivity. With the constant improvements in the resolution and brilliance of synchrotron sources, when combined with XEOF and styrene-based probe reactions, X-ray microscopy can be

used to study directly the structure-performance relationship of individual zeolite crystals.

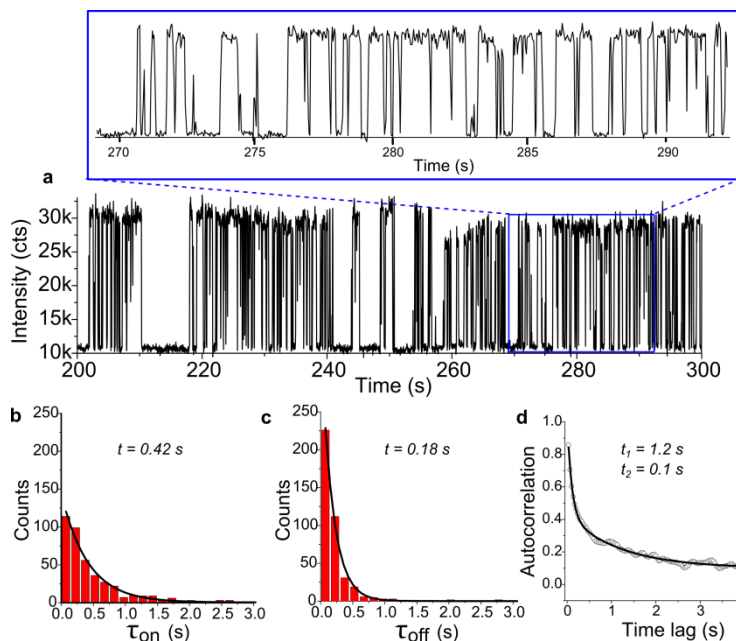


Figure 7.2 The single molecule fluorescence trajectory of an exemplified emitter of 4-methoxystyrene, formed in an H-ZSM-5-MT zeolite crystal in n-heptane. a) Fluorescence intensity trajectory of the molecule with zoom-in illustrating the temporal dynamics of on/off states. b,c) Distribution of the bright t_{on} (b) and dark t_{off} times (c) measured for the single molecule trajectory shown in (a). d) Autocorrelation function for the same trajectory. The values of t indicate time constants for the fitted exponential decays.

The atomic and molecular perspectives of catalytic processes are essential for understanding the structure-reactivity relationships in single catalyst particles. The APT method offers a lot of prospect for the atomic, structural characterization of zeolite-based heterogeneous catalysts currently used in chemical and oil-refining industries. Furthermore, it has the potential to answer some fundamental questions of zeolite science, such as, T-site distribution and nearest-neighbor atomic distributions that may play an important role in understanding the atomic coordination of Al in zeolites during synthesis, steaming, and deactivation. Quantitative single molecule fluorescence microscopy methods can quantify the reactivity of zeolite domains even in structurally complex catalyst particles. NASCA microscopy has already shown the capability to quantify and visualize large inter-particle differences in reactivity of industrial catalysts. The SOFI methodology can quickly assess the distribution and

activity of zeolite domains, producing background-free images even in the demanding experimental conditions of high background fluorescence. The improvements in this field are certainly a matter of time, as high-resolution in 3-D (< 50 nm) can be routinely achieved in single molecule experiments. The mentioned single molecule fluorescence microscopy methodologies are promising to study the proton and hydride transfer processes in different molecular environments, as demonstrated for the styrene oligomerization reaction. The exceptional photostability of the formed photo-products can be used to follow their temporal dynamics and time-scales of their interactions with the zeolite framework environment, as illustrated for an individual fluorescent molecule in Figure 7.2. Developing new fluorescent probes, sensitive to particular chemical features of single catalyst particles, such as the strength and accessibility of Brønsted and Lewis acid sites in zeolites, and redox sites of metal catalysts, represents an important aspect of future research. In this respect, single molecule fluorescence microscopy has the potential to disclose numerous spatiotemporal aspects of heterogeneous catalysis and accumulate the knowledge hidden behind the ensemble averaging of bulk characterization methods.

7.4 Nederlandse Samenvatting

De katalytische activiteit, selectiviteit en stabiliteit van een katalysatordeeltje worden sterk bepaald door zijn structuur en samenstelling. Het is daarom van groot belang de precieze opbouw van individuele katalysatordeeltjes te begrijpen en hun structurele veranderingen in ruimte en tijd te volgen. Meer specifiek is de kennis van de initiële katalysatorstructuur onvoldoende wanneer real-time veranderingen in de katalysatorstructuur en katalytische activiteit optreden tijdens reactie. Het in-situ monitoren van katalytische processen is daarom essentieel, bij voorkeur op het niveau van individuele moleculen. Dit proefschrift zet een belangrijke stap voorwaarts in het doorgronden van de lokale structuur en reactiviteit van zeolietkristallen. Hiertoe werd gebruik gemaakt van een aantal methodes die i) de kristallografische structuur van een individuele zeolietkristal bepalen en tegelijkertijd inzicht verschaffen in de verdeling van aluminium atomen; ii) de 3-D concentratie van individuele aluminium atomen en hun naaste buren bepalen, en iii) real-time veranderingen in katalytische activiteit kunnen waarnemen met een gevoeligheid voor individuele moleculen.

Het centrale thema van dit proefschrift is het ontrafelen van de chemie van zeoliet H-ZSM-5 op het niveau van individuele deeltjes, moleculen en atomen. De kristallografische en atomaire structuur van H-ZSM-5 zeolietkristallen werd bestudeerd door micro-diffractiebeeldvorming (μ -XRD), vluchttijd secundaire ionen massaspectrometrie (TOF-SIMS) en atomaire probe tomografie (APT). Hoge resolutie fluorescentiemicroscopie en röntgenstraal geëxciteerde optische fluorescentie (X-ray excited optical fluorescence, XEOF) werden gebruikt om de reactiviteitsveranderingen in ruimte en tijd van verschillende types H-ZSM-5 zeolietkristallen te volgen, namelijk verse H-ZSM-5-P, licht gestoomde H-ZSM-5-MT, en sterk gestoomde H-ZSM-5-ST kristallen, en H-ZSM-5 bevattende partikels gebruikt voor vloeibaar katalytisch kraken (Fluid Catalytic Cracking, FCC).

In **Hoofdstuk 2** werden drie verschillende soorten H-ZSM-5 zeolietkristallen geïntroduceerd als modelsystemen met verschillende gradaties van zuurheid en mesoporositeit. Hun vergroeiingsstructuur en de precieze verdeling van aluminium atomen werden bepaald door drie karakteriseringsmethodes. μ -XRD beeldvorming van een individueel H-ZSM-5-P zeolietkristal ontrafelde de kristallografische oriëntatie van de vergroeiingsstructuur, bestaande uit 90° geroteerde kristaldomeinen.

Subtiele veranderingen in de roosterparameters wezen op een aanrijking van aluminium atomen in de buitenste lagen van de H-ZSM-5 zeolietkristallen. Deze lokale aanrijking werd bevestigd door de TOF-SIMS analyse gecombineerd met verstuivingsdiepteprofilering. De laatstgenoemde methode was eveneens in staat significante verschillen in aluminium concentratie te detecteren nabij het kristaloppervlak van de verse en licht gestoomde H-ZSM-5 zeolietkristallen. Verse H-ZSM-5-P zeolietkristallen vertoonden een afwezigheid in aluminium tot 100 nm onder het zeolietoppervlak, terwijl de licht en sterk gestoomde zeolietkristallen in die regio een significante accumulatie van aluminium buiten de zeolietstructuur tentoonspreiden. Een opmerkelijke doorbraak werd gerealiseerd door het gebruik van atomaire probe tomografie. Met behulp van deze techniek werd het mogelijk om een driedimensionale scan van aluminium atomen in een H-ZSM-5 zeolietkristal te maken. Deze techniek achterhaalde de exacte ruimtelijke verdeling van individuele aluminium atomen met nanometer resolutie en leverde fundamenteel nieuwe inzichten op in de naaste atoomburen. Meer specifiek was het mogelijk om de precieze verdeling van aluminium atomen in verse H-ZSM-5-P kristallen te bevestigen door toepassing van statistische methodes. De 3-D verdeling van aluminium atomen bij een sterk gestoomd H-ZSM-5-ST kristal duidde op de clustering van aluminium atomen alsook hun migratie naar andere gebieden in het zeolietkristal met een hoge concentratie van Al buiten de zeolietstructuur.

De invloed van de structurele eigenschappen van H-ZSM-5 zeolietkristallen op de lokale reactiviteit werd in meer detail onderzocht in **Hoofdstuk 3**. Hierbij werd een methode gebruikt om individuele fluorescente producten te lokaliseren die gevormd werden op zure Brønsted reactieplaatsen in het zeolietkristal. Meer concreet werd door middel van stochastische katalytische omzetting de oligomerisatie van furfurylalcohol gerealiseerd, resulterend in een fluorogeen molecule dat zeer precies kon worden gelokaliseerd met behulp van fluorescenciemicroscopie. Deze methode werd gebruikt om de reactiviteit van de drie eerder genoemde types H-ZSM-5 zeolietkristallen te kwantificeren. De snelle destructie van fluorescente producten onder invloed van laserlicht maakte het mogelijk om de reactiviteit in real-time te volgen op verschillende kristaldieptes. Zoals verwacht vertoonden de H-ZSM-5-P en H-ZSM-5-MT zeolietkristallen significant hogere omzetfrequenties dan H-ZSM-5-ST. De hoogste omzetsnelheden werden waargenomen nabij het kristaloppervlak van

H-ZSM-5-P en H-ZSM-5-MT zeolieten. Daarnaast vertoonden H-ZSM-5-MT zeolietkristallen ook een meer heterogene oppervlaktereactiviteit dan H-ZSM-5-P zeolietkristallen. Het milde stoomproces vergemakkelijkt duidelijk de migratie van aluminium atomen vanuit het zeolietkristal naar het oppervlak toe.

In **Hoofdstuk 4** werd een nieuwe meetmethodiek geïntroduceerd op basis van fluorescentiemicroscopie. Hierbij werd de zuur-gekatalyseerde oligomerisatie van furfurylalcohol gebruikt als probe om de lokale reactiviteit en verdeling van H-ZSM-5 zeolietdomeinen te bestuderen binnen een hiërarchisch gestructureerd en industrieel relevant FCC katalysatordeeltje. Twee fluorescentiemicroscopiemethodes werden hiervoor gebruikt, namelijk “nanometer nauwkeurigheid door stochastische chemische reacties” (nanometer accuracy by stochastic chemical reactions, NASCA) en “super-resolutie optische fluctuatiedeeldvorming” (SOFI). Door een combinatie van deze twee technieken werd het mogelijk om de fluorescentie-activiteit van H-ZSM-5 zeolietdomeinen en de inherent lage signaal-tot-ruisverhouding te vertalen in lokale reactiviteitsverschillen. Op basis van de SOFI methode was het mogelijk een schatting te maken van de reactiviteit van individuele H-ZSM-5 zeolietdomeinen. De gemiddelde grootte van de zeolietdomeinen was steeds kleiner dan 500 nm. Daarnaast werd een lineair verband vastgesteld tussen de intensiteit van het SOFI signaal en de omzettsnelheid van de katalytische activiteit. Ook vertoonden de resultaten significante verschillen in de omzettingssnelheden voor de individueel waargenomen zeolietdomeinen.

In **Hoofdstuk 5** werd de hoge-resolutie fluorescentiemethode – beschreven in Hoofdstuk 3 en 4 – uitgebreid naar de zuur-gekatalyseerde oligomerisatie van styreen-afgeleide probemoleculen, namelijk 4-methoxystyreen en 4-fluorostyreen. Uit de experimenten blijkt dat deze reagentia een significant verschillende reactiviteit vertonen tijdens de oligomerisatiereacties in H-ZSM-5 zeolietkristallen. Door middel van gecombineerde UV-Vis en confocale fluorescentiemicroscopie werden verschillende absorptie- en emissiebanden gedetecteerd die werden toegeschreven aan een lineaire di- en trimeer, en een cyclisch carbokation. De lokale zeolietstructuur en de toegankelijkheid van de zure reactieplaatsen in een zeolietkristal bepaalden welke fluorescerende producten van 4-methoxystyreen werden gevormd. De minder fotostabiele dimerische carbokationen werden gemakkelijk gevormd in de microporiën van het zeolietkristal, terwijl de meer fotostabiele trimeren en cyclische carbokationen

voornamelijk gevormd werden in kristallijne defecten, ontstaan tijdens stomen of synthese. Het introduceren van mesoporositeit in het zeolietrooster door een stoombehandeling had een enorme impact op de fluorescentierespons, en vergemakkelijkte de vorming van trimeren en cyclische carbokationen. De uitstekende fluorescentie-eigenschappen van deze carbokationen werden vervolgens gebruikt ter visualisatie van de toegankelijke mesoporiën in mild gestoomde H-ZSM-5 zeolietkristallen. De reactiekinetiek werd drastisch veranderd door het gebruik van 1-butanol als polair oplosmiddel. De polariteit van het oplosmiddel beïnvloedt de toegankelijkheid naar de zure reactieplaatsen in een zeolietkristal omdat 1-butanol sterk gechemisorbeerd wordt. Op basis van een reeks experimenten in n-heptaan en 1-butanol werd het mogelijk om de oppervlaktereactiviteit in kaart te brengen voor de onderzochte probemoleculen onder sterk uiteenlopende reactieomstandigheden.

Een interessante combinatie van X-stralenmicroscopie en styreen fotochemie wordt gepresenteerd in **Hoofdstuk 6**. μ -XRD beeldvorming werd gebruikt in combinatie met μ -X-stralen geëxciteerde optische fluorescentie (μ -XEOF) om de lokale kristalstructuur en reactiviteit van een vers en sterk gestoomd H-ZSM-5-ST zeolietkristal te visualiseren. De XEOF emissiespectra vertoonden opvallende gelijkenissen met de klassieke fluorescentiespectra van styreen carbokationen. Het stomen van de zeolietkristallen leidde tot sterke dealuminering van de zeolietstructuur en de vorming van cyclische styreenmoleculen. Hoofdcomponentenanalyse (PCA) toonde aan dat binnendenin sterk gestoomde H-ZSM-5-ST zeolietkristallen een sterke weerstand bestond tegen stomen. Dit staat in schril contrast met de gebieden nabij het zeolietoppervlak, dewelke meer vatbaar zijn voor dealuminering als gevolg van de initieel hogere aluminiumconcentratie. Een oorzakelijk verband kon worden vastgesteld tussen de lokale reactiviteit van het zeolietkristal, opgemeten door XEOF, en zijn lokale kristalstructuur, geobserveerd door μ -XRD. Meer specifiek werden veranderingen in de vergroeiingsstructuur van het zeolietkristal geobserveerd, alsook de graad van dealuminering van de individuele bouweenheden in het zeolietkristal. Door een gedetailleerde analyse van de ontstane roosterspanning in het zeolietkristal werd aangetoond dat het kristalrooster op anisotrope wijze vervormd werd tijdens de stoombehandeling, als gevolg van de grotere schade die werd toegebracht aan de sinusoïdale zeolietporiën.

List of Abbreviations

ACF	Autocorrelation function
AFM	Atomic force microscopy
APT	Atom probe tomography
BEA	Zeolite beta
BW	Black-white
CARS	Coherent anti-Stokes Raman scattering
CFM	Confocal fluorescence microscopy
DFT	Density functional theory
EBSD	Electron backscatter diffraction
EDX	Energy-dispersive X-ray fluorescence spectroscopy
EMCCD	Electron multiplying charge coupled device
EMSL	Environmental Molecular Science Laboratory
ESRF	European Synchrotron Radiation Facility
EXAFS	Extended X-ray absorption fine structure
FA	Furfuryl alcohol
FAU	Faujasite
FCC	Fluid catalytic cracking
FER	Ferrierite
FIB	Focused ion beam
FWHM	Full width at half maximum
HIM	Helium ion microscopy
HOMO	Highest occupied molecular orbital
H-ZSM-5	Acidic form of zeolite ZSM-5
H-ZSM-5-MT	Acidic form of zeolite ZSM-5, steamed at 773 K
H-ZSM-5-ST	Acidic form of zeolite ZSM-5, steamed at 973 K
IR	Infra-red
IZA	International Zeolite Association
LUMO	Lowest unoccupied molecular orbital
MAS-NMR	Magic-angle spinning nuclear magnetic resonance
MEL	Framework type of zeolite ZSM-11
MFI	Framework type of zeolite ZSM-5
MOR	Mordenite
MTO	Methanol to olefins
NA	Numerical aperture
NASCA	Nanometer accuracy by stochastic chemical reactions
NMR	Nuclear magnetic resonance

List of Abbreviations

NN	Nearest neighbors
PCA	Principal component analysis
PNNL	Pacific Northwest National Laboratory
PSF	Point spread function
SEM	Scanning electron microscopy
SOFI	Super-resolution optical fluctuation imaging
STEM	Scanning transmission electron microscopy
TOF	Turnover frequency
TOF-SIMS	Time-of-flight secondary ion mass spectrometry
TPA	tetrapropylammonium
TPD	Temperature programmed desorption
UC	Unit cell
UHV	Ultra-high vacuum
UV-Vis	Ultraviolet-visible
XEOF	X-ray excited optical fluorescence
XPS	X-ray photoelectron spectroscopy
XRD	X-ray diffraction
XSOCS	X-ray strain orientation calculation software
XSW	X-ray standing wave
ZSM-5	Zeolite Socony Mobil 5

List of Publications and Presentations

A. List of Publications

Z. Ristanović, J. P. Hofmann, U. Deka, T. U. Schülli, M. Rohnke, A. M. Beale, and B. M. Weckhuysen, "Intergrowth Structure and Aluminium Zoning of a Zeolite ZSM-5 Crystal as Resolved by Synchrotron-Based Micro X-Ray Diffraction Imaging", *Angew. Chem. Int. Ed.* **2013**, *52*, 13382-13386.

Featured as the ESRF Highlights 2015.

Z. Ristanović and B. M. Weckhuysen, "Breakthroughs in Hard X-ray Diffraction: Towards a Multiscale Science Approach in Heterogeneous Catalysis", *Angew. Chem. Int. Ed.* **2014**, *53*, 8556-8588.

Z. Ristanović, M. M. Kerssens, A. V. Kubarev, F. C. Hendriks, P. Dedecker, J. Hofkens, M. B. J. Roeffaers, and B. M. Weckhuysen, "High-Resolution Single-Molecule Fluorescence Imaging of Zeolite Aggregates within Real-Life Fluid Catalytic Cracking Particles", *Angew. Chem. Int. Ed.* **2015**, *54*, 1836-1840.

A hot paper of the issue and highlighted in [C₂W].

Z. Ristanović, J. P. Hofmann, G. De Cremer, A. V. Kubarev, M. Rohnke, F. Meirer, J. Hofkens, M. B. J. Roeffaers, and B. M. Weckhuysen, "Quantitative 3D Fluorescence Imaging of Single Catalytic Turnovers Reveals Spatiotemporal Gradients in Reactivity of Zeolite H-ZSM-5 Crystals upon Steaming", *J. Am. Chem. Soc.* **2015**, *137*, 6559-6568.

Featured as a cover of the journal, highlighted in JACS Spotlights and in [C₂W].

D. E. Perea, I. Arslan, J. Liu, Z. Ristanović, L. Kovarik, B. W. Arey, J. A. Lercher, S. R. Bare, and B. M. Weckhuysen, "Determining the Location and Nearest Neighbours of Aluminium in Zeolites with Atom Probe Tomography", *Nat. Commun.* **2015**, *6*, 7589.

Highlighted in [C₂W] and Chemical & Engineering News (C&EN).

Z. Ristanović, A. V. Kubarev, J. Hofkens, M. B. J. Roeffaers, and B. M. Weckhuysen, "Acid-Catalyzed Oligomerization of Styrenes as a Versatile Probe for Single Molecule Fluorescence Studies of Zeolite H-ZSM-5 Crystals", *in preparation.*

Z. Ristanović, J. P. Hofmann, M.-I. Richard, T. Jiang, G. Chanine, T. U. Schülli, F. Meirer, and B. M. Weckhuysen, "X-ray Excited Optical Fluorescence and Diffraction Imaging of Chemical Reactivity and Crystallinity in a Zeolite Crystal: Crystallography and Molecular Spectroscopy in One X-ray Shot", *submitted.*

List of Publications and Presentations

Z. Ristanović, D. Valencia, R. Y. Brogaard, U. Osbye, J. Hofkens, M. B. J. Roeffaers, and B. M. Weckhuysen, "Temporally Correlated Changes in Single Molecule Fluorescence Trajectories of Styrene-Derived Carbocations in Zeolite H-ZSM-5", *in preparation*.

S. C. C. Wiedemann, Z. Ristanović, G. T. Whiting, V.R. R. Marthala, J. Kärger, J. Weitkamp, B. Wels, P. C. A. Bruijnincx, and Bert M. Weckhuysen, "Large Ferrierite Crystals as Models for Catalyst Deactivation during Skeletal Isomerisation of Oleic Acid: Evidence for Pore Mouth Catalysis", *Chem. Eur. J.* **2016**, 22, 199-210.

D. Vasić, Z. Ristanović, I. Pašti, and S. Mentus, "Systematic DFT-GGA study of hydrogen adsorption on transition metals", *Russ. J. Phys. Chem. A* **2011**, 85, 2373-2379.

B. Oral Presentations

Z. Ristanović, G. De Cremer, M. B. J. Roeffaers, D. E. De Vos, J. Hofkens, and B. Weckhuysen, "Nanoscale Chemical Imaging of Catalytic Solids: Single Turnover Quantification of Brønsted Acid Sites in Large H-ZSM-5 Zeolite Crystals", Netherlands Catalysis and Chemistry Conference XIV, Noordwijkerhout, The Netherlands, March 2013.

Z. Ristanović, G. De Cremer, M. B. J. Roeffaers, D. E. De Vos, J. Hofkens, and B. Weckhuysen, "Quantitative Super-resolution Chemical Imaging of Brønsted Acidity in Micro- and Mesoporous ZSM-5 Zeolite Crystals", International Photochemistry Conference, Leuven, Belgium, July 2013.

Z. Ristanović, J. P. Hofmann, G. De Cremer, U. Deka, T. U. Schülli, M. Rohnke, A. M. Beale, M. B. J. Roeffaers, D. E. De Vos, J. Hofkens, and B. M. Weckhuysen, "Aluminium Zoning and Related Acidity Gradients in Large Zeolite ZSM-5 Crystals Studied on Single Particle – Single Molecule Level", Netherlands Catalysis and Chemistry Conference XV, Noordwijkerhout, The Netherlands, March 2014.

C. Invited Presentations

Z. Ristanović, "Nanoscale Chemical Imaging of Catalytic Solids: Single Turnover Quantification of Brønsted Acid Sites in Large H-ZSM-5 Zeolite Crystals", Max-Planck-Institut für Kohlenforschung, Mülheim an der Ruhr, Germany, April 2013.

D. Poster Presentations

Z. Ristanović, G. De Cremer, M. B. J. Roeffaers, J. Hofkens, and B. Weckhuysen "Single Molecule Nanoscale Chemical Imaging of Zeolites: Probing Brønsted Acid Sites using the Styrene Oligomerization Reaction", Netherlands Catalysis and Chemistry Conference XIII, Noordwijkerhout, The Netherlands, March 2012.

Z. Ristanović, J. P. Hofmann, U. Deka, T. U. Schülli, M. Rohnke, A. M. Beale, and B. M. Weckhuysen, "Micro X-ray Diffraction Imaging of a Single Zeolite ZSM-5 Crystal: Intergrowth Structure and Aluminium Zoning", Shell Centennial Analytical Conference, Amsterdam, The Netherlands, March 2014.

Z. Ristanović, A. V. Kubarev, F. Meirer, J. Hofkens, M. B. J. Roeffaers, and B. M. Weckhuysen, "Quantitative Super-Resolution Fluorescence Imaging of Reactivity in Zeolite Catalysts", International Conference on Sustainability, Utrecht, The Netherlands, October 2015.

Acknowledgements

At the end of this exciting journey, I would like to thank a number of remarkable people that have made my PhD days so enjoyable and memorable, both professionally and privately. Their presence has been constantly encouraging and without them I would not have succeeded in making this thesis. In this respect, I have been very fortunate, as I believe that the true values of life lay in people that we share life with.

Above all, I would like to sincerely thank my supervisor and promotor. **Bert**, thank you for this incredible opportunity to do a PhD in your group. I may have started like a “butterfly” but I am crossing the finish line with invaluable scientific experience. This would not be possible without your scientific guidance and supervision. I admire your way of working and constantly challenging yourself and your students with ambitious goals. Thank you for opening extraordinary scientific horizons to my inquisitive nature; the visits to Stanford and Leuven, many synchrotron-related projects and a chance to work with brilliant scientists and people – I am truly grateful for these opportunities. Our scientific endeavors seem to continue and I hope they will be equally fruitful and exciting in the future.

Two important projects have shaped this thesis and for them I would like to express gratitude to people that have provided essential support and scientific guidance. **Jan Philipp**, thank you for all the help and support with numerous publications and experiments that we had over the years. Your inspiring ideas and creative approach to science, combined with amusing beamtimes at the ESRF, have made a great impression on me. **Maarten** and **Johan**, this thesis would have looked totally different if it were no experiments in Leuven. Thank you for the generous microscopy time and always welcoming atmosphere that I had in your group. Maarten, I greatly appreciate numerous skype discussions and your brilliant comments that have always challenged my knowledge of (single molecule) chemistry – and this continues to be the case.

The scientific content described in this thesis would not be present without help of numerous colleagues and collaborators. **Florian**, our data wizard, the group is very fortunate to have you and I am very happy that this is partially my fault. Your brilliance and enthusiasm to discuss science are truly inspiring. **Gert**, **Alexey**, and **Peter**, thank you for your dedicated help with the experiments, *Localizer*, and manuscripts. **Tobias**, thank you for hosting us on several occasions and providing the

“the last minute before a shutdown” beamtimes at ID01. **Andy**, it was a great pleasure working with you in the group, I learned a lot from you. **Marcus, Ilke, Danny, Simon, Maarleen, Frank, Upakul, Marie-Ingrid, Gilbert, and Tao**, thank you all for the great scientific contribution to this thesis. **Sophie**, I enjoyed working together on your fatty acid project and having conversations on a train to Rotterdam.

Dymph and Monique, there are no words to thank you for your always present help and welcoming attitude. I am truly thankful for all the time you have invested in unreservedly supporting all of us. **Emke, Iris, and Ines**, I appreciate your help and professionalism during writing of my thesis.

Ad^E, all our beamtimes and long night shifts at synchrotrons were very enjoyable – I still remember the welcoming cup of thee before my interview in the group and appreciate your help and patience with practicing Dutch. **Ad^M, Marjan, and Fouad**, thank you for the assistance with many inquiries.

Zafer, Gareth, Christoph, Dina, Marta, Genziana, and Raphael, your help with the beamtimes in Grenoble was essential. **Rasmus and Diego**, although we did not (yet!) succeeded in publishing the theoretical part of the styrene chemistry I am very thankful for all the discussions that we had on this topic. **Jarich and Jogchum**, thank you for being my first students and doing a great job even when I was not around.

Nanorangers, working hard in the lab requires good spirits and people always ready to help and laugh. **Javi, Lukasz, Davide, Inge, Luis, Qingyun, and Hendrik** – thank you for the most welcoming atmosphere and great times in the microscopy lab. The lab keeps on doing great with great people and scientists: **Gareth, Joris, Frank, Ramon, Marjolein, Katinka, Abhishek, Tom, Joel, Suzanne, and Özgün**.

Javi, I am very thankful for all your wise words of advice in any situation and friendly chats that we had over the years. I wish you, **Sandra, and Elisa** lovely future. **Hendrik**, I greatly enjoyed our SOLEIL beamtrips and numerous lively and humorous discussions at work and out of office. Your advice and practical understanding of many situations were comforting. **Luis**, driving together every day to work, Las Vegas and Death Valley, and philosophical debates in the parks of Palo Alto will always stay close to my heart.

During summer 2012, I spent exciting 4 months as a visiting scholar at the SUNCAT center and SSRL synchrotron facility of Stanford University. **Joy and Jens**, thank you for your hospitality and great scientific experience that I had in your research groups.

My love and passion for science are not accidental and for this I am deeply grateful to all my teachers of physics and chemistry. Duboko sam zahvalan svojim nastavnicima hemije i fizike u osnovnoj i srednjoj školi, Olgi Antonijević, Veri Tomašević, Zori Ostojić i Milenku Stankoviću. Veliku zahvalnost za akademsko obrazovanje dugujem izuzetnim profesorima na Fakultetu za fizičku hemiju, a za posebnu inspiraciju, prof. dr. Miljenku Periću, prof. dr. Ljiljani Damjanović i dr. Igoru Paštiju.

A very strong influence on my scientific education had Research Center Petnica where I have been attending chemistry classes and later on became a teaching associate. Drage **Nina i Buba**, hvala vam za sve divne seminare hemije koji su mi usadili ljubav prema nauci.

I have been very fortunate to share offices with great colleagues. **Inés** and **Siswati**, thank you for the friendly atmosphere in my first office. The working environment changed completely with moving to DdW and I was quickly (and at the moments literally) surrounded by **Carlo, Daniel, Thomas E., Joe, Hendrik, Peter, Jesper, Ilona, Rob, Yuen, Raphael, Mita, JX, Korneel, Thomas H., Qingyun, Wenhao, Evelien, Clare, Arjen, Arjan, Mustafa, Boyang, and Jelle**. Quite friendly (and somewhat distracting!) working environment. Thank you guys for all great moments that we had working together! Finalizing the thesis in the new office was enjoyable with **Manuel, Tom, Tao, Thomas, Yann, Peter N., and Pierre**.

The size of our group makes it possible to have an excellent football team! Disregarding football skills, for which I am quite a demanding person, I truly enjoyed playing with **Thomas E. – Carlo, Fouad, Javi, Jesper, Hendrik, Sam - Joe, Roy, Rob, Wenhao, Thomas vH. – Gonzalo, Gareth, Wouter**. What has started as “20 seconds of fun” has become something very important in our daily lives over the years – a real matter of friendship. The team chemistry was translated off the football pitch and was present during many out-of-work activities.

I have a feeling that the group has doubled the size since I came to Utrecht. My lengthy stay in the group has witnessed many remarkable people. I would like to thank all of them for the great atmosphere in the group, numerous social gatherings and uitjes. Special mention in this booklet for **Zafer, JX, Hirsa and David, Jinbao, Dilek, Fernando, Sam, Fiona, Ana, Ara, Inés, Annelie, Tamara, Rogier, Sankar, Selvedin, Matti, Pieter M., Sang-Ho, Pieter B., Monica, Rosa, Marianna, Mozzafar, Nazila, Oscar, Pascal, Pasi, Gang, Peter B., Anton, Egor, Michal, Miguel, Homer, Baira, Iván, Jamal, Donglong, and Matthias**.

My last words go to my friends and family. Moving to a new country definitely makes you home-sick. Away from work, it was never boring with many compatriots and long-time friends. **Cane, Daca, Stefan, Nemanja, Milica, Marija, Manas, Ana, Ivan, Nevena, Maja, Cobe, Jelena, and Eli**, thank you all for great memories.

Trajko, Kalanj, Pope, Slavka, Sale, Jeco, Jeco i Pero, hvala vam za nezaboravne studentske dane, za uvek prisutnu podršku i vreme da se vidimo. Iako ste nedostajali svih ovih godina, drago mi je da naše prijateljstvo ne poznaje vremenske granice. Posebnu zahvalnost za jake mentalne treninge i naviku da brojne poteze vučem u poslednjim minutima dugujem mojim šahistima iz Studenjaka: **Milančetu, Danijelu, Miroslavu, Ivani, Novaku, Radu, Milici, Borku i Krpu**.

Joco, koliko smo samo priča ispredali o životu i Srbiji uz svakodnevne kafe i ručkove. Jos od davnog Klaustala i dalje se držimo zajedno u istoj grupi. Hvala ti za svu podršku i savete tokom pisanja doktorata. Želim ti neizmernu radost i uživanje uz divnu **Milu**!

Carlo, we had so much fun sitting across each other. I finally must admit it now – your football skills and sense of humor were always very entertaining. I miss you in the office but I am very happy that you and **Gosia** are still around in Utrecht!

Joe, brate mili, from the first days of our PhD we went through many exciting and memorable moments together and you were always a great friend and support. Whenever I was struggling you were there to show me the bright side of things and to make me aware of what I can achieve. Our passion for football and sports – although not many people come close to you in that – has bonded us even stronger. I wish you and dear **Elena** great life in Brussels.

Stefane, od bezbrižnih gimnazijskih dana do ženidbe, kumstva i mladih naraštaja! Malo toga mogu dodati za nekoga uz koga se slave svi bitni događaji u životu. Tvoje prisustvo i životni saveti svih ovih godina su neprocenjivi. Veliko hvala za sve, kume!

Mito, dragi druže i cimeru velikog srca, toliko toga smo proživeli zajedno. Hvala ti za uvek vedar pristup životu i bratska ohrabrenja kada su mi najviše trebala – mnogo mi je značilo tvoje prisustvo u Utrehtu svih ovih godina. Oduvek sam se divio tvojoj praktičnosti, nadljudskim treninzima za Ironman-a, a ponajviše pitama i sarmama. Srećan sam sto ćemo stajati jedan za drugoga na samome kraju naših doktorata, hrabro i ponosno! Želim ti svu sreću sa novim poslom i životom u našoj dragoj Srbiji.

Moji najdraži **Ristanovići, Sparići i Krupeži**, hvala vam za sve divne uspomene i nesebičnu podršku u mnogim situacijama. Jedva čekam da vas sve ponovo vidim!

Drage Šaponje, **teta Milena** i **čika Mirko**, neizmerno sam vam zahvalan za svu pomoć i srdačnost svih ovih godina. Teta Milena, koliko ste me puta samo “odmenili” da bih napisao ovu knjigu – i to uz najbolju srpsku hranu! Ljubav, pažnja i požrtvovanost koju posvećujete Aleksi je neizmerna. **Marinko, Ivana** i **Vito**, život u Rotterdamu je mnogo zanimljiviji uz vaše prisustvo. Nastavljamo da rastemo zajedno!

Bato i **seko**, toliko ste mi nedostajali svih ovih godina! Siguran sam da znate sa kakvim emocijama i uspomenama pišem ove redove. Hvala vam za najdivnije detinjstvo i neograničenu ljubav. Kada mislim o vama uvek se setim Makinih nevidljivih džempera satkanih od ljubavi i radosti i shvatim da sam jako srećan i ponosan što vas imam. Želim vam svu sreću sveta i znajte da vas vaš najstariji brat voli svim srcem.

Mama i **tata**, ovu knjigu i životni uspeh posvećujem vama i vašoj nesebičnoj borbi za našu porodicu. Sada kada se penjem na poslednji akademski stepenik znam da nijedna diploma nije vredna koliko životne vrednosti i ljubav prema porodici koju ste nam usadili. Tata, hvala ti što si me stalno podsećao koliko su obrazovanje i ljudskost bitni u životu. Mama, do neba sam ti zahvalan za sve životne borbe koje si vodila zbog mene, za neograničenu majčinsku ljubav i požrtvovanost. Ti si moj najveći heroj!

Maki i **Aleksa**, moji životi, kako sam ponosan na našu porodicu. Maki, znam koliko si nestrpljiva da vidiš ove redove, ali istina je da ljubav koju osećam prema tebi i Aleksi ne mogu uobičiti nikakvim rečima. Hvala ti što si moja najveća snaga, što si me hrabrilas i pomagala na ovom, na momente izuzetno napornom, poduhvatu zvanom doktorat. Hvala ti i na najvećem blagu koje si nam podarila – našem Aleksi i našoj porodici. Jos jedna životna etapa je gotova a ja sam jako srećan jer znam da imam vas i da ćemo zajedno koračati kroz sve životne izazove. Jedva čekam naše sledeće putovanje i Aleksinih “1000 zašto, 1000 zato”!

Jedan život malo je...

About the Author

Zoran Ristanović was born on November 26, 1985 in Čačak, Serbia. In 2004, he finished Gymnasium in Čačak as a valedictorian with distinguished achievements in physics and chemistry. In 2009, he obtained a Diploma (MSc equivalent) from the Faculty of Physical Chemistry, University of Belgrade. During this period he was a recipient of several awards and fellowships for extraordinary achievements during studies and extra-curricular activities. His diploma thesis entitled "*DFT Study of Hydrogen Adsorption on (111) Surfaces of FCC Transition Metals*" was awarded the best thesis in natural sciences from the University of Belgrade. In 2008, he completed an internship at the Institute of Metallurgy, TU Clausthal, Germany, working on the electrochemical corrosion of aluminium alloys. From 2004 to 2010 he has been active in the promotion of science among high school students and teaching chemistry in Petnica Science Center, Serbia.

In 2010 he started a PhD project in the Group of Inorganic Chemistry and Catalysis at Utrecht University, under the supervision of Prof. dr. ir. Bert Weckhuysen. The results of this research are in part described in this thesis and published in scientific journals. During this time, he has been a visiting scholar at KU Leuven and Stanford University for the total period of 6 months. From September 2015, Zoran is appointed as a postdoctoral fellow in the same group. His main research interests are in the field of functional materials and applied visible and X-ray microspectroscopy.

Away from science, Zoran likes traveling and enjoying time with his family and friends. He is a passionate football and chess player.

...

*A na umu uvek da ti Itaka bude.
Tamo da stigneš tvoja je sudbina.
Al' nipošto ne žuri na putu tom.
Bolje nek' mnogo godina traje
i da na ostrvo kao starac stigneš već.
Sa blagom koje si na putu stekao
ne očekujući išta da ti Itaka da.*

*Lepo putovanje Itaka ti je dala.
bez nje nikada na put krenuo ne bi.
Ona ništa više nema da ti da.*

*Siromašnom ako je nadеš,
znaj, prevarila te nije.
Mudar si postao, iskustvo stekao,
i znaćeš već šta te Itake znače.*

Konstantin Kavafī